Ceramic membranes for industrial wastewater treatment: Fabrication, membrane fouling and fouling characterization

Qin, G.

DOI
10.4233/uuid:c494c0c6-e111-4dc9-8757-e2f3d5e2d56f

Publication date
2025

Document Version
Final published version

Citation (APA)
Qin, G. (2025). *Ceramic membranes for industrial wastewater treatment: Fabrication, membrane fouling and fouling characterization*. [Dissertation (TU Delft), Delft University of Technology]. https://doi.org/10.4233/uuid:c494c0c6-e111-4dc9-8757-e2f3d5e2d56f

Ceramic membranes for industrial wastewater treatment: Fabrication, membrane fouling and fouling characterization

Guangze Qin

Ceramic membranes for industrial wastewater treatment: Fabrication, membrane fouling and fouling characterization

DISSERTATION

To obtain

the degree of doctor in environmental engineering at the Delft University of Technology,

on the authority of the rector magnificus,

Prof. dr.ir. T.H.J.J van der Hagen

chair of the Board for Doctorates,

to be publicly defended on

Thursday 20 November year 2025 at 12:30 o'clock

by

Guangze QIN

Master of Science in Applied Earth Sciences, Delft University of Technology

Born in Shan Dong, China

This dissertation has been approved by the promotors.

Composition of the doctoral committee:

Rector Magnificus,	Chairperson
Prof.dr.ir. L.C. Rietveld	Delft University of Technology, promotor
Dr.ir. S.G.J. Heijman	Delft University of Technology, promotor

Independent members:

Prof.dr.ir. J.B. van Lier	Delft University of Technology
Prof.dr. Y.C. Dong	The Chinese University of Hong Kong, China
Prof.dr.ir. M. Vanoppen	Universiteit Gent, Belgium
Dr.ir. A. Haidari	Iv-Water b.v., NL

Reserve members:

Prof.dr.ir. D. van Halem	Delft University of Technology

This research was conducted at the Sanitary Engineering Section, Department of Water Management, Faculty of Civil Engineering, Delft University of Technology, The Netherlands, and was financially supported by the China Scholarship Council.

Cover by: Guangze Qin

Keywords: Silicon carbide membrane; Membrane fouling; Surface charge; DLVO model

ISBN(Paperback/softback): 978-94-6496-493-6

ISBN(E-book): 978-94-6518-182-0

An electronic version of this dissertation is available at https://repository.tudelft.nl/

Table of Contents

Summary

Rapid industrialization and urbanization over the past two decades have made water scarcity and water pollution the most serious and persistent challenges for people around the world. Membrane technologies have emerged as crucial solutions to tackle the global water shortage crisis, especially for the re-use of industrial effluents. Inorganic ceramic membranes are gaining increasing attention in industry due to their high mechanical and chemical stability, hydrophilicity, water permeability, antifouling abilities. Silicon carbide (SiC) membranes have shown the lowest fouling compared with other ceramic membranes. Therefore, recently, new methods have been developed to fabricate SiC membrane at a low temperature of 860 ºC, using low pressure chemical vapor deposition (LPCVD).

This thesis focuses on the fabrication and application of SiC-coated membranes, detailing their preparation via LPCVD and their performance in treating nano-sized oil-in-water (O/W) emulsions, real produced water, and laundry wastewater.

First of all, a novel approach is presented for effectively separating microemulsions via SiC (3C-SiC)-coated alumina (Al_2O_3) membranes, fabricated based on LPCVD. With the increase in deposition time, up to 25 min, the pore size of the membranes decreased from 41 nm (without deposition) to 33 nm (deposition time of 25 min). The polycrystalline 3C-SiC-coated membranes also showed an improved hydrophilicity (water contact angle of 15º) and highly negatively charged surfaces (-65 mV). Oil-in-water (O/W) microemulsions filtration experiments were carried out at a constant permeate flux (80 $Lm^{-2}h^{-1}$) for six cycles with varying deposition time, pH, surfactant types, and pore sizes. The fouling of the SiC-coated membrane was, compared to the Al_2O_3 membrane, effectively mitigated due to the enhanced electrostatic repulsion and hydrophilicity. Surfactant adsorption mainly occurred when the surface charge of the microemulsion and the membranes were opposite. Therefore, the surface charge of the Al_2O_3 membrane changed from positive to negative when soaked in negatively charged microemulsions, whereas SiC-coated membranes remained negatively charged regardless of surfactant type. The membrane fouling was alleviated when the membrane and oil droplets had the same charge.

Subsequently, the effects of the ionic strength (1, 20, and 100 mM) as well as different surfactants in O/W emulsions on the membrane fouling were studied. Four surfactants, including sodium

dodecyl sulfate (SDS, anionic), alkyl polyglycoside (APG, non-ionic), cetyltrimethylammonium bromide (CTAB, cationic) and N-dodecyl-N,N-dimethyl-3-ammonio-1-propanesulfonate (DDAPS, zwitterionic), were selected for this study. The Derjaguin-Landau-Verwey-Overbeek (DLVO) and extended DLVO (XDLVO) models were used to quantify interactions between the membrane-oil droplet and deposited oil layer-oil droplet surfaces and to compare these interactions with the fouling experiments. The (X)DLVO interaction energies of the membrane-oil droplet exhibited a strong agreement with the fouling tendencies at 1 mM salinity. The SiC-deposited membrane showed less (ir)reversible membrane fouling than the Al_2O_3 membrane when filtering O/W emulsions stabilized with SDS, APG, or DDAPS. The DLVO model predicted a higher tendency at higher salinity levels during the filtration of SDS, APG, or DDAPS-stabilized O/W emulsions and a decreased fouling tendency for CTAB-stabilized emulsion with the SiC-deposited membrane. However, at higher salinity levels, the XDLVO energy barrier was affected by both the repulsive electrostatic double layer (EL) interaction and attractive Lewis acid-base (AB) interaction. For the Al_2O_3 membrane, the XDLVO model obscured EL and Lifshitz-van der Waals (LW) interactions since the AB component was dominant, confirmed by the diminished XDLVO energy barrier, whereas for the SiC-deposited membrane, the EL interaction prevailed since the energy barrier value was positive.

Then real oilfield produced water with high salinity (142 mS/cm) and COD (22670 mg/L) was successfully treated by SiC-coated Al_2O_3 membranes in constant flux mode. The major findings were that pore blockage served as the initial (irreversible) fouling mechanism and that the (reversible) cake layer, a mixture of organic and inorganic components, dominated the rest of the filtration cycle, where the SiC coated membrane performed better than the original Al_2O_3 membrane. In addition, it was found that the application of the SiC coating, and the selection of the appropriate pore size (62 nm) and crossflow velocity (0.8 m/s) increased the fouling mitigation, potentially advancing the utilization of ultrafiltration in treating saline produced water for reuse purposes.

Finally, synthetic wastewater containing cotton, linen, polyester, and nylon fibres and real laundry wastewater were characterized and prepared for filtration experiments, which were conducted at a flux of 70 $Lm^{-2}h^{-1}$ using an Al_2O_3 membrane and a SiC-coated membrane. Results revealed that natural textiles, particularly cotton and linen, released higher COD loads than synthetic fibers when tested at equal mass, in the trend of, cotton>linen>polyester>nylon, which was further supported by microscopic and SEM images. Both the Al_2O_3 membrane and the SiC-coated membrane showed a high fiber rejection (100 %), whereas the SiC-coated membrane showed lower reversible and irreversible fouling than the Al_2O_3 membrane, due to highly negatively charged surface. The fouling order of the fibers were in line with the COD concentration of the synthetic laundry wastewater containing these fibers. Finally, treatment of hot real laundry wastewater by the ceramic membranes not only mitigated membrane reversible and irreversible fouling, but also enabled the simultaneous recovery and reuse of water, surfactants, and thermal energy, offering a sustainable strategy to reduce both water consumption and energy costs.

Chapter 1

Introduction

1.1 Background

Over the past two decades, rapid industrialization and urbanization have intensified water scarcity and water pollution, with an estimated 4.4 billion people lacking access to safe drinking water and 48% of wastewater discharged untreated worldwide [1, 2]. Among various types of industrial wastewater, oily wastewater originating from petrochemical, pharmaceutical, food, and beverage industries poses a particular challenge [3]. Its improper discharge can severely contaminate both surface and groundwater, posing serious risks to human health, as oil droplets—ranging from a few nanometers to several hundred micrometers—are difficult to separate by conventional means [4, 5].

Currently, treatment methods for oily wastewater include: (i) dissolved air flotation [6], (ii) gravity-based separation [7], (iii) hydrocycloning [8], and (iv) adsorption [9]. The selection of an appropriate treatment method depends on factors such as oil droplet size and concentration, wastewater composition, and regulatory discharge limits [10, 11]. However, these conventional techniques are often inadequate for oily wasetwater with nano-sized oil droplets. In response, membrane technologies have become essential tools in treating oily wastewater. A wide range of water filtration systems, including conventional pressure-driven nanofiltration (NF)[12], ultrafiltration (UF)[13-15], and microfiltration (MF)[16], have been introduced to the market. Meanwhile, academic research in membrane-based water treatment technologies, spanning fundamental, applied, and translational studies, continues to flourish, driven by advancements in material science and engineering [17-19].

Polymeric membranes are at the forefront of wastewater treatment technologies, thanks to their well-established presence and proven long-term performance [20]. However, a major challenge in using polymeric membranes for industrial wastewater treatment is their chemical instability and high membrane fouling tendency. In contrast, inorganic ceramic membranes are attracting growing interest because of their high mechanical and chemical stability, hydrophilicity, water permeability, and antifouling abilities [3, 14, 21]. One notable type of industrial wastewater is laundry wastewater, generated during the washing of synthetic garments, which releases over five trillion plastic microfragments into the ocean [22]. Given their robustness in high-temperature and chemically aggressive conditions, ceramic membranes are particularly well-suited for treating such challenging laundry wastewater streams [23, 24].

However, still membrane fouling is inevitable. Therefore, effective mitigation strategies are essential to prolong the operation of ceramic membranes. These strategies may include membrane surface modification and adjustment of feed water characteristics. This thesis also presents membrane fouling characterization, which provides fundamental insights into the fouling structure and, in turn, informs the development of appropriate fouling mitigation approaches.

1.2 Ceramic membrane fabrication techniques

Ceramic membranes can be classified into symmetric and asymmetric types. Among these, asymmetric membranes typically exhibit higher water permeability [25]. Currently, the main techniques used to prepare the separation layer include sol-gel [26], co-sintering [27, 28], chemical vapour deposition (CVD) [29], Polymer-derived ceramic process [30], and recrystallization sintering method [31, 32].

1.2.1 Sol-gel

Sol-gel is a chemical synthesis method that forms a gel from a colloidal suspension (sol), which is then dried and heat-treated to form a ceramic [33]. The sol-gel process is one of the most commonly used techniques for fabricating ceramic membranes, as it enables the production of thin, porous separation layers with adjustable porosity using a variety of materials [26]. Li et al. fabricated a zirconium dioxide–silicon carbide (ZrO_2–SiC) ultrafiltration membrane using a combination of the sol-gel and dip-coating methods [26]. Specifically, a 48 nm ZrO_2 separation layer was prepared by synthesizing a zirconia sol from zirconium oxychloride ($ZrOCl_2$), which was then deposited onto a SiC support via dip-coating [26]. γ-Al_2O_3/α-Al_2O_3 hollow fiber nanofiltration membranes with a molecular weight cut-off of 1.4 kDa have also successfully been prepared by dip-coating a γ-AlOOH sol onto an α-Al_2O_3 support with an average pore size of 229 nm. These membranes exhibited a low pure water permeability of 17.4 $Lm^{-2}h^{-1}bar^{-1}$ and demonstrated low retention percentages for Na^+ (30.7%) and NH_4^+ (27.3%) [34]. The separation layer of SiC membranes has typically been fabricated using the sol-gel method. During this process, the resulting gel is dried in an argon atmosphere at a temperature of 850 °C. The resulting membranes have had a pore size distribution ranging from 200 to 500 nm [35].

1.2.2 Co-sintering

Co-sintering is a thermal processing method where two or more ceramic layers (e.g. support layer and separation layer) are sintered at the same time to bond together [36]. Co-sintering involves the formation of a support layer with coarse particles, a separation layer with fine particles is applied on top, using fabrication techniques like dip-coating or spray-coating. After drying, the layered structure is co-sintered in one thermal step [27, 28]. Key advantages of this method is the shortening of the preparation time and the lower overall production costs [36]. Al_2O_3 MF membranes have been fabricated with the co-sintering method with an average pore size of 249 nm, a water permeability of 5040 $Lm^{-2}h^{-1}bar^{-1}$ and a rejection of 96.2% to carbon ink [37]. In addition, Zou et al. reported that tight α-alumina UF membranes with a water permeability of 2000 $Lm^{-2}h^{-1}bar^{-1}$ have been produced via the co-sintering process on an Al_2O_3 support [38]. Apart from the Al_2O_3 membrane, co-sintering has been used to synthesize the SiC membranes [27]. Li et al. reported the fabrication of a SiC selective layer with a pore size of 0.28 μm, which was applied onto a SiC-boron carbide (B_4C) green substrate, using a spray coating technique [27]. In this method, a well-dispersed SiC slurry is atomized into fine droplets and sprayed onto the substrate surface, allowing uniform layer formation. The membrane was then co-sintering at 1900 ºC. After the sintering process, the membrane layer exhibited a strong adhesion to the substrate, with no obvious particle infiltration [27].

1.2.3 Chemical Vapor Deposition

CVD is a process in which one or more volatile precursors are transported in the gas phase to a heated substrate, where they react or decompose on the surface to form a solid material, while by-products are removed in the gas phase [39]. It has been widely used for the production of silica membranes used for the gas separation [40]. It includes low pressure CVD (LPCVD), Normal-Pressure Thermally-Activated CVD, and Plasma-enhanced CVD [41]. Akamatsu et al. have reported the fabrication of amorphous silica membranes via CVD with the precursor Dimethoxydimethylsilane (DMDMS) at a temperature of 699.85ºC, with considerable hydrogen gas permeability [40].

LPCVD is a specific type of CVD. Our group was the first to develop an innovative method for fabricating SiC coatings using LPCVD, successfully depositing a SiC layer onto Al_2O_3 UF membranes at 750 °C for the separation of an O/W emulsion [29]. The benefit of this technique lies in its ability to consistently reproduce and replicate the SiC layer. However, the SiC separation layer coated at 750 ºC by LPCVD was deteriorated when soaking into a 5% NaClO solution due to the amorphous structure of SiC [42]. Similar phenomenon was also observed with amorphous SiO_2 or TiO_2 membranes, which exhibited a faster corrosion compared to their crystalline counterparts [43].

The LPCVD coating process including the following five distinct steps [29, 44]:

- **Ceramic membrane pre-treatment**: Rinse the surface of the ceramic membrane with deionized water, then dry it in an oven at 100°C. After drying, soak it in anhydrous ethanol for 30 minutes. Allow it to air dry, then set it aside for later use.

- **Take out the wafer boat** and place the membranes at the center of the wafer boat.

- **Insert the wafer boat** into the chamber. Use a vacuum pump to slowly evacuate air for 6 minutes, then stop the vacuum pump. Introduce nitrogen gas through the gas pipeline to purge the system for 1 minute. Check for any leakage in the reactor chamber by comparing the baseline pressure with the calibrated pressure. Then, heat the reactor at a rate of 10°C/min until it reaches 750°C.

- **Deposition stage**: The structure of the deposited SiC is strongly influenced by the deposition temperature and the flow rate ratio of dichlorosilane to acetylene. To deposit amorphous SiC, maintain a gas flow ratio of dichlorosilane to acetylene at 3. Set the deposition temperature to 860°C, with a deposition rate of 0.9 nm/min. The total gas flow should be 500 sccm, pressure at 60 Pa, and total deposition time between 60 and 150 minutes.

- **Post-deposition purge**: After the deposition process, residual gases used during deposition need to be purged. First, evacuate the gas from the pipelines and the furnace, then introduce nitrogen gas to clean the system. During the back-pressure stage, the pressure inside the reactor is brought back to atmospheric pressure to allow for safe removal of the wafer boat. Finally, remove the membrane from the wafer boat, completing the entire process of depositing SiC film on the Al_2O_3 ceramic membrane.

1.2.4 Polymer-derived ceramic process

In the polymer-derived ceramic process, polymer derivation refers to the transformation of a preceramic polymer into a ceramic material through controlled pyrolysis (thermal decomposition) in an inert or reactive atmosphere [45]. The first study on the fabricating SiC UF flat sheet membrane was conducted by König et al [30], utilizing a single-step deposition method with an allylhydridopolycarbosilane (AHPCS)/α-SiC ratio of 0.8. Experiments have shown a water permeability of 0.05 Lm^{-2} $h^{-1}bar^{-1}$ and a molecular cut-off ranging between 35 and 100 kDa. The polymer-derived ceramic process is also applicable for the production of SiC tubular membrane using AHPCS and SiC powder [46]. In this process, porous SiC support tubes are first prepared by uniaxial cold-pressing of β-SiC powder with appropriate sintering aids and sintered at 1800 °C in a helium atmosphere for 3 hours. For the formation of the membrane layer, a slip-casting suspension is prepared by dispersing nano-sized SiC particles (∼100–200 nm) in a 10 wt% AHPCS solution in hexane. The support tubes are coated by dip-coating (12 seconds immersion, 2 mm/s withdrawal rate), followed by staged pyrolysis in flowing argon: first to 200 °C (1 h), then 400 °C (1 h), and finally 750 °C (2 h). This thermal treatment enables the conversion of AHPCS into an amorphous SiC ceramic, forming a dense separation layer without relying on conventional sintering of SiC particles [46].

1.2.5 Recrystallization sintering method

Commercial SiC membranes are mainly fabricated using the recrystallisation technique [31, 32]. This method involves sintering of a mixture of SiC particles with varying sizes in specific ratios. At high temperatures (1800-2200 °C), the fine particles evaporate and subsequently agglomerate and recrystallize at the necks of the larger particles [47]. However, achieving a narrow and uniform pore size distribution requires either uniform agglomerates or monodisperse SiC particles. This is typically accomplished by carefully controlling the raw powder characteristics (e.g., particle size distribution, morphology, and purity) and optimizing the sintering conditions [25]. In some cases, advanced techniques such as colloidal processing or the use of sacrificial pore formers with controlled sizes are employed to enhance packing uniformity and pore structure control [47]. The resulting SiC membrane exhibits a high mechanical strength and resistance to thermal shocks. The main drawbacks of this method are the high sintering temperature (exceeding 2000 °C), due to the strong covalent Si-C bonds, and the need for a protective atmosphere (such as argon), both of which increase the fabrication costs of SiC ceramic membranes [47].

1.3 Ceramic membrane fouling in wastewater treatment

1.3.1 Effect of wastewater characteristics on membrane fouling

The composition of feed water plays a vital role in membrane fouling, especially the physicochemical properties of foulants, such as functional groups, size, and surface charge [48, 49].

Salinity

Salts, commonly found in industrial wastewater (e.g., produced water), can alter the properties of oil droplets and the interactions at the oil-membrane interface, thereby also influencing membrane fouling [50, 51]. Tanudjaja et al. have, e.g., reported that the Anopore^{TM} Al_2O_3 membrane became less negative at a higher salinity level, which contributed to more membrane fouling and a reduced critical flux [50]. In addition, Chen et al. have reported that increasing the ionic strength can intensify membrane fouling due to double-layer compression and charge screening effects on both the oil droplets and the SiC membrane surface. These effects reduce the electrostatic repulsion between the oil droplets and the membrane surface, thereby promoting the deposition and accumulation of oil droplets on the membrane surface [10].

pH

The pH value affects the charge of the membrane, thus, affecting the rejection efficiencies of foulants [10]. Lobo et al. , e.g., have found that the ZrO_2/TiO_2 UF membrane surface became positively charged at pH values below 4. As a result, a considerable flux reduction was observed, when filtering an O/W emulsion stabilized with and anionic surfactant, due to the shift from electrostatic repulsion to electrostatic attraction between the negatively charged oil droplets and the positively charged membrane surface [52]. Wang et al. have reported that increasing the pH value led to improvements in both the initial and stable fluxes. A higher pH also resulted in a reduced flux decline when a negatively charged zirconia ceramic membrane was used to filter nano-sized emulsions [3].

1.3.2 Effect of membrane properties on membrane fouling

Surface roughness

There are conflicting results regarding the impact of the surface roughness on membrane fouling. One perspective suggests that a rough membrane surface can exacerbate the reversible and irreversible fouling of O/W emulsions. For example, Zhong et al. have reported that oil droplets are prone to accumulate in the valleys of the rough Al_2O_3 MF membranes, thus, leading to a more severe permeability decline than with smooth membranes [53]. The other perspective suggests that ceramic membranes with a higher roughness tend to form a more loosely packed fouling layer during filtration, which can be more easily removed during physical cleaning, compared to the tightly compacted fouling layer that develops on smoother membrane surfaces [54]. Wang et al., e.g., have conducted a molecular dynamics simulation that accounted for the shear forces present under cross-flow conditions, providing microscopic insights into the impact of surface roughness on the fouling tendencies of Al_2O_3 membranes [55]. This study has indicated that the valleys on rough membrane surfaces resulted in weaker interactions with two types of foulants (sucralose and bisphenol A), making them easier to detach from the ceramic membranes [55].

Surface hydrophilicity

A highly hydrophilic membrane surface is advantageous for wastewater treatment, as it promotes higher water flux by attracting water molecules into the membrane pores. Moreover, the hydration layer, formed on such surfaces, acts as a barrier against the adhesion of hydrophobic colloids, thereby reducing the fouling tendencies [43]. Ceramic membranes composed of metal oxides, are inherently hydrophilic due to their abundance of hydroxyls groups [56]. The degree hydrophilicity of ceramic membranes is further affected by the density of the hydroxyl groups and the strength of the O-H bonds on the membranes surface [57]. Among the commonly used ceramic membranes, the hydrophilicity follows the order $SiC>TiO_2>ZrO_2>Al_2O_3$, as illustrated in Fig.1.1a.

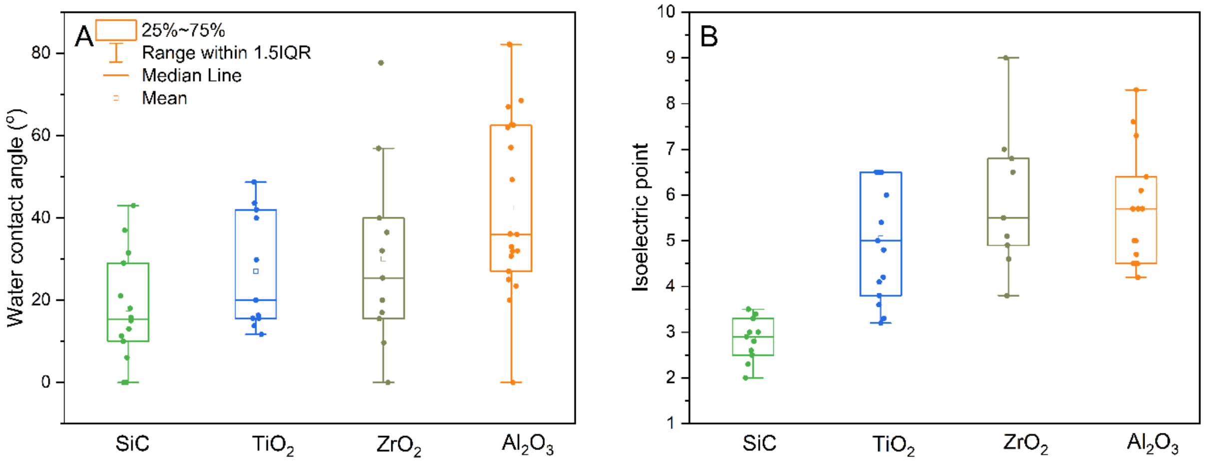

Fig.1.1 Comparison of (a) water contact angle and (b) isoelectric point of ceramic membranes made from SiC, TiO_2, ZrO_2, and Al_2O_3. The data and references used are shown in Table.S1.1.

Surface charge

In the separation process, the membrane surface charge plays a key role in governing electrostatic interactions with charged foulants, which in turn influences the severity of the membrane fouling. When the membrane and foulant show the same charge, electrostatic repulsion occurs between the membrane surface and foulants, and the fouling is alleviated [58]. Also in the Derjaguin-Landau-Verwey-Overbeek (DLVO) model, the electrostatic component consistently exhibits a repulsive interaction between the membrane surface and foulants of the same charge, especially for the spherically shaped oil droplets. Among the commonly used ceramic membranes, the isoelectric point, indicating the pH at which its surface carries no net electrical charge, follows the order SiC>TiO_2>ZrO_2>Al_2O_3, as illustrated in Fig.1.1b. However, to date, no studies have quantitatively analyzed or compared O/W emulsion fouling using DLVO modeling across these specific ceramic membrane materials (e.g., SiC).

Pore size

Membrane fouling experiments are commonly conducted at either a constant flux or a constant pressure mode [59]. At the constant pressure filtration mode, Nagasawa et al. have reported that for porous TiO_2 membranes with small pores, fouling by O/W emulsions is induced by the deposition of oil droplets on the membrane surface, which results in the formation of a cake layer and a reduction in water permeability. For membranes with larger pores, specifically, when the size of the membrane pores is larger than the size of the droplets, pore blockage is the main fouling mechanism [58]. Zhao et al. have also reported that during the treatment of raw apple cider fouling of tubular ceramic membranes made of Al_2O_3 with smaller pore sizes (0.2 µm and 0.45 µm) was dominated by external fouling, such as cake layer formation, whereas the fouling of membranes with larger pore sizes (0.8 µm and 1.4 µm), was dominated by internal fouling, such as pore constriction and pore blocking [60]. However, at a constant flux mode, the effects of the pore size on the SiC membrane fouling was not reported.

1.3.3 Effect of operational parameters on membrane fouling

Crossflow velocity

Chen et al. have reported that at a constant pressure of 0.1 bar, increasing the crossflow velocity leads to higher shear stress, which in turn enhances the mass transfer coefficient, resulting in a higher permeate flux for a spinel-based hollow fibre ceramic membrane [61]. Similarly, at the constant pressure mode, Xue et al. have reported that an increase in crossflow velocity leads to a higher steady-state flux of the SiC membrane, because higher crossflow velocities enhance the drag force exerted by the brine, which reduces the size of settling particles and limits their deposition on the membrane surface. As a result, higher crossflow velocities lead to a lower reversible fouling resistance and a slower rate of flux decline [62]. Under constant flux condition, Sim et al. have found that increasing the crossflow velocity reduces the thickness of the cake layer, but does not have an effect on its porosity on a polyethersulfone UF membrane [63]. However, the effect of crossflow velocity on SiC membrane fouling under constant flux mode remains unexplored.

Flux

Liu et al. have reported, conducting constant-flux fouling experiments using a polyvinylidene fluoride (PVDF) polymeric membrane to filter traditional Chinese medicine water extracts, that when the permeate flux is below the threshold, the transmembrane pressure (TMP) gradually increases. However, when the flux exceeds the threshold, severe fouling occurs, leading to a rapid rise in TMP [64]. In addition, Kirschner et al. have conducted constant flux crossflow fouling experiments using polyethersulfone UF membrane at permeate fluxes ranging from 20 to 130 $Lm^{-2}h^{-1}$, in 10 $Lm^{-2}h^{-1}$ increments. As the flux approached the threshold flux of the membrane, the TMP curves exhibited a slow increase, and the intermediate pore blocking model closely matched the experimental data. When the flux exceeded the threshold, the TMP curves exhibited a rapid increase, and a combination of the intermediate pore blocking and cake filtration models provided the best fit [13]. With the increase in the filtration time, the continuous rise in TMP under constant flux conditions suggests that the cake layer continues to grow without limit. In contrast, under constant pressure filtration, the cake layer eventually stabilizes at a constant thickness [65]. Sim et al. have observed that the increase in flux, thus, leads to a higher TMP and larger cake layer thickness, which has been associated with a decrease in cake layer porosity, from 0.7 at 60 $Lm^{-2}h^{-1}$ to 0.4 at 100 $Lm^{-2}h^{-1}$, on a polyethersulfone UF membrane [63]. The first work of the effect of the permeate flux on SiC UF membrane is reported by Chen et al, who found that near the threshold flux, SiC membrane fouling is primarily governed by foulant-membrane interactions. When the flux exceeds the threshold, both foulant-membrane and foulant-foulant (i.e., deposited layer) interactions become obvious [10].

1.3.4 Effect of types of fabrics fibers on membrane fouling

Synthetic fabrics such as nylon and polyester, as well as natural fabrics, including cotton and linen, are commonly used in fabric production [66]. It has been reported that the natural fibers can constitute up 55% of the total fibers found in laundry wastewater and these fibers take between 1 to 5 months to fully biodegrade in the natural environment [66, 67]. The natural fibers, being organic and biodegradable, pose a minimal environmental risk [68]. For example, natural fibers, such as cotton and silk, have shown no toxicity toward *Daphnia magna*, whereas synthetic fibers like nylon caused acute toxic effects on this organism [68]. However, natural fibers could also act as carriers for harmful substances, as fabrics made from organic fibers are often treated with chemicals such as chemical colorants and finishes [69]. These chemical additions could also slow down the biodegradation process of natural fibers [70]. Despite this, most studies have primarily focused on ceramic membrane fouling caused by filtering synthetic laundry wastewater containing synthetic fibers rather than the natural fibers [23, 71, 72]. To the best of our knowledge, ceramic membrane fouling caused by natural fiber has not been quantitatively analyzed yet.

1.4. Membrane fouling characterization techniques for wastewater treatment

Advanced characterization techniques such as FIB-SEM, OCT, and DOTM could provide complementary insights into membrane fouling beyond conventional surface imaging. FIB-SEM enables precise, artifact-free cross-sectioning and nanometer-scale imaging of the internal microporous structure, making it powerful for identifying irreversible fouling by pore blockage [73, 74]; in this thesis, it is applied for the first time to ceramic membranes. However, although OCT, offers non-invasive, real-time 3D visualization of fouling layer development at micrometer resolution [75], its limited penetration depth, and high costs have restricted its application mainly to ultra-thin polymeric membranes. DOTM allows direct optical observation of early-stage fouling events such as droplet attachment, deformation, and coalescence, but since it requires transparent membranes and provides only 2D information [76, 77], it is not applicable to the opaque SiC-coated ceramic membranes studied in this work.

1.4.1 FE-SEM and FIB-SEM

The Focused Ion Beam-Scanning Electron Microscope (FIB-SEM) is a dual-beam system that combines the capabilities of a FIB and a SEM. This integrated system is a powerful tool for visualizing irreversible fouling, allowing for quantitative comparison across the different membrane samples [78]. While surface morphology of the fouling (cake) layer have often been studied using surface imaging with Field Emission SEM (FE-SEM), traditional methods for preparing membrane cross-sections, such as mechanical cutting, can result in material loss and structural artifacts during sample fixation [79, 80], compromising the accuracy of fouling layer characterization.

FIB-SEM overcomes these limitations by allowing precise, site-specific milling to expose membrane cross-sections without introducing deformation or artifacts. This enables high-resolution (5-10 nm) imaging of the internal microporous structure of membranes, which is critical for identifying and comparing internal (irreversible) fouling by pore blockage [73, 74]. Furthermore, FIB-SEM allows measurements of fouling depth, offering insight into the three-dimensional structure of the fouling layer, which cannot be provided by conventional SEM and FE-SEM techniques [81]. However, this techniques has not yet been applied to ceramic membranes and, firstly, we applied FIB-SEM to analysis the reversible and irreversible fouling of ceramic membranes.

1.4.2 OCT

Optical Coherence Tomography (OCT) employs infrared light with wavelengths ranging from 800 to 1300 nm. It is a non-invasive technique that enables real-time monitoring [82]. However, the signal quality and resolution decrease with increasing sample depth (typically within 500 micrometers), making quantitative analysis of OCT tomograms challenging [83]. It generates three dimensional (3D) images of foulant deposition with depth resolution of 2 µm and lateral resolution of 4 µm [75]. Trinh et al. have reported that OCT can monitor the oil internal irreversible fouling in real time when filtering an O/W emulsion over a 0.45 µm polyvinylidene fluoride membrane in a dead-end filtration mode [82]. This technique is applicable for studying the internal fouling mechanisms caused by 0.45 µm polystyrene particles with varying surface charges, using a polycarbonate track-etched membrane with a pore size of 2 µm [84]. This technique has also enabled both visualization and quantification of the structural characteristics of different fouling types at the mesoscopic scale, which is crucial for understanding and optimizing operational performance (Fig.1.2.). However, current studies utilizing OCT primarily focus on the fouling analysis of polymeric membranes [82, 84, 85]. One of the primary limitations of using OCT in fouling monitoring is its inability to provide qualitative details about the compositions of the fouling layer [75]. Additionally, the application of OCT in real-world water treatment plants remains limited due to both economic and technical challenges [86].

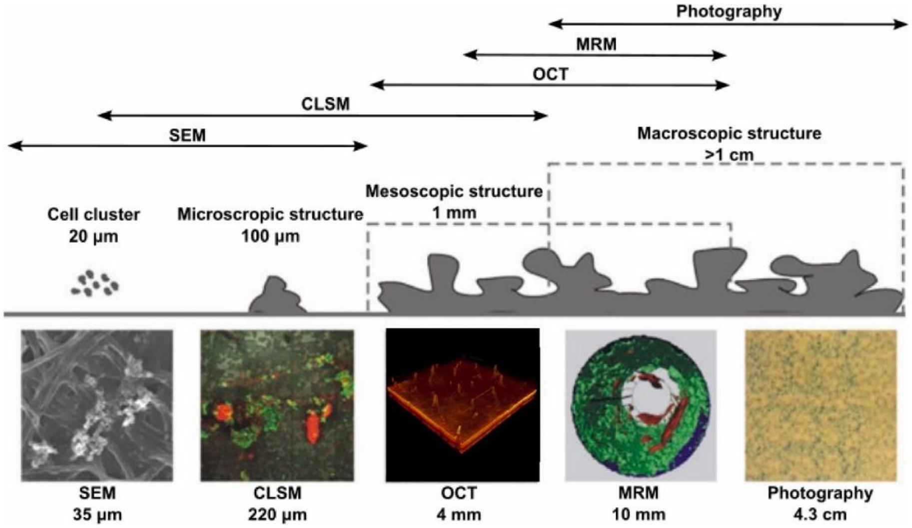

Fig. 1.2. Various techniques are used to study biofilm structures across different spatial scales. It is important to note that as the field of view increases from left to right, the resolution correspondingly decreases. Mesoscopic structures, typically spanning several millimeters, serve

as a bridge between the microscopic and macroscopic scales. These techniques include SEM, CLSM (Confocal Laser Scanning Microscopy), OCT, and MRM (Magnetic Resonance Microscopy), as adapted from Ref. [75].

1.4.3 DOTM

DOTM (direct observation through the membrane), which uses an optical microscope to examine the feed-membrane interface, is restricted to transparent membranes, making it less practical [76, 77]. Additionally, it is limited to two-dimensional (2D) imaging, resulting in the loss of depth information [87]. However, Tummons et al. have reported that with DOTM, when filtering SDS-stabilized O/W emulsions, three distinct stages of membrane fouling can be identified: (1) attachment and clustering of oil droplets, (2) deformation of the droplets, and (3) coalescence of the droplets [87]. In addition, Tanis et al. have reported that, based on DOTM images, unmodified polystyrene particles show a higher fouling tendency on a 0.2 µm Anopore Al_2O_3 membrane than aminated polystyrene and carboxylated polystyrene particles, respectively [77].

1.5. State of the art and knowledge gaps

Membrane fouling remains the main constraint in oil–water separation using membranes [88]. One strategy to mitigate fouling is to alter the surface wettability by coating the membrane with hydrophilic materials rich in hydroxyl groups, such as ZrO_2 and TiO_2 nanoparticles [89, 90]. Pore size is another critical factor affecting fouling [58, 91, 92]. For instance, Jiang et al. reported that SiC membranes with the largest pore size (0.67 µm) exhibited the highest flux decline and lowest stable flux when filtering 500 ppm O/W emulsion at a constant pressure of 0.5 bar [92]. Nagasawa et al. also reported that severe fouling was induced for porous TiO_2 membranes with the largest pores (1.4 µm), since more oil droplets accumulated into the pores, leading to a high irreversible fouling [58]. Despite these findings, studies examining the effect of pore size on O/W emulsion separation under crossflow, constant-flux operation remain limited.

To further understand the role of solution chemistry, recent work has employed DLVO/XDLVO modeling to study the influence of ionic strength and surfactant type on fouling with polymeric membranes [93, 94]. For example, He et al. reported that for oil-in-water (O/W) emulsions, stabilized by the non-ionic surfactant (Triton ^{TM} X-100), the interaction energies predicted by the DLVO model were consistent with the fouling tendencies at various salinities for the PVDF MF membrane in the constant flux filtration mode [93]. Likewise, the group of Chew reported that fouling tendencies during the filtration of O/W emulsions stabilized with SDS, CTAB, and Tween 20 correlated more strongly with DLVO rather than XDLVO predictions for a 0.22 μm PVDF membrane under constant pressure operation [94]. However, no prior studies have quantitatively analyzed and compared fouling by O/W emulsions with the DLVO and XDLVO models using specific ceramic materials, such as SiC.

In terms of fouling characterization, existing studies primarily rely on surface imaging techniques (SEM, FE-SEM) or real-time visualization methods (OCT, DOTM), most of which have been applied to polymeric membranes [73, 74]. While these techniques provide valuable mechanistic insights, they are limited in assessing internal (irreversible) fouling within ceramic membranes. Focused Ion Beam-SEM (FIB-SEM) represents a promising yet underexplored approach, as it enables quantitative evaluation of fouling depth and internal morphology. Nevertheless, systematic studies applying FIB-SEM to ceramic membranes are still scarce.

Beyond O/W separation, ceramic membranes are also investigated for treating laundry wastewater. It has been reported that natural fibers account for up to 55% of the total fibers in laundry effluents, with biodegradation times ranging from one to five months in the environment [66, 67]. However, most studies on ceramic membrane fouling have focused on synthetic Yet, most studies on ceramic membrane fouling have focused on synthetic wastewater containing only synthetic fibers [23, 71, 72], while fouling caused by natural fibers has not been quantitatively studied. This thesis addresses these gaps by applying FIB-SEM to ceramic membranes for the first time and by focusing on performance evaluation of SiC-coated membranes under realistic wastewater conditions, thus bridging fabrication, application, and advanced fouling characterization.

From the information described above, it can be concluded that for the filtration of industrial wastewater by ceramic membranes, still some knowledge gaps exist:

- The effect of pore size on SiC membrane fouling by O/W emulsions under constant flux mode remains unexplored.
- No studies have quantitatively analyzed or compared O/W emulsion fouling using DLVO modeling across these specific ceramic membrane materials (e.g., SiC).

- The FIB-SEM techniques have not yet been applied to ceramic membranes for characterizing reversible and irreversible fouling.
- Ceramic membrane fouling caused by natural fiber has not been quantitatively investigated.

1.6. Scope of this thesis

To tackle these knowledge gaps, the main objective of this thesis is to systematically investigate the influence of membrane properties (e.g., pore size) and operational parameters (e.g., crossflow velocity) on the performance and fouling behavior of SiC-coated ceramic membranes in treating industrial wastewater, including oil-in-water (O/W) emulsions and natural fiber-laden effluents. In particular, this study aims to explore the application of advanced characterization techniques such as FIB-SEM for differentiating reversible and irreversible fouling, and to employ DLVO modeling for quantitative analysis and comparison of fouling mechanisms across various ceramic membranes. To achieve this objective, a series of research questions were formulated and explored throughout the chapters of this thesis. The schematic overview of the main chapters of this thesis is shown in Figure 1.3.

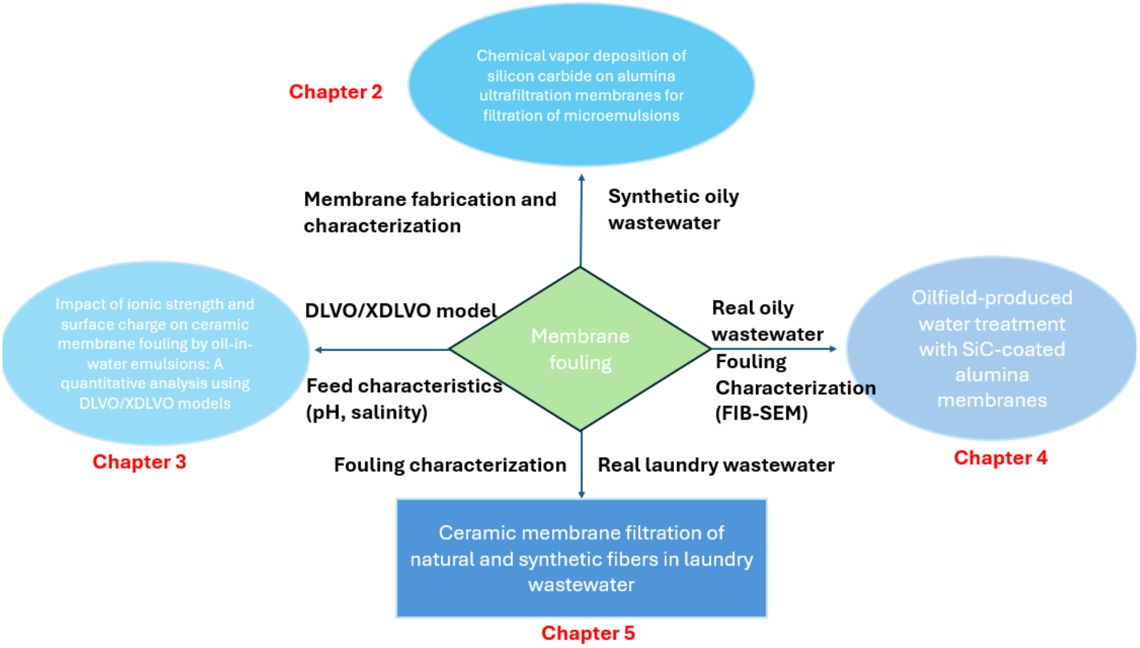

Fig. 1.3. Schematic overview of the main chapters of this thesis.

Research question 1: *How do LPCVD deposition time, emulsion pH, surfactant type, and membrane pore size influence the fouling of SiC-coated ultrafiltration membranes during filtration of synthetic oil-in-water emulsions?*

Chapter 2 demonstrates the potential of using SiC-coated membranes for the separation of nano-sized emulsions. These membranes were fabricated via LPCVD at 860 °C. We then evaluated the membranes in terms of pore size, surface morphology, water permeability, mechanical strength, surface charge, and water contact angle. Additionally, the effects of deposition time, pH, surfactant type, and membrane pore size on fouling during UF of synthetic O/W emulsions were reported.

Research question 2: *Do the DLVO and extended DLVO (XDLVO) models align with the observed fouling trends of the* Al_2O_3 *and SiC-coated membranes when filtering oil-in-water emulsions stabilized by different types of surfactants and under varying salinity levels?*

In **Chapter 3,** the effects of the ionic strength (1, 20, and 100 mM) as well as surfactants types on the membrane fouling are reported. Four surfactants, including SDS (anionic), APG (non-ionic), CTAB (cationic) and DDAPS (zwitterionic), were selected for this study. The DLVO and XDLVO models were used to quantify interactions between the membrane-oil droplet and deposited oil layer-oil droplet surfaces and to compare these interactions with the fouling experiments.

Research question 3: *How does the fouling of SiC-coated membranes vary when treating real produced water under different fluxes, crossflow velocities, and pore sizes, and how do the fouling mechanisms evolve as filtration time increases by FIB-SEM?*

In **Chapter 4**, for the first time, direct ceramic UF of real produced water is reported, using SiC-coated UF membranes in constant flux mode. Firstly, the effect of the salinity on membrane fouling was determined by filtering synthetic O/W emulsions. Secondly, the fouling resistance was evaluated under various pore sizes and operating conditions (flux, CFV), using two types of real produced water with varying water quality. Finally, the (ir)reversible fouling transition mechanisms were visualized using FIB-SEM images.

Research question 4: *What is the fouling of positively charged Al_2O_3 membranes and negatively charged SiC-coated ceramic membranes during the treatment of synthetic laundry wastewater containing natural fibers and synthetic fibers, as well as real laundry wastewater?*

In **Chapter 5**, we report on the fouling of the Al_2O_3 and SiC-coated membranes when filtering synthetic laundry wastewater containing natural fibers (cotton, nylon) and synthetic fibers (polyester, nylon) at a constant flux of 70 $Lm^{-2}h^{-1}$. In addition, the real laundry wastewater was filtered at different operational conditions, including varying flux and temperature, thus, giving proper solutions for membrane fouling mitigation and promoting water reuse and heat recycling in laundry industry.

Finally, **in Chapter 6**, with the obtained knowledge from the previous chapters, conclusions of this thesis and a future outlook and challenges of ceramic membranes for industrial wastewater treatment are presented.

Appendix

Table S1.1 Summary of contact angle and isoelectric point values of SiC, TiO_2, ZrO_2 and Al_2O_3 membranes (N.A.: not available).

Separation layer	Contact angle (°)	Isoelectric point	Ref.
SiC	N.A.	2.6	[95]
SiC	N.A.	<3	[58]
SiC	0	<2	[10]
SiC	0	N.A.	[96]
SiC	37	3	[28]
SiC	43	3	[28]
SiC	11.3	2.9	[21]
SiC	13	N.A.	[92]
SiC	6	2.8	[97]
SiC	10	N.A.	[97]
SiC	31.5	N.A.	[98]
SiC	N.A.	2.5	[99]
SiC	N.A.	2.3	[100]
SiC	N.A.	3.3	[100]
SiC	N.A.	3.4	[100]
SiC	N.A.	3.5	[100]
SiC	15.8	N.A.	[101]
SiC	15,18,21,29	2.0	[15]
TiO_2	15.6	N.A.	[102]
TiO_2	N.A.	4.8	[103]
TiO_2	N.A.	5	[58]
TiO_2	20	N.A.	[104]
TiO_2	29.8	3.2	[105]
TiO_2	N.A.	6.5	[106]
TiO_2	42	N.A.	[107]

TiO_2	N.A.	6.5	[108]
TiO_2	16.3	N.A.	[109]
TiO_2	48.7	N.A.	[110]
TiO_2	13.8	N.A.	[111]
TiO_2	N.A.	4.2	[112]
TiO_2	N.A.	3.6	[113]
TiO_2	N.A.	4.1	[114]
TiO_2	40	N.A.	[115]
TiO_2	15.6	N.A.	[116]
TiO_2	N.A.	5.4	[117]
TiO_2	N.A.	3.3	[118]
TiO_2	N.A.	6	[119]
TiO_2	N.A.	6.5	[120]
TiO_2	N.A.	6.5	[121]
TiO_2	N.A.	3.8	[122]
TiO_2	11.7	N.A.	[123]
TiO_2	43.6	N.A.	[124]
ZrO_2	15.5	6.5	[125]
ZrO_2	17	N.A.	[126]
ZrO_2	77.7	3.8	[57]
ZrO_2	0	N.A.	[127]
ZrO_2	32	5.1	[3]
ZrO_2	20	N.A.	[128]
ZrO_2	N.A.	4.6	[112]
ZrO_2	N.A	6.8	[113]
ZrO_2	9.6	N.A.	[129]
ZrO_2	36.5	N.A.	[130]
ZrO_2	40	N.A.	[131]
ZrO_2	25.4	7	[132]
ZrO_2	N.A.	4.9	[133]
ZrO_2	56.9	N.A.	[123]

ZrO_2	N.A.	5.5	[134]
ZrO_2	N.A.	9	[134]
Al_2O_3	N.A.	5	[135]
Al_2O_3	25	5.7	[136]
Al_2O_3	57.1	4.7	[57]
Al_2O_3	62	N.A.	[137]
Al_2O_3	33	N.A.	[128]
Al_2O_3	0	N.A.	[138]
Al_2O_3	36.1	4.2	[139]
Al_2O_3	32	N.A.	[140]
Al_2O_3	N.A.	4.5	[141]
Al_2O_3	N.A.	5.7	[142]
Al_2O_3	N.A.	6.1	[143]
Al_2O_3	23.4	7.3	[21]
Al_2O_3	62.7	N.A.	[144]
Al_2O_3	31.9	N.A.	[111]
Al_2O_3	N.A.	4.5	[145]
Al_2O_3	N.A.	4.5	[146]
Al_2O_3	N.A.	4.3	[112]
Al_2O_3	N.A.	7.6	[113]
Al_2O_3	27	8.3	[147]
Al_2O_3	N.A.	5.7	[136]
Al_2O_3	67	N.A.	[148]
Al_2O_3	N.A.	5	[135]
Al_2O_3	30.7	N.A.	[34]
Al_2O_3	62.5	N.A.	[34]
Al_2O_3	82.2	N.A.	[34]
Al_2O_3	68.5	N.A.	[149]
Al_2O_3	20	N.A.	[150]
Al_2O_3	49.3	N.A.	[124]
Al_2O_3	36	6.4	[15]

Chapter 2

Chemical vapor deposition of silicon carbide on alumina ultrafiltration membranes for filtration of microemulsions

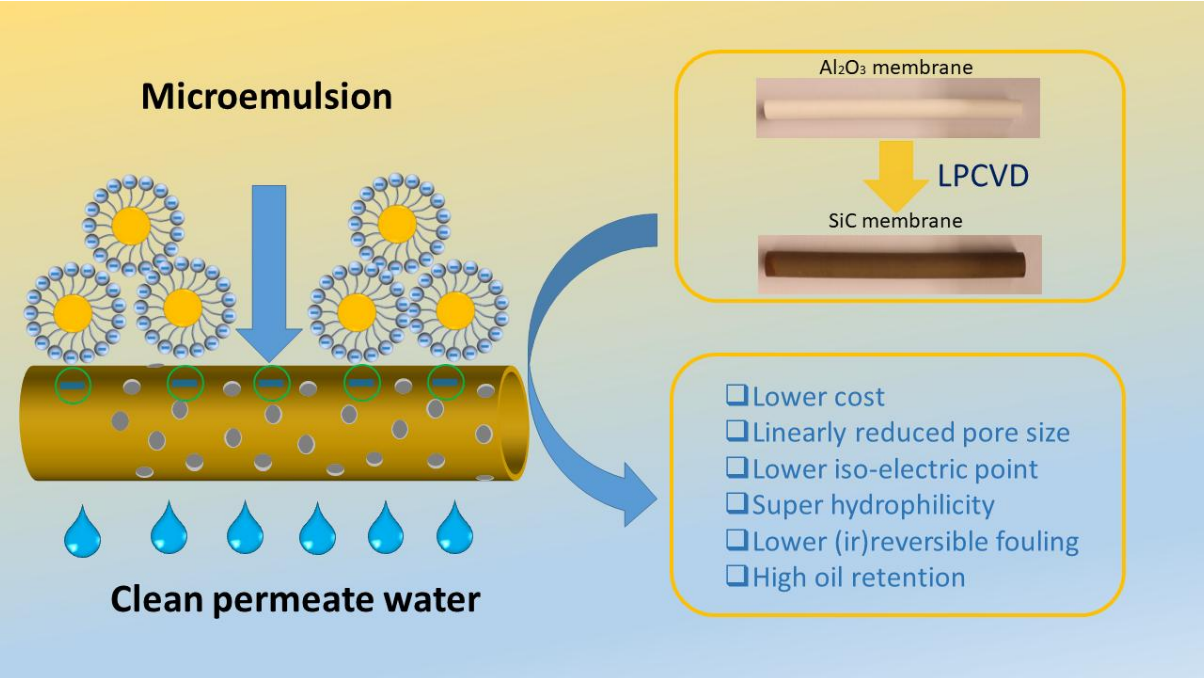

This chapter is based on:

Qin, G., Jan, A., An, Q., Zhou, H., Rietveld, L. C., & Heijman, S. G. (2024). Chemical vapor deposition of silicon carbide on alumina ultrafiltration membranes for filtration of microemulsions. *Desalination*, *582*, 117655, http://dx.doi.org/10.1016/j.desal.2024.117655.

Abstract

Worldwide, a considerable amount of oily wastewater is generated, with oil droplets from 2 to 200 nm that are difficult to separate because of their size and colloidal stability. This study presents a novel approach for effectively separating microemulsions via cubic silicon carbide (3C-SiC)-coated alumina (Al_2O_3) membranes fabricated based on low pressure chemical vapor deposition (LPCVD). SiC was deposited at a relatively low temperature at 860 ºC on 100 nm Al_2O_3 membranes using two precursors: SiH_2Cl_2 and C_2H_2. With the increase in deposition time, up to 25 min, the pore size decreased from 41 nm to 33 nm, which is a smaller pore size of a SiC membrane than previously used for oil/water separation. The polycrystalline 3C-SiC-coated membranes showed improved hydrophilicity (water contact angle of 15º) and highly negatively charged surfaces (-65 mV). Microemulsion filtration experiments were carried out at a constant permeate flux (80 $Lm^{-2}h^{-1}$) for six cycles with varying deposition time, pH, surfactant types, and pore sizes. The fouling of the SiC-coated membrane was, compared to the Al_2O_3 membrane, effectively mitigated due to the enhanced electrostatic repulsion and hydrophilicity. Surfactant adsorption mainly occurred when the surface charge of the microemulsion and the membranes were opposite. Therefore, the surface charge of the alumina membrane changed from positive to negative when soaked in negatively charged microemulsions, whereas SiC-coated membranes remained negatively charged regardless of surfactant type. The membrane fouling was alleviated when the membrane and oil droplets had the same charge. Lastly, the 62 nm SiC-coated membrane with 20 min coating time was the best choice for the filtration of the microemulsion, because of the high rejection of the oil droplets and low fouling tendency.

2.1. Introduction

Worldwide, oily wastewater is generated from the petrochemical, pharmaceutical, food, and beverage industries [89, 151]. However, the discharge of oily wastewater can severely contaminate groundwater and surface water and is harmful to human health [4, 5]. At present, the typical and conventional technologies for the treatment of oily wastewater include (i) dissolved air flotation [6], (ii) gravity-based separation [7], (iii) hydrocycloning [8], and (iv) adsorption [9]. The choice between the various oil-water separation technologies depends on oil droplet size/concentration, properties of oily wastewater, and the maximum allowable emission concentration [11, 152]. Meanwhile, the emerging membrane separation technology is regarded as a promising and sustainable approach for effectively treating wastewater due to its distinct advantages, including a small footprint and high separation efficacies [153, 154]. Compared with polymeric membranes, inorganic ceramic membranes have attracted increasing attention due to their high mechanical/chemical stability, hydrophilicity and water permeance [3, 14, 21].

Most oil-in-water (O/W) emulsions have oil droplet sizes ranging from a few nanometers to several hundred micrometers. For emulsions with micron-sized oil droplets, ceramic ultra/microfiltration (UF/MF) membranes show satisfactory rejection, typically in the range of 90-99 percent [29, 152]. However, some industrial operations also generate large quantities of oily wastewater with oil droplets from 2-200 nm [155]. These emulsions are predominantly thermodynamically stable "microemulsions" with sizes ranging from 10 to 100 nm [155, 156]. So effective and widely applicable strategies for separating different emulsions with nano-sized oil droplets are highly required. Some studies [89, 157-159] have addressed the treatment of nano-sized oil emulsions using inorganic membranes such as zirconia and carbon nanotubes. Silicon carbide (SiC) membranes are usually fabricated using the sol-gel technique at a high temperature (up to 2100 ºC), resulting in long production times and high costs [160]. To save costs and diminish the environmental impact of membrane production, in our previous work, we developed an innovative method for producing a SiC coating based on low pressure chemical vapor deposition (LPCVD) onto Al_2O_3 UF membranes at 750 ºC. In addition, our previous studies found that the SiC-coated alumina (Al_2O_3) membranes perform better than the Al_2O_3 membranes in separating micro-sized SDS stabilized oil/water emulsions with lower reversible and irreversible fouling [152]. However, on the one hand, the SiC layer deposited at 750 ºC, which was reported in our previous studies, was not chemically stable due to the amorphous structure of SiC [29]. It has also been reported that 3C cubic and 6H hexagonal are the most stable structures compared with other SiC polytypes [161]. To solve this problem, the deposition temperature was increased from 750 ºC to 860 ºC to deposit the polycrystalline 3C-SiC on the 100 nm Al_2O_3 membrane surface [162]. The fouling behavior of the filtration of microemulsions using SiC-coated UF membranes has not yet been performed and reported. Therefore, we developed 3C-SiC membranes with smaller pore sizes and similar permeabilities compared with the previous work, to achieve high rejection of nano-sized emulsions.

Fouling is the main constraint when using membranes for oil-water separation [88]. One possible way to address fouling is to modify the wetting property of the membrane surface by coating hydrophilic materials, rich in hydroxyl groups (e.g., ZrO_2 and TiO_2 nanoparticles) [89, 90]. Pore size is another critical factor influencing fouling [58, 91, 92]. Jiang et al. reported that SiC membranes with the largest pore size (0.67 µm) showed the highest flux decline rate and lowest stable flux when filtering 500 ppm O/W emulsion at a constant pressure of 0.5 bar [92]. Nagasawa et al. also reported that severe fouling was induced for porous TiO_2 membranes with the largest pores (1.4 µm) since more oil droplets accumulated into the pores, leading to a high irreversible fouling [58]. However, studies on the effect of pore size on O/W emulsion separation in a crossflow, constant flux mode are lacking. Therefore, the objective of this study was to better understand the effect of surface charge, hydrophilicity, and pore size of the SiC-coated UF membranes on membrane fouling by O/W microemulsions in a constant flux mode. Firstly, deposition times determine the layer thickness, affecting the pore size and permeabilities of the membranes. Therefore, deposition times ranging from 10 to 25 min were employed to tune membrane pore sizes and surface properties. The effect of deposition time on membrane fouling was investigated to find the optimum deposition time. We then evaluated ceramic membranes in terms of pore size, surface morphology, water permeance, mechanical strength, surface charge, and water contact angle before the filtration experiments. These experiments were conducted in crossflow filtration with constant fluxes for the filtration of O/W microemulsions, stabilized with anionic, cationic, and non-ionic surfactants. The effect of pH of the feed solution on fouling was also studied to find which types of oily wastewater (alkaline or acidic) are much more suitable for the treatment by

SiC-coated membranes. Finally, by comparing the oil rejection and (ir)reversible fouling, the best pore size was chosen.

2.2. Materials and methods

2.2.1 Materials

Soybean oil (S7381, Sigma-Aldrich, the Netherlands), sodium dodecyl sulfate (SDS, 75746, Sigma-Aldrich, the Netherlands), Span 80 (85548, Sigma-Aldrich, the Netherlands), Tween 80 (P1754, Sigma-Aldrich, the Netherlands), Hexadecyltrimethylammonium bromide (CTAB, H5882, Sigma-Aldrich, the Netherlands), calcium chloride (≥ 97%, 746495, Sigma-Aldrich, the Netherlands) and sodium chloride (≥ 99%, Sigma-Aldrich, the Netherlands), were employed to prepare the O/W microemulsions. HCl (0.1 mol/L, 1090601003, Sigma-Aldrich, the Netherlands) and NaOH (97%, powder, Sigma-Aldrich, the Netherlands) were used for pH adjustment. The citric acid (≥ 99.5%, powder, Sigma-Aldrich, the Netherlands) was used for membrane cleaning. Demineralized (DI) water was used to prepare the microemulsion, clean the filtration tube, and backwash or forward flush the fouled membranes. Commercial single-channel tubular Al_2O_3 ceramic UF membranes used in the experiments were made of α- Al_2O_3 for both the 600 nm support layer and the selective layer with a maximum pore size of 100 nm (CoorsTek, the Netherlands), where the information on pore size was provided by the membrane manufacturer. The Al_2O_3 membranes chosen for LPCVD had similar permeabilities in the range of 360 to 380 $Lm^{-2}h^{-1}bar^{-1}$. Flat sheet Al_2O_3 membranes with 100 nm pore size were produced by Inopor (Germany) with a rectangular shape (1cm × 2cm) and a thickness of 1 mm. These membranes were coated under the same circumstances as the tubular membranes for contact angle and zeta potential measurements.

2.2.2 Low-pressure chemical vapor deposition

Dichlorosilane (SiH_2Cl_2) and acetylene (C_2H_2) were used as precursors for the SiC layers deposition. The Al_2O_3 membranes were put on two half wafers, which were located in the center of the LPCVD chamber. The deposition temperature was 860 °C, and the precursors flow ratio (SiH_2Cl_2/C_2H_2) was 6.7 to obtain polycrystalline SiC [44]. The amount of gas flowing into the tube was controlled by mass flow meters with ranges from 0 to 500 standard cm^3/min, and 100

cm^3/min was chosen based on a previous study [44]. The Al_2O_3 membranes without deposition and with deposition times of 10 min, 15 min, 20 min, and 25 min were denoted as H0, H10, H15, H20, and H25, respectively. The 200 nm and 600 nm Al_2O_3 tubular membranes without deposition and with deposition times of 20 min were denoted as H0-200, H0-600, H20-200, and H20-600, respectively.

2.2.3. Membrane characterization

Scanning electron microscope (SEM) measurements were carried out on a Helios NanoLab 650. In addition, the SEM was attached to an Energy Dispersive X-ray (EDX) spectroscopy (Apollo 40 Silicon Drift Detector, Ametek EDAX^{TSL}) and EDAX Genesis software, which was employed to define the chemical composition of both the pristine Al_2O_3 and LPCVD modified SiC-Al_2O_3 membranes. The Helios Nanolab G3 UC (Thermo Fisher Scientific, USA), which integrates a focused ion beam with an SEM, was used to examine the cross-section of SiC-coated membranes. Using the Focused Ion Beam method, the top thin layers of the SiC-coated sample were removed by directing the gallium ion beam onto it, sequentially revealing a new cross-section. This newly exposed surface was then visualized using the electron beam of an SEM. XRD (X-ray Diffraction) was conducted with an X-ray diffractometer (D8-Discover, Bruker, USA) and Eiger-2 500k 2D-detector to measure the SiC crystal structure. Surface roughness measurements were performed by atomic force microscopy (AFM) (Dimension Icon, Bruker, USA) in tapping mode in the air. The Gwyddion software was used to analyze the AFM images and provide quantitative roughness data. Transmission electron microscopy (TEM) images were collected using a Titan aberration-corrected transmission electron microscope (Thermos Fisher, FEI company).

The water contact angle (WCA) and underwater oil contact angle (UOCA) of the pristine Al_2O_3 membranes and the LPCVD-modified SiC-Al_2O_3 UF membranes were performed by a contact angle instrument with a manual adjustable zoom lens (Dataphysics OCA25, Germany). The WCA measurements, conducted on a minimum of three times at distinct locations of each membrane, were measured by dosing 2 µl water on the membrane surface. The UOCA measurements were conducted using captive bubble mode, where a droplet of soybean oil was captured by the bent dosing needle (SNC 050/026, Benelux Scientific BV, the Netherlands) under the membrane holder (SHC 20, Benelux Scientific BV, the Netherlands), which fixed the commercial flat Al_2O_3 and

SiC-coated Al_2O_3 membrane in the aqueous phase in a glass cell (GC 50, Benelux Scientific BV, the Netherlands).

The zeta potential was used to estimate the surface charge of the membranes using an electrokinetic analyzer (SurPASS, Anton Paar, Graz, Austria). The instrument measured the streaming current coefficient, and the Helmholtz–Smoluchowski equation was used for the calculation of the zeta potential of the flat membrane. The isoelectric point (IEP) was measured in a titration system, encompassing a pH range of 3 to 10 with a pH interval of 1. Three-point bending tests were performed, using a mechanical testing system (ElectroPuls E20000, Instron, USA), to measure the bending strength of the membranes. The capillary flow porometry (Porolux 500, IBFT GmbH, Germany) was employed to measure the bubble point, mean pore size, and pore size distribution of the membranes. The pore size distribution was calculated based on the Young-Laplace equation (Eq. (2.1)) [163]:

$$\mathrm{D} = \frac{4\gamma \cdot \cos\theta}{P} \tag{2.1}$$

Where D is the effective diameter of membrane pores (m), γ is the surface tension of the wetting liquid (0.016 N/m), θ is the contact angle at the fluid and membrane surface interface (0^{o}), and P is the applied pressure (N/m^2).

2.2.4. Oil-in-water microemulsions

Various nano-sized O/W emulsions, namely non-ionic Tween 80-stabilized microemulsion, anionic SDS-stabilized microemulsion, and cationic CTAB-stabilized microemulsion, all in combination with co-surfactant Span 80, were prepared for membrane filtration experiments, to study the impact of the charge of the emulsions on fouling of the membranes, respectively. To obtain 500 mg/L Tween-80 stabilized microemulsion, 2 g Soybean oil, 0.2g Span 80, and 0.2g Tween 80 with a mass ratio of 10:1:1 were added into 1L DI water (pH = 5.6), followed by continuously high speed stirring at 2000 rpm with a magnetic stirrer (L32, LABINCO, the Netherlands) for one day and ultrasonication in a sonifier (3800, Branson, USA) for one day, in accordance with previous studies [89, 164, 165]. Prior to each experiment, the preparation of the fresh emulsion involved the dilution of 1 L O/W microemulsion with 4 L DI water to a constant oil concentration of 500 mg/L since 50-1000 mg/L oil and grease content are typically present in oily wastewater [154]. The same procedures were used for the SDS and CTAB-based microemulsions. 1 mM NaCl were added to the microemulsion to adjust the ionic strength. The pH of the microemulsions was measured by a pH meter (228HTE, PCE Brookhuis B.V., the Netherlands). The sizes and size distributions of the oil droplets were measured with a particle size analyzer (Bluewave, Microtrac, USA), while the zeta potential of the microemulsions was obtained using a Malvern Zetasizer Nano instrument (ZS90, Malvern, UK). The stability of the microemulsions were confirmed by similar oil droplet size distribution after the emulsions were left to stand for 1 day and 7 days (Fig.S14).

2.2.5 Determination of threshold flux

The conventional flux stepping method was employed to estimate the threshold flux [166, 167]. This method involved incrementally increasing the permeate flux while simultaneously recording the transmembrane pressure (TMP) for each step. The threshold flux was determined by using the average TMP (TMP_{avg}). The flux stepping tests use a range of fluxes varying from 40 $Lm^{-2}h^{-1}$ to 100 $Lm^{-2}h^{-1}$. Each step in the test lasted for 20 minutes, with intervals of 10 $Lm^{-2}h^{-1}$.

2.2.6. Fouling experiments with microemulsions

Fouling experiments with constant permeate flux

Microemulsion filtration experiments were carried out with a constant permeate flux crossflow setup (Fig.2.1). The concentrate stream was discharged back into the feed during filtration, while a steady flow was provided by the digital diaphragm metering pump (DDA17-7, Grundfos, Denmark). The gear pump (VGS Standard, Verder Liquids, the Netherlands), employed as a circulation pump, was utilized to maintain a consistent crossflow velocity (CFV) of 0.59 m/s. The TMP was calculated by averaging the inflow and outflow pressures on both sides of the membrane module. To avoid a discrepancy between the feed pump flow and the permeate flux, a digital balance (FZ-3000iWP, Japan) was utilized to measure the weight of the permeate, and then it was converted to permeate flux.

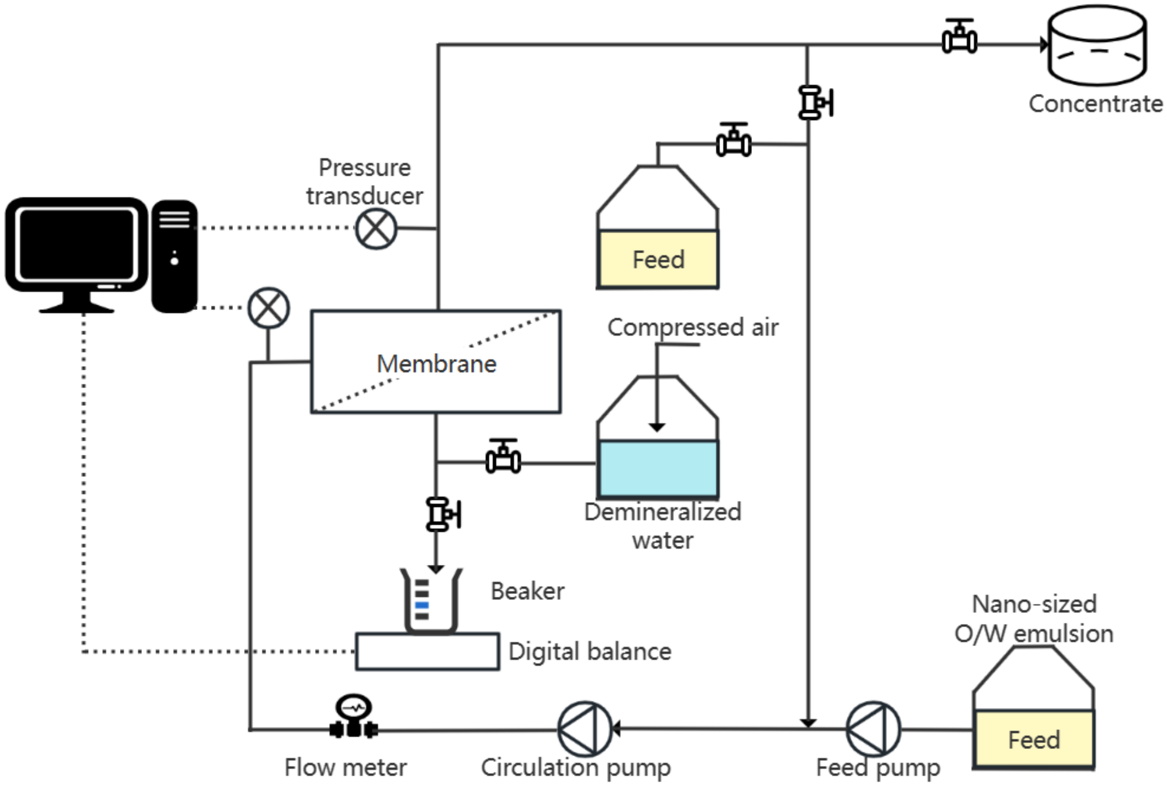

Fig. 2.1. Schematic diagram of constant flux filtration system.

Filtration protocol

Each filtration experiment began with a pure water permeance test in a crossflow mode, using the same permeate flux and crossflow used for microemulsion filtration. The fouling experiments for the SiC-coated membranes with different deposition times comprised multiple cycles, which were reliant upon the microemulsions properties (pH and surfactant type). Each filtration cycle consisted of three stages: (i) filtering the microemulsions at a specified flux for 20 min; (ii) backwashing to remove reversible fouling at a constant backwash flux of 1080 $Lm^{-2}h^{-1}$; (iii) forward flushing with microemulsion for 10 s at a CFV of 0.59 m/s to drain the concentrated water. To have a fair comparison of backwash efficacy, due to the decreased permeance of the SiC-coated membranes, the fouled H0, H10, H15, H20, and H25 membranes were backwashed for 1 min with DI water at pressures of 3 bar, 3.375 bar, 3.857 bar, 4.5 bar, 5.4 bar, 6.75 bar, respectively to obtain the same backwash flux in every membrane. Every experiment was conducted in duplicate.

Data analysis

Permeate fluxes and water temperature were measured at 10-second intervals. The pure water permeance was assessed by filtering DI water at 5 bar. This preliminary step was conducted to verify the thorough cleaning of the membranes prior to the start of the experiments using Eq. (2.2) [168]:

$$L_{P,20^{\circ}\mathrm{C}} = \frac{J \cdot e^{-0.0239 \cdot (T-20)}}{\Delta P} \tag{2.2}$$

Where $L_{p,20\ ^{\circ}C}$ represents the water permeance at 20 °C ($Lm^{-2}h^{-1}bar^{-1}$), J denotes the membrane flux ($Lm^{-2}h^{-1}$), and T denotes the water temperature (°C).

The relation between the permeate flux, TMP, viscosity, and membrane resistance is shown in Eq. (2.3):

$$J = \frac{TMP}{\mu R} \tag{2.3}$$

Where R represents the resistance to mass transfer (m^{-1}), μ denotes the permeate viscosity (Pa·s), and J denotes the permeate flux through the membranes (m/s). The calculation of the membrane resistance is based on the resistance-in-series model [169, 170].

$$TMP_{Normalized} = \frac{TMP}{TMP_0} \tag{2.4}$$

The normalized TMP is the ratio of TMP divided by TMP_0, as shown in Eq. (2.4). The TMP_0 is the TMP corresponding to the required flux (80 $Lm^{-2}h^{-1}$) with a clean membrane.

The methods used to determine oil and chemical oxygen demand (COD) rejection are provided in the supporting information, as shown in Fig.S2.16 and S2.17.

2.3. Results and discussion

2.3.1. Membrane morphology

EDX spectroscopy analyses were conducted to probe and verify the elemental compositions of the Al_2O_3 membranes and SiC-coated Al_2O_3 membranes. The main composition of the SiC membrane, C and Si, was confirmed by the two strong peaks at 0.277 keV and 1.739 keV, respectively (see Fig. S2.1). As shown in Fig.2.2a, with the increase in deposition time from 0 min (without deposition) to 25 min, the weight percentages of Si increased from 0 to 25.09 wt%, while the weight percentages of Al decreased from 89.96 to 61.03 wt%. EDX mapping distribution analysis, as shown in Fig. S2.2, confirms these observations. Fig.2.2b shows the XRD patterns of the H0 and the H20 membrane. The upper spectrum (red line) shows the characteristic XRD pattern of the polycrystalline layer for the H20 membrane, and the main phase identified is 3C-SiC polytype with diffraction peaks at 35.61°, 41.4° and 60°, respectively, ascribed to (111), (200), (220) diffraction planes of the beta phase SiC.

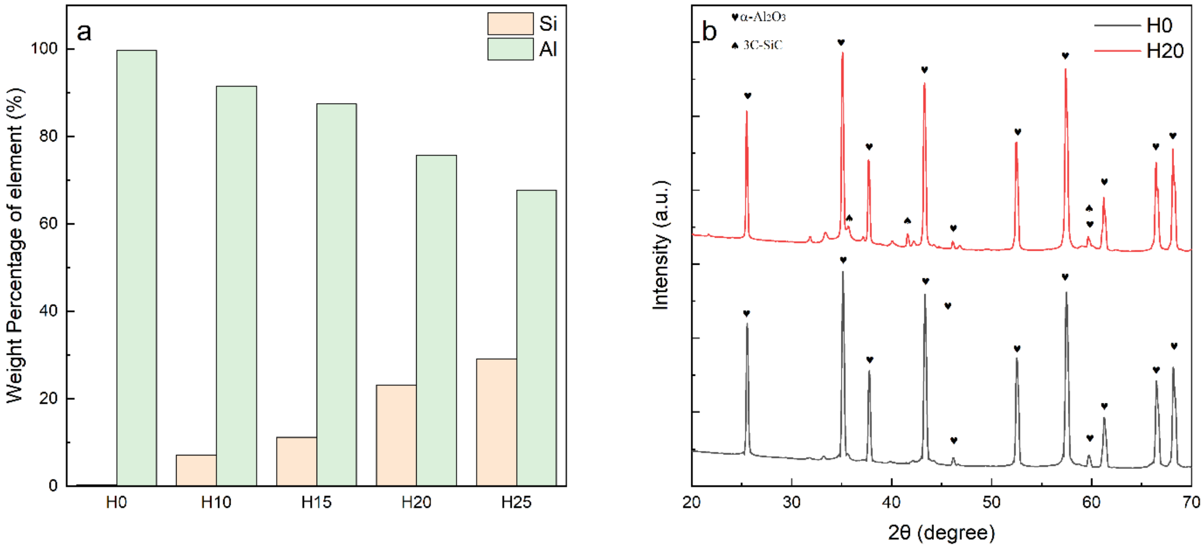

Fig. 2.2. (a) Weight percent of element for the H0, H10, H15, H20, and H25 membranes. (b) XRD patterns of the H0 and H20 membranes.

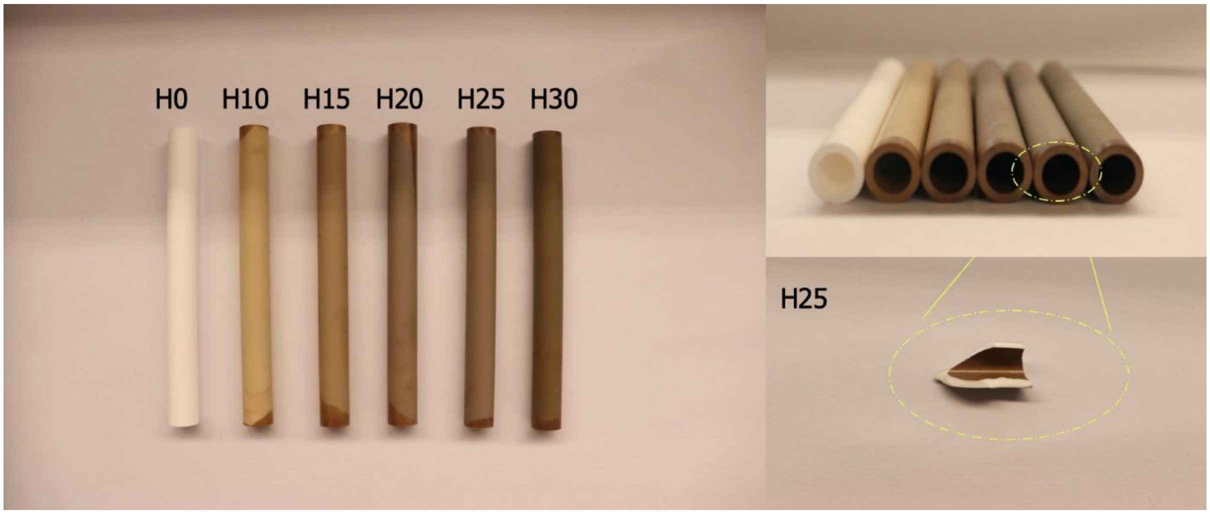

Fig. 2.3. Photographs of the Al_2O_3 (H0) membrane and SiC-coated Al_2O_3 (H10, H15, H20, H25) membranes.

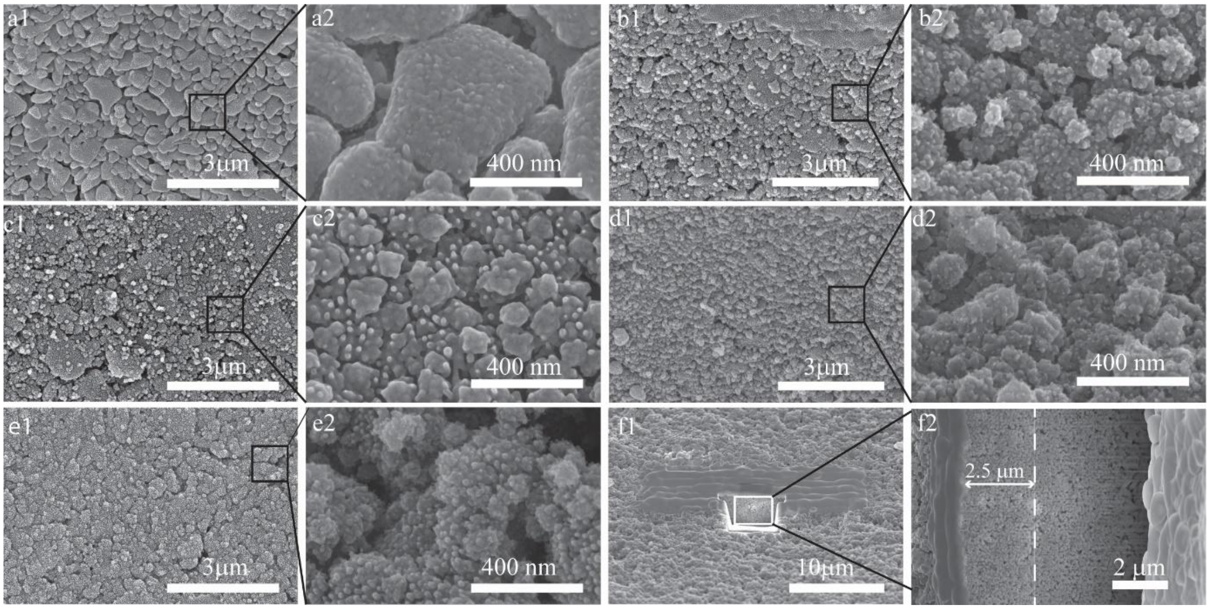

Fig. 2.4. SEM images for the surface of the (a) H0 and (b) H10, (c) H15, (d) H20, (e) H25 membranes, and (f) the cross-section of the H20 membrane.

An SEM was employed to examine further the surface and cross-section structure of the Al_2O_3 membrane and SiC-coated Al_2O_3 membranes. The separation layer of the membranes was in the range of 24 to 30 µm (Fig. S2.3). Fig.2.3 shows one pristine Al_2O_3 membrane and SiC-coated membranes with various deposition times. SiC has been deposited on both sides of the membranes. The deposition on the support layer did not affect the membrane's permeability due to the relatively small layer thickness of SiC compared to the pore size of the support layer, as evidenced by the SEM image in Fig. S20. With the increased deposition time, the color changed from white to golden and dark grey, and SiC nanoparticles aggregated on the Al_2O_3 surface, leading to the formation of pronounced nano-scale protrusions (Fig.2.4) [171]. With the deposition time further increased to 25 min, nanoparticles of larger sizes were observed. To evaluate the coating depth of SiC, a combination of the focused ion beam and SEM was applied to obtain high-resolution SEM images of the cross-section of the H20 membrane, as depicted in Fig. f. The results showed that the deposition mainly happened on the surface (2.5 µm) at the deposition time of 20 min, which was confirmed by the results of SEM-EDAX line scan (Fig. S2.3f and Fig.S2.15 a-c). These scans indicated that the Si intensity stayed constant, and higher than the background noise, over the entire separation layer, indicating adequate infiltration of the precursors into the membrane, where the penetration depth of SiC was around 2.5 µm.

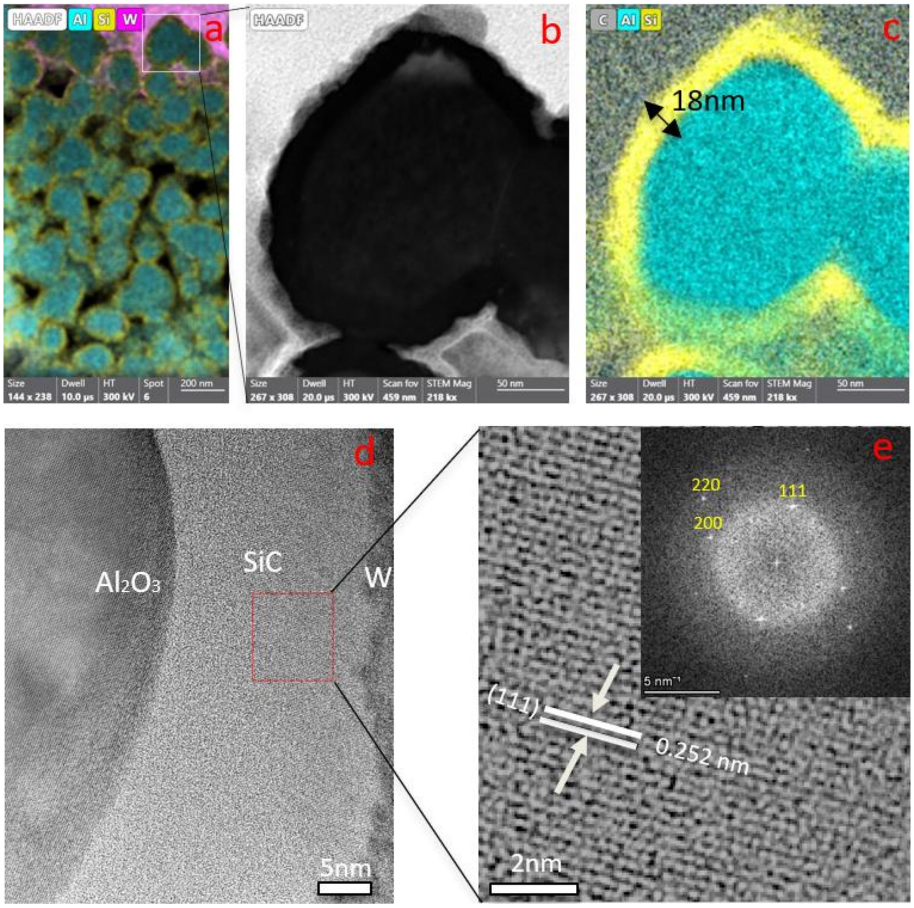

Fig. 2.5. (a) STEM EDX net intensity maps of the cross section of the H20 membrane. (b) STEM images and (c) EDX net intensity maps of a SiC coated alumina particle near the top. (d) and (e) High-resolution TEM images of the H20 membrane with SAED patterns (upper right).

Fig.2.5 shows the thickness of the uniform SiC layer on the surface of the Al_2O_3 particles for the H20 membrane, observed by TEM, being 18 ± 1 nm. The interface between the Al_2O_3 particles and SiC coating layer is clearly visible. Besides, high-resolution TEM images show an amorphous SiC layer with some 5-10 nm crystalline 3C-SiC (β-SiC) particles. A laminated structure, embedded in the amorphous SiC matrix, confirmed the presence of the 3C-SiC polytype (Fig.2.5d). The lattice plane distances were 2.517, 2.180, 1.541Å, respectively, corresponding to the {111}, {002} and {022} planes of 3C-SiC (Fig.2.5e). This finding is in accordance with the XRD results, described in previous section.

The membrane surface morphology was also studied by AFM, and the results are shown in Fig. S2.5. The average surface roughness (R_a) and the root-mean-square surface roughness (R_q) values of the Al_2O_3 membrane (Fig. S2.5a) were 55 ± 3nm and 43 ± 4 nm, respectively, illustrating a relatively smooth surface. With the increase in deposition time, from 10 min to 25 min, the R_a increased from 66 ± 1 nm to 82 ± 2 nm (Fig. S2.5b-e), respectively, indicating that the deposition of SiC nanoparticles provided an increase in roughness of the membrane surface. The increase of R_a could be explained by the increase in the size of the SiC nanoparticles, which covered the Al_2O_3 particles, as also illustrated by the SEM images (Fig.2.4), which is consistent with the work of Lin et al. [172]. Increased surface roughness contributes to a rise in turbulence, and oil droplets could gain momentum to slip away from the pores, leading to less fouling [43]. In addition, the relationship between the size of the oil droplet and the characteristic length of roughness also influences fouling since the underwater superoleophobicity of the coated membranes reduces fouling if the size of oil droplets exceeds the characteristic length [173].

2.3.2. Membrane hydrophilicity and zeta potential

The effectiveness of membranes for oil/water separation is significantly influenced by surface wettability. Membranes with hydrophilic surface (WCA < 90º) are underwater oleophobic or even superoleophobic when the UOCA is >150º [174]. All SiC-deposited Al_2O_3 membranes (H10, H15, H20, H25) were in-air hydrophilic (Fig.2.7a and Fig. S2.6) and underwater superoleophobic (Fig. S2.7). These properties can be attributed to a significant number of hydroxyl groups on the SiC-deposited Al_2O_3 membrane surface [160], which is essential for their oil fouling resistance. Due to the porous structure of H10, H15, H20, and H25, a static WCA measurement was impossible since all the water drops were easily dispersed on the membrane surface and rapidly infiltrated into the pores. Fig. S2.8 shows the real-time, dynamic WCA of the membranes, indicating that the WCA of the Al_2O_3 membranes decreased from 36° to less than 5° within 2.8 s, while for the SiC-coated membranes, the WCA rapidly declined to less than 5° within 1 s. Therefore, only the initial WCA was determined, being 37° ± 1.2° for the Al_2O_3 membrane and 29° ± 1.2° to 21° ± 0.6 °, 18° ± 0.3° and 15° ± 0.1° for the H10, H15, H20 and H25 membrane, respectively. This is consistent with a previous study where the WCA of SiC hollow fiber membranes is 11.3° [21]. In addition, according to Wenzel's equation, increasing the roughness of hydrophilic surfaces enhances their hydrophilicity [175], which is consistent with our finding that the surface roughness increased with deposition time. Besides, the UOCA of H0 and H20 were 137° and 168°, respectively. This indicates the underwater oleophobicity was increased with the deposition of the SiC layer. Soybean oil adhered to the Al_2O_3 underwater membrane surface, while the soybean oil droplets remained spherical for the SiC-coated membrane, and no evident oil adhesion after pulling down the oil droplet from the SiC-coated surface was observed, as shown in Fig. S2.9. These observations indicate the improved hydrophilicity and superoleophobicity of the membranes after SiC deposition.

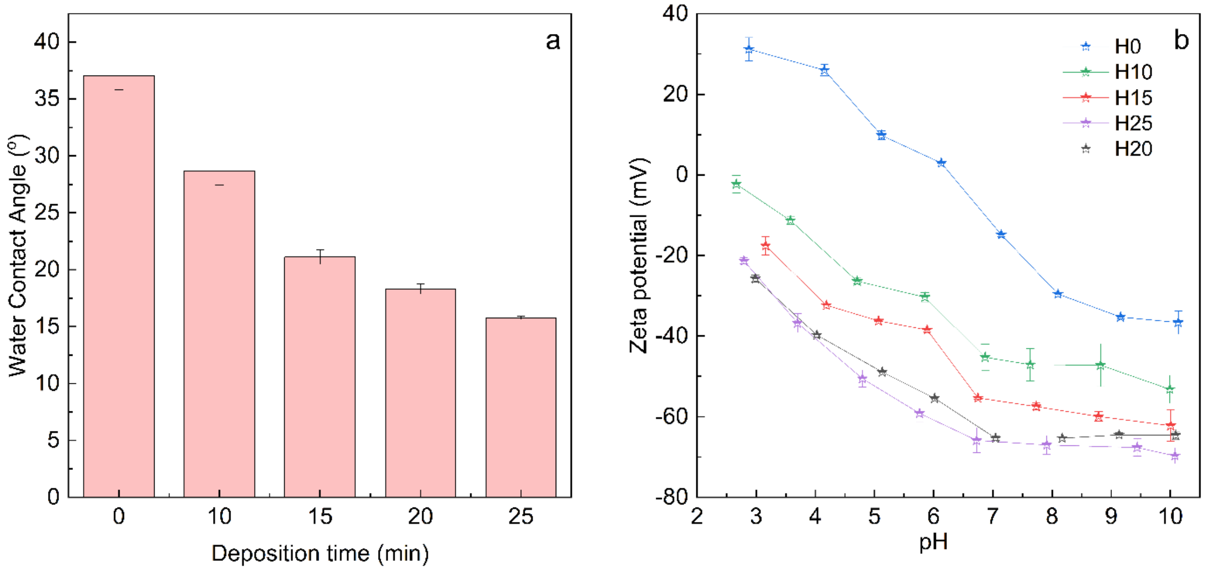

Fig. 2.6. Initial water contact angle (a) and zeta potential (b) of Al_2O_3 membrane (H0) and SiC-coated Al_2O_3 membranes (H10, H15, H20, H25) with increasing deposition times.

The zeta potential of the membrane is an indication of the surface charge, and, for a specific surface, it is usually dependent, amongst others, on the pH. Usually, the membrane surface becomes more negatively charged with an increase in pH [152]. Fig.2.6b shows that the zeta potential of membranes indeed decreased with an increase in pH and that the IEP of the Al_2O_3 membranes became 6.4, which is consistent with the results reported by Nagasawa et al. [58]. Besides, all SiC-coated membranes were negatively charged in the measured pH range (3-10) and were more negatively charged compared with the Al_2O_3 membranes. The zeta potentials of the H20 and H25 membranes showed similarities but were lower than those of the H0, H10, and H15 membranes. A possible explanation is that the SiC layer is not closed at lower deposition time, and all the alumina is covered by SiC after 20 min of deposition [176].

From Table S2.2, it can be observed that the pH value had little impact on the zeta potential of the oil droplets, which is in accordance with previous studies, where it has been reported that the pH of the solution does not have an effect on the surface charge of emulsions stabilized with ionic surfactants due to the strong acid sulfonate heads of surfactant [177].

2.3.3. Pure water permeance, membrane pore size and oil rejection

Pure water permeance tests were carried out, and the results are depicted in Fig.2.7a. The permeance of the membranes exhibited a linear reduction, ranging from 368 ± 8 to 165 ± 3 $Lm^{-2}h^{-1}bar^{-1}$, respectively, as the deposition time increased from 0 min (no deposition) to 25 min. This can be explained by the linear decrease of the mean membrane pore size, from 41.2 nm (H0) to 33.6 nm (H25), respectively (Fig. b). The bubble point diameter, which reflects the maximum pore size of the membrane, also showed a decrease with an increase in deposition time from 93 nm (H0) to 73 nm (H25), respectively (Fig.2.7c). Therefore, the rejections of the nano-sized oil droplets (104 nm) of both the Al_2O_3 membrane and SiC-coated membranes were over 99% due to the size-sieving effect (Fig. S2.10), as indicated by Zhang et al. [178]. Additionally, the small oil droplets could potentially be trapped within the irregular channels of the membrane support. However, the COD rejection (98 ± 0.4 %) was lower than the oil rejection, probably because the small surfactant molecules can pass through the membrane pores. In the meantime, the porosity of the membranes dropped linearly with the increase in the SiC deposition time. According to data gathered through Image J analysis of the SEM images (Fig.2.7d and Fig. S2.4), the porosity decreased to 19.9 % when the deposition time was increased to 25 min. The decreased porosity, improved grain bonding (Fig. S2.18) and deposition of the SiC on the defects of the H0 membrane surface (Fig. S2.19) contributed to the improved bending strength from 76 ± 9 MPa to 106 ± 10 MPa of the H0 membrane and H25 membrane, respectively (Fig.2.7d).

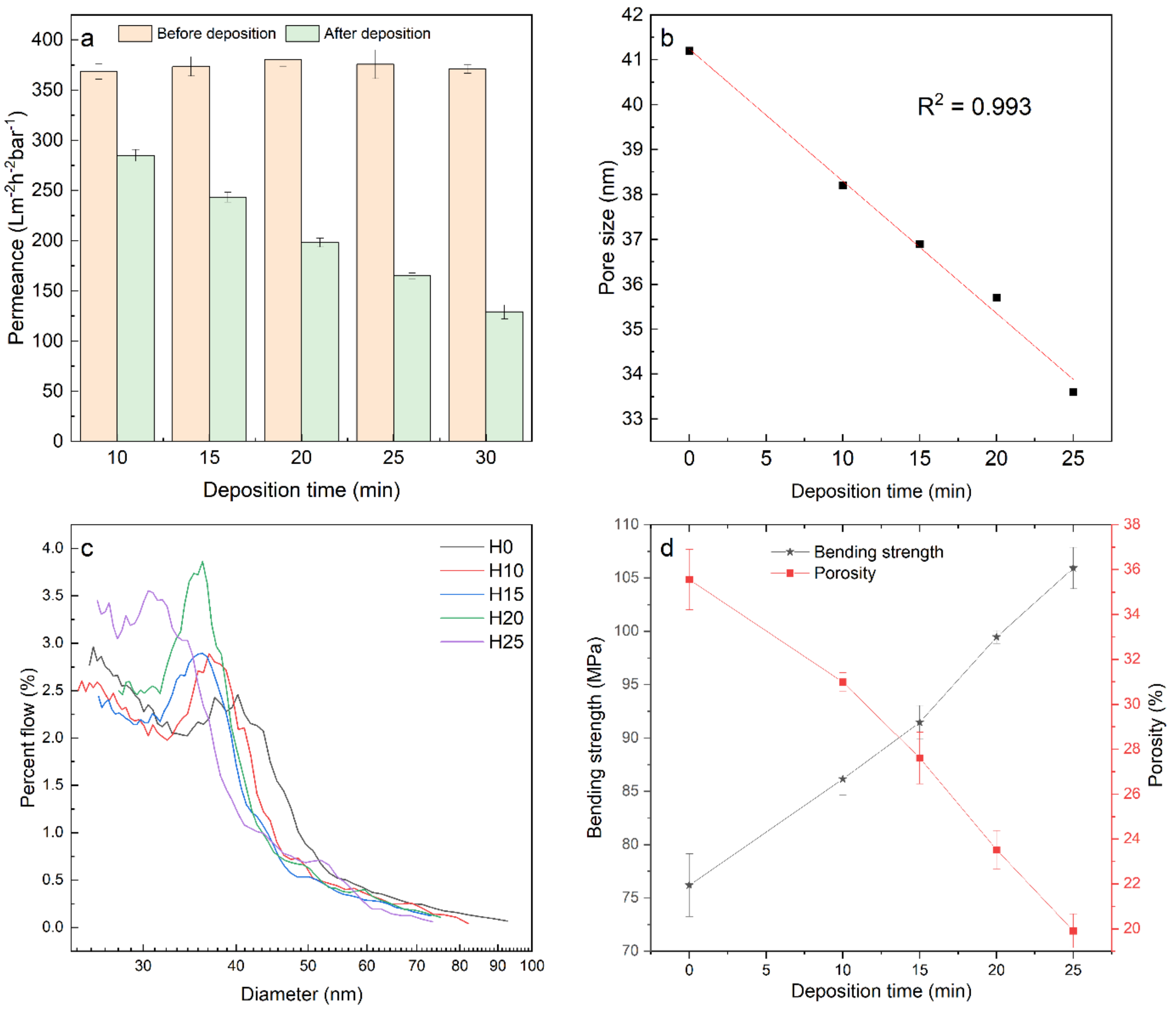

Fig. 2.7. (a) Permeance, (b) pore size, (c) pore size distribution, and (d) bending strength and porosity of the Al_2O_3 membrane (H0), and the SiC-coated Al_2O_3 membranes with increasing deposition times: H10, H15, H20, H25.

2.3.4. Comparison of fouling of the various membranes

Fig2.8 shows the comparison of the fouling of the Al_2O_3 membrane (H0) and the four SiC- Al_2O_3 membranes (H10, H15, H20, H25) for microemulsion filtration at a constant flux of 80 $Lm^{-2}h^{-1}$, respectively. This flux was selected based on the threshold fluxes of the H0 membrane (76 Lm^{-2}

h^{-1}) and the H20 membrane (86 $Lm^{-2}h^{-1}$) (Fig. S2.11). The normalized TMP curve (Fig.2.8a) shows that the H0 membrane showed the greatest fouling tendency. However, it is worth noting that the normalized TMP curves showed similarities across all membranes in the initial cycles. Following the initial cycle, the backwash was effective, indicating little irreversible fouling. However, with an increasing number of filtration cycles, irreversible fouling gradually accumulated, causing a more rapid increase in TMP.

The fouling resistance was also used to calculate the reversible and irreversible fouling. Fig.2.8b illustrates the fouling resistance observed in the six cycles for all membranes. Both irreversible fouling and reversible fouling decreased with the increase in deposition time until 20 min. The R_r and R_{ir} were reduced by 77% and 72%, from 14.31×10^{12} to 3.29×10^{12} m^{-1} and from 9.69×10^{12} to 2.76×10^{12} m^{-1}, respectively, as the deposition time increased to 20 min. However, more fouling was noticed for the H25 membrane, probably due to the lower permeance and smaller pore size, resulting in higher TMPs at constant flux and, thus, more accumulation of irreversible fouling [179].

With the increase in deposition time, the membranes became more hydrophilic and more negatively charged (Fig.2.6). Both electrostatic interactions and hydrophilic interactions affect the membrane fouling in crossflow filtration [180]. The pH of the microemulsion was 5.6 and, at this pH, the zeta potentials of the H0, H10, H15, H20, H25 membranes (Fig.2.7c) were -20.0 mV, -30 mV, -38 mV, -55.5 mV and -59.6 mV, respectively. This means that the surface of all the membranes was negatively charged. The microemulsions stabilized by Tween 80 and Span 80 were slightly negatively charged (-21.30 ± 0.73 mV) due to the deprotonation of the hydroxyl groups present in Tween 80 [94]. Therefore, weak electrostatic repulsion between the nano-sized oil droplets and the Al_2O_3 membrane surface led to an increased fouling potential, whereas stronger electrostatic repulsion forces occurred for SiC-coated membranes. This observation is consistent with the results obtained with the filtration of negatively charged oil droplets over a negatively charged ZrO_2/TiO_2 membrane, leading to a decrease in cake layer formation and the accumulation of fouling [181]. Probably, the hydrophilicity of the membranes, which improved after SiC deposition (Fig.2.6a), also prevented the membrane from adsorbing or depositing oil. It has also been reported that the improved hydrophilicity of isotropic PES membrane leads to less fouling due to decreased oil layer formation [88].

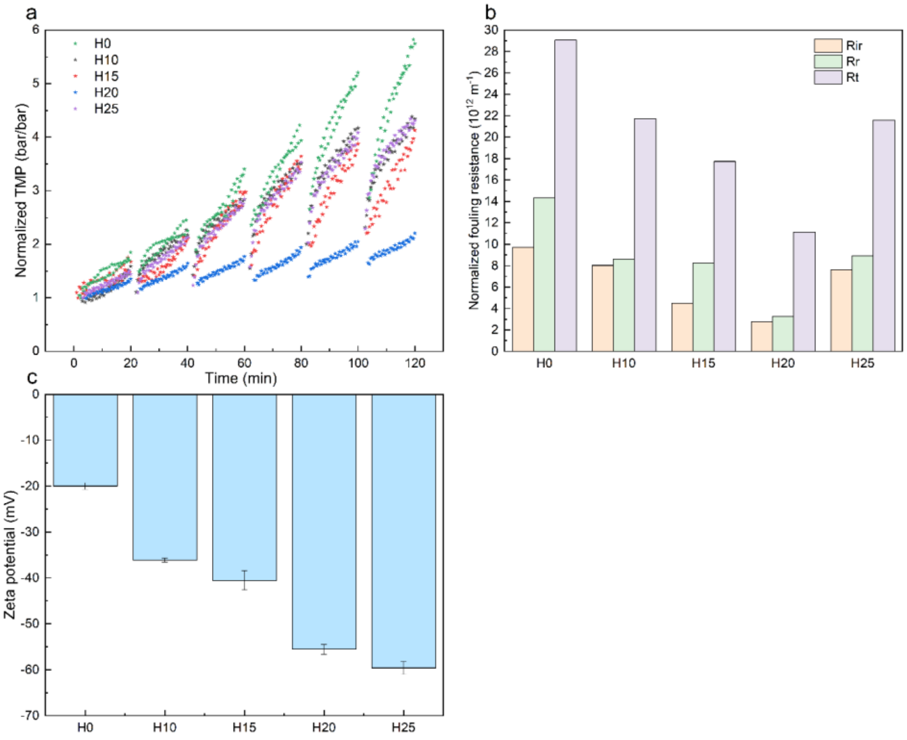

Fig. 2.8. The normalized (a) TMP and (b) fouling resistance of the H0, the H10, the H15, the H20, the H25 membrane for the filtration of microemulsion (500 mg/ L soybean oil with 50 mg/ L Span 80 and 50 mg L^{-1} Tween 80)； (c) is the zeta potential of the H0 the H10, the H15 the H20, the H25 membranes in the surfactant solution with 50 mg/ L Span 80 and 50 mg/ L Tween 80.

2.3.5 Fouling behavior at various pHs, surfactants and pore sizes

Fouling behavior at various pHs

To investigate the influence of pH on the fouling of the H0 and the H20 membrane, three different pH values (4, 5.6, and 8) were selected. The normalized TMP curves of H0 and H20 are shown in Fig.2.9, which reveals that with an increase in pH of the microemulsion, the performance of both the H0 and the H20 membranes improved, while the fouling was more severe in the H0 membrane compared to the H20 membrane at the same pH. This phenomenon can be ascribed to the fact that as the pH rises, the surface charge of the membrane becomes increasingly negative [147]. The zeta potential of the H20 membrane, e.g., experienced a reduction from -48.2 mV to -65.1 mV as a result of a rise in pH from 4 to 8, respectively, while the zeta potential of microemulsions remained constant with the change in pH, as shown in Table. S2.2. At a pH of 5.6, the H20 membrane (-61.8 mV) would repulse oil droplets more strongly. Therefore, the H20 membrane would retain oil droplets on the surface and showed less susceptibility to fouling by negatively charged oil droplets. However, the surface charge of the H0 membrane was less negative (-39.2 mV), as can be seen from Fig.2.9e, compared with the H20 membrane, leading to more fouling. When filtering the microemulsion at a pH of 8, the zeta potential of the H0 membrane was further decreased to -45.8 mV, and the electrostatic repulsion enhanced and decreased fouling. The zeta potential value of the H20 (-65.1 mV) was nearly 1.5 times lower than that of the H0 (-45.8 mV). Thus, a higher electrostatic repulsion existed, which supports the results of better fouling resistance of H20 at a pH of 8.

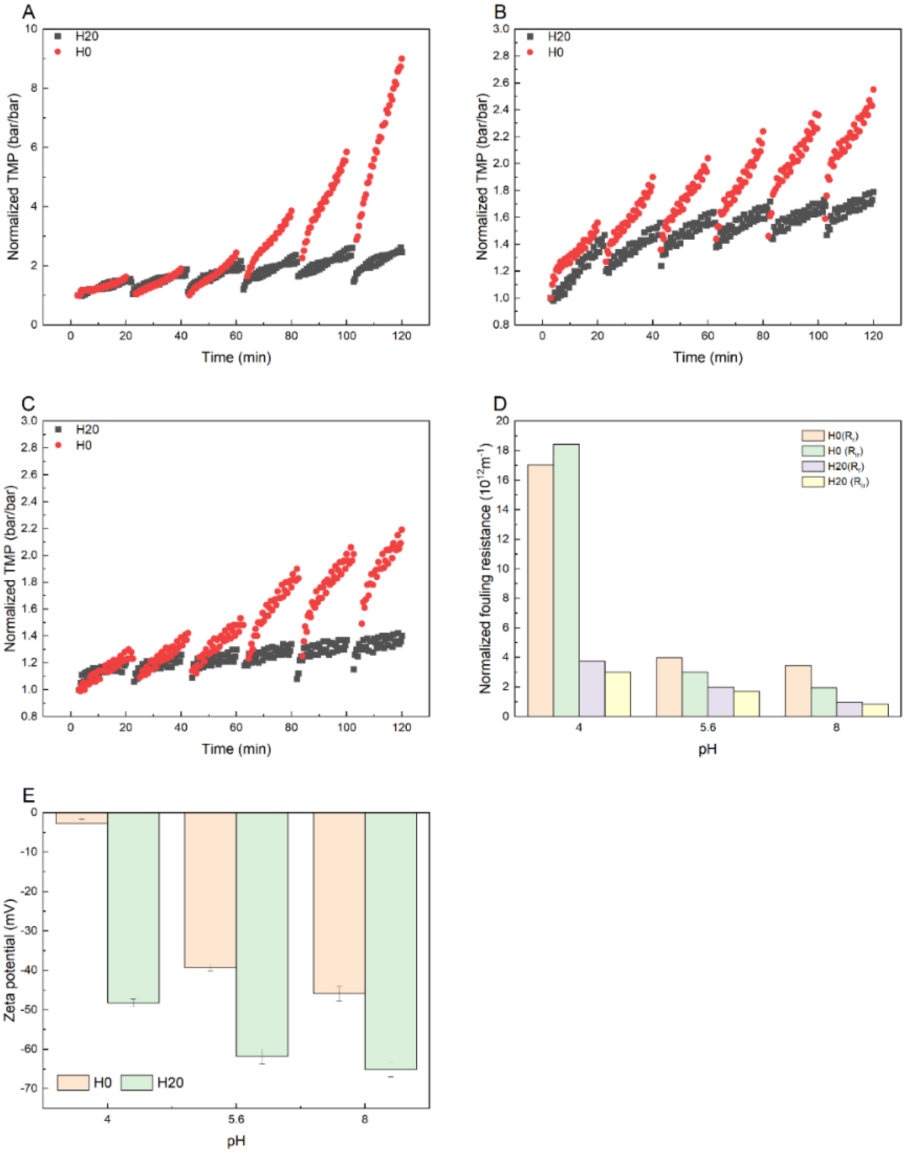

Fig. 2.9. Normalized TMP of the H0 and the H20 membrane or the filtration of microemulsion stabilized with 50 mg/L Span 80 and 50 mg/L SDS at the pH of (a) 4, (b) 5.6, and (c) 8; (d) is the normalized fouling resistance of the H0 and the H20 membrane at the pH of 4, 5.6 and 8; (e) is the zeta potential of the H0 and the H20 membrane at the pH of 4, 5.6 and 8.

With the increase in pH, stronger repulsive electrostatic interactions led to the accumulation of oil droplets above the membrane surface and formed a cake layer [180]. Therefore, it became more difficult for the oil droplets to squeeze and enter the pores, and thus, less irreversible fouling existed. Fig.2.9d shows a reduction in the R_r and R_{ir} of H0, specifically, from 7.04×10^{12} to 3.46×10^{12} m^{-1} and from 18.43×10^{12} to 1.97×10^{12} m^{-1}, respectively, when the pH climbed from 4 to 8. Nevertheless, the R_r and R_{ir} of H20 exhibited a moderate drop, from 3.74×10^{12} to 0.98×10^{12} m^{-1} and from 3.00×10^{12} to 0.83×10^{12} m^{-1}, respectively.

Fouling behavior with various surfactant types

The stability of O/W microemulsions depends on the surfactants present in oily wastewater. The type of surfactant has a significant effect on membrane fouling since the colloidal surface charge strongly influences fouling [14, 58, 94, 182]. Microemulsions with combinations of surfactant Span 80 with three different surfactants, Tween 80, SDS and CTAB, respectively, had similar oil droplet average sizes as shown in Table. S2.1 and Fig. S2.12, being 99, 108 and 123 nm, respectively.

To investigate the impact of free surfactant molecules on the fouling of the membranes, a series of ultrafiltration (UF) experiments were carried out using pure Span 80 and Tween 80, SDS, CTAB (50 mg/L) in DI water (Fig. S2.13). The results showed that TMPs remained constant, and no fouling occurred since no micelles formed, and the small surfactant molecules could pass through the membrane pore and go into a permeate solution. As shown in Fig.2.10e, the zeta potentials of both the H0 and the H20 membrane followed the order: Span 80 + CTAB > Span 80 + Tween 80 > Span 80 + SDS (H20: -30.9 ± 1.4, -55.5 ± 1.1, -61.8 ± 1.9 mV, respectively; H0: 14.1 ± 3.8, -20.0 ± 0.7, -39.3 ± 0.8 mV, respectively). As depicted in Fig.2.10a,e and Table S2.2, the H20 membrane filtering the microemulsion stabilized with Span 80 and Tween 80 (-21.30 ± 0.73 mV) showed a lower fouling tendency than the H0 membrane due to a more negatively charged surface of the H20 membrane (-55.5 ± 1.1 mV) than that of the H0 membrane (-20.0 ± 0.7 mV).

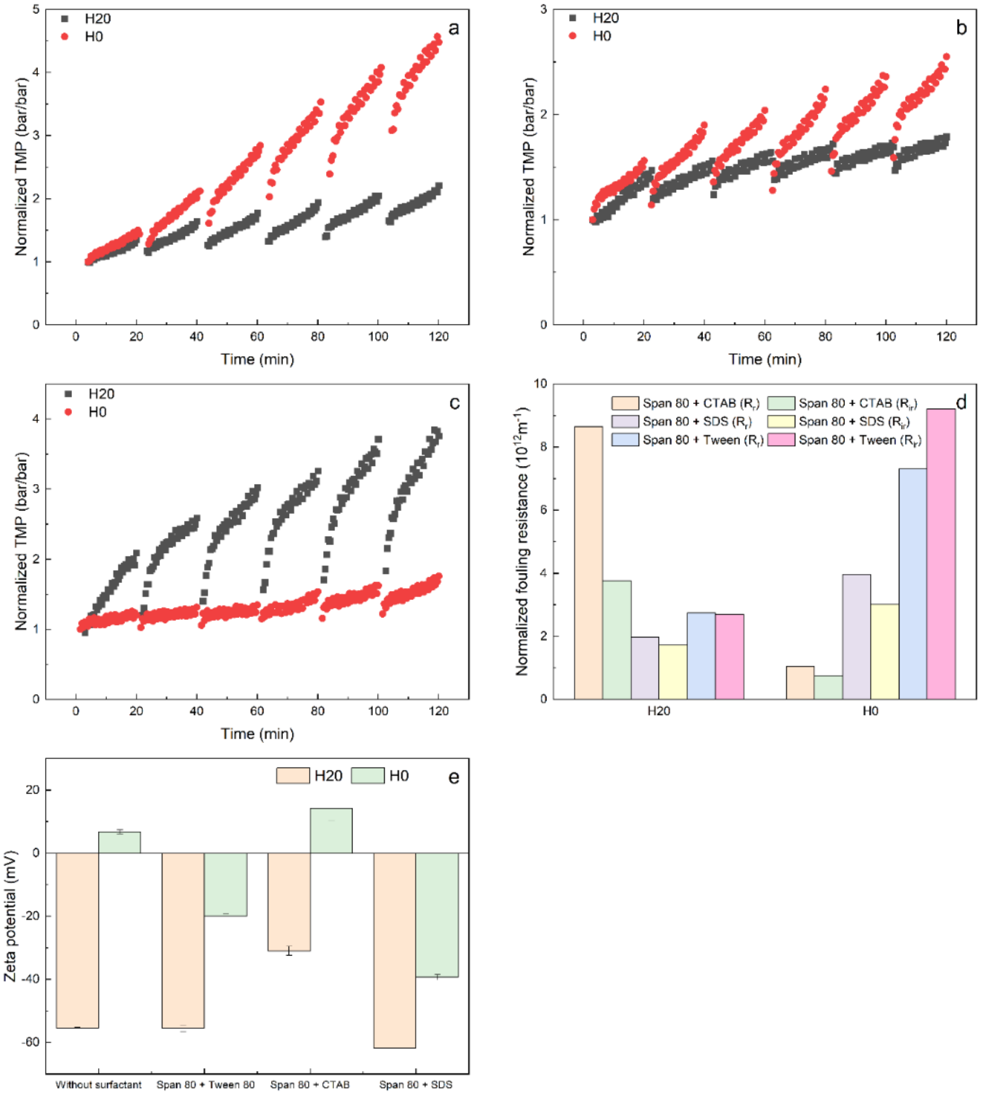

Fig. 2.10. Fouling comparison of the H0 and the H20 membrane during the filtration of microemulsions stabilized with various types of surfactant: 50 mg/L Span and 50 mg/L (a) Tween 80, (b) SDS, (c) CTAB. (d) is the normalized fouling resistance of the H0 and H20 membranes at various surfactant types. (e) is the zeta potential of the H0 and the H20 membrane in different surfactant solutions.

Similarly, as depicted in Fig.2.10b,e and Table S2.2, the microemulsion stabilized with Span 80 and SDS (-58.3 ± 0.82 mV), the H0 membrane showed a higher fouling tendency and (ir)reversible fouling than the H20 membrane (Fig.2.10d), due to weaker electrostatic repulsion between oil droplets and the negatively charged H0 membrane's surface (-39.3 ± 0.8 mV) than that of the H20 membrane's surface (-61.8 ± 1.9 mV). The H0 membrane surface charge changed from highly positive to slightly/moderately negative under the influence of Span 80 and Tween 80/SDS. Therefore, the electrostatic attraction between oil droplets and the H0 membrane surface changed to electrostatic repulsion and contributed to decreasing membrane fouling. Thien et al. also reported that the surfactant-stabilized oil droplets and surfactant-soaked membranes have the same charges due to surfactant adsorption, independent of surfactant type [94], leading to electrostatic repulsion.

However, the fouling behavior of the H0 membrane and the H20 membrane for the positively charged Span 80 and CTAB stabilized microemulsions (62.67 ± 0.76 mV) was different compared with the two previous microemulsions (Fig.2.10c). The H0 membrane showed the least membrane fouling compared with the other two types of microemulsions due to strong electrostatic repulsion between the positively charged membrane surface (14.1 ± 3.8 mV) and oil droplet. A higher reversible and irreversible fouling was found for the H20 membrane (Fig.2.10d), compared to the H0 membrane, due to the electrostatic attraction. The reason probably is that, although CTAB molecular adsorbed on the H20 membrane surface, charge inversion was not observed for the H20 membrane with a highly negatively charged surface, which was supported by the observation of a decrease of zeta potential from -55.4 mV to -30.9 mV. Therefore, the CTAB and Span 80 stabilized microemulsions fouled the H20 membrane rapidly.

Fouling behavior with various membrane pore sizes

Based on the findings of previous researchers, the early stage of colloidal fouling is characterized by pore blocking [183]. Specifically, in this work, oil droplets smaller than the diameter of membrane pores can result in pore blocking, whereas droplets much bigger than membrane pores can result in the cake layer formation. As shown in Fig.2.11 a-c and Table 2.1, the oil rejection decreased with the increase of the membrane pore sizes. When the average pore sizes of the membranes were far less than the average particle size of oil droplets, the membranes were more effective at retaining the oil droplets due to the pore size sieving effect. As a result, the oil rejection rate of the H0 membrane (41 nm) and the H20 membrane (35 nm) were 99.4 % and 99.2 %, respectively (Fig.2.11 a and e). When the mean pore sizes further increased to 139 nm (H20-600) and 181nm (H0-600), the sieving capacity of pore size was reduced. Therefore, it was less probable that the nano-sized oil droplets would pass through the pores of membrane, leading to the lowest oil rejection rate of 71.3% (H20-600) and 54.9% (H0-600) (Fig.2.11c and e). It is noticeable that the particle size distribution of the microemulsion revealed that 40.3% of the oil droplets had a size below 80 nm. Interestingly, the 81 nm H0-200 membrane demonstrated an oil rejection of 94.2% (Fig.2.11b and e). The phenomenon observed can be attributed to the deposition of nano-sized oil droplets on the membrane surface during the initial stage of the filtration process, resulting in the formation of a cake layer and subsequent rejection of the nano-sized droplets.

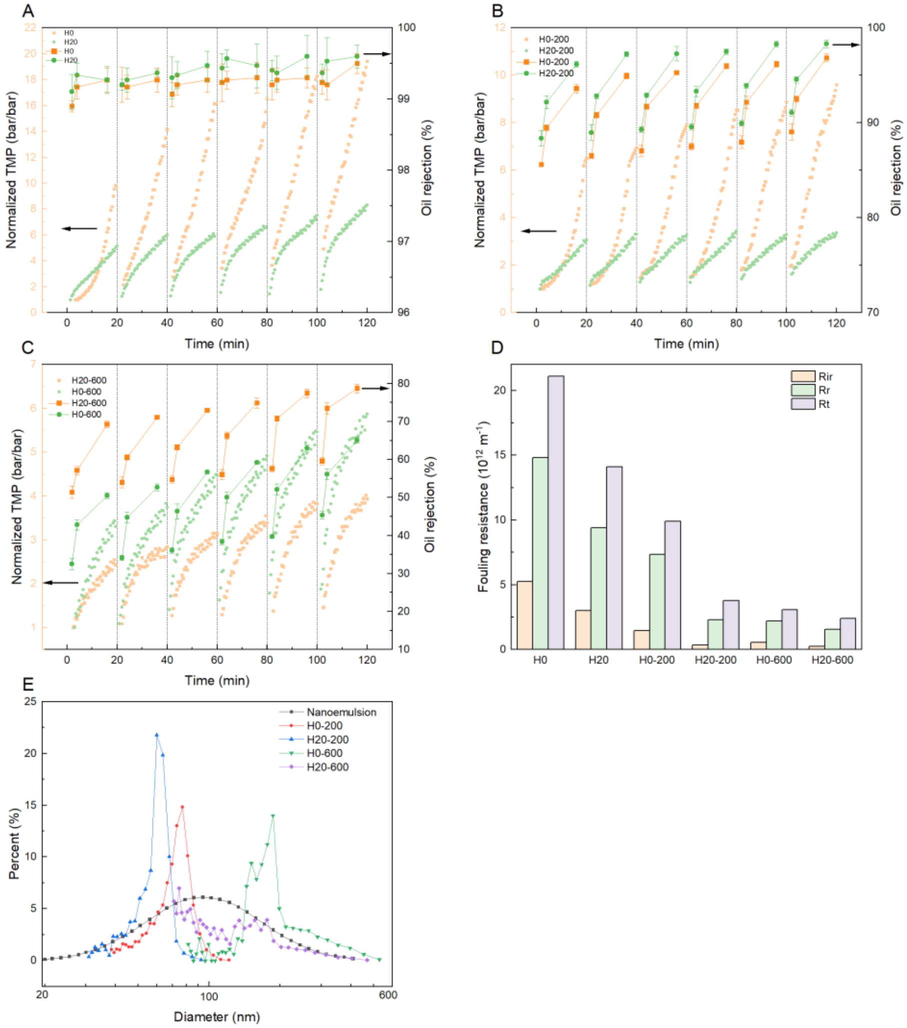

Fig.2.11. Fouling comparison of (a) the H0 and the H20 membrane, (b) the H0-200 and the H20-200 membrane, (c) 600 nm during the filtration of microemulsions stabilized with 50 mg/L Span 80 and 50 mg/L Tween 80 at the salinity of 1 mM. (d) is the normalized fouling resistance of the membranes at various pore sizes. (e) is the pore size distribution of the membranes and particle size distribution of the microemulsions stabilized with 50 mg/L Span 80 and 50 mg/L Tween 80 at the salinity of 1 mM.

To verify the build-up of the cake layer, the oil rejection was measured at three different time intervals: 0 to 2 min, 2 to 4 min, and 4 to 20 min in every cycle of the experiment using the H0-200 membranes. The results depicted in Fig.2.11b indicate that there was an observed rise in oil rejection from 85.6 % to 93.6 % for the H0-200 membrane in the first cycle, which confirmed the cake layer formation. Besides, the large percentage of reversible fouling shown in Fig.2.11d verified that the dominant fouling mechanism was cake filtration. A similar phenomenon was also observed for the H20-200, H0-600, and H20-600 membranes. As expected, the irreversible fouling decreased as the pore size increased. Particularly, the irreversible fouling of the H0 membrane was significantly greater than that of the other membranes since higher TMP led oil droplets to deform and go into pores.

Table 2.1. Properties of the Al_2O_3 and SiC-coated membranes.

Sample name	Coating time (min)	Pore size (nm)	Permeance ($L\ m^{-2}h^{-1}\ bar^{-1}$)
H0	0	41	380
H20	20	35	195
H0-200	0	81	498
H20-200	20	62	235
H0-600	0	181	985
H20-600	20	139	827

Overall, considering the fouling resistance and a constant oil rejection over 98% after the cake layer formed, the 62 nm H20-200 membrane is a promising choice for the separation of the microemulsions.

2.3.6 Long term filtration performance of the SiC-coated membrane

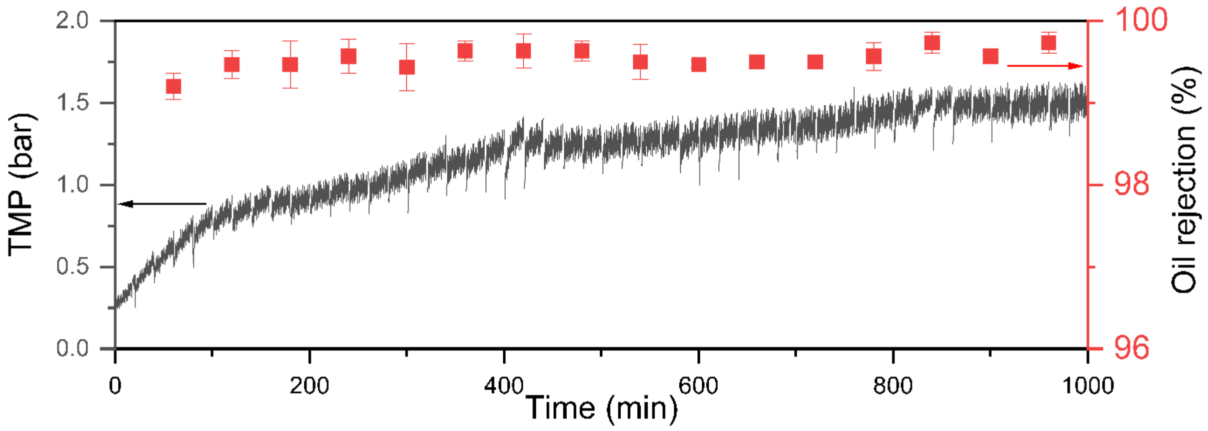

Fig. 2.12. Fouling behavior of the H20 membrane for 1000 min during the filtration of microemulsions stabilized with 50 mg/L Span 80 and 50 mg/L SDS at the salinity of 1mM.

We assessed the long-term performance of the SiC-coated membrane (H20) by conducting O/W separation for 1000 min (20 min per cycle with backwashing between cycles), as shown in Fig.2.12. Initially, during the early stage of the filtration process (within the first 160 min), the H20 membrane showed a relatively fast fouling tendency, requiring backwashing of the H20 membrane every 20 min. After the first eight cycles, the H20 membranes reached a dynamic stable filtration status with both a low per-cycle TMP increase and a high recovery of water permeance. Besides, the oil rejection during the fifty-cycle filtration experiments was 99.6 ± 0.2 %. After soaking the H20 membrane in citric acid (0.01 M, 70 °C) for 60 min, the permeance of the H20 membrane could be recovered to 99%, showing the reusability of the SiC-coated membranes.

2.3.7 Comparison with other ceramic membranes

Different hydrophilic ceramic membranes for oil/water separation are described in Table 2.2, based on the membrane pore size, water permeance, and the rejection of oil droplets. Compared with ceramic MF membrane, the SiC-coated alumina membrane in this work has a smaller pore size and a higher oil rejection, although the water permeance is lower [21, 92, 184, 185]. Moreover, to the best of our knowledge, the SiC membrane (H20) of this work had the smallest membrane pore size (35 nm) used for oil/water separation compared with other reported state-of-the-art SiC membranes [29, 92, 152, 186, 187].

Table 2.2. Comparison of the optimum membrane in this work with other reported hydrophilic ceramic membranes for oil/water separation

Membrane	**Pore size (nm)**	**Water permeance ($Lm^{-2}h^{-1}bar^{-1}$)**	**Oil droplet size (nm)**	**Rejection (%)**	**Ref**
αAl_2O_3-ZrO_2	50	80	1360	>90	[188]
ZrO_2	78	300.55	18	99.7	[89]
Si_3N_4	680	260	680	91	[184]
Graphene oxide	220	534	100-500	99.9	[185]
SiC	710	654	50-200	93.5	[21]
SiC	400	324	1000	98.5	[187]
ZrO_2/SiC	60	300	1350	99.9	[186]
SiC	430	300	850	90	[92]
SiC-coated Al_2O_3	47	177	5000	99	[29, 152]
SiC-coated Al_2O_3	35	195	99	99.7	This work
SiC-coated Al_2O_3	62	235	99	96.2	This work
SiC-coated Al_2O_3	139	827	99	71.3	This work

The pore size of SiC membranes prepared by traditional fabrication techniques generally depends on the size of the starting SiC particles. In most cases, smaller SiC particles lead to smaller membrane pores [25]. Since SiC powders typically range from 0.5 to 41 µm, the resulting pore sizes of membranes fabricated by methods such as spray coating, dip coating, and co-sintering usually fall within 0.4–3 µm, as shown in Figure 2.13 [17, 26-28, 92, 96, 160, 187, 189, 190]. The smallest reported pore size for a full SiC membrane is 78 nm, achieved with the dip-coating method, where oxidation bonding creates a silica phase that narrows the pores, combined with the use of fine SiC powder (0.55 µm) [191]. However, because the SiC particles are irregular in shape, their non-ideal packing introduces uncertainties in pore size control for ceramic membranes [25]. In contrast, the LPCVD method can deposit a homogeneous SiC layer onto an Al_2O_3 support by forming nano-sized SiC particles at relatively low temperatures (860 °C), enabling precise control of pore size at the nanometer scale.

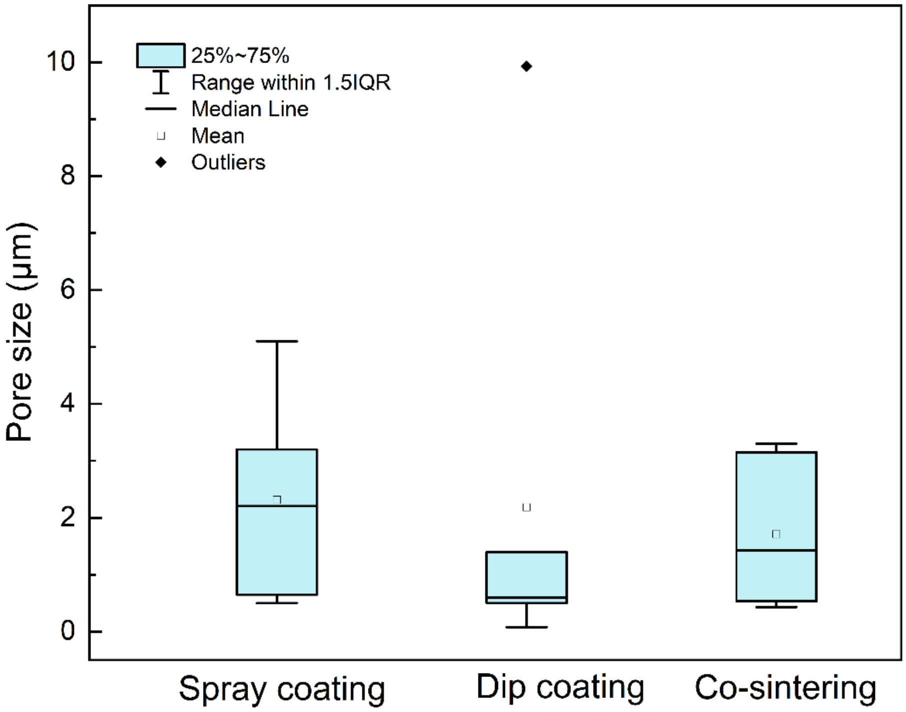

Fig. 2.13. Pore size of SiC membranes fabricated by spray coating, dip coating and co-sintering methods.

2.4. Conclusion

The preparation and characterization of a pristine Al_2O_3 membrane (H0) and, innovatively, chemically stable SiC-coated Al_2O_3 UF membranes (H10, H15, H20, H25) and the fouling of these membranes by surfactant-stabilized O/W microemulsions was studied. A comparative analysis was conducted to examine the physicochemical properties (e.g., surface morphologies, mechanical strength, and wettability) of both Al_2O_3 membrane (H0) and SiC-coated Al_2O_3 UF membranes. Co-surfactant Span 80 was combined with three different surfactants, non-ionic Tween 80, anionic SDS, and cationic CTAB, to prepare the microemulsions. Fouling experiments were carried out at a constant flux of 80 $Lm^{-2}h^{-1}$, which was around the threshold flux. To study the influence of electrostatic interactions on membrane fouling, membrane filtration experiments were conducted at various pHs, surfactant types, and pore sizes. The findings are summarized as follows. Firstly, polycrystalline 3C-SiC deposition decreased the porosity and pore size of the membrane and improved its bending strength. Secondly, SiC-coated membranes with different deposition times, filtering O/W microemulsions, had a lower (ir)reversible fouling compared with the pristine Al_2O_3 membranes due to a more hydrophilic and negatively charged surface. The 20 min SiC-coated membranes showed the lowest (ir)reversible fouling and a lower (ir)reversible fouling was observed at higher pH due to the larger electrostatic repulsive force between the more negatively charged membrane surface and nano-sized oil droplets. Thirdly, the Al_2O_3 membrane filtering microemulsions stabilized with Span 80 and Tween 80/SDS showed a higher fouling tendency than the SiC-coated Al_2O_3 membrane due to stronger electrostatic repulsion. However, the SiC-coated Al_2O_3 membranes showed a higher fouling tendency for the positively charged (CTAB-stabilized) microemulsion than the Al_2O_3 membrane due to the electrostatic interactions (attraction for the SiC-coated Al_2O_3 membrane and repulsion for the Al_2O_3 membrane). Lastly, the 62 nm SiC-coated membrane performed best for the filtration of the microemulsion, because of the high rejection of the oil droplets and the low fouling tendency.

Supplementary information

Table S2.1. The average size of the microemulsion stabilized with Span 80/SDS, Span 80/Tween 80 and Span 80/CTAB.

Name	MV(μm)	MN(μm)	MA(μm)
Span 80/SDS-stabilized microemulsion	147	69	108
Span 80/Tween 80-stabilized microemulsion	130	64	99
Span 80/CTAB-stabilized microemulsion	161	83	123

Table S2.2. Characteristics of nano-sized O/W emulsions.

Solution	Oil concentration (mg/L)	Tween 80 (mg/L)	Span 80 (mg/L)	SDS (mg/L)	CTAB (mg/L)	NaCl (mM)	$CaCl_2$ (mM)	pH	Zeta potential (mV)
1	500	0	50	50	0	0	0	4	-55.6±0.86
2	500	0	50	50	0	0	0	5.6	-58.3±0.82
3	500	0	50	50	0	0	0	8	-60.3±1.64
4	500	50	50	0	0	0	0	5.6	-21.3±0.73
6	500	0	50	0	50	0	0	5.6	62.3±0.76
7	500	0	50	50	0	1	0	5.6	-50.1±0.41
8	500	0	50	50	0	10	0	5.6	-42.8±0.86
9	500	0	50	50	0	1	1	5.6	-38.2±0.65

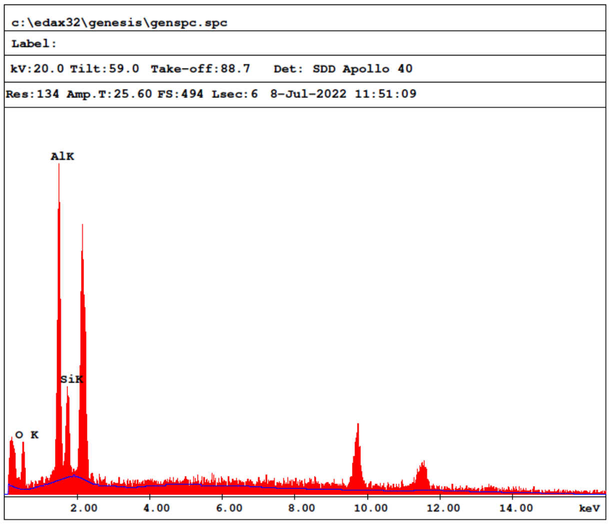

```
c:\edax32\genesis\genspc.spc
Label:
kV:20.0 Tilt:59.0  Take-off:88.7   Det: SDD Apollo 40
Res:134 Amp.T:25.60 FS:494 Lsec:6  8-Jul-2022 11:51:09
```

Fig. S2.1. EDAX analysis of the H25 membrane.

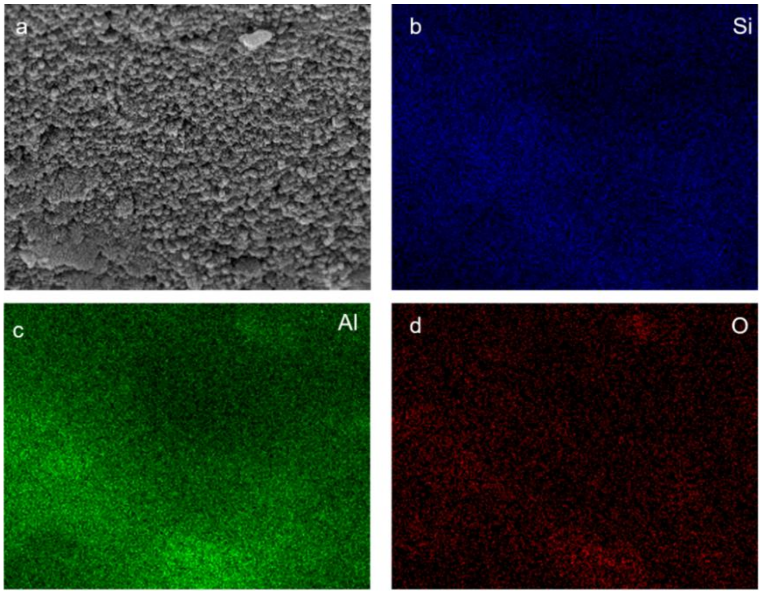

Fig. S2.2. Multi-elemental (Si, Al, and O) EDX mapping of the H20 membrane.

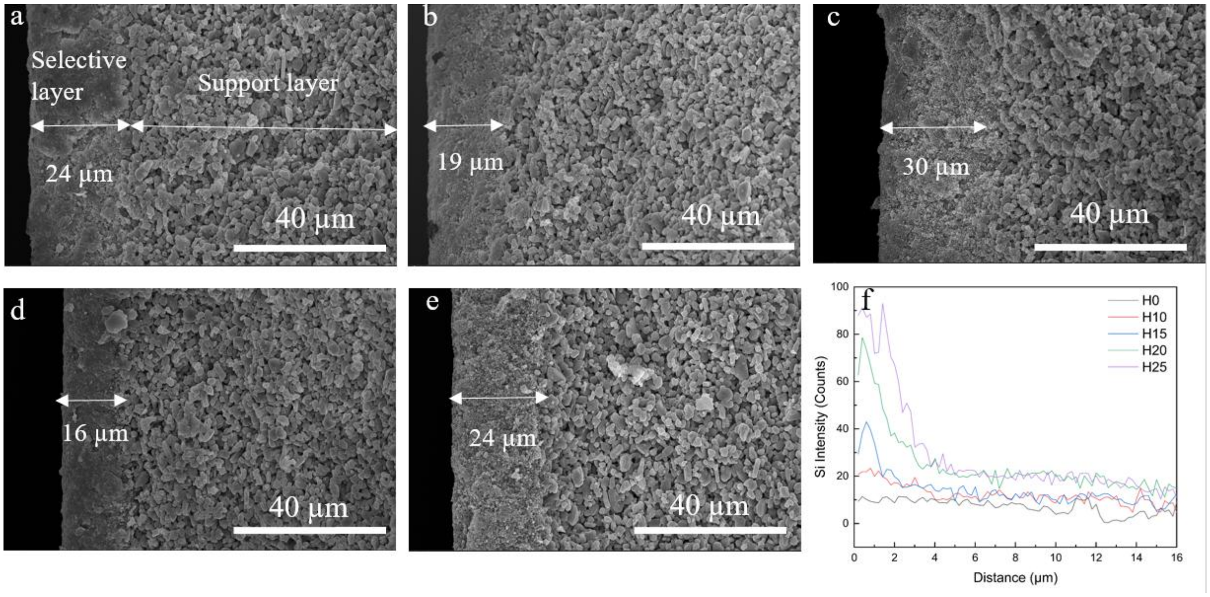

Fig. S2.3. SEM images of the cross-section of the (a) H0, (b) H10, (c) H15, (d) H20, (e) H25 membranes and corresponding (f) EDAX line-scan spectra.

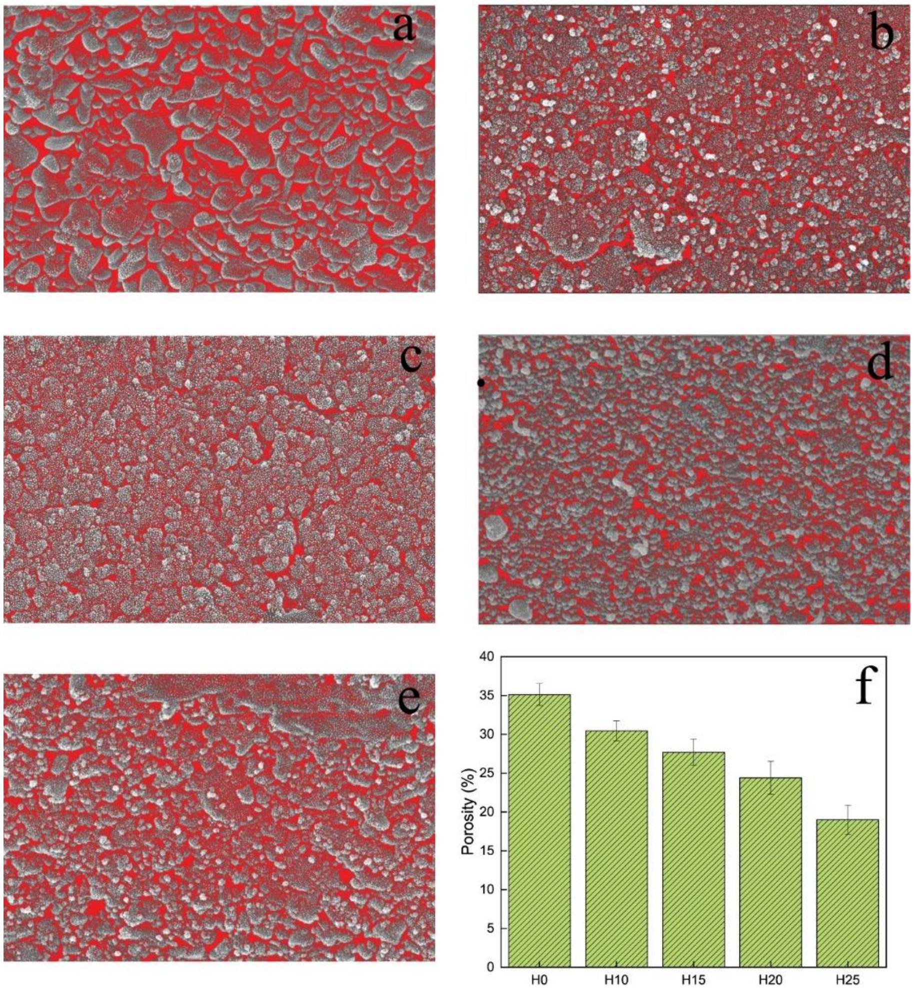

Fig. S2.4. Image J analysis of the SEM images for the (a) H0, (b) H10, (c) H15, (d) H20, (e) H25 membranes, and (f) porosity of the membranes.

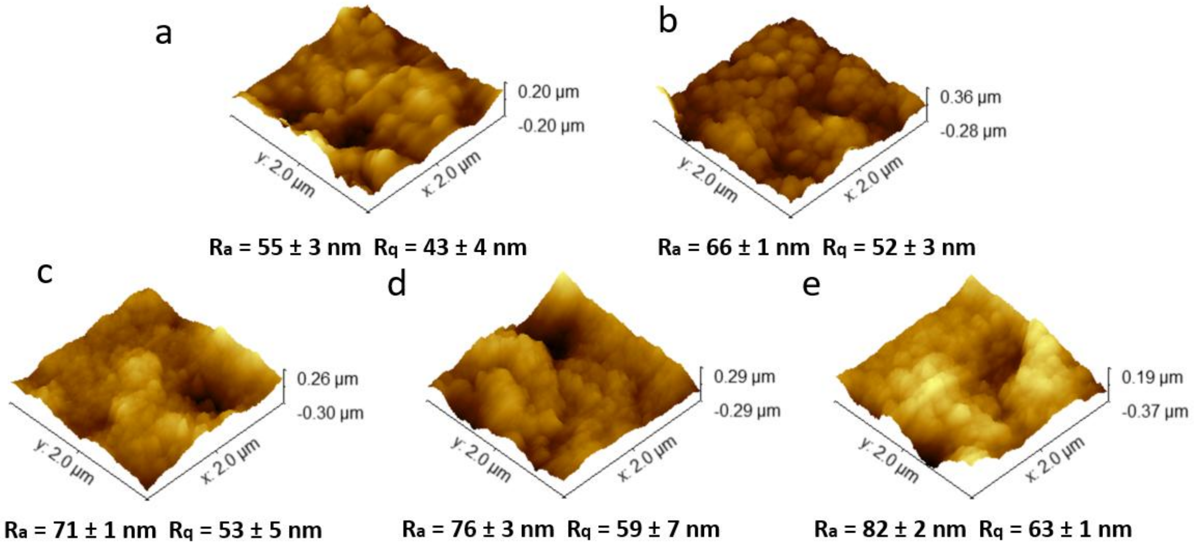

Fig. S2.5. The average surface roughness (R_a) and the root-mean-square surface roughness (R_q) of the (a) H0 and (b) H10, (c) H15, (d) H20, and (e) H25 membranes.

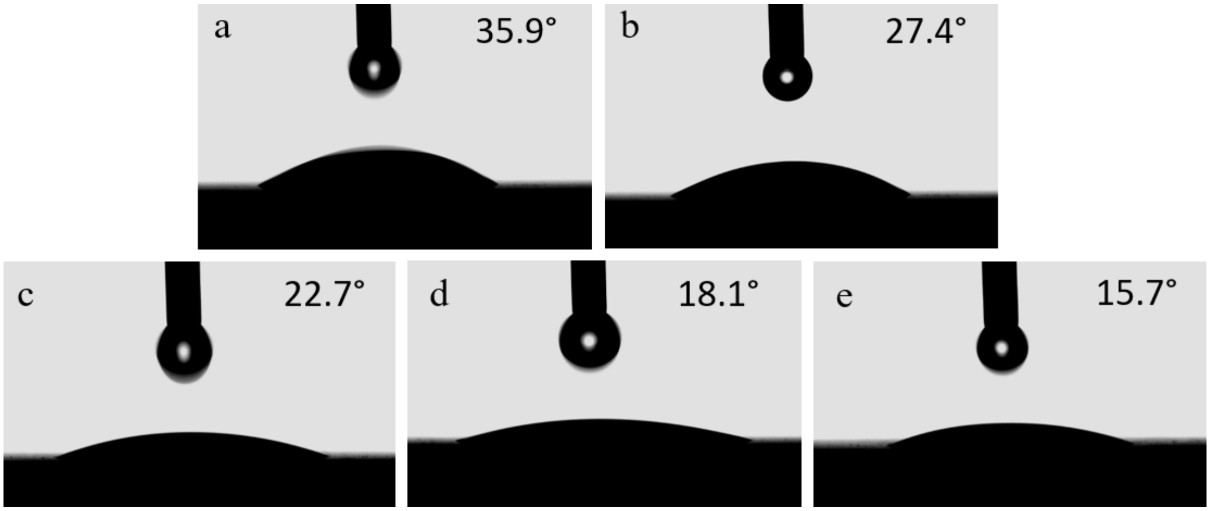

Fig. S2.6. Initial water contact angle for the (a) H0, (b) H10, (c) H15, (d) H20, (e) H25 membranes.

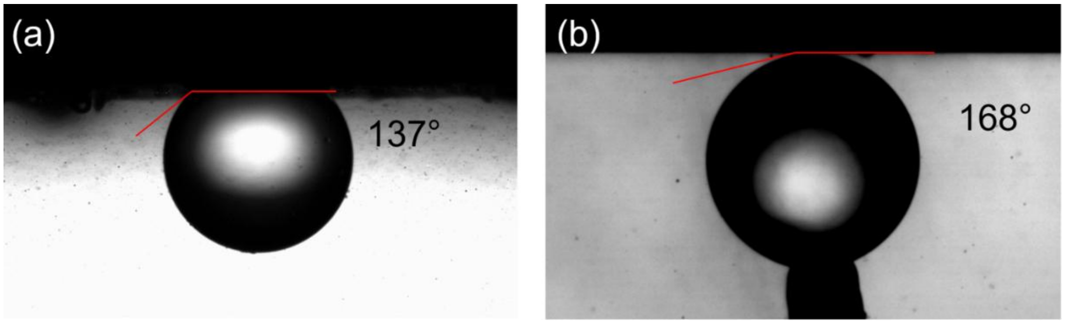

Fig. S2.7. Underwater oil contact angle of the (a) H0 and the (b) H20 membrane.

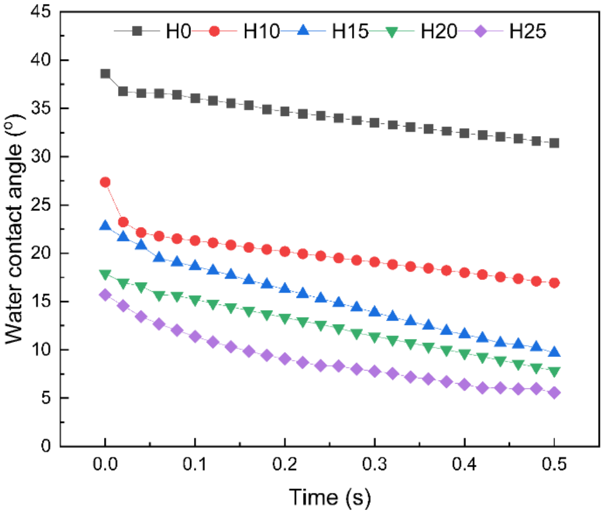

Fig. S2.8. Dynamic water contact angle for the H0, H10, H15, H20, H25 membranes.

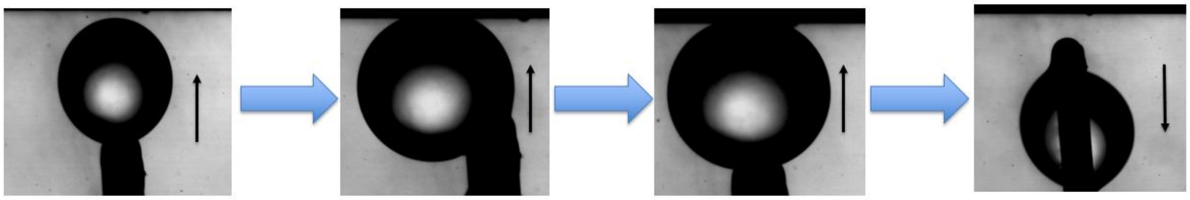

Fig. S2.9. Dynamic underwater oil adhesion property on the H20 membrane.

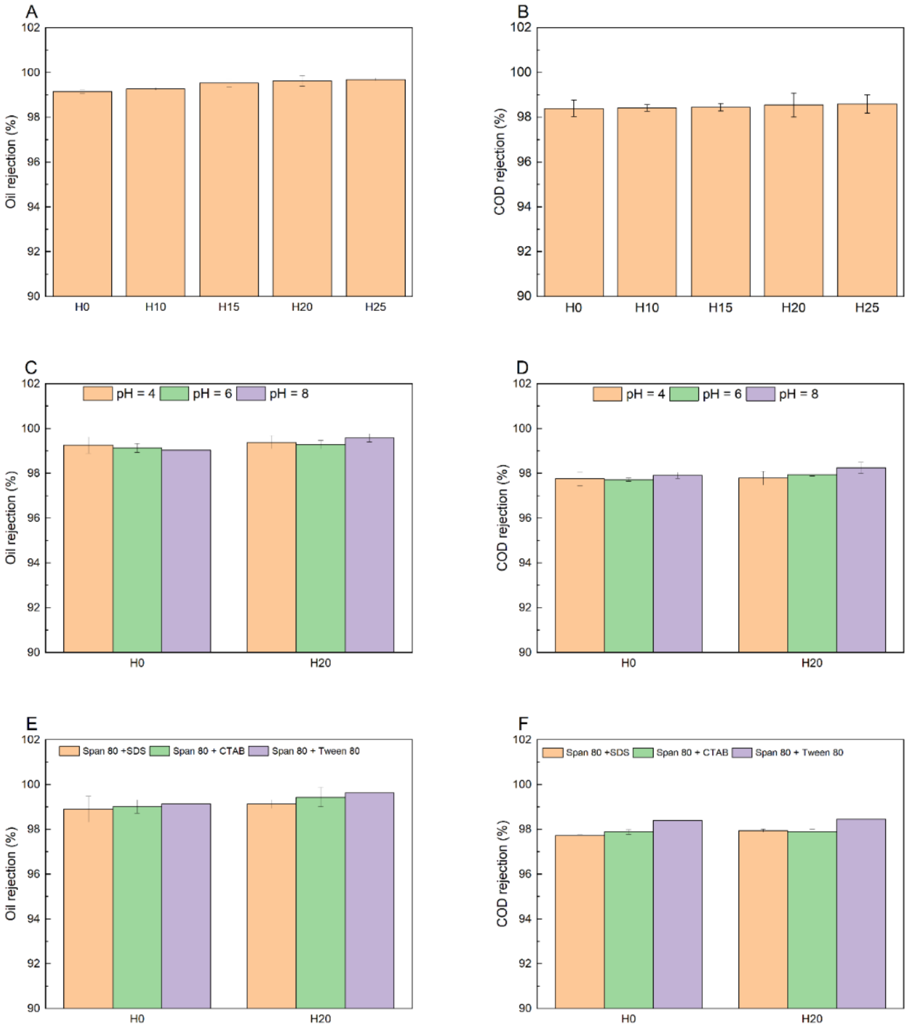

Fig. S2.10. (a) The oil rejection and (b) the COD rejection of the H0, H10, H15, H20, and H25 membranes challenged with 500 mg/L soybean oil microemulsion (pH = 5.6, 50 mg/L Span 80 and 50 mg/L Tween 80). (c)The oil rejection and (d) the COD rejection of the H0 membrane and the H20 membrane were challenged with 500 mg/L soybean oil microemulsion feed with various pH. (e) The oil rejection and (f) the COD rejection of the H0 membrane and H20 membrane were challenged with 500 mg/L soybean oil microemulsion feed with various surfactants.

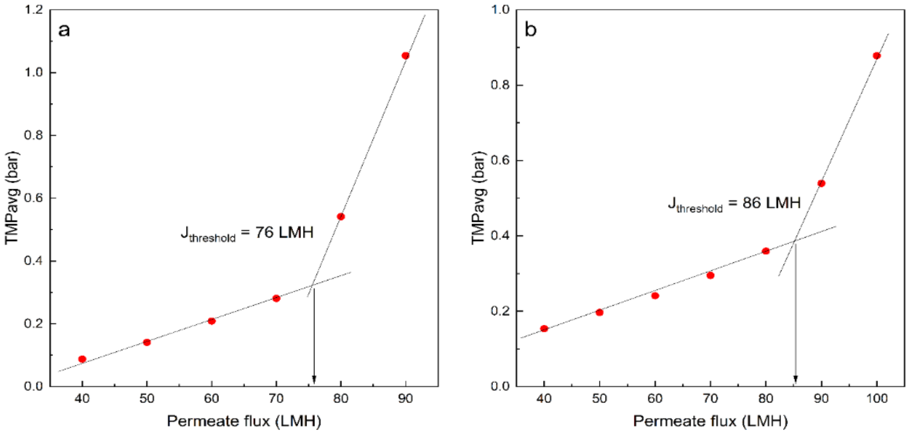

Fig. S2.11. Threshold flux for the H0 membrane and the H20 membrane challenged with 500 mg/L soybean oil microemulsion feed (pH = 5.6, 50 mg/L Span 80 and 50 mg/L Tween 80). The threshold flux is determined by TMP_{avg} method for (a) the H0 membrane and (b) the H20 membrane, respectively. The threshold flux values are denoted by the arrows pointing to the flux axis.

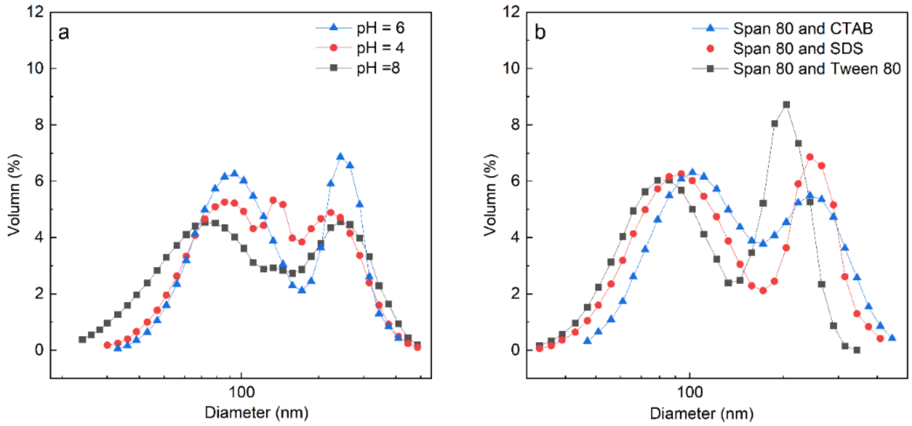

Fig.S2.12. Particle size distribution of microemulsion at various (a) pHs = 4, 6, 8; (b) surfactants (Span 80 and Tween, Span 80 and SDS, Span 80 and CTAB).

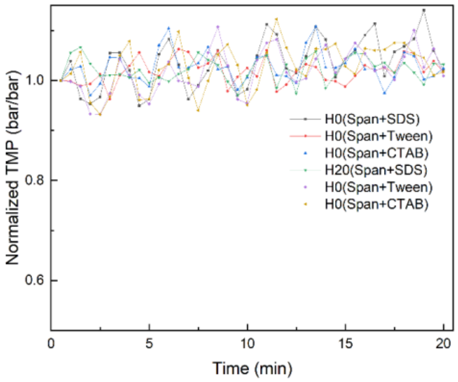

Fig. S2.13. Fouling comparison of the H0 and the H20 membrane during the filtration of solutions with various types of surfactant: 50 mg/L Span 80 and 50 mg/L (a) Tween 80, (b) SDS, (c) CTAB.

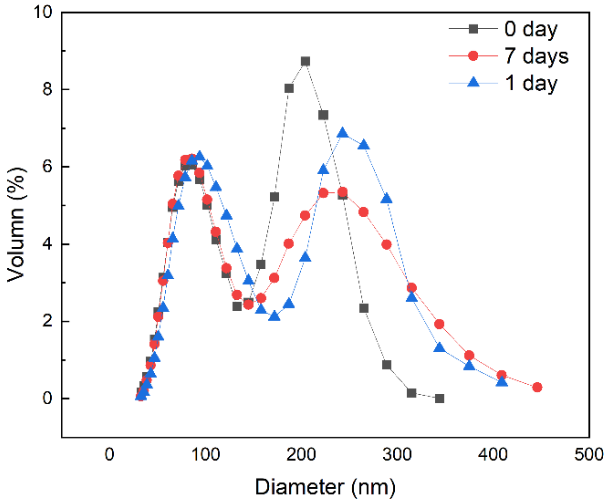

Fig. S2.14. Particle size distribution of microemulsion after standing for 0 days, 1 day, and 7 days.

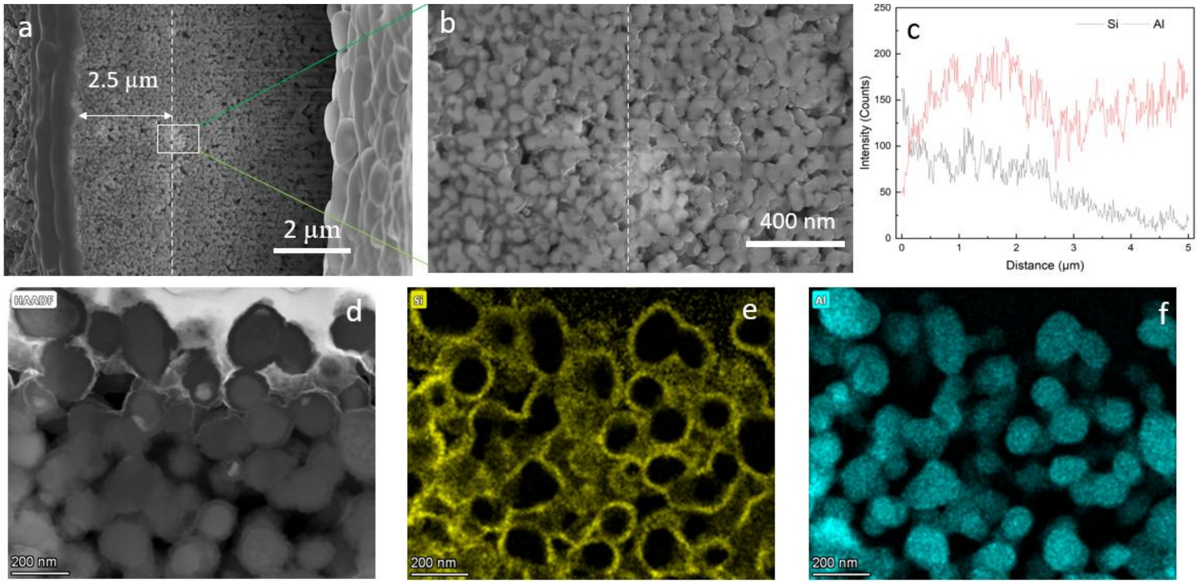

Fig. S2.15. SEM image of the cross-section of the H20 membrane with (a) low magnification and (b) high magnification. (c) STEM-EDX mapping of the H20 membrane. (d) Cross-sectional high-angle annular dark-field imaging (HAADF) image with the corresponding EDX mapping of (e) Si and (f) Al.

The oil concentration in both feed and permeate was assessed using a UV/Vis spectrophotometer (GENESYS 10S UV-Vis, Thermo scientifical, US) at 275 nm [128]. Meanwhile, the chemical oxygen demand (COD) of the samples was determined using a Hach spectrophotometer (DR 3900, US) equipped with COD cuvettes (LCK 314 and LCK 514, Hach) [192]. The feed was diluted to establish a calibration curve, and the measurement was conducted as depicted in Fig. S16 and Fig.S2.17.

The soybean oil and COD rejection were calculated by Eq. (S2.1):

$$R = \left(1 - \frac{C_p}{C_f}\right) \times 100\% \tag{S2.1}$$

where R is the rejection, Cp is the oil (mgL^{-1}) or COD concentration (mgL^{-1}) in the permeate, and Cf is the oil (mgL^{-1}) or COD concentration (mgL^{-1}) in the feed.

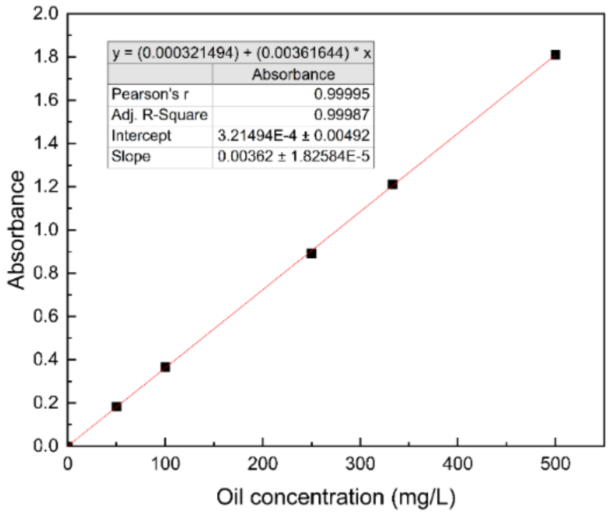

Fig. S2.16. Linear relationship of soybean oil concentration with UV-vis absorbance.

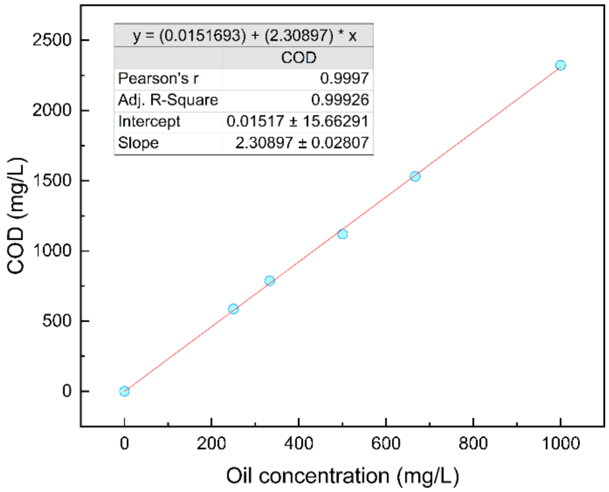

Fig. S2.17. Linear relationship of soybean oil concentration with COD.

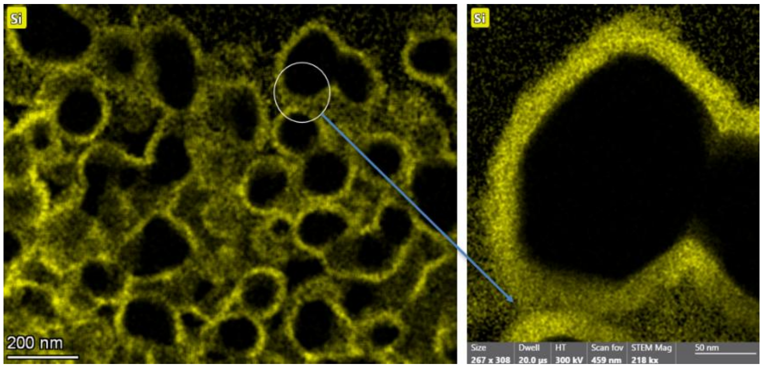

Fig. S2.18. Improved interface bonding between the Al_2O_3 grains due to the coating of the SiC layer.

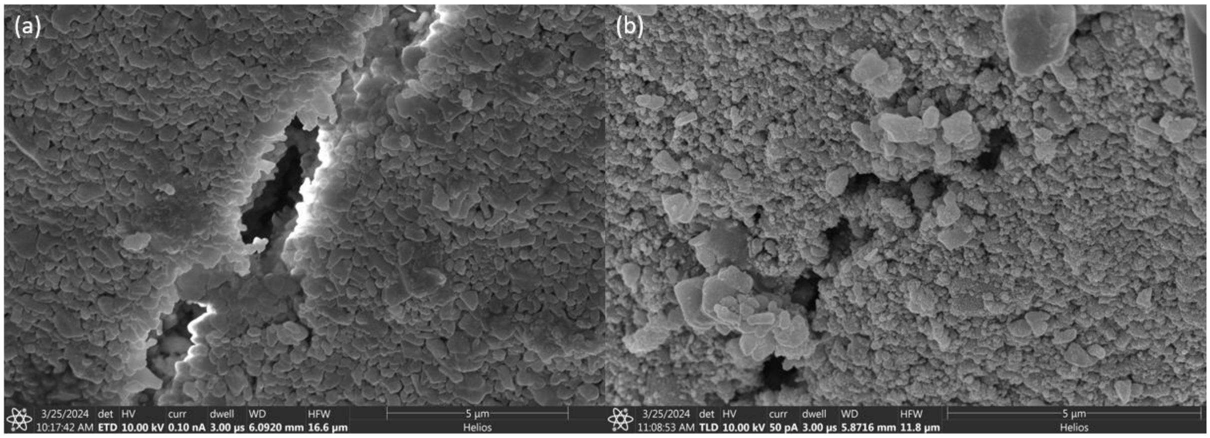

Fig. S2.19. Defects on the surface of (a) the H0 membrane and (b) the H20 membrane.

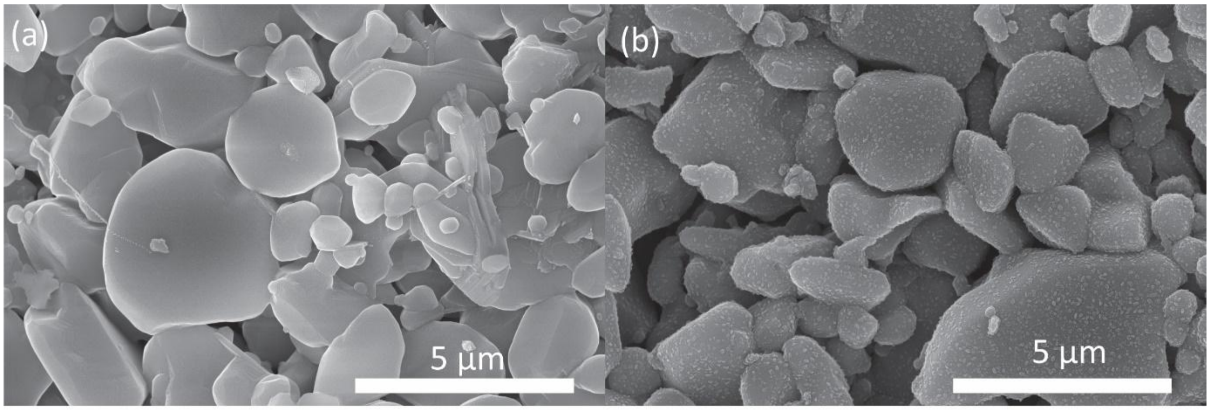

Fig. S2.20. SEM images for the surface of the support layer for the (a) H0 and (b) the H20 membrane.

Chapter 3

Impact of ionic strength and surface charge on ceramic membrane fouling by oil-in-water emulsions: A quantitative analysis using DLVO and XDLVO models

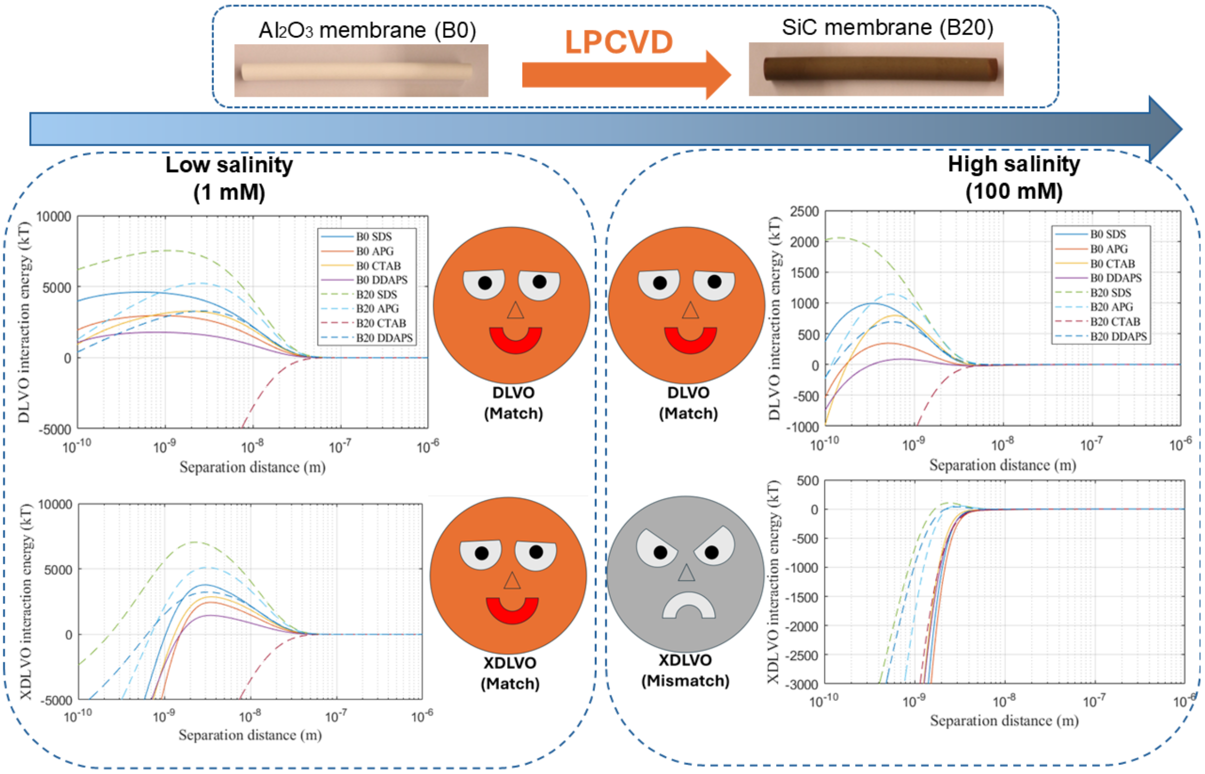

This chapter is based on:

Qin, G., Zhou, H., M.B. Tanis-Kanbur, Rietveld, L. C., & Heijman, S. G. (2025). Impact of ionic strength and surface charge on ceramic membrane fouling by oil-in-water emulsions: A quantitative analysis using DLVO and XDLVO models. *Under review by Separation and Purification Technology*.

Abstract

Large amounts of oily wastewater, which can be defined as produced water, are generated in oilfields. Ultrafiltration (UF) serves as an effective and economical method to purify produced water. Unfortunately, membrane fouling during produced water treatment is severe. In this paper, the effects of the ionic strength (1, 20, and 100 mM) as well as different surfactants on the membrane fouling are investigated. Four surfactants, including SDS (anionic), APG (non-ionic), CTAB (cationic) and DDAPS (zwitterionic), were selected for this study. The Derjaguin-Landau-Verwey-Overbeek (DLVO) and extended DLVO (XDLVO) models were used to quantify interactions between the membrane-oil droplet and deposited oil layer-oil droplet surfaces and to compare these interactions with the fouling experiments. The (X)DLVO interaction energies of the membrane-oil droplet exhibited a strong agreement with the fouling tendencies at 1 mM salinity. The SiC-deposited (B20) membrane showed less reversible and irreversible membrane fouling than the Al_2O_3 (B0) membrane when filtering negatively charged O/W emulsions stabilized with SDS, APG, or DDAPS. The DLVO model predicted a higher fouling tendency at higher salinity levels during the filtration of SDS, APG, or DDAPS-stabilized O/W emulsions and a decreased fouling tendency for CTAB-stabilized emulsion with the B20 membrane. However, at higher salinity levels, the XDLVO energy barrier was affected by both the repulsive electrostatic double layer (EL) interaction and attractive Lewis acid-base (AB) interaction. By comparing both experiments and (X)DLVO modeling, this study improves the fundamental understanding of the effect of ionic strength and surfactant types on reversible and irreversible fouling of the Al_2O_3 and SiC-coated membranes fouling by O/W emulsions.

3.1. Introduction

Large quantities of produced water are discharged concurrently with oil and gas extraction at a global average rate of about 39.75 million m^3 per day [18, 193]. Several studies have investigated various treatment techniques to enhance produced water reuse including Microfiltration (MF) [194], ultrafiltration (UF) [4], electroflocculation [195], reverse electrodialysis (ED) [196], membrane distillation [197, 198], adsorption [199], sand filtration [200], gas flotation [201], chemical precipitation [202], and advanced oxidation [203]. However, among other water treatment technologies, UF is considered to be the most promising approach for removing oil, grease, and colloidal particle removal, making it an effective pretreatment option for the reuse of the produced water [4, 204].

The main challenge with the use of UF membranes for produced water treatment is fouling, which occurs due to the aggregation of oil droplets on the surface or in the membrane pores. To effectively control membrane fouling, it is crucial to understand the oil droplet-membrane interactions and oil droplet-oil layer interactions. Here, the presence of surfactants, used during oil extraction, is considered to play a vital role [5]. Surfactants absorb on both the oil-water interface of the droplets and the membrane surface. Therefore, the surfactants influence both the interactions between the oil droplets and membrane surface and the oil droplet-oil layer interactions. Sodium dodecyl sulfate (SDS, anionic), alkyl polyglycoside (APG, non-ionic), and cetyltrimethylammonium bromide (CTAB, cationic) are frequently used in oil extraction [14, 94, 205], allowing for a more practical investigation of the membrane fouling mechanism. However, previous research by De Vos et al. has highlighted the advantage of the application of zwitterionic surfactants, such as N-dodecyl-N,N-dimethyl-3-ammonio-1-propanesulfonate (DDAPS), due to its low fouling propensity under high salt concentrations [48, 49, 206]. The Derjaguin-Landau-Verwey-Overbeek (DLVO) theory has been widely used in various fouling studies. However, it sometimes falls short of accurately describing interactions at shorter separation distances between two surfaces. To address this limitation, the Lewis acid-base (AB) interaction, which accounts for electron donor-acceptor interactions at distances less than 10 nm, was integrated into the DLVO model, resulting in the extended DLVO (XDLVO) model [207]. While the XDLVO model is more commonly employed than the DLVO model to analyze colloidal fouling on membrane surfaces, its application to apolar foulants, such as oil, remains less thoroughly understood. Previous studies have typically focused on either the effects of different surfactants at a single salinity level or on oil-water emulsions with varying salinity without considering surfactants variations [93, 94]. He at. al., e.g., reported that for oil-in-water (O/W) emulsions stabilized by the non-ionic surfactant (Triton ^{TM} X-100), the interaction energies predicted by the DLVO model were consistent with the fouling tendencies at various salinities for the PVDF MF membrane in the constant flux filtration mode [93]. The group of Chew reported that the DLVO correlated well with the fouling tendencies, rather than the XDLVO model, for the filtration of the O/W emulsion stabilized with SDS, CTAB and Tween 20 for the 0.22 µm PVDF membrane in the constant pressure filtration mode [94]. However, Zhang et al. reported that the fouling tendency for a Span 80-stabilized O/W emulsion mismatched with the DLVO/XDLVO model for the polyethersulfone (PES) UF membrane in the constant pressure filtration mode [208].

Silicon carbide (SiC) and alumina (Al_2O_3) ceramic membranes are commercially available and widely used in wastewater treatment applications, standing out among other ceramic membranes [19, 43, 100, 209, 210]. Increasing the adsorption-free energy between oil and the membrane alleviates membrane fouling by changing the membranes' hydrophilicity and surface zeta potentials. Therefore, SiC membranes are preferred over Al_2O_3 for produced water treatment due to their super hydrophilic and highly negatively charged surface [15]. To the best of our knowledge, no prior studies have quantitatively analyzed and compared fouling by O/W emulsions with the DLVO and XDLVO models using these specific membrane materials. This study is the first to examine the combined impact of both varying salinities and different surfactants, utilizing positively charged Al_2O_3 membranes and negatively charged SiC ceramic membranes by combining fouling experiments and the DLVO/XDLVO model. Various studies focused on the relationship between the DLVO/XDLVO model and membrane fouling in the dead-end constant pressure mode [94, 208, 211]. However, there are limited studies on fouling in the crossflow constant flux mode for the separation of O/W emulsion [13, 50], although this is the operational mode in full-scale installations. The filtration experiments were conducted in the constant flux crossflow mode, assessing how membrane surface properties and emulsion characteristics, such as salinity levels and surfactant types, affect membrane fouling. Additionally, the study explored the relationship between the DLVO/XDLVO models and the reversible and irreversible fouling.

Reversible fouling, namely cake layer fouling, has been the subject of several studies [55, 212, 213]. A practical and cost-effective method is to differentiate between reversible and irreversible fouling is to backwash the membrane with demineralized (DI) water. The extent of reversible and irreversible fouling can then be calculated based on the resistance-in-series model [169, 170]. To the authors' knowledge, this is the first time that a study was performed, combining constant flux, backwashing (related to the reversible and irreversible fouling) and DLVO theory. This integration provides a comprehensive understanding of fouling behavior under practical operating conditions in full scale application.

Consequently, the objective of the present is to enhance the fundamental understanding of the interaction between oil droplets and ceramic membranes in the crossflow constant flux mode, with a focus on studying the correlation between the DLVO/ XDLVO interaction energy and reversible and irreversible fouling, varying salinity and surfactant types.

3.2. Materials and methods

3.2.1 Materials

N-hexadecane (296317), sodium dodecyl sulfate (SDS, L4509-250G), APG (49122), Hexadecyltrimethylammonium bromide (CTAB, H5882), DDAPS (≥ 97%, 40232) and sodium chloride (S9998-1KG), which were supplied by Sigma-Aldrich Co., Ltd, the Netherlands, were used for the preparation of the O/W emulsions.

SiC-deposited Al_2O_3 membranes were obtained via low-pressure chemical vapor deposition (LPCVD), as reported in our previous studies [15]. The tubular Al_2O_3 membranes, provided by the CoorsTek Co., Ltd, were chosen as substrate for LPCVD with permeabilities in the 350 ±10 $Lm^{-2}h^{-1}bar^{-1}$ range. Polycrystalline 3C-SiC was coated on Al_2O_3 membranes using two precursors (SiH_2Cl_2 and C_2H_2) with coating time of 20 min at a temperature of 860°C via LPCVD. The membranes without coating and those with a coating time of 20 min were labeled as B0 and B20, respectively. The pore size of the B0 and B20 membrane were 41 nm and 33 nm, respectively, as determined from our previously reported results [15].

3.2.2. Membrane characterization

Surface SEM images of the B0 and B20 membrane was obtained by NovaNanoLab 600 (FEI company, USA). The water contact angle (WCA) of both the pristine B0 membranes and the LPCVD-coated B20 membranes was performed by a contact angle instrument (Dataphysics

OCA25, Germany). The WCA measurements were performed by the sessile drop method by dosing 2 μl liquid (ultrapure water, formamide, diiodomethane) on the flat sheet membrane surface. Each measurement was repeated five times per sample, and average values were obtained for the surface tension component calculation. Detailed information on the WCA measurements can be found in Text S1. The zeta potential of both B0 and B20 membranes was measured with an electrokinetic analyzer (SurPASS 3, Anton-Paar, Graz, Austria). However, the membrane zeta potential could not be measured in electrolyte solutions with high concentrations (e.g., 100 mM NaCl) because of the range limit (<50 mM NaCl) of the SurPASS electrokinetic analyzer. Hence, the Freundlich ion adsorption model was used to estimate ζ_m at 100 mM NaCl concentration [93, 214].

3.2.3 Oil-in-water emulsions

To study the effect of the charge of the emulsions on membrane fouling, various micro-sized O/W emulsions were prepared for the membrane fouling experiments. These included an anionic SDS-stabilized emulsion, a non-ionic APG-stabilized emulsion, a zwitterionic DDAPS-stabilized emulsion, and a cationic CTAB-stabilized emulsion. To prepare a 500 mg/L SDS stabilized emulsion, 2 g N-hexadecane and, 956.4 mg SDS were added into 1L of deionized (DI) water. The mixture was stirred continuously at 1500 rpm using a magnetic stirrer (C-MAG HS 10, IKA, the Netherlands) for twelve hours, followed by ultrasonication using a Branson Ultrasonics sonifier (CPX3800H, USA) for two hours, as described in previous studies [3, 164, 165]. A fresh emulsion was prepared by diluting 1 L of O/W emulsion with 3 L of DI water, ensuring a consistent oil concentration of 500 mg/L. This concentration aligns with the typical oil and grease content of 100-1000 mg/L in oily wastewater [154]. To prepare 4 L of O/W emulsions with salinity concentrations of 1 mM, 20 mM, and 100 mM, 0.234 g, 4.68 g, and 23.38 g of NaCl were added, respectively. The same preparation method was used for the preparation of the APG, DDAPS, and CTAB-based emulsions. O/W emulsions were prepared using 0.1 times the critical micelle concentration (CMC) of each surfactant. The CMC values for SDS, APG, CTAB, and DDAPS were 2391 mg/L, 348 mg/L, 346 mg/L, and 1006 mg/L [48, 215], respectively. For a total emulsion volume of 4 L, the corresponding amounts of used surfactants were 957.6 mg for SDS, 139.2 mg for APG, 138.4 mg for CTAB, and 402.4 mg for DDAPS, respectively. The micro-sized oil droplets and their distributions were analyzed using a particle size analyzer (Bluewave, Microtrac, USA), while the emulsions' zeta potential was measured with a Malvern Zetasizer Advance analyzer (Zetasizer Lab, Malvern, UK).

3.2.4. Filtration experiments with mico-sized O/W emulsions

A constant permeate flux crossflow setup was used for O/W emulsion fouling filtration experiments (Fig.S3.1). A constant flux of 80 $Lm^{-2}h^{-1}$ (Fig.S3.2) was maintained by a digital feed pump (DDA12-10, Grundfos, Denmark). This flux was estimated based on the threshold flux determined though the conventional flux stepping method [15, 166, 167]. The fouling resistance was calculated according to the resistance-in-series model [169, 170]. Detailed information about the filtration protocol can be found in the Supporting Information (Text S3.2).

3.2.5. DLVO and XDLVO models

According to classical DLVO theory, the total interaction energy between an oil droplet and the B0 or B20 membrane is expressed as the combination of the Lifshitz-van der Waals (LW) interaction energy and the electrostatic double layer (EL) interaction energy [216]:

$$U_{mlo}^{DLVO}(h) = U_{mlo}^{LW}(h) + U_{mlo}^{EL}(h) \tag{3.1}$$

Where $U_{mlo}^{DLVO}(h)$ is the total interaction energy between the B0/ B20 membrane (m) and an oil droplet (o), immersed in a surfactant solution (l); h is the separation distance between the oil droplet and B0/B20 membrane; $U_{mlo}^{LW}(h)$ is the LW interaction term and, $U_{mlo}^{EL}(h)$ is the EL interaction term. In addition to the LW and EL interaction energies, the AB interaction energy can also be considered in energy balances for aqueous systems because of the hydrogen bonds in polar liquids like water [17]. The XDLVO model includes the AB interaction component and can be written as:

$$U_{mlo}^{XDLVO}(h) = U_{mlo}^{LW}(h) + U_{mlo}^{EL}(h) + U_{mlo}^{AB}(h) \tag{3.2}$$

Where $U_{mlo}^{XDLVO}(h)$ is the total interaction energy between the B0/B20 membrane and oil droplet immersed in the surfactant solution, and $U_{mlo}^{AB}(h)$ is the AB interaction term.

$\Delta G_{mlo}^{LW}(h_0)$, $\Delta G_{mlo}^{EL}(h_0)$ and $\Delta G_{mlo}^{AB}(h_0)$ denote the adhesion energies per unit area for LW, EL, and AB interactions, respectively, between two infinite planar surfaces [94, 216-218]:

$$\Delta G_{mlo}^{LW}(h_0) = -2\left(\sqrt{\gamma_m^{LW}} - \sqrt{\gamma_l^{LW}}\right)\left(\sqrt{\gamma_o^{LW}} - \sqrt{\gamma_l^{LW}}\right) \tag{3.3}$$

$$\Delta G_{mlo}^{EL}(h_0) = \frac{\varepsilon_0\varepsilon_r \kappa}{2}(\zeta_m^2 + \zeta_o^2)\left[1 - \coth(\kappa h_0) + \frac{2\zeta_m\zeta_o}{(\zeta_m^2 + \zeta_o^2)}\operatorname{csch}(\kappa h_0)\right] \tag{3.4}$$

$$\Delta G_{mlo}^{AB}(h_0) = 2\left[\sqrt{\gamma_l^+}\left(\sqrt{\gamma_o^-} + \sqrt{\gamma_m^-} - \sqrt{\gamma_l^-}\right) + \sqrt{\gamma_l^-}\left(\sqrt{\gamma_o^+} + \sqrt{\gamma_m^+} - \sqrt{\gamma_l^+}\right) - \sqrt{\gamma_o^-\gamma_m^+} - \sqrt{\gamma_o^+\gamma_m^-}\right] \tag{3.5}$$

Where h_0 is the minimum equilibrium cut-off distance, which is 0.158 nm [219], ε_0 is the permittivity of the vacuum, which is 8.8542 $*10^{-8}$ F/M, ε_r is the relative permittivity of water, ζ_m and ζ_o are the zeta potentials of the B0/B20 membrane and the oil droplets, respectively. The three unknown surface tension parameters of the membrane surface (γ_m^{LW}, γ_m^-, γ_m^+) can be determined by measuring the contact angle of three probe liquids with known surface tension (γ_l) and surface tension parameters (γ_l^{LW}, γ_l^+, γ_l^-), as shown in Table.S3.1. Detailed information about the calculation is provided in the supporting information (Text.S3.3).

To calculate the real interaction energy between the B0/B20 membrane and a spherical oil droplet, the Derjaguin approximation is used to calculate the corresponding interaction energy between a flat membrane and a spherical oil droplet [216]:

$$U_{mlo}^{LW}(h) = 2\pi\Delta G^{LW}(h_0)\frac{{h_0}^2 a}{h} \tag{3.6}$$

$$U_{mlo}^{EL}(h) = \pi\varepsilon_0\varepsilon_r a\left[2\zeta_m\zeta_o \ln\left(\frac{1+e^{-\kappa d}}{1-e^{-\kappa d}}\right) + (\zeta_m^2 + \zeta_o^2)\ln(1 - e^{-2\kappa d})\right] \tag{3.7}$$

$$U_{mlo}^{AB}(h) = 2\pi a\lambda\Delta G^{AB}(h_0)\exp\left(\frac{h_0 - h}{\lambda}\right) \tag{3.8}$$

Where a is the radius of the oil droplet, h is the surface separation distance between the B0/B20 membrane and a spherical oil droplet, and λ is defined as 0.6 nm, representing the characteristic decay length of AB interactions [94]. The DLVO/XDLVO interaction energies and surface tension components were calculated using MATLAB software (Matlab R2020b).

3.3. Results and discussion

3.3.1. Emulsion properties

The particle size distribution of the oil droplets stabilized with various salinity levels and surfactant type is shown in Table.S3.2. With increasing salinity and varying surfactant types, the particle size distribution of the emulsions kept constant, with an average particle size of 5 ± 1 µm. In addition, the absolute value of the zeta potential of the emulsions decreased with the salinity (Fig.3.1), due to the compression of the diffuse double layer. The charge screening effect of the compressed diffuse double layer decreases the absolute zeta potential, by diminishing the electric field and thus reducing the electrophoretic mobility of the emulsion droplets [220]. Additionally, the colloidal stability of the emulsion may decrease, as Na^+ ions reduce the electrostatic repulsion between oil droplets [221].

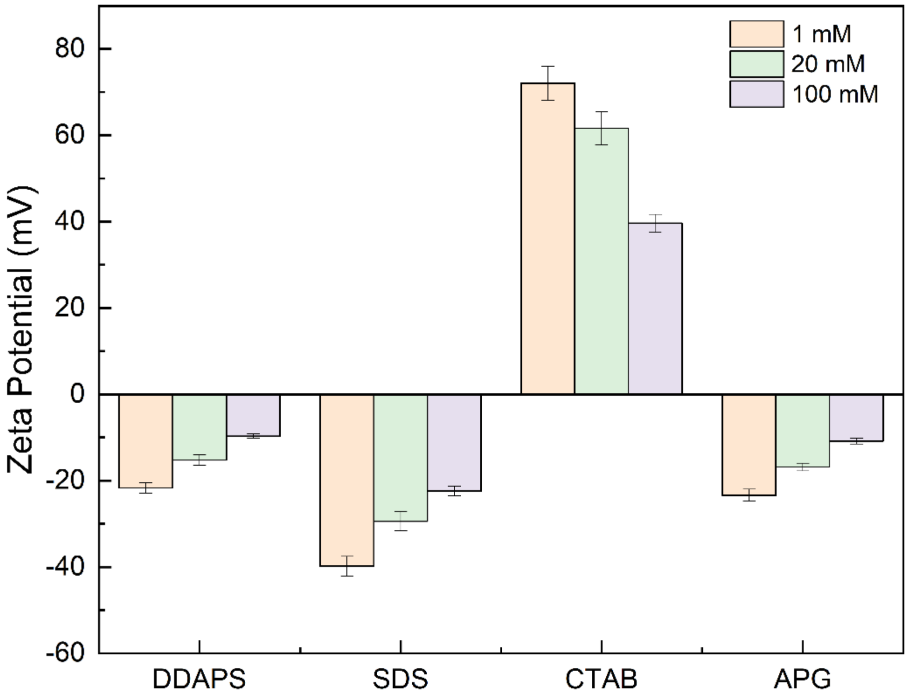

Fig. 3.1. ζ_o of the O/W emulsions stabilized with various surfactants in various ionic strength (1, 20, and 100 mM).

3.3.2. Hydrophilicity and zeta potential of the membranes

The effects of the types of surfactants and various salinity levels on fouling of the B0 membrane and the B20 membrane were examined using four types of surfactants (SDS, APG, CTAB, and DDAPS) at the salinity levels of 1 mM, 20 mM, and 100 mM. The Freundlich ion adsorption model was used to estimate ζ_m at 100 mM NaCl concentration, which is outside the experimental range of the Surpass equipment (Fig. S3.3). The absolute value of the zeta potential of the membranes decreased with increasing salinity, regardless of the types of surfactant, for both the B0 and B20 membranes (Fig.3.2).

When a layer of SiC was coated, the total surface tension increased, showing stronger intermolecular forces than the pristine Al_2O_3 membrane [222]. Particularly, the enhanced electron donor surface tension component (γ^-) suggests a stronger affinity between water molecules and the material [223] due to the higher presence of the oxygen-containing functional group (-OH) in the B20 membranes. Moreover, the B20 membranes had a higher acid-base component (γ_{AB}), indicating the increased polarity of the membranes. The polarity of a material is generally related to its hydrophilicity. Al_2O_3 is a highly polar compound due to the abundance of hydroxyl groups on its surface, which readily form hydrogen bonds with water molecules, giving it a hydrophilic nature [224]. SiC, on the other hand, is relatively less polar, but its surface tends to oxidize, forming a silicon dioxide layer, which introduces polar functional groups to the surface. These oxide layers increase the hydrophilicity of SiC [225, 226], making it more hydrophilic than the Al_2O_3 membrane. This is confirmed by the decrease in the WCA from 36.8º± 0.9º for the B0 membrane to 19.1º ± 0.5º for the B20 membranes, respectively (Fig.S3.4). Therefore, the increased hydrophilicity and polarity from SiC coating help reduce membrane fouling caused by the oil droplets.

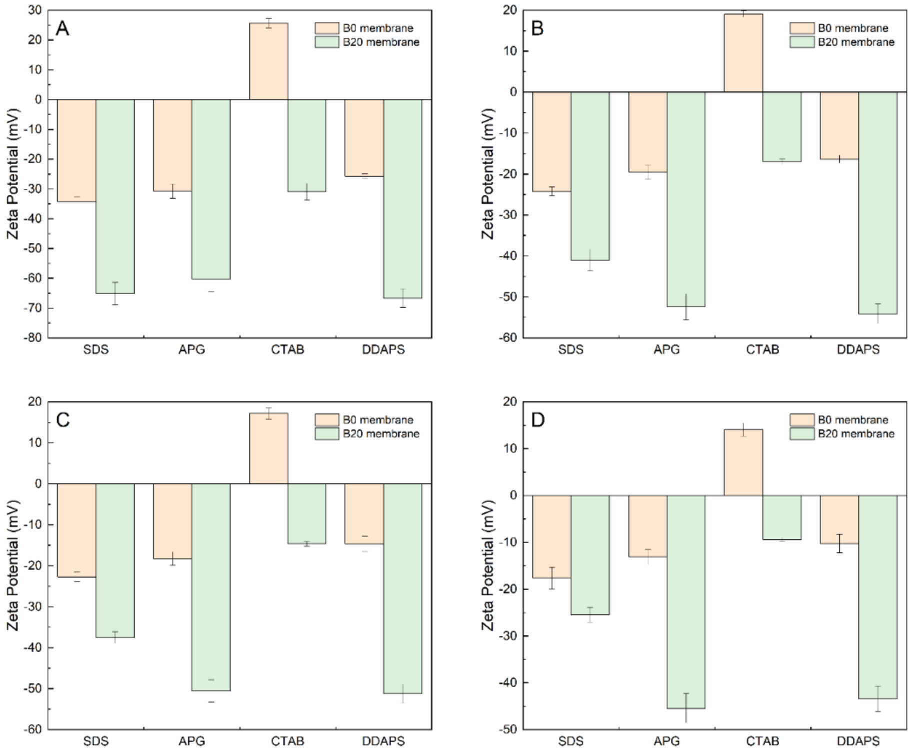

Fig. 3.2. ζ_i of the B0 membrane and the B20 membrane immersed in different surfactant solutions (SDS, APG, CTAB, or DDAPS) with different salinity: (a)1 mM, (b)10 mM, (c) 20 mM, and (d)100 mM.

3.3.3. Comparison of fouling at various salinities

Regarding the 1 mM salinity, Fig.3.3 shows that the B20 membrane exhibited less fouling compared to the B0 membrane when filtrating O/W emulsions stabilized with SDS, APG, or DDAPS. However, the B0 membrane showed less fouling than the B20 membrane when filtrating the O/W emulsions stabilized with CTAB. The electrostatic repulsion and attraction between the membrane and oil droplets, the degree of hydrophilicity of the membrane surface, and surfactant adsorption were used to illustrate this phenomenon. The B0 membrane was positively charged at a pH of 5.8 [10, 15], and the zeta potential of the B0 membrane shifted from positive to negative when immersed in 0.1 Critical micelle concentration (CMC) solutions of SDS, APG, and DDAPS (Fig.3.2), while the highly negatively charged B20 membrane showed no charge inversion when immersed in the 0.1 CMC solutions of positively charged CTAB. Additionally, its zeta potential was much more negative than that of the Al_2O_3 membrane using four types of surfactant solutions. When dealing with negatively charged O/W emulsions stabilized with SDS, APG, or DDAPS, the SiC-deposited membrane showed less membrane fouling due to the enhanced electrostatic repulsion between the B20 membrane and O/W emulsions compared to the B0 membrane. However, when filtrating the CTAB-stabilized O/W emulsion which was positively charged, electrostatic repulsion occurred between the positively charged B0 membrane and CTAB-stabilized O/W emulsions. In contrast, the B20 membrane experienced electrostatic attraction with the CTAB-stabilized O/W emulsions, leading to greater fouling than the B0 membrane. From the normalized TMP curve (Fig.3.3a-b), the B0 membrane showed a higher fouling tendency compared with the B20 membrane when filtering O/W emulsions stabilized with SDS, APG, or DDAPS, but a lower fouling tendency for CTAB-stabilized O/W emulsions. As shown in Fig.3.3c, the B20 membrane showed less total and reversible and irreversible fouling resistance when dealing with the O/W emulsions stabilized with SDS, APG, or DDAPS. When filtrating O/W emulsions stabilized with CTAB, B20 membranes exhibited more fouling than B0 membranes, with the reversible fouling dominant (Fig.3.3c), likely due to cake filtration, which can be removed through hydraulic backwash.

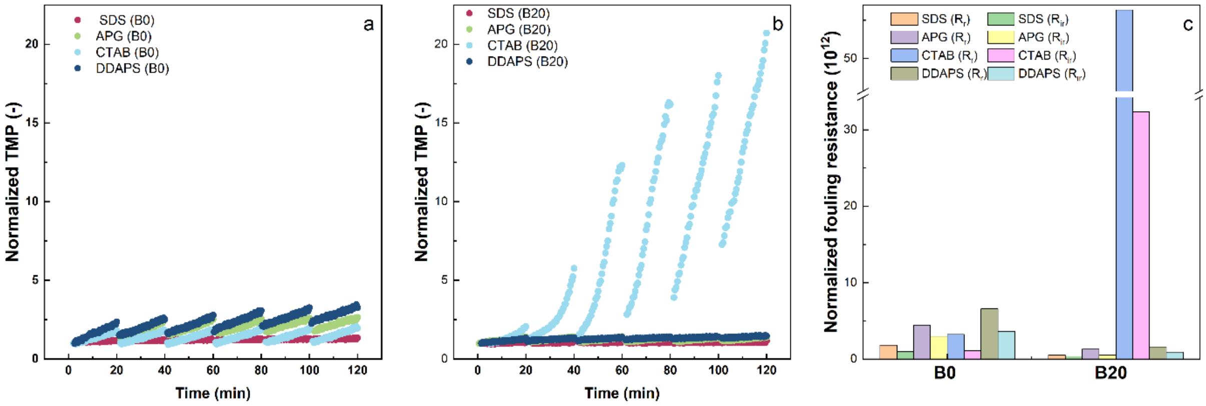

Fig. 3.3. The normalized fouling curve of (a) B0 membrane and (b) B20 membrane when filtering micro-sized SDS, APG, CTAB, DDAPS stabilized O/W emulsion at the 1 mM salinity; (c) is the normalized fouling resistance of the B0 and B20 membrane at the 1 mM salinity.

When the concentration of NaCl increased from 1 mM to 20 mM (Fig.3.4) and then to 100 mM (Fig.3.5), both membranes (B0 and B20) showed an increased fouling when filtrating SDS, APG, and DDAPS-stabilized O/W emulsions. At the same time, the surface tension of oil droplets decreased, making oil droplets more prone to deformation and coalescence, which led to increased irreversible fouling [205]. Although, the B20 membrane still exhibited less fouling than the B0 membrane when filtrating SDS, APG, and DDAPS-stabilized O/W emulsions, the B20 membrane, when filtering the CTAB-stabilized O/W emulsion, showed less fouling, compared to the conditions at 1 mM salinity due to the lower electrostatic attraction, but still had more fouling than the B0 membrane. As shown in Fig.3.1 and Fig.3.2, lower absolute zeta potentials of O/W emulsions and membranes were observed at 20 mM salinity compared to 1 mM salinity due to the charge screening effect [48]. So both the electrostatic repulsion and electrostatic attraction would decrease with the increase in the salinity. Fig.3.4a-b and Fig.3.5a-b showed that the membrane fouling trend for both B0 and B20 membranes also remained consistent at the higher salinity levels (20 mM, 100 mM) compared to the fouling observed at 1 mM salinity. The fouling order for the B0 membrane was SDS < CTAB < APG < DDAPS, while for the B20 membrane, it was SDS < APG < DDAPS < CTAB (Fig.3.4c and Fig.3.5c). This can, again, be explained by the electrostatic interactions. Notably, the increased irreversible fouling of the B0 and B20 membrane with increasing salinity can be explained by the decreased charge repulsion. At low salinity, apparently, there was a strong electrostatic repulsion between DDAPS-stabilized droplets and the B20 membrane, as well as a strong electrostatic attraction between CTAB-stabilized droplets and the B20 membrane. However, as salinity increased, both interactions weakened, which means that the strong electrostatic attraction (CTAB) became weaker, and the strong electrostatic repulsion (DDAPS) also diminished. Consequently, the difference in fouling between the two emulsions became less obvious at higher salinity. At the higher salinities, the normalized TMP of the B20 membrane was much lower than that of the B0 membrane when filtrating SDS, APG, and DDAPS-stabilized O/W emulsions, while it was higher than that of the B0 membrane when dealing with CTAB-stabilized O/W emulsions, hence the B20 membrane had better performance when filtrating SDS, APG and DDAPS-stabilized O/W emulsions at 20 mM and 100 mM salinity.

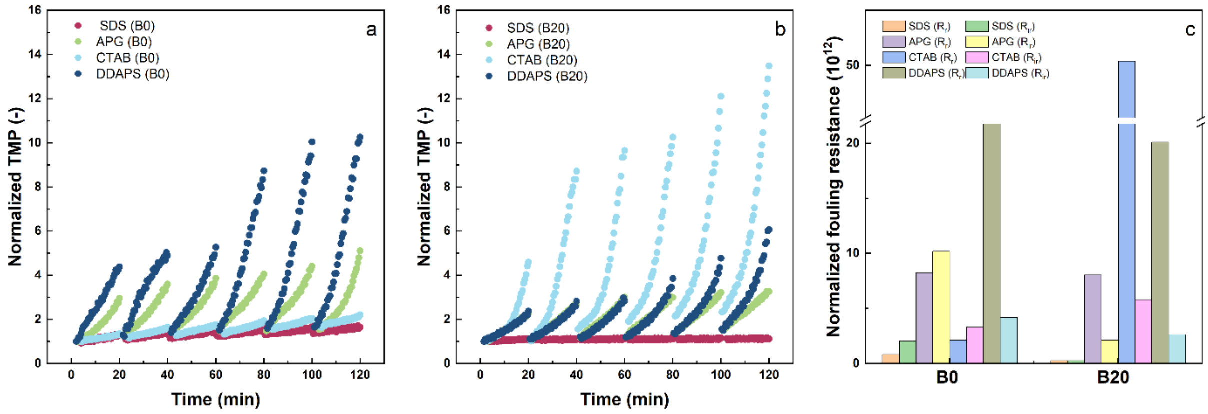

Fig. 3.4. The normalized fouling curve of (a) B0 membrane and (b) B20 membrane when filtering micro-sized SDS, APG, CTAB, DDAPS stabilized O/W emulsion at the 20 mM salinity; (c) is the normalized fouling resistance of the B0 and B20 membrane at the 20 mM salinity.

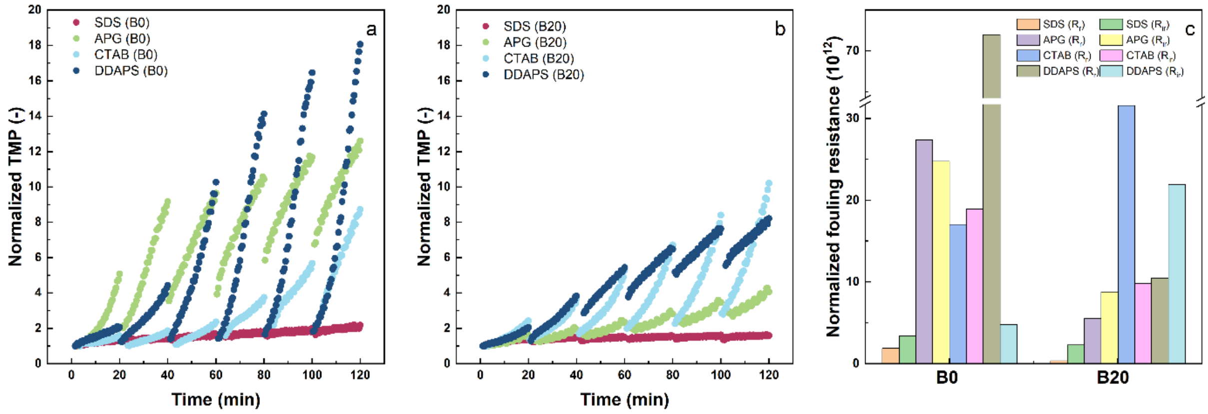

Fig.3.5. The normalized fouling curve of (a) B0 membrane and (b) B20 membrane when filtering micro-sized SDS, APG, CTAB, DDAPS stabilized O/W emulsion at the 100 mM salinity; (c) is the normalized fouling resistance of the B0 and B20 membrane at the 100 mM salinity.

3.3.4 DLVO and XDLVO models

Interaction between membrane and oil droplets

The contact angle and zeta potential of the B0 and B20 membranes, as well as the oil droplets, were measured to calculate the interaction energy between the oil droplets and the surface of the B0 and B20 membranes. The interaction energy components versus the separation distance at the salinity of 1 mM are shown in Fig.3.6. The negative value of the interaction energy means an attractive force and the higher the absolute negative value thus indicates severe fouling. Specifically, the LW and AB interactions energies between the B0 and the B20 membranes and oil droplets were attractive at separation distances smaller than 10 nm and 3 nm (Fig.3.6a and c), respectively, indicating an attractive adhesion force. However, as shown in Fig.3.6b, the EL energy for the B20 membrane was repulsive and long-range (< 50 nm) due to the negative charge of both the membrane surface and the oil droplets. Therefore, overcoming the electrostatic repulsion requires sufficient energy to bring the oil droplets closer to the membrane surface. The B20 membrane, having a more negative zeta potential, thus displayed a stronger electrostatic double-layer repulsion than the B0 membrane. Additionally, the higher zeta potential enhanced the repulsion of negatively charged oil droplets, potentially improving the antifouling ability of the membranes. The DLVO energy barrier values of the B20 membrane for the SDS, APG, and DDAPS stabilized emulsions were 7529, 5230, and 3282 KT (Fig.3.6d), respectively, indicating the lowest fouling potential for SDS-stabilized emulsions, due to the higher energy barrier. The trend of the DLVO energy values is consistent with the fouling tendencies discussed in Section 3.3.3. For the B0 membrane, the DLVO energy barrier values were 4536, 2876, and 1778 KT for the SDS, APG, and DDAPS surfactants, respectively. The lower energy barrier for the B0 membrane compared to B20 membrane indicates a higher membrane fouling potential. By comparison, for the positively charged CTAB-stabilized emulsions, no energy barrier was observed at the B20 membrane, indicating a high potential. The LW and AB attractive interactions effectively neutralized the EL repulsive interaction, enabling the oil droplets to overcome the energy barrier and facilitating their adhesion onto the surfaces of the B0 and B20 membranes. Therefore, oil droplets stabilized with negatively charged SDS, APG, and DDAPS faced a higher energy barrier before being adsorbed onto the surface of the B0 and B20 membranes.

With the increase in salinity from 1 mM to 100 mM, the DLVO model still maintains a good agreement with the increased membrane fouling, can be confirmed by the decreased energy barrier. The DLVO energy barrier is associate with the energy barrier of the EL component (Fig.3.6d, Fig.3.7d, and Fig.3.8d). In other words, the electrostatic interaction energy plays a vital role for the fouling tendencies of the negatively charged B0 membranes and B20 membranes. Zhao et al. also reported that EL interaction is crucial for the anti-fouling ability of the ceramic membranes, especially for the low-pressure gravity-driven system [227]. As shown in Table.S3 and Table.S4, the reduction of the Lewis base (γ^-), from 47.22 to 43.04 for the B0 membrane and 57.42 to 55.22 for the B20 membrane with a salinity increase from 1 mM to 100 mM, respectively, caused lower membrane fouling. Zhao et al. indicated that γ^- is an indicator of membrane fouling. They explain that the larger the value of γ^-, the greater the total interfacial energy, and the smaller the membrane fouling [228]. Therefore, the increase in salinity reduced the electron donor tension on the membrane surface, thus, decreasing the fouling resistance of the B0 and the B20 membrane.

Based on the XDLVO model, the lower negative value of the AB component for the B20 membrane compared to the B0 membranes indicates a lower attractive AB force (Fig.3.6c, Fig.3.7c, and Fig.3.8c). This also contributed to less fouling of the B20 membrane than of the B0 membrane. Current literature on membrane fabrication or modification also suggests that reducing WCA (θ_w) can increase hydrophilicity and the AB interaction energy, thereby mitigating membrane fouling [213, 229]. Thus, as salinity increases, the absolute value of the AB component decreased. However, when comparing membrane fouling under different surfactants and salinity levels, the trend of the AB component was not aligned with that of the membrane fouling curve (Fig.3.3c, Fig.3.4c, Fig.3.5c, Fig.3.6c, Fig.3.7c, and Fig.3.8c). One possible explanation is that the differences in WCAs are not significant enough to effectively distinguish the fouling caused by different surfactants. At the salinity of 1 mM, when filtering SDS stabilized emulsions, the B0 and the B20 membrane showed XDLVO energy barriers of 3779 kT and 7046 kT, respectively (Fig.3.6e). However, at high salinity levels (20 and 100 mM), the interfacial energy barrier of the B0 membrane disappeared as the XDLVO interaction energy became negative and the energy barrier of the B20 membrane still existed, with values of 1927 kT and 93 kT, respectively (Fig.3.7e, and Fig.3.8e). The reason is that the interfacial energy barrier of the XDLVO model depends on the EL component at low salinity (1 mM). However, due to the higher charge screening effects caused by high salinity (20 mM, 100 mM), the EL interaction energy was decreased significantly. At the same time, the Debye length, calculated as 9.6 nm at the salinity of 1 mM and 0.956 nm at the salinity of 100 mM [230], respectively, decreased, indicating that at high salinity, the electrostatic interaction played a role at a shorter distance, thus, the energy barrier affected by the both the repulsive EL interaction and attractive AB interactions. Specifically, for the B0 membrane, the dominance the AB interaction was due to the diminished XDLVO energy barrier whereas for the B20 membrane, the EL interaction prevailed since the energy barrier was positive. A similar phenomenon was observed with the other negatively charged emulsions (APG and DDAPS), confirming the anti-fouling ability of the B20 membrane under varying salinity levels and different surfactant types. Thus, the increased B20 membrane fouling can be explained by the reduction in the energy barrier due to increased salinity. When filtering the SDS-stabilized emulsion through the B0 membrane, the energy barrier also diminished and eventually disappeared with the increase in salinity from 1 mM to 100 mM, respectively. For example, as shown in Fig.3.6e and Fig.3.8e, at a separation distance of 2 nm, which was close to the separation distance corresponding to the energy barrier of the B20 membrane at 1 mM salinity level, the corresponding interaction energy of B0 membrane was 3375 kT at 1 mM and then decreased to -1023 kT (100 mM), indicating that the attractive interactions between the oil droplets and the membrane surface became stronger, thereby, potentially, intensifying membrane fouling. The XDLVO model, thus, accurately predicted the fouling tendency of the B0 and B20 membrane at the salinity of 1 mM, based on the energy barrier values whereas at high salinities (20 mM, 100 mM), due to the dominance of the AB component, a mismatch between the fouling tendency and XDLVO occurred for the B0 membrane. It can be inferred that at low salinity levels, the interaction between oil droplets and the membrane surface was primarily governed by electrostatic forces, while at high salinity levels, adhesion behavior was mainly driven by AB interactions.

To further evaluate the effect of salinity on various interactions, in addition to analyzing the DLVO/XDLVO curves and energy barriers, we also examined the interfacial free energy components of the micro-sized oil droplets and B0/B20 membranes at a separation distance of 0.158 nm. There, the impact of electrostatic free energy (ΔG^{EL}) on the overall interfacial free energy (ΔG^{TOT}) was minimal, given its long-range properties. At low salinity (1 mM), as shown in Table.S3.5, the B0 membrane exhibited the highest ΔG^{TOT} (-9.37 mJ/m²), e.g. compared to 100 mM salinity (-10.71 mJ/m²), consistent with the increased membrane fouling observed at high salinity (Fig.3.5). The Lifshitz–van der Waals Free Energy (ΔG^{LW}) values remained nearly unchanged across different salinities (ranging from -0.93 to -1.03 mJ/m²) (Table.S3.5), indicating that salinity has a limited effect on van der Waals interactions. This aligns with the findings of Xie et al., who reported that van der Waals interactions are insensitive to the variation in electrolyte type, concentration, and pH [231]. At low salinity, after SiC deposition, the absolute value of the LW component (-0.093 mJ/m²) was lower for the B20 membrane than for the B0 membrane (Table.S3.6). This is because the weaker dispersion forces between the surface of B20 membrane and the liquid reduced the tendency of the liquid to maintain a spherical shape on the surface, making it easier for the liquid to spread, resulting in a more hydrophilic surface. Meanwhile, the Acid-Base Free Energy (ΔG^{AB}) increased considerably from -8.44 mJ/m² (B0) to -2.71 mJ/m² (B20), indicating that fouling caused by acid-base interactions was effectively reduced after SiC deposition. A similar phenomenon was observed at high salinities (Table S3.5 and S3.6). The increase in ΔG^{AB} at different salinities suggests that SiC deposition enhanced the interaction between surface functional (hydroxide) groups and polar water molecules [232]. This enhancement is primarily due to hydrogen bonding interactions between water molecules and electron-donating (γ^{+}) or accepting (γ^{-}) groups. These stronger interactions create a high surface energy, which effectively resists fouling [233].

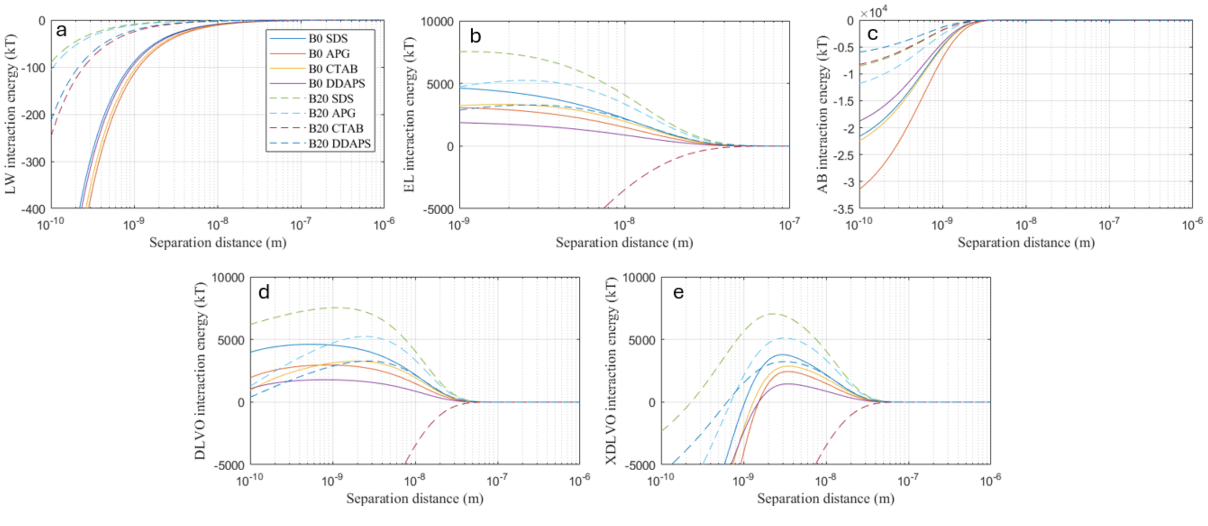

Fig. 3.6. Effect of surfactants on membrane-oil droplet ineraction energy for B0 and B20 membranes: (a) LW, (b) EL, (c) AB, (d) DLVO, and (e) XDLVO interaction energy at 1 mM salinity.

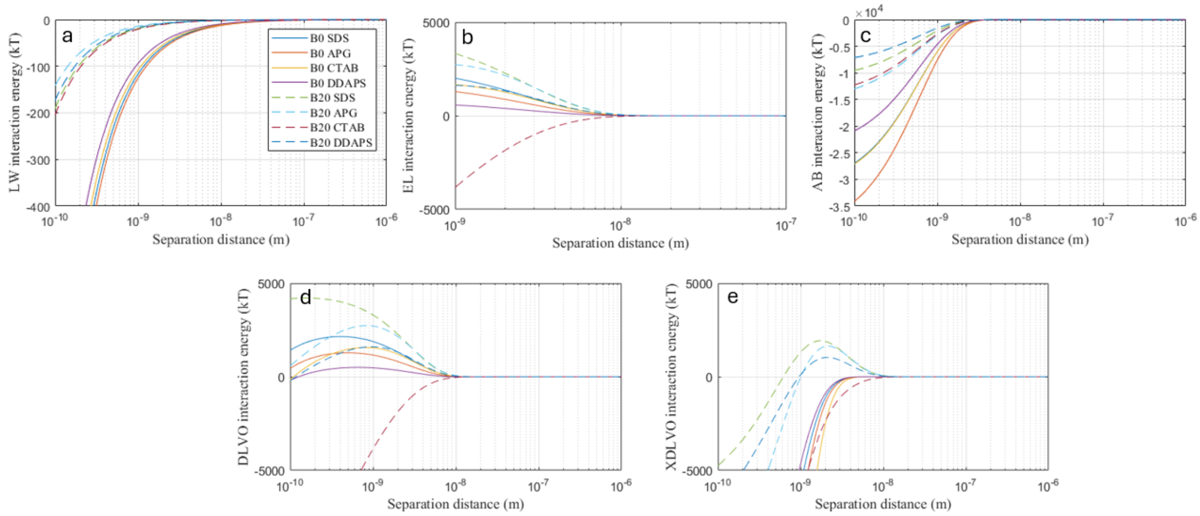

Fig. 3.7. Effect of surfactants on membrane-oil droplet interaction energy for B0 and B20 membranes: (a) LW, (b) EL, (c) AB, (d) DLVO and (e) XDLVO interaction energy at 20 mM salinity.

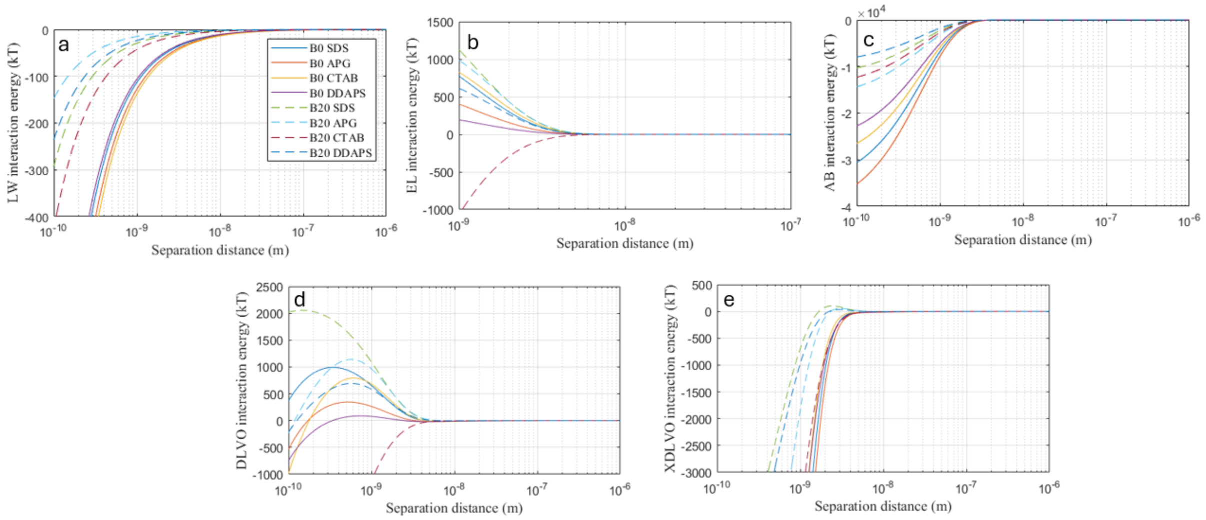

Fig. 3.8. Effect of surfactants on membrane-oil droplet interaction energy for B0 and B20 membranes: (a) LW, (b) EL, (c) AB, (d) DLVO and (e) XDLVO interaction energy at 100 mM salinity.

Interaction between deposited oil layer and oil droplet

With the increase in filtration time, the oil droplets aggregated, eventually forming a cake layer to serve as an extra filter layer. The oil droplet-oil droplet interaction was determined entirely by the properties of the oil rather than the membrane characteristics. Thus, when the cake layer was formed, the same zeta potentials and contact angles resulted in an overlap of the DLVO and XDLVO curves for the fouled B0 and B20 membranes (Fig.3.9 and Fig.S3.5). As shown in Fig.3.9, when the cake layer was formed, the influence range of each energy component varied. All three interaction energies decreased to zero as the separation distance increased, but the ranges of their influence varied. For both fouled membranes, the influence range of the EL component was the then longest (Fig.3.9b), with magnitudes decreasing to 0 at d ≥ 60 nm, while the AB (Fig.3.9c) surpassed the EL and LW interactions and dominated the curve of attraction and repulsion at a separation distance smaller than 3 nm. This can be explained by the hydrophobicity of the oil cake layer and the corresponding improved AB interfacial force [234]. Fig.3.9d shows that oil droplets stabilized with CTAB had to overcome the largest energy barrier to adsorb or deposit on the oil layer, followed by SDS, APG, and DDAPS. The reason is that the absolute value of the CTAB stabilized oil droplets was the largest, contributing to the larger EL component, which was dominant in the DLVO interaction. The energy barrier of the oil-membrane interaction was thus lower than that for the oil droplet-oil layer interaction, indicating that the accumulation of the fouling in the later stages of filtration was less than in the initial stage (0-3 min). Based on the membrane-oil droplet DLVO interaction energy in

Section 3.3.4.1, the B20 membrane was expected to show severe fouling when filtering CTAB stabilized O/W emulsions over 20 minutes. However, the positive DLVO interaction energy between the CTAB-stabilized oil droplets and the deposited oil layer on the B20 membrane alleviates the membrane fouling. However, during the filtration, it was found that there was no decline in the slope of the TMP curve (Fig.3.3). The possible reasons would be that the filtration time of each cycle was too short (20 min) to develop the oily cake layer, and that the drag force/crossflow could reduce the generation of the cake layer. Thus, the membrane surface was not fully covered with the cake layer and the fouling mechanism was the combination of the pore blocking (membrane-oil interaction) and the cake filtration (oil droplet-oil droplet interaction). For these two types of fouling, the oil-membrane interaction dominated over the oil-oil interactions, confirmed by the surface SEM images and Energy Dispersive X-ray (EDX) mapping images of the B0 and B20 membranes. This is particularly apparent for the B20 membrane, where the oil coverage area on the surface (35%) was smaller than the clean membrane surface area (65%) (Fig.3.10). In contrast, the B0 membrane had a higher oil coverage of 46%, indicating that oil-membrane interactions influenced 54% of the surface, while oil-oil interactions accounted for the remaining 46%. The calculation of the total DLVO interaction energies were based on the percentage of oil-oil and oil-membrane interactions [235]. For example, in SDS-stabilized emulsions at 1 mM salinity, the DLVO interaction barrier for the oil-membrane interaction for the B0 and B20 membranes were 7529 kT and 4536 kT, respectively. The DLVO interaction for the oil-oil interaction was 15012 kT. Thus, under the combined fouling mechanism, the total DLVO interaction energy barriers for the B0 and B20 membranes were 10135 kT and 9354 kT, respectively. Moreover, Fig.3.9e indicates that the XDLVO interaction energy barrier was slightly positive due to the dominance of the AB component. This XDLVO energy barrier is smaller than the oil-membrane XDLVO interaction energy barrier, indicating a higher fouling tendency. This finding is consistent with results from the fouling experiment. Thus, the XDLVO model better predicted the fouling at the later stage of the fouling experiment.

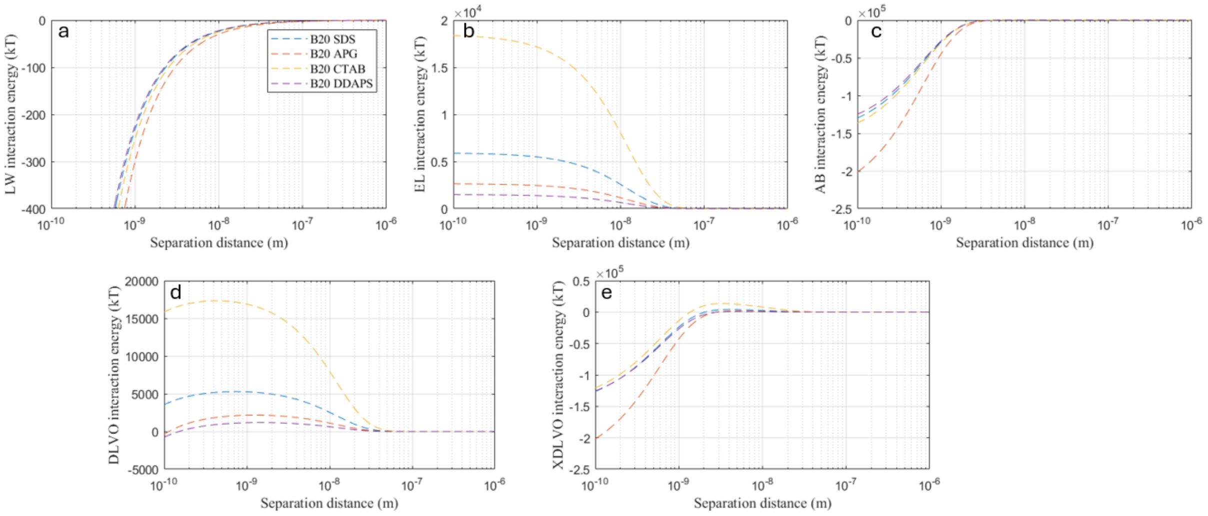

Fig. 3.9. Effect of surfactants on the deposited oil layer-oil droplet interaction energy for the B20 membrane: (a) LW, (b) EL, (c) AB, and (d) DLVO, and (e) XDLVO interaction energy at 1 mM salinity.

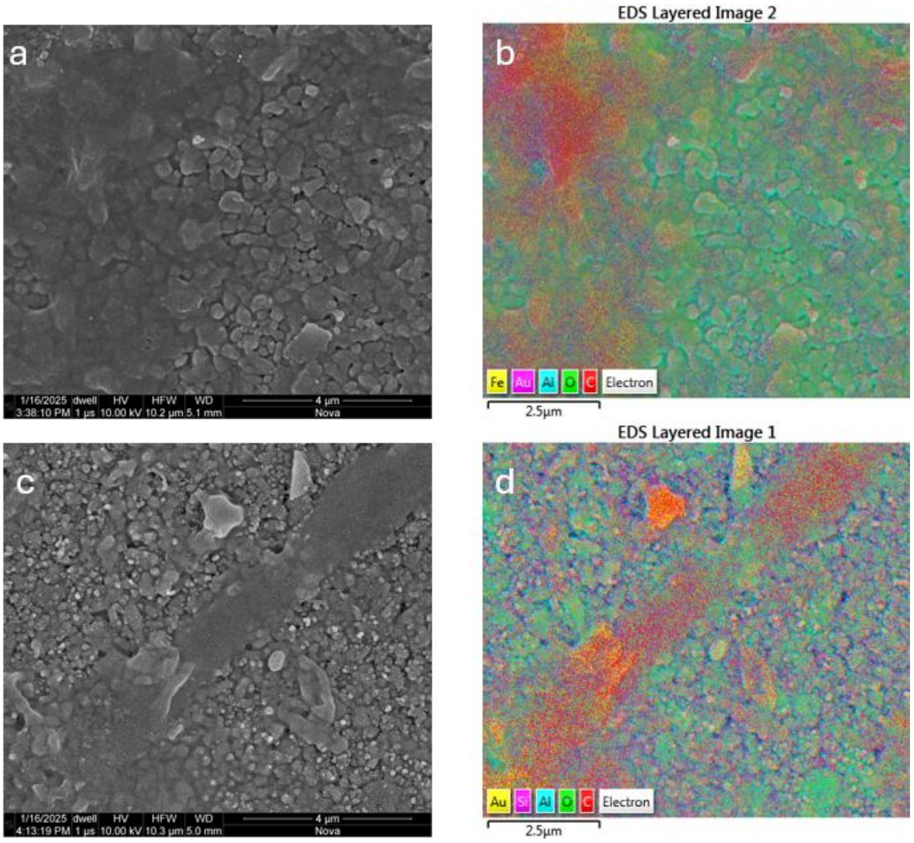

Fig. 3.10. (a) Surface SEM images of the fouled B0 membrane following a 20 min filtration cycle; (b) Corresponding EDX mapping images; (c) Surface SEM images of the fouled B20 membrane and (d) Corresponding EDX mapping images.

DLVO model and membrane fouling resistance

As shown in Fig.3.11, the connection between the DLVO interaction energy of the oil droplet-membrane surface interaction and the membrane fouling resistance is illustrated, using a separation distance of 1 nm, as proposed by Lin et al. [234]. Based on the DLVO theory, a positive repulsive interaction energy between a membrane and an oil droplet indicates the alleviation of membrane fouling, while a negative value suggests an attractive effect that could increase membrane fouling. The B0 membrane exhibited a positive DLVO interaction energy for all types of the surfactants, while the B20 membrane also showed a higher positive value for the emulsions stabilized by the negatively charged SDS, APG, DDAPS. Meanwhile, as indicated by the direction of the blue arrow (from top left to the bottom right), both B0 and B20 membranes showed that reversible and irreversible fouling decreased with increased DLVO interaction energy, owing to the higher electrostatic repulsive interactions with negatively charged emulsions. The electrostatic interaction was the primary contributor to the DLVO interaction energy. A similar phenomenon can be observed at the salinity of 20 mM (Fig.S3.6) and 100 mM (Fig.S3.7). These findings offer valuable insights into reducing membrane fouling after the SiC coating at various salinities and surfactant types, attributed to the higher positive value of DLVO interaction energy.

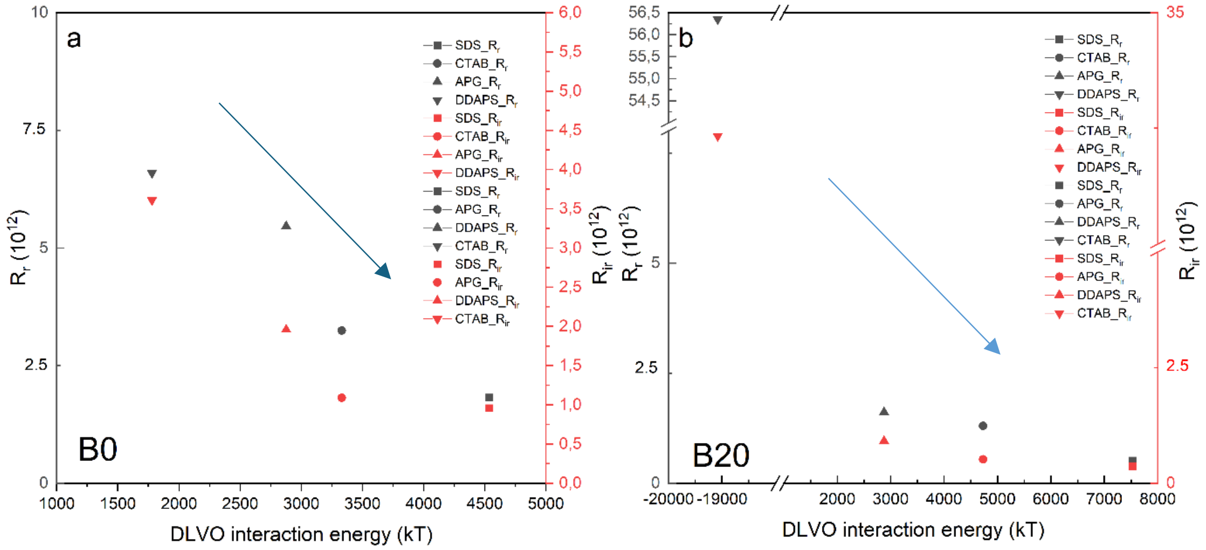

Fig. 3.11. The relationship between the DLVO interaction energy of the membrane-oil droplet surface interaction at the separation distance of 1 nm and the membrane fouling resistance for (a) the B0 membrane and (b) the B20 membrane filtrating 500 mg/L micron-sized O/W emulsions at 1 mM salinity. The red marks represent the irreversible fouling, and the black marks represent the reversible fouling.

3.3.5 Limitations and Recommendations

DLVO and XDLVO models cannot consider the effects of drag and shear forces due to the hydrodynamic effects generated at the cross flow mode. Dead-end filtration, shows the advantage of focusing on the interfacial interactions in the absence of shear effects, since the interfacial interactions decrease with the increase in hydrodynamic effects [236]. In a comparative study, oil fouling was compared under both constant pressure dead-end and cross-flow configurations. Results showed that cake filtration dominated in the dead-end setup, whereas in constant-flux cross-flow mode, the extent of cake formation was reduced due to the continuous cleaning effect of shear when filtering SDS-stabilized O/W emulsions [236]. Furthermore, in dead-end mode, emulsions with a more negative charge resulted in higher permeate flux, as the negatively charged oil droplets were more strongly repelled from the negatively charged polyamide membrane surface (-17.1 mV) and therefore fouled the membrane more slowly. However, under cross-flow filtration conditions, the rank order of permeate flux for the four surfactants was no longer aligned with the zeta potential of the foulant. Instead, flux performance in cross-flow mode was found to correlate with the oil contact angle. This fouling behavior is consistent with XDLVO theory, where both electrostatic and acid–base interactions contribute to fouling [236]. Our findings differ because the membranes in this reported study had relatively low absolute zeta potential, diminishing the contribution of electrostatic interactions [236].

Although XDLVO is a more complex model for identifying the total interaction energy and membrane fouling, the AB compound dominates the XDLVO total energy value, ignoring the contributions of LW and EL compounds and obscuring the fouling tendencies of various O/W emulsions. Therefore, the DLVO model can better predict and compare the fouling of various O/W emulsions, particularly for the foulant-membrane interactions at higher salinity. During the filtration experiments, a single foulant-membrane interaction may not fully represent the overall interactions near the membrane surface, as multiple interactions, such as foulant-foulant interaction, also occur. Additionally, the electricity-enhanced electrified SiC membrane is recommended for future studies to mitigate fouling, given the dominance of EL interaction energy. In this study, the average surface roughness for the B0 and B20 membranes is slightly increased, with values of 55 ± 3 nm and 76 ± 3 nm, respectively (Fig. S3.8). Therefore, the effect of the surface roughness of the B0 and B20 membrane on the DLVO/XDLVO model was not considered in this study.

3.4. Conclusion

Utilizing DLVO models to quantify the interaction between the micro-sized oil droplets and the B0/B20 membrane helped predict the membrane fouling at the same hydrodynamic conditions. Variations in hydrodynamic effects were reduced by maintaining consistent crossflow velocities and permeate fluxes. In constant flux crossflow experiments, the B20 membrane had less reversible and irreversible membrane fouling than the B0 membrane when filtrating O/W emulsions stabilized with negatively charged surfactants (SDS, APG, and DDAPS). Additionally, the B20 membrane exhibited higher DLVO interaction energies than the B0 membrane. The EL components, which have the longest interaction range, mainly influence membrane fouling. In contrast, the LW and AB components, which act as the middle and short-range force, have little impact on membrane fouling. Notably, both the (X)DLVO interaction energies between the membrane and oil droplets strongly aligned with the reversible and irreversible fouling at a low salinity of 1 mM. At higher salinities (20 and 100 mM), the DLVO model also aligned well with the observed fouling trends for both B0 and B20 membranes. Additionally, the (X)DLVO model indicated that an increase in salinity from 1 mM to 100 mM resulted in a decreased (X)DLVO interaction energy barrier, aligning with increased reversible and irreversible fouling during filtration with SDS, APG, and DDAPS-stabilized O/W emulsions for the B20 membrane. Conversely, the observed increase in DLVO interaction energy for CTAB-stabilized emulsion aligned with a decreased fouling propensity and lower reversible and irreversible fouling for the B20 membrane. In summary, by coupling fouling experiments with (X)DLVO modeling, this study enhances the fundamental understanding of the impact of ionic strength and surfactant types on reversible and irreversible fouling by micro-sized oil droplets in crossflow constant flux mode.

Supplementary information

Text S3.1. Measurement of contact angle

The WCA measurements were measured by the sessile drop method by dosing 2 µl liquid (ultrapure water, formamide, diiodomethane) on the Al_2O_3 and SiC-coated membrane surface. The oil-contaminated membrane surfaces using a contact angle analyzer (Dataphysics OCA25, Germany). The membrane samples used for the contact angle measurements were prepared as follows: the membrane was soaked in the ultrapure water for 1 h to remove any impurities on the membrane surface. Finally, the membrane was taken out and air-dried. The oil-contaminated flat sheet membrane used for the contact angle measurement was chosen at the end of the filtration cycle, and dried at room temperature for 24 h. Each sample was tested five times, and the average value was used for the surface tension calculation.

Text S3.2. Filtration protocol

The fouling experiments, consisting of six cycles, were conducted at the constant flux of 80 $Lm^{-2}h^{-1}$ (Fig.S1). This flux was estimated based on the threshold flux using the conventional flux stepping method [15, 166, 167]. Each filtration cycle started with filtering the O/W emulsions at a specified flux with a crossflow velocity of 0.59 m/s for 20 min. Between the filtration cycles, backwashing was applied to eliminate reversible fouling, maintained at a constant flux of 1080 $Lm^{-2}h^{-1}$ for 30 seconds. Finally, forward flushing with the feed emulsions for 15 s at a CFV of 0.6 m/s to drain the concentrated water. Every experiment was conducted in duplicate.

Text S3.3. Surface tension calculation

The surface free energy per unit area is represented by the surface tension, γ, of a liquid or solid. γ is the sum of the apolar Lifshitz-van der Waals (LW) surface tension component (γ^{LW}) and the polar Lewis acid-base (AB) surface tension component (γ^{AB})[1]:

$$\gamma = \gamma^{LW} + \gamma^{AB} \tag{S1}$$

Where γ^{AB} consists of an electron acceptor (γ^{+}) and an electron donor (γ^{-}) component [237]:

$$\gamma^{AB} = 2\sqrt{\gamma^{+}\gamma^{-}} \tag{S2}$$

Contact angle measurements are frequently used to describe surface tension components and interfacial tensions [237, 238]. θ between the liquid (l) and solid (s) phases in air is a function of the surface tension components of two materials [237]:

$$(1 + cos\theta)\gamma_l = 2\left(\sqrt{\gamma_l^{LW}\gamma_s^{LW}} + \sqrt{\gamma_l^{+}\gamma_s^{-}} + \sqrt{\gamma_l^{-}\gamma_s^{+}}\right) \tag{S3}$$

In equation S3, the three unknown surface tension parameters of the solid surface (γ_s^{LW}, γ_s^{-}, γ_s^{+}) could be determined by measuring the contact angle measurements of three probe liquids with known surface tension (γ_l) and surface tension parameters (γ_l^{LW}, γ_l^{+}, γ_l^{-}). By calculating the free energy of interaction between two similar surfaces submerged in water (ΔG_{sws}), the surface hydrophobicity/hydrophilicity could be assessed [239]. The surface is considered hydrophobic if the interaction between two surfaces is greater than that of each surface with water ($\Delta G_{sws} < 0$) and vice versa ($\Delta G_{sws} > 0$). The surface tension elements of the interacting entities are used to calculate ΔG_{sws} [239]:

$$\Delta G_{sws} = -2\gamma_{sw} = -2\left(\sqrt{\gamma_s^{LW}} - \sqrt{\gamma_w^{LW}}\right)^2 - 4\left(\sqrt{\gamma_s^{+}\gamma_s^{-}} + \sqrt{\gamma_w^{+}\gamma_w^{-}} - \sqrt{\gamma_s^{+}\gamma_w^{-}} - \sqrt{\gamma_w^{+}\gamma_s^{-}}\right) \tag{S4}$$

Parafilm with $\gamma^{LW} = 25.5$ mJ/m^2 [240] was used as a planar surface because of its apolarity ($\gamma^{AB} = 0$). The contact angle of the selected surfactant solutions on parafilm was measured (Dataphysics OCA 25, Germany), hence the corresponding γ^{LW} of the selected surfactant solution could be calculated by equation S3 [94].

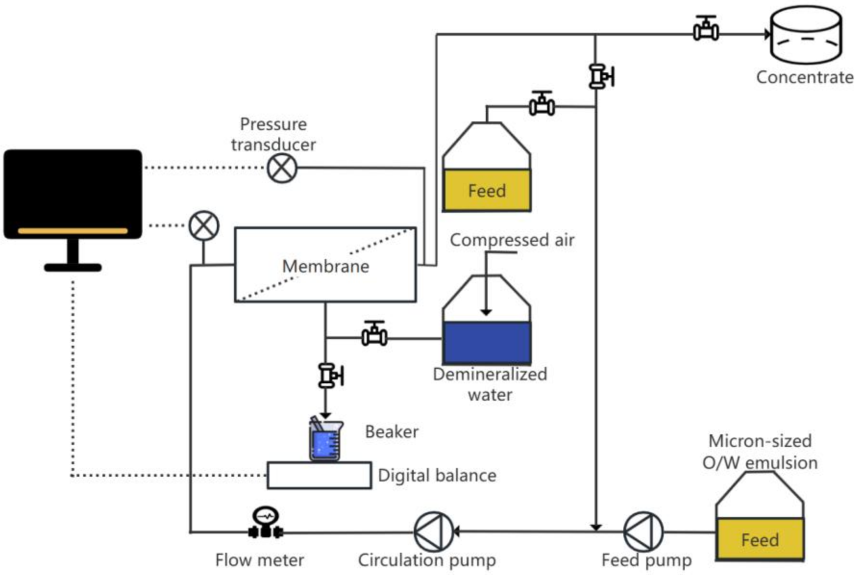

Fig. S3.1. Schematic diagram of constant flux membrane filtration system.

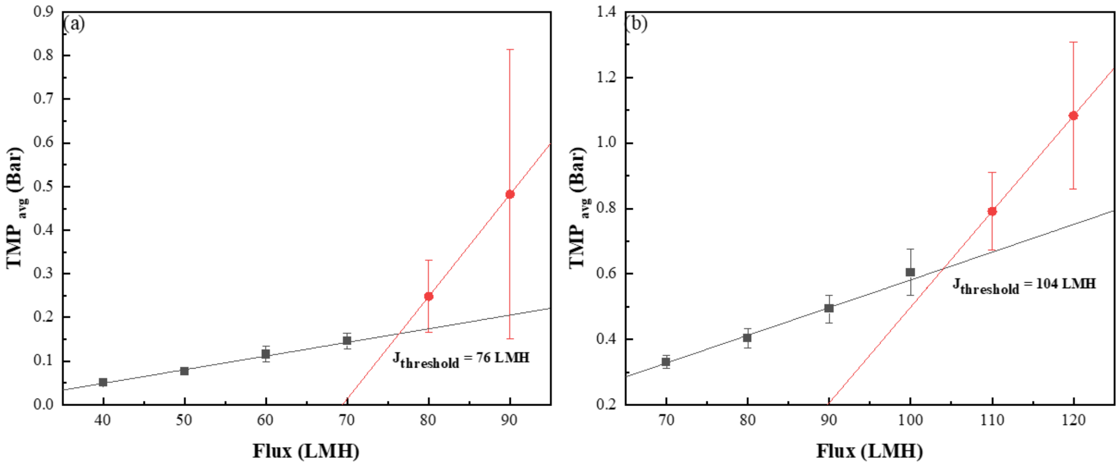

Fig. S3.2. The threshold flux determination by flux stepping method for (a) the B0 membrane and (b) the B20 membrane filtering 500 mg/L micron-sized O/W emulsions stabilized with 239.1 mg/L SDS at 1 mM salinity with the crossflow velocity of 0.59 m/s.

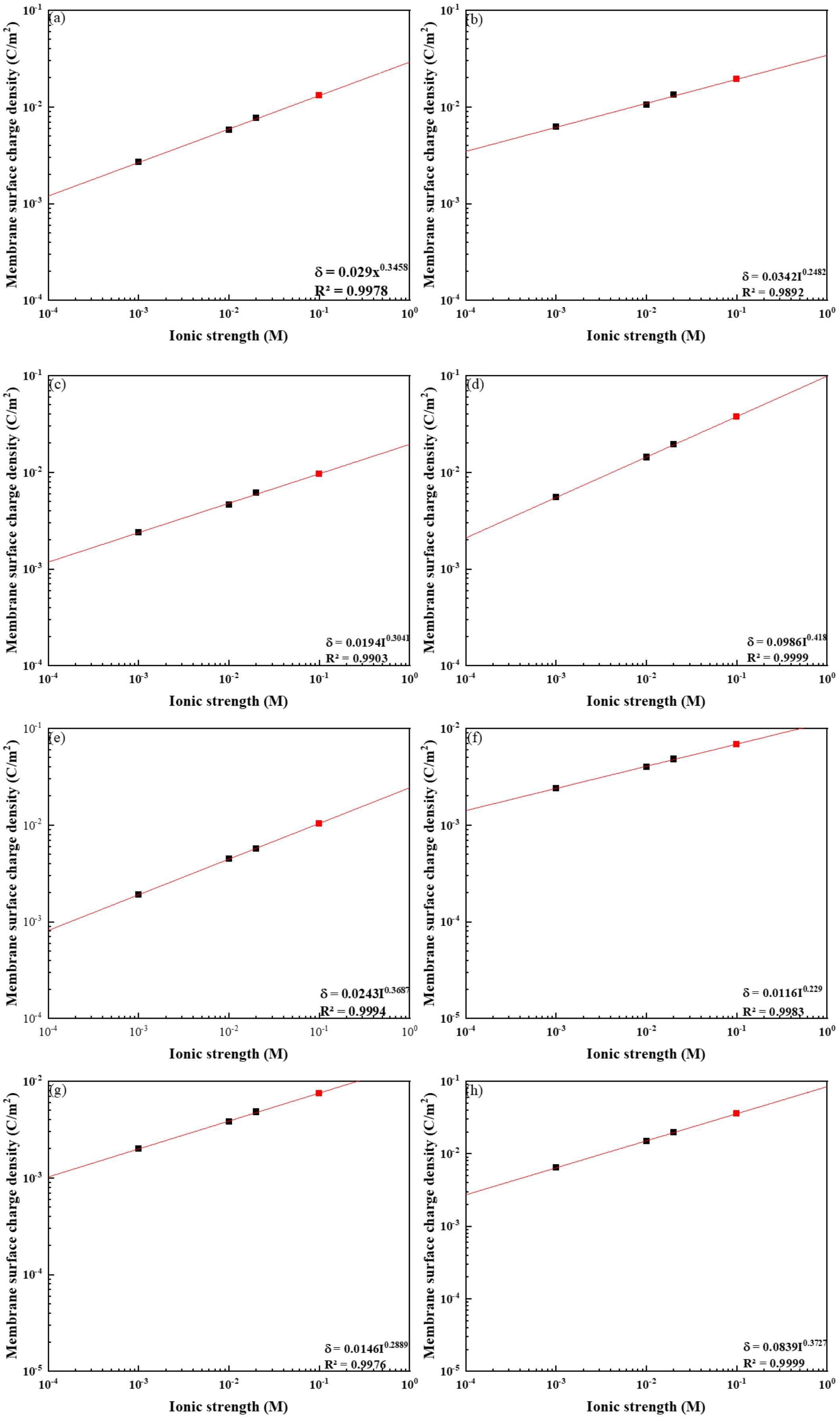
(a)
δ = 0.029x^0.3458
R² = 0.9978
(b)
δ = 0.0342I^0.2482
R² = 0.9892
(c)
δ = 0.0194I^0.3041
R² = 0.9903
(d)
δ = 0.0986I^0.418
R² = 0.9999
(e)
δ = 0.0243I^0.3687
R² = 0.9994
(f)
δ = 0.0116I^0.229
R² = 0.9983
(g)
δ = 0.0146I^0.2889
R² = 0.9976
(h)
δ = 0.0839I^0.3727
R² = 0.9999
Membrane surface charge density (C/m²)
Ionic strength (M)
10⁻⁴
10⁻³
10⁻²
10⁻¹
10⁰
10⁻⁵

Fig. S3.3. The membrane surface charge density under 100 mM salinity was estimated by using the Freundlich ion adsorption model for (a) the B0 membrane with SDS solution, (b) the B20 membrane with SDS solution, (c) the B0 membrane with APG solution, (d) the B20 membrane with APG solution, (e) the B0 membrane with CTAB solution, (f) the B20 membrane with CTAB solution, (g) the B0 membrane with DDAPS solution, and (h) the B20 membrane with DDAPS solution.

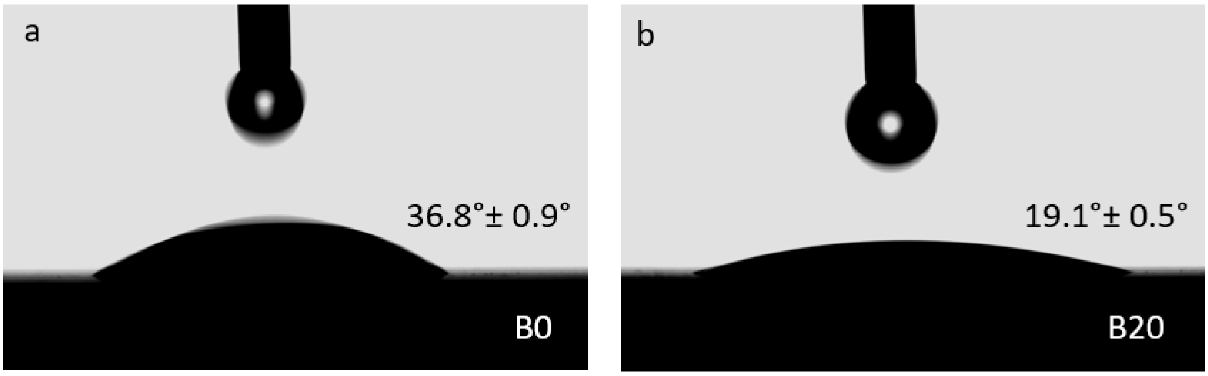

Fig. S3.4. Water contact angle of the (a) B0 membrane and the (b) B20 membrane.

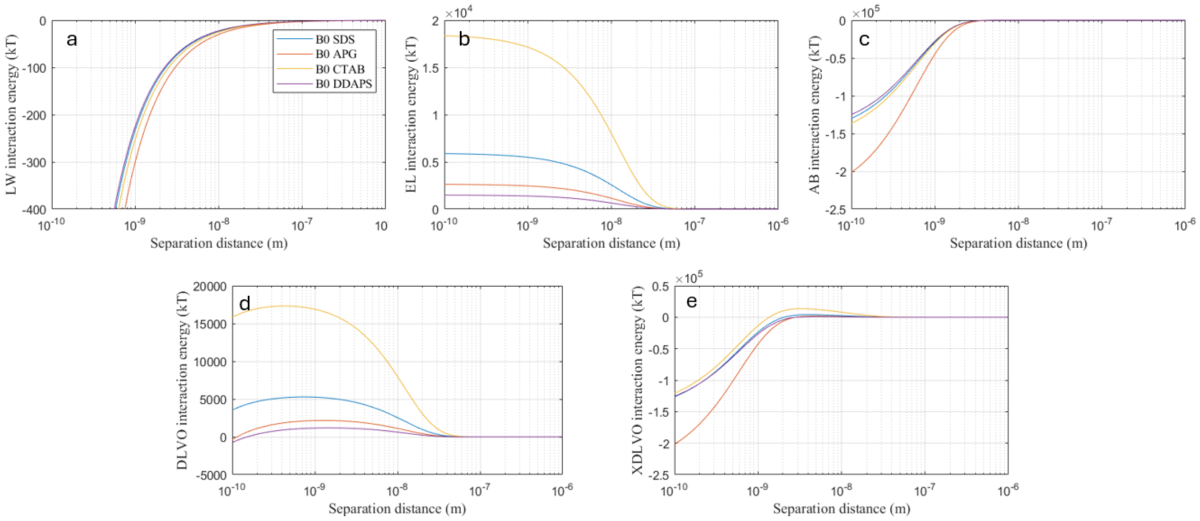

Fig. S3.5. Effect of surfactants on the deposited oil layer-oil droplet interaction energy for the B0 membrane: (a) LW, (b) EL, (c) AB, and (d) DLVO, and (e) XDLVO interaction energy at 1 mM salinity.

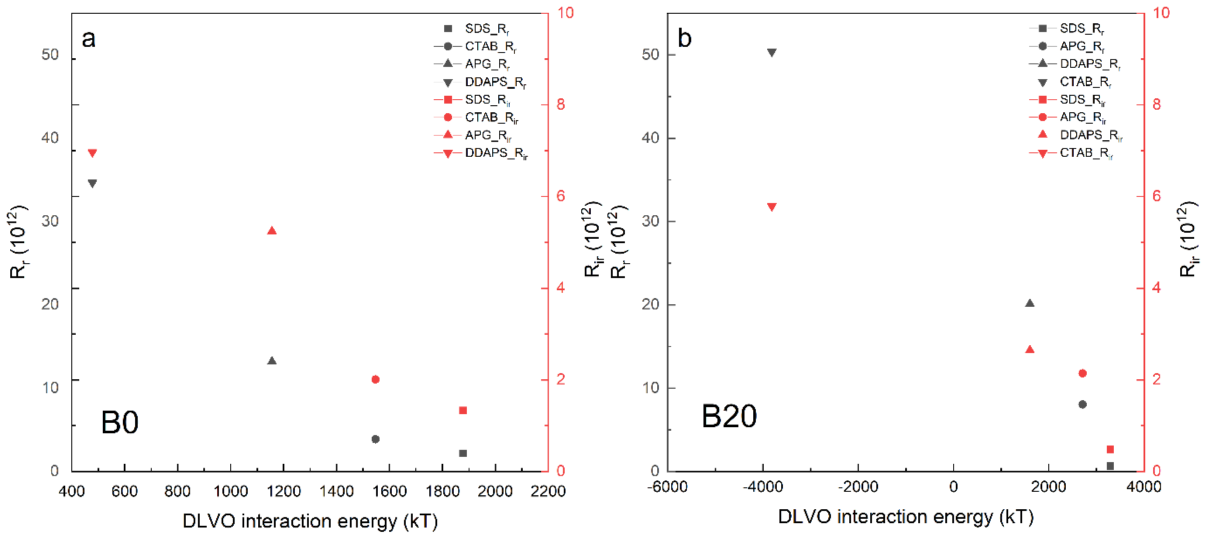

Fig. S3.6. The comparison of the relationship between the DLVO interaction energy of the membrane-oil droplet surface interaction at the separation distance of 1 nm and the membrane fouling resistance for (a) the B0 membrane and (b) the B20 membrane filtrating 500 mg/L micron-sized O/W emulsions at 20 mM salinity. The red marks represent the irreversible fouling, and the black marks represent the reversible fouling.

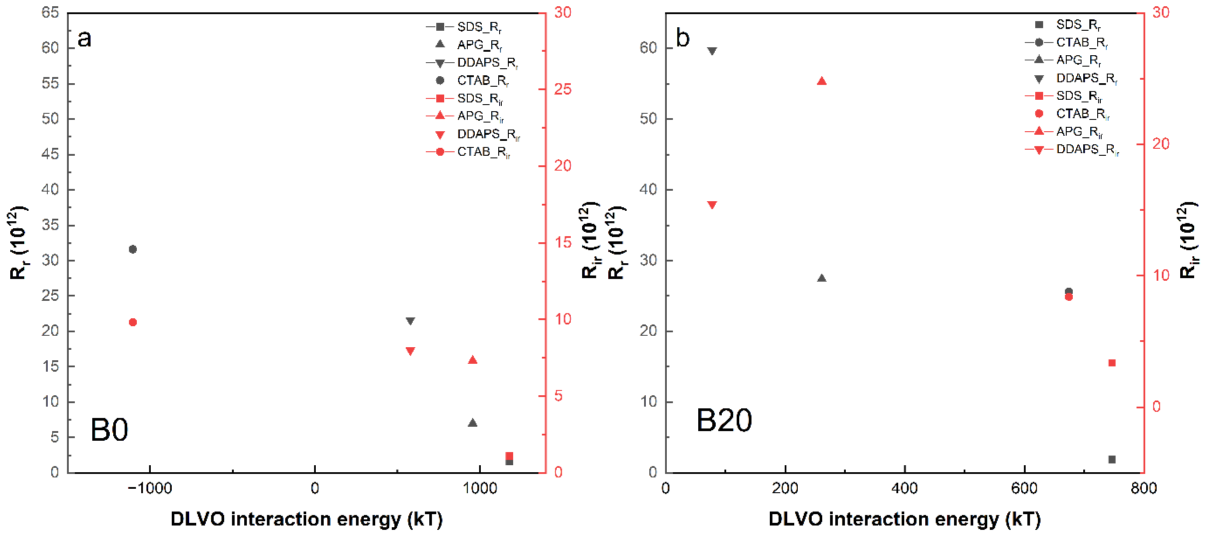

Fig. S3.7. The comparison of the relationship between the DLVO interaction energy of the membrane-oil droplet surface interaction at the separation distance of 1 nm and the membrane fouling resistance for (a) the B0 membrane and (b) the B20 membrane filtrating 500 mg/L micron-sized O/W emulsions at 100 mM salinity. The red marks represent the irreversible fouling, and the black marks represent the reversible fouling.

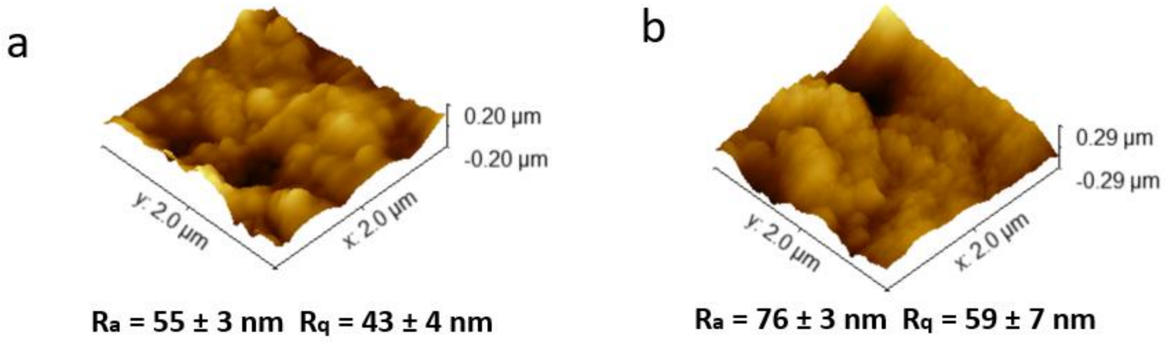

Fig. S3.8. The average surface roughness (R_a) and the root-mean-square surface roughness values (R_q) of the (a) B0 and (b) B20 membranes.

Table. S3.1. Surface tension and surface tension components of ultrapure water, formamide, diiodomethane, and n-hexadecane in mJ/m^2 [238, 241].

	γ	γ^{LW}	γ^{AB}	γ^{+}	γ^{-}
Ultrapure water	72.8	21.8	51	25.5	25.5
Formamide	58	39	19	2.28	39.6
Diiodomethane	50.8	50.8	0	0	0
n-hexadecane	27.5	27.5	0	0	0

Table. S3.2. The average particle size of micron-sized O/W emulsions at various salinity levels stabilized with a single surfactant: SDS, APG, CTAB, or DDAPS.

Surfactant	1 mM	20 mM	100 mM
SDS	5.00	5.86	6.12
APG	6.50	6.84	6.91
CTAB	4.78	5.17	5.25
DDAPS	4.27	4.55	4.80

Table. S3.3. Contact angle with the parafilm (°), the Al_2O_3 (B0) membrane (°), and corresponding surface tension /surface tension components (mJ/m^2).

Sample	θ (parafilm)	θ (B0)	γ	γ^{LW}	γ^{AB}	γ^{+}	γ^{-}
Membrane (0 mM)	-	-	43.016	34.995	8.021	0.335	48.051
Membrane (1 mM)	-	-	43.145	34.995	8.150	0.352	47.221
Membrane (20 mM)	-	-	43.334	34.995	8.338	0.378	45.974
Membrane (100 mM)	-	-	43.756	34.995	8.760	0.446	43.038
SDS (1 mM)	91.3±0.6	37.4±0.7	65.52	40.199	25.321	7.077	22.649
SDS (20 mM	91.2±0.7	38.3±0.5	65.73	40.605	25.125	6.794	23.228
SDS (100 mM)	91.8±0.9	40.5±0.4	66.18	40.293	25.887	7.385	22.686
APG (1 mM)	95.2±1.1	37.8±0.6	70.37	40.147	30.223	11.013	20.735
APG (20 mM)	94.5±0.6	38.6±0.5	69.55	40.274	29.276	10.132	21.148
APG (100 mM)	95.0±1.2	40.0±0.5	70.23	40.294	29.936	11.225	19.959
CTAB (1 mM)	93.5±1.0	39.2±1.0	68.97	41.116	27.854	8.907	21.776
CTAB (20 mM)	92.8±0.7	40.5±0.7	67.82	40.795	27.025	7.799	23.412
CTAB (100 mM)	92.3±0.8	42.3±0.6	68.07	41.854	26.216	7.632	22.513
DDAPS (1 mM)	94.0±1.2	38.2±0.3	69.58	41.073	28.507	9.806	20.718
DDAPS (20 mM)	94.5±1.3	38.8±0.5	68.92	40.752	28.168	9.336	21.014
DDAPS (100 mM)	94.2±0.5	40.2±0.9	69.81	41.048	28.772	10.412	19.876

Table. S3.4. Contact angle with the parafilm (°), the SiC-deposited (B20) membrane and corresponding surface tension/surface tension components (mJ/m^2).

Sample	θ (parafilm)	θ(B20)	γ	γ^{LW}	γ^{AB}	γ^{+}	γ^{-}
Membrane (0 mM)	-	-	48.656	39.660	8.996	0.350	57.842
Membrane (1mM)	-	-	48.723	39.660	9.063	0.358	57.426
Membrane (20 mM)	-	-	48.832	39.660	9.172	0.371	56.745
Membrane (100 mM)	-	-	49.072	39.660	9.412	0.401	55.218
SDS (1 mM)	91.3±0.6	19.6±0.2	65.52	40.199	25.321	7.614	21.051
SDS (20 mM)	91.2±0.7	20.4±0.1	65.73	40.605	25.125	7.598	20.772
SDS (100 mM)	91.8±0.9	22.3±0.3	66.18	41.013	25.167	7.599	20.839
APG (1 mM)	95.2±1.1	19.5±0.6	70.37	40.147	30.223	11.586	19.709
APG (20 mM)	94.5±0.6	20.3±0.2	69.55	40.274	29.276	10.758	19.918
APG (100 mM)	95.0±1.2	22.0±0.4	70.23	40.294	29.936	11.197	20.008
CTAB (1 mM)	93.5±1.0	21.6±0.4	68.97	41.116	27.854	9.599	20.206
CTAB (20 mM)	92.8±0.7	23.8±0.2	67.82	40.795	27.025	8.437	21.641
CTAB (100 mM)	92.3±0.8	26.4±0.7	68.07	41.854	26.216	7.846	21.900
DDAPS (1 mM)	94.0±1.2	19.9±0.3	69.58	41.074	28.507	10.458	19.425
DDAPS (20 mM)	93.7±1.3	20.5±0.4	68.92	40.752	28.168	10.002	19.831
DDAPS (100 mM)	94.2±1.5	21.9±0.6	69.81	41.048	28.772	10.562	19.594

Table. S3.5. Interface free energy at the separation distance of h_0 (mJ/m^2) of the B0 membrane and solutions at different salinities (1 mM, 20 mM, and 100 mM).

Sample	G_{LW} (h_0) (mJ/m^2)	G_{AB} (h_0) (mJ/m^2)	G_{ToT}(h_0) (mJ/m^2)
SDS (1 mM)	-0.931	-8.436	-9.367
SDS (20 mM	-1.030	-8.976	-10.006
SDS (100 mM)	-0.953	-9.758	-10.711
APG (1 mM)	-0.919	-9.436	-10.355
APG (20 mM)	-0.949	-9.732	-10.681
APG (100 mM)	-0.953	-9.947	-10.900
CTAB (1 mM)	-1.160	-9.157	-10.371
CTAB (20 mM)	-1.078	-10.229	-11.307
CTAB (100 mM)	-1.357	-9.849	-11.206
DDAPS (1 mM)	-1.149	-8.579	-9.728
DDAPS (20 mM)	-1.067	-8.954	-10.021
DDAPS (100 mM)	-1.142	-9.252	-10.394

Table. S3.6. Interface free energy at the separation distance of h_0 (mJ/m^2) of the B20 membrane and solutions at different salinities (1 mM, 20 mM, and 100 mM).

Sample	G_{LW} (h_0) (mJ/m^2)	G_{AB} (h_0) (mJ/m^2)	G_{ToT}(h_0) (mJ/m^2)
SDS (1 mM)	-0.093	-2.714	-2.807
SDS (20 mM)	-0.168	-3.174	-3.342
SDS (100 mM)	-0.247	-3.285	-3.532
APG (1 mM)	-0.084	-3.547	-3.631
APG (20 mM	-0.107	-3.704	-3.811
APG (100 mM)	-0.110	-4.053	-4.163
CTAB (1 mM)	-0.268	-3.375	-3.643
CTAB (20 mM)	-0.205	-4.624	-4.829
CTAB (100 mM)	-0.421	-4.574	-4.995
DDAPS (1 mM)	-0.259	-2.728	-2.987
DDAPS (20 mM)	-0.196	-3.265	-3.461
DDAPS (100 mM)	-0.254	-3.232	-3.486

Chapter 4

Oilfield-produced water treatment with SiC-coated alumina membranes

a

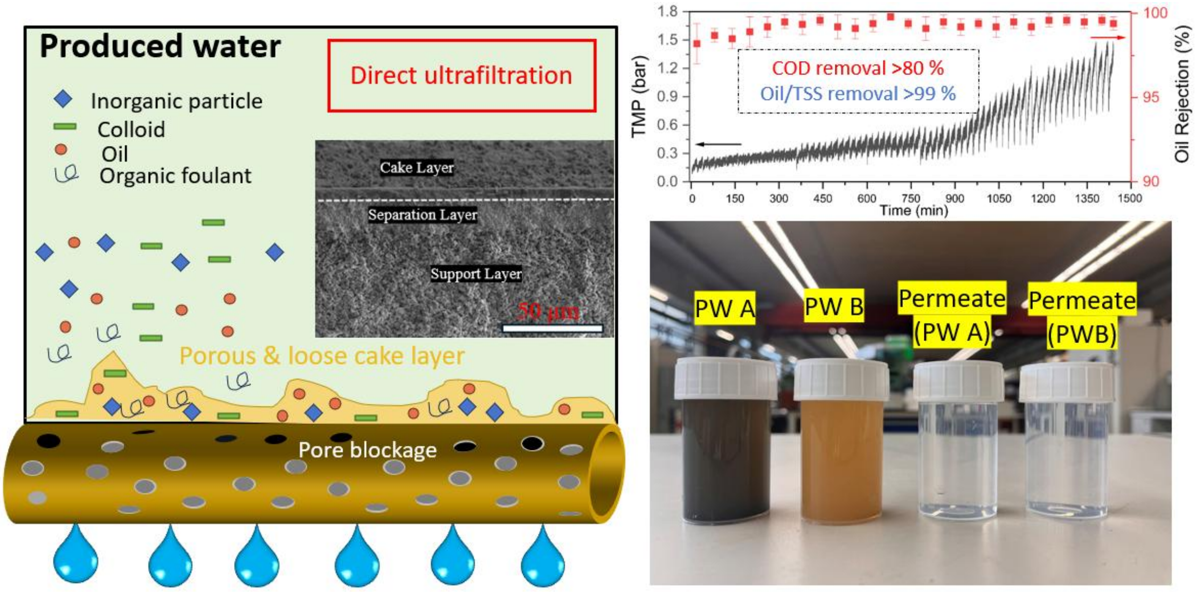

This chapter is based on:

Qin, G., Liu, Y., Rietveld, L. C., & Heijman, S. G. (2025). Oilfield-produced water treatment with SiC-coated alumina membranes. *Separation and Purification Technology*, 362,131841, http://dx.doi.org/10.1016/j.seppur.2025.131841.

Abstract

During the extraction of fossil fuels, a complex waste stream is produced simultaneously, also known as produced water (PW). Membrane filtration is a promising technology that can successfully enable the treatment and reuse of PW. Silicon carbide (SiC) membranes are preferred for PW treatment, due to their low (ir)reversible fouling compared to other ceramic membranes. However, full SiC membrane is expensive and thus economically less feasible. Therefore, we established a method for coating SiC on alumina (Al_2O_3) ultrafiltration membranes, based on low-pressure chemical vapor deposition at 860°C. In the presented study, the fouling resistance and behavior of these novel membranes, with various pore sizes and under different operating conditions, including flux and crossflow velocity, were evaluated. We also used Al_2O_3 membranes and SiC-coated Al_2O_3 membranes in constant flux mode to treat real oilfield PW with high salinity (142 mS/cm) and COD (22670 mg/L). Additionally, the fouling mechanisms in the SiC-coated and Al_2O_3 membranes were analyzed with the help of Focused Ion Beam-Scanning Electron Microscopy imaging. The major findings were that pore blockage served as the initial (irreversible) fouling mechanism and that the (reversible) cake layer, a mixture of organic and inorganic components, dominated the rest of the filtration cycle, where the SiC coated membrane performed better than the original alumina membrane. In addition, it was found that the application of the SiC coating, and the selection of the appropriate pore size (62 nm) and crossflow velocity (0.8 m/s) increased the fouling mitigation, potentially advancing the utilization of ultrafiltration in treating saline PW for reuse purposes.

4.1. Introduction

The substantial amount of produced water (PW), generated from the oil and gas industry, represents a source of oily wastewater that poses a threat to marine ecosystems [242-244]. Several authors have studied various treatment technologies to enhance PW reuse [4, 194, 195, 197, 198, 245]. Microfiltration (MF) [194], electro flocculation [195], ultrafiltration (UF) [4], membrane distillation [197, 198], electrodialysis (ED)[245], adsorption [199], and advanced oxidation [199] are some of the methods that have been documented. Regarding oil, grease, and colloidal particle removal, membrane separation technologies appear promising for pretreating PW for desalination. However, fouling is the primary challenge for PW treatment using membranes, caused by the accumulation of particles and/or oil droplets on the membrane surface or within its pores. Water quality, operational conditions, and membrane properties influence the extent of fouling, resulting in permeability reduction during PW treatment. The main water characteristics determining the severity of fouling on the membrane surface are the content of organic matter, measured as total organic carbon (TOC), suspended solids, measured as total suspended solids (TSS), salts, measured as total dissolved solids (TDS), and oil and grease concentrations. In addition, the particle size of the suspended solids in water can play a determining role during membrane fouling [194, 195]. Additionally, hydrodynamic and operational conditions, such as cross-flow velocity (CFV), operational flux, and backwash conditions, affect membrane fouling [3]. Finally, the fouling severity is related to the pore geometry, hydrophilicity, and surface charge of the membrane [58].

Polymeric membranes, including PVDF, polysulfide (PS), and polyether sulfone (PES), are commonly used for PW filtration [4, 194, 246]. He et al. reported that PVDF MF membranes have successfully been applied for treating shale flowback water, which consisted of the injected fracturing fluid and the connate water of the formation [194]. However, ceramic membranes have gained popularity in treating PW due to a higher mechanical and chemical stability, compared with polymeric membranes, [209, 210, 225, 247]. These ceramic membranes have been produced from various materials, including zirconium oxide (ZrO_2), alumina (Al_2O_3), and titanium oxide (TiO_2)[58, 90]. Zsirai et al. have reported that, although SiC MF membranes show the highest water flux during filtration of the PW at constant pressure mode, they also showed the largest fouling, compared with SiC UF and TiO_2 UF/MF membranes. This was attributed to its highest initial flux, which was observed to be ten times greater than that of other ceramic membranes at the same pressure [247]. In practice, water treatment plants operate in a constant flux crossflow mode to avoid buffering after or before the other treatment steps, and to date, fouling of SiC MF/UF membranes treating real PW in constant flux crossflow mode has, to the authors' knowledge, not yet been studied.

During the treatment of PW with high salinity, the hydrophilicity of the membrane plays a crucial role in membrane fouling, since it has been reported that the zeta potential of oil droplets in PW is close to 0 mV when the NaCl concentrations of PW are higher than 50,000 mg/L [5]. Therefore, some studies have focused on the improvement of the hydrophilicity of membranes by modification techniques, such as low-pressure chemical vapor deposition (LPCVD) [29] and atomic layer deposition (ALD) [168] on the pristine membranes, to alleviate membrane fouling and achieve a better filtration efficacy. These studies have, however, mainly focused on the effect of hydrophilicity on reversible fouling because of practical reasons. Field Emission Scanning Electron Microscopy (FE-SEM) typically provides surface images and, thus, cannot directly access the internal structure of the ceramic membrane and cannot provide insight into the third dimension (depth) of the fouling layer [81]. However, Focused Ion Beam-Scanning Electron Microscopy (FIB-SEM) is a powerful tool for visualizing irreversible fouling by producing artifact-free cross sections with high-resolution (5-10 nm) ultrastructural details [74], allowing for quantitative comparison across the different membranes [78], but, to the authors' knowledge, has not yet been applied to ceramic membranes.

Pretreatment processes to alleviate the fouling, such as sedimentation, coagulation, and rapid sand filtration, are mostly performed before the UF process [18]. In the present study, for the first time, direct ceramic UF of real PW was conducted, using the SiC-coated UF membranes in constant flux mode. We established a method for producing SiC-Al_2O_3 UF membranes based on LPCVD. Firstly, the effect of the salinity on membrane fouling was determined by filtering the synthetic O/W emulsions. Secondly, the fouling resistance and behavior were evaluated under various pore sizes and operating conditions (flux, CFV) using two types of real PW with varying water quality. Finally, the (ir)reversible fouling transition mechanisms were investigated using FIB-SEM images.

4.2. Materials and methods

4.2.1 Materials and Synthetic O/W emulsions preparation

Sodium hydroxide (1.09141, Sigma-Aldrich, the Netherlands) and citric acid (251275, Sigma-Aldrich, the Netherlands) were chosen for the chemical cleaning of the fouled membranes. Detailed information about the chemicals and procedure of the synthetic O/W emulsion preparation is included in the supporting information S4.1.

4.2.2 Membrane preparation

Commercial single-channeled tubular Al_2O_3 membranes were purchased from CoorsTek, the Netherlands of which the selective and support layers are made of α-alumina. The pore sizes of the two selective layers and the support layer, as provided by the manufacturer, are 100, 200, and 600 nm, respectively. The alumina membranes with these pore sizes exhibited measured permeabilities of 350 ± 10, 478 ± 21, and 985 ± 64 $Lm^{-2}h^{-1}bar^{-1}$, respectively.

SiC-coated membranes were prepared by LPCVD. A schematic of the LPCVD system is shown in Fig.S4.1; Dichlorosilane (SiH_2Cl_2) and acetylene (C_2H_2) were chosen as precursors for the SiC layers deposition. The deposition temperature was 860 ^oC, the precursors flow ratio (SiH_2Cl_2 /C_2H_2) was 6.7 and the deposition time was 20 minutes [15], as recommended for the formation of polycrystalline SiC [42, 44]. The pristine 100, 200, and 600 nm Al_2O_3 membranes and the corresponding SiC-coated membranes are referred to as A0, A0-200, A0-600, A20, A20-200, and A20-600, respectively.

4.2.3. Membrane characterization

The water contact angle (WCA) of the A0 membranes and A20 membranes was determined by Dataphysics OCA25, Germany. The zeta potential of flat sheet A0 and A20 membranes, with salinities from 10^{-3}M to 10^{-2}M, was measured by SurPASS 3 (Anton Paar, Graz, Austria), which was coated in the same way as the tubular membrane. In addition, as it is difficult to measure the zeta potential of the membrane at high salinity (10^{-1}M) by SurPASS 3, the zeta potential of the membranes at 10^{-1}M salinity was estimated using the Freundlich ion adsorption model [93], as shown in Fig.S4.2. SEM measurements of virgin and fouled membranes were conducted using FEI Nova NanoSEM 450 and Energy Dispersive X-ray (EDX) spectroscopy. FIB-SEM images were acquired using a 10 kV accelerating voltage and an 800 pA ion beam.

The actual mean pore size was obtained by capillary flow porometry (Porolux^{TM} Revo, IBFT GmbH, Germany).

4.2.4. Produced water characterization

Two types of PW, provided by the Norwegian Technology company, were characterized. The first PW sample (PW A) was collected from the Mongstad refinery, originating from the Troll field. The second PW (PW B) was a mix of batches obtained from the SAR Dusavik offshore base collected from various oilfields in southern Norway. The PW samples were kept at a temperature of 4 °C until they were further processed. Typically, the PW from oil fields tends to exhibit high levels of TOC and salinity compared to the PW from gas production facilities [248]. We primarily analyzed membrane fouling caused by high-salinity PW B, with relatively low-salinity PW A as the control group for comparison.

The pH and electrical conductivity of the PW were respectively measured by multiparameter benchtop meters (inoLab® Multi 9630 IDS - WTW). The droplet sizes and distributions were measured using a Bluewave particle size analyzer (Microtrac, USA). TSS and TDS in the feed and permeate water were measured following the Standard Methods [249]. The measurement and rejection of oil and COD concentration of both feed and permeate are described in the supporting information (Fig. S4.3 and Fig.S4.4).

4.2.5 Estimation of threshold flux

The threshold flux was estimated using the flux stepping method [166, 167]. The average TMP (TMP_{avg}) was then calculated and used to determine the threshold flux. Fluxes ranging from 20 $Lm^{-2}h^{-1}$ to 55 $Lm^{-2}h^{-1}$, with intervals of 5 $Lm^{-2}h^{-1}$, were employed in the flux stepping tests, and each step lasted 20 minutes.

4.2.6. Fouling experiments with synthetic and real produced water

Constant permeate flux crossflow fouling experiments

A constant permeate flux crossflow setup (Fig.4.1) was employed for synthetic O/W emulsions and real PW filtration experiments. The concentrate stream was recirculated to the feed during filtration, having a negligible effect on the feed concentration, while the feed pump provided a stable permeate flux (DDA12-10, Grundfos, Denmark). The constant CFVs were controlled by a circulation gear pump (VerderGear Process H1F, Verder Liquids, the Netherlands). The fouling experiments consisted of six cycles, each with three stages. The first stage was to filtrate the PW at a specific flux for 20 minutes. In the second stage, the fouled membranes were backwashed at a constant backwash flux, being approximately 1050 $Lm^{-2}h^{-1}$. Based on the membrane's permeability, the fouled A0 and A20 membranes were backwashed for 30 seconds with demineralized (DI) water under 3 and 5.25 bar, respectively. The third stage involved forward flushing the membrane with feed PW water for 15 seconds at a CFV of 0.8 m/s to remove and replace the feedwater.

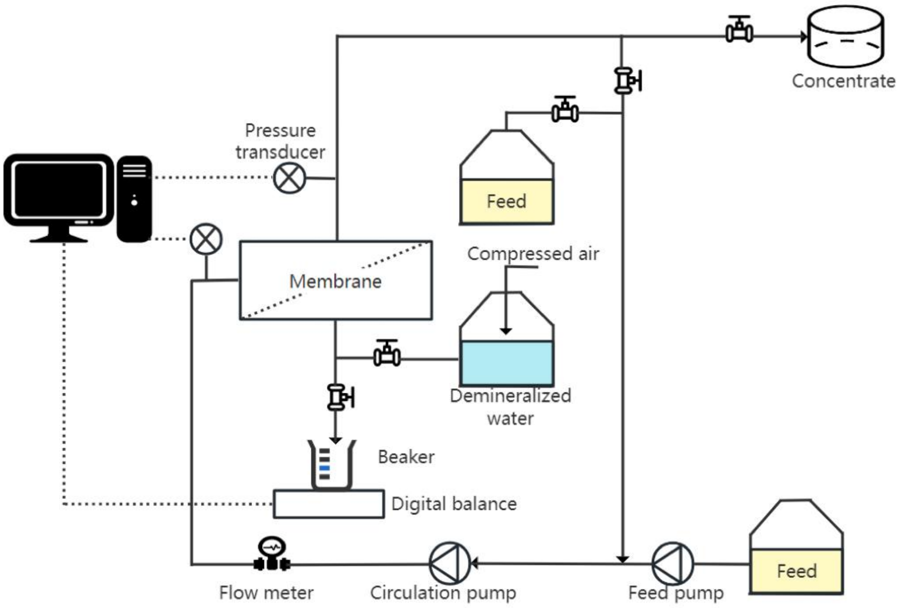

Fig. 4.1. Schematic view of filtration set up with constant flux.

Data analysis

The fouling resistance of the pristine A0 and coated A20 membranes was calculated based on the resistance-in-series model [169, 170], as shown in Eq. (1), Eq (2), Eq. (3), Eq. (4) and Eq. (5):

$$R_t = \frac{TMP}{\mu J} = R_m + R_r + R_{ir} \tag{1}$$

$$R_m = \frac{TMP_0}{\mu J} \tag{2}$$

$$R_t = \frac{TMP_1}{\mu J} \tag{3}$$

$$R_{ir} = \frac{TMP_2}{\mu J} - \frac{TMP_0}{\mu J} \tag{4}$$

$$R_r = R_t - R_m - R_{ir} \tag{5}$$

$$TMP_{Normalized} = \frac{TMP}{TMP_0} \tag{6}$$

Where TMP_0 represents the TMP needed to achieve the required flux with a clean membrane, TMP_1 refers to the TMP after each cycle, and TMP_2 reflects the TMP following the backwash processes, R_t (m^{-1}), R_r, R_{ir}, R_m denotes the overall resistance, reversible fouling resistance, irreversible fouling resistance, and intrinsic membrane resistance. The value of R_m was obtained by conducting filtration experiments using DI water. The value of R_t was calculated by using the final filtration pressure at the end of each filtration cycle. After backwashing the fouled membranes using DI water for 30 seconds, the R_{ir} was calculated by subtracting the TMP_0 from TMP_2 and then dividing the result by the viscosity and permeate flux. The R_r value was then determined by subtracting the sum of R_{ir} and R_m from R_t. The normalized TMP was calculated using the TMP to divide the TMP_0, as indicated in Eq. (6).

4.3. Results and discussion

4.3.1. Characteristics of the raw produced water

Characteristics of the real PWs are shown in Table 1. The results indicate that PW B contained higher levels of COD (22670 ± 524 mg/L) than PW A (9160 ± 168 mg/L). The conductivity of PW A (51.2 ± 2.6 mS/cm) was comparable to that of the feed water in a seawater desalination plant (52.8± 0.2 mS/cm) [250]. By comparison, PW B's conductivity (142.1 ± 4.2 mS/cm) and TDS (105567 ± 1066 mg/L) were about three times higher than those of seawater and similar to those of the PW from a well site in Midland, USA [4]. Based on the particle size distribution analyses of the PW, the mean particle sizes of PW A and B were 0.24 ± 0.09 and 4.85 ± 0.84 µm, respectively (Fig.4.2). For PW A, particles smaller than 10 µm accounted for 90.6 % of the total volume; for PW B, this proportion was only 59.4% (Fig.4.2). The difference in water characteristics between the two PWs may lead to varying degrees of membrane fouling.

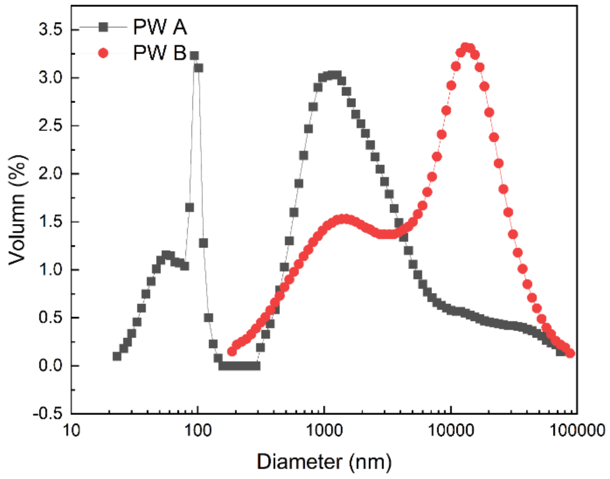

Fig. 4.2. The particle size distribution of the (a) PW A and (b) PW B.

Table 1. Characteristics of the raw PW.

Parameters	**Raw (PWA)**	**Raw (PW B)**
Turbidity	234±19	4032±62
pH	7.44±0.29	8.29±0.21
Conductivity (mS/cm)	51.7±2.6	142.1±4.2
COD (mg/L)	9160±168	22670±524
TOC (mg/L)	1856±47	5335±122
Mean particle size (µm)	4.22±0.09	11.31±1.84
TDS (mg/L)	30833±1389	105567±1066
TSS (mg/L)	4567±1327	8067±2185

4.3.2. Fouling of membranes by synthetic O/W emulsions at various salinities

The effect of the salinity on the fouling of both membranes (A0 and A20, respectively) was conducted by adding 10^{-3} M NaCl, 10^{-2} M NaCl, and 10^{-3} M NaCl+10^{-3} M $CaCl_2$ to the O/W emulsions stabilized with SDS (Fig.4.3). As shown in Fig. S5, these emulsions had similar particle size distributions. It can be observed that the fouling in the A20 membrane appeared to be lower, compared to the A0 membrane, probably due to the more negatively charged surface. With the addition of NaCl from 10^{-1} M to 10^{-3} M (Fig.4.3 a-b,d,f), the fouling of the A0 and A20 membranes increased as the salinity increased. This increased fouling can be explained by the compression of the diffuse double layer of positive ions around the negative oil droplet and the simultaneous compression of the diffuse double layer on the surface of the negatively charged membrane with increased salinity and thus ionic strength, resulting in a lower negative charge of both the O/W emulsion and the membrane [220]. The above explanation is supported by the results of the absolute values of the zeta potential of the O/W emulsion, which showed a decrease from -50.7 ± 0.6 mV to -31.5 ± 0.8 mV, respectively, with an increase in salinity from 10^{-1} M to 10^{-3} M (Table.S4.1). In the meantime, as depicted in Fig.4.3e, the zeta potentials of the A0 and A20 membranes decreased from 50.1 ±1.6 mV to -17.6 ± 1.5 mV and -55.4 ± 1.2 mV to -25.5 ± 1.3 mV, respectively. The A0 membrane surface charge changed from slightly positive (3.0 ± 0.5 mV) to highly negative (–50.1 ±1.6 mV) probably due to the adsorption of the SDS [15]. The surfactant molecules form a layer at the surface of the hydrophilic A0 membrane, with their negative head groups oriented toward the surface. Subsequently, the second layer is adsorbed on the first layer, orienting the adsorbed surfactant with the negatively charged, hydrophilic head groups to the solvent, making the hydrophilic surface even more hydrophilic and negatively charged [251]. The results are consistent with previous studies, which reported that the absolute zeta potential of the membrane decreased with the increase in salinity [50, 146, 220]. The WCA increased from 27° ± 1.2° to 54° ± 2.6° (Table.S4.1) with the salinity increase from 10^{-1} M to 10^{-3} M, indicating sodium ions interacted with the hydrophilic group of the membrane surface, and that the salinity affected the hydrogen-bonding structures of the O/W emulsions [85].

With the addition of the Calcium ions (Ca^{2+}), irreversible fouling was higher than at other salinity levels (Fig.4.3c and Fig.4.3f). $Ca^{2+}$are commonly present in PW, while membrane fouling can be accelerated by divalent cations such as Ca^{2+}, which cause the diffuse double layer to compress more than monovalent ions [252]. In addition, Ca^{2+} and the sulfate group of SDS may react with each other, forming a complex [253, 254], thus increasing the irreversible fouling [255]. However, the irreversible fouling of the A20 membrane was still lower than that of the A0 membrane (Fig.3c) since a lower zeta potential of the A20 membrane (-29.4 mV), compared to the A0 membrane (-19.0 mV), was measured (Fig.4.3e), although the repulsion was weaker than without adding Ca^{2+}.

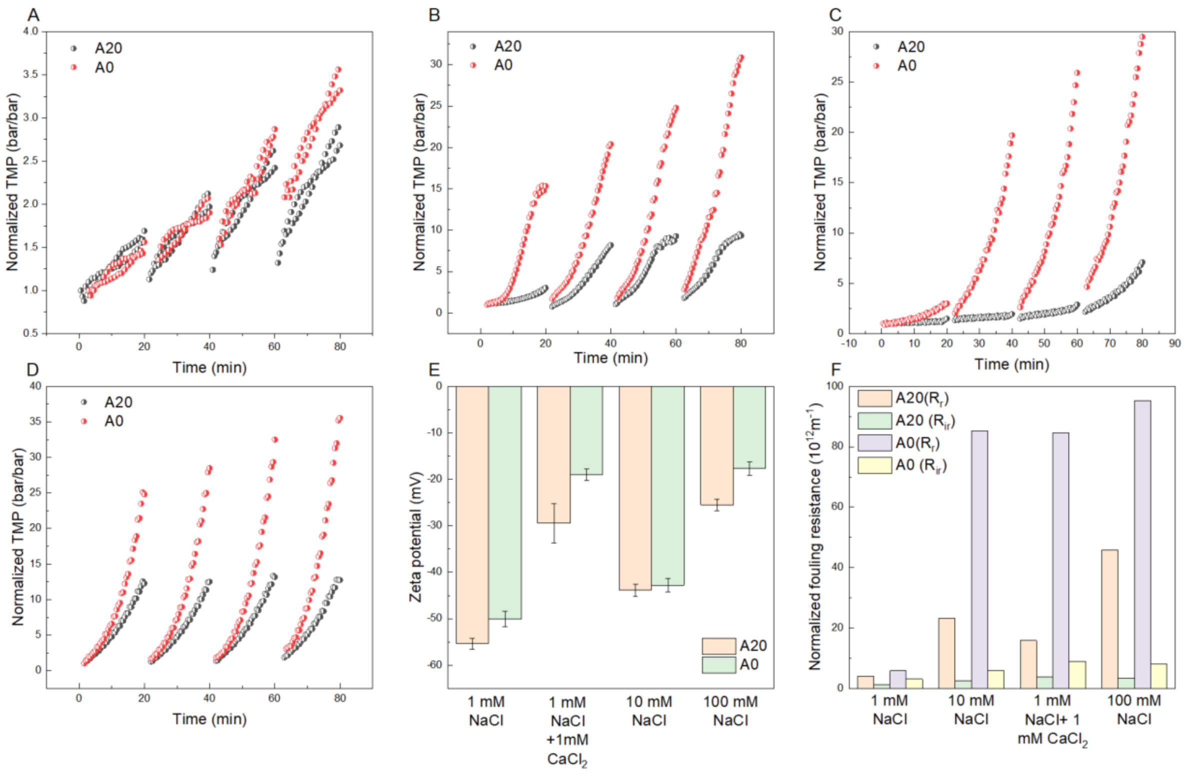

Fig. 4.3. The normalized TMP curves of the A0 and the A20 membrane during the filtration of synthetic O/W emulsions at varying salinity: (a) 10^{-3} M NaCl, (b) 10^{-2} M NaCl, (c) 10^{-3} M NaCl + 10^{-3} M $CaCl_2$, (d) 10^{-1} M NaCl. (e) Zeta potential of the A0 and A20 membranes with varying salinity and ion compositions. (f) The normalized resistance of the A0 and A20 membranes.

4.3.3. Effects of flux on membrane fouling by real produced water

The threshold flux of the A0 and A20 membrane, when filtering PW B, were 39 and 42 $Lm^{-2}h^{-1}$, respectively (Fig. S4.6), thus, three distinct permeate fluxes were chosen, approximately at and higher than the threshold flux, being 30, 40, and 50 $Lm^{-2}h^{-1}$, respectively, to study the effect of permeate flux on membrane fouling by PW B (Fig.4.4). At a flux of 30 $Lm^{-2}h^{-1}$, which was lower than the threshold flux, the interactions between foulants and membrane led to pore blockage of the A0 membrane, followed by the formation and continuous growth of the reversible cake layer on the membrane surface [12]. However, the SiC coating probably inhibited the deposition of the hydrophobic foulants, slowing down the cake layer formation. In addition, the starting point of the normalized water permeance curves of the A0 membrane showed a downward shift with each cycle, this trend was not observed in the A20 membrane, indicating that irreversible fouling existed in the A0 membrane and not in the A20 membrane (Fig. S4.7 a and b). When the flux exceeded the threshold flux (50 $Lm^{-2}h^{-1}$), the interactions between the foulant and the deposited foulant probably represented the dominant fouling mechanism, which is supported by the FBI-SEM images as presented in section 4.3.6, leading to the formation of an (oily) cake layer and a consequent rapid increase in TMP. At the same time, the high TMP probably led to the compaction of the cake layer, and forced the small-sized foulants into the membrane pores, leading to increased irreversible fouling of the A0 and A20 membranes, as confirmed by every cycle's lower initial normalized permeance (Fig. S4.7 c). At this high flux, hydraulic cleaning is still effective in removing the foulant cake layer, which can be confirmed by the relatively low irreversible fouling compared with reversible fouling and the high permanence recovery (PR). The normalized permeance (64 % PR) of the A20 membrane was still higher than that of the A0 membrane (47 % PR) in the final cycle at 50 Lm^{-2}h^{-1} (Fig. S4.7). Moreover, the PR of the A20 membrane after backwashing with DI water was as high as 95 ± 2 % of the original permeability at 40 Lm^{-2}h^{-1}, suggesting promising backwashing efficiencies and implying its suitability for long-term separation of the PW(Fig. S4.7). In addition, Fux and Ramon have reported that during filtration experiments at fluxes lower than the threshold flux, the oil droplets are spherical, and can be easily removed by forward crossflow flushing. However, when the flux exceeds the threshold flux, the droplets deform and cause irreversible fouling inside the membrane pores [256].

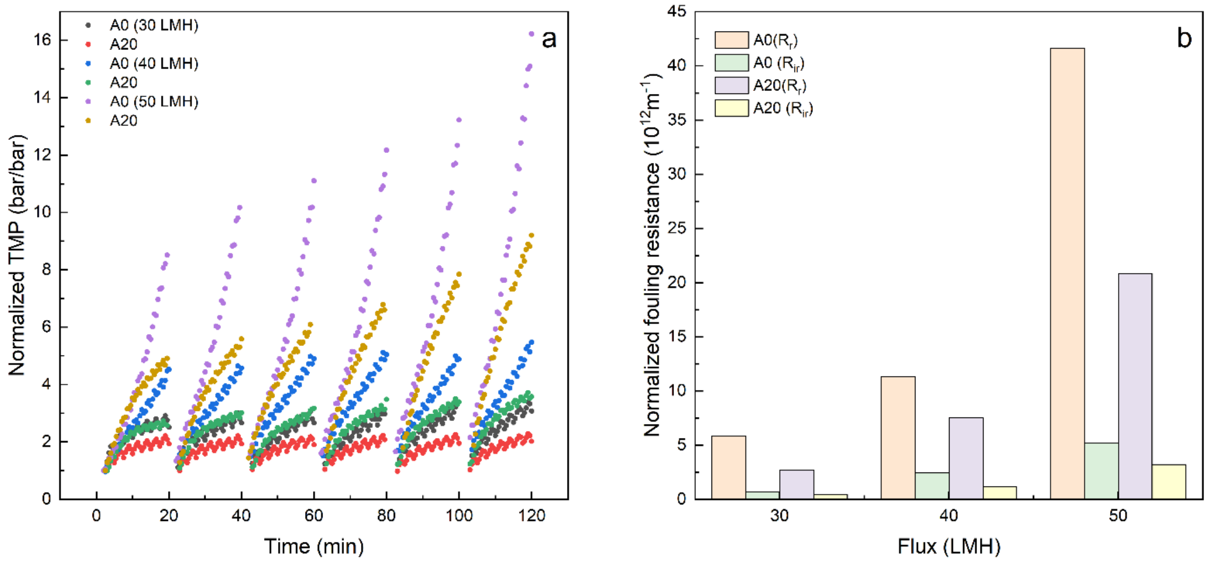

Fig. 4.4. The normalized (a) fouling curve and (b) resistance of the A0 and A20 membranes for the filtration of PW B at the flux of 30, 40, and 50 L m^{-2} h^{-1} with CFV of 0.8 m/s.

4.3.4. Effects of crossflow velocities on membrane fouling

The membrane filtration performances, filtering PW B under different CFVs (0.4, 0.8, and 1.2 m/s) were compared at 50 Lm^{-2}h^{-1}. This high flux is preferred in full-scale installations because a smaller membrane surface is needed to treat PW. At low CFV (0.8 m/s), the higher TMP at the constant flux of 50 L m^{-2} h^{-1} probably compacted the cake foulants, thereby facilitating the development of a denser, low porosity cake layer [257], impacting permeability, since the hydraulic resistance of the cake layer is highly influenced by its porosity. As shown in Fig.4.5a, increasing the filtration CFVs from 0.8 to 1.2 m/s reduced the TMP increase rate (dTMP/dt), thus alleviating membrane fouling, as also reported by Hube et al. [258]. The reversible fouling was dominant for both the A0 and A20 membranes (Fig.4.5b). However, much higher reversible fouling was observed for the A0 membrane than for the A20 membrane at different CFVs. The A20 membrane, for example, exhibited much lower reversible fouling (22.1×10^{12} m^{-1}) than the A0 membrane (54.9×10^{12} m^{-1}) at the CFV of 0.8 m/s. This can be explained by the higher hydrophilicity of the A20 membrane compared to the A0 membrane, which is confirmed by the WCA, decreasing from 37° (A0) to 18° (A20) (Fig.S4.8). Since the zeta potential of the PW is close to 0 mV when the salinity of PW is higher than 50,000 mg/L [5], a low adhesion to the hydrophilic A20 membrane therefore led to a thin cake layer. The reversible fouling further decreased from 16.88×10^{12} m^{-1} to 3.97×10^{12} m^{-1} for the A20 membrane when the CFV increased from 0.8 m/s to 1.2 m/s, respectively (Fig.4.5b). The increased turbulence and shear forces close to the membrane surface apparently reduced the concentration polarization, preventing further accumulation and deposition of foulants onto the membrane [259]. This is supported by an increase of the Reynolds number (Re) from 3573 to 5359 (Table.S4.2), and the flow patterns changed from Laminar-turbulent flow to turbulent flow since the turbulent flow is typically characterized as Re greater than 4000 [260]. In addition, the oil rejection by the A0 membrane increased from 98.4 ± 0.3% to 99.0 ± 0.5% with an increase in CFV from 0.4 m/s to 0.8 m/s, indicating an increased oil droplet concentration near the membrane at lower CFV, see Fig. S4.9b. This phenomenon was also observed for PW A (Fig. S4.10b), where the oil rejection increased from 96.5 ± 0.6 to 98.2 ± 0.4% at CFVs of 0.4 m/s and 0.8 m/s, respectively, while high CFVs lead to much higher consumption. It thus indicates a cross-flow (0.8 m/s) of Reynolds number about 3573 as an optimal cross-flow regime.

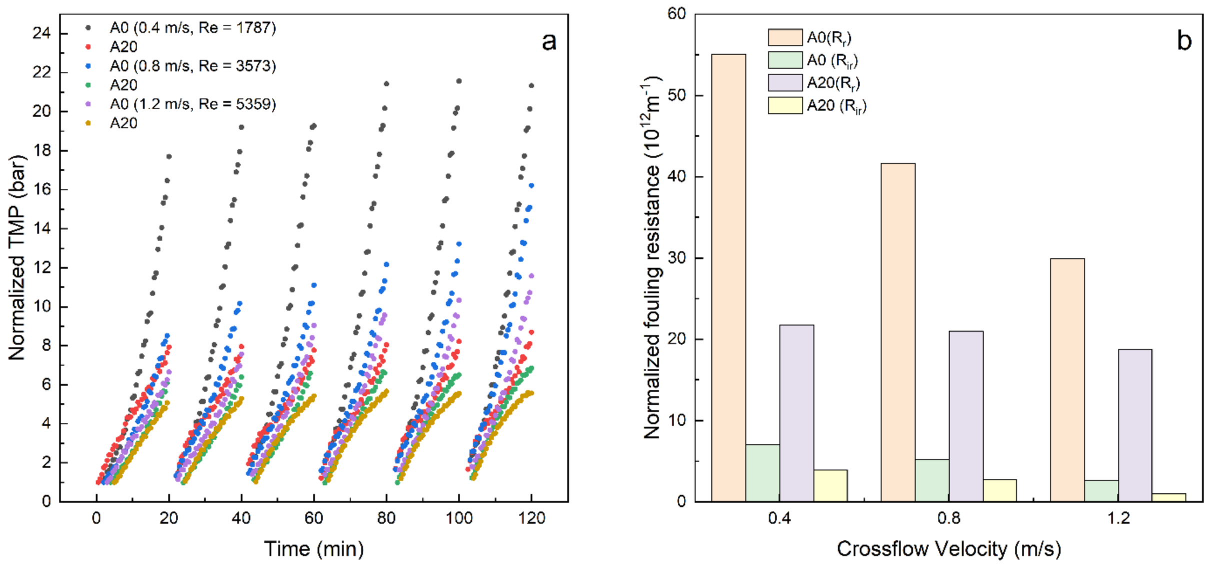

Fig. 4.5. The normalized (a) fouling curve and (b) resistance of the A0 and A20 membranes for the filtration of PW B at the CFVs of 0.4, 0.8, and 1.2 m/s at 50 L m^{-2} h^{-1}.

4.3.5. Effects of membrane pore size on membrane fouling

At the constant pressure filtration mode, Liu et al. reported that MF membranes with larger pore sizes are more susceptible to membrane fouling compared to UF membranes when filtering the PW [261]. However, in the present study, the UF membrane (A0, A20) showed higher fouling tendencies compared with the MF membrane (A0-600, A20-600), as shown in Fig.4.6a. The observed, initial sharp permeance decline can be explained by adsorption and deposition of foulants smaller than the membrane pore sizes into these pores, followed by a slow and steady permeance decline due to the progressive cake layer formation on the membrane surface [183]. As can be observed, the cake layer only partly covered the A0-600 membrane surface at the end of the filtration cycle (Fig.4.7a). In addition, it can be observed that the cake layer surface was rough (Fig.4.7b), with a thickness of 1.5 μm, and the sandwich structure of the cross section of the membrane is visible, with the three layers representing the porous cake layer, pore blockage, and open pores (Fig.4.7c and d). Finally, it can be observed that oil rejection increased as membrane pore sizes decreased (Fig. S4.9c), and the A0 (41 nm) and A20 membrane (35 nm) achieved oil removal efficiencies of 99.5 ± 0.3 % and 99.7 ± 0.2 %, respectively (Fig.S4.9c).

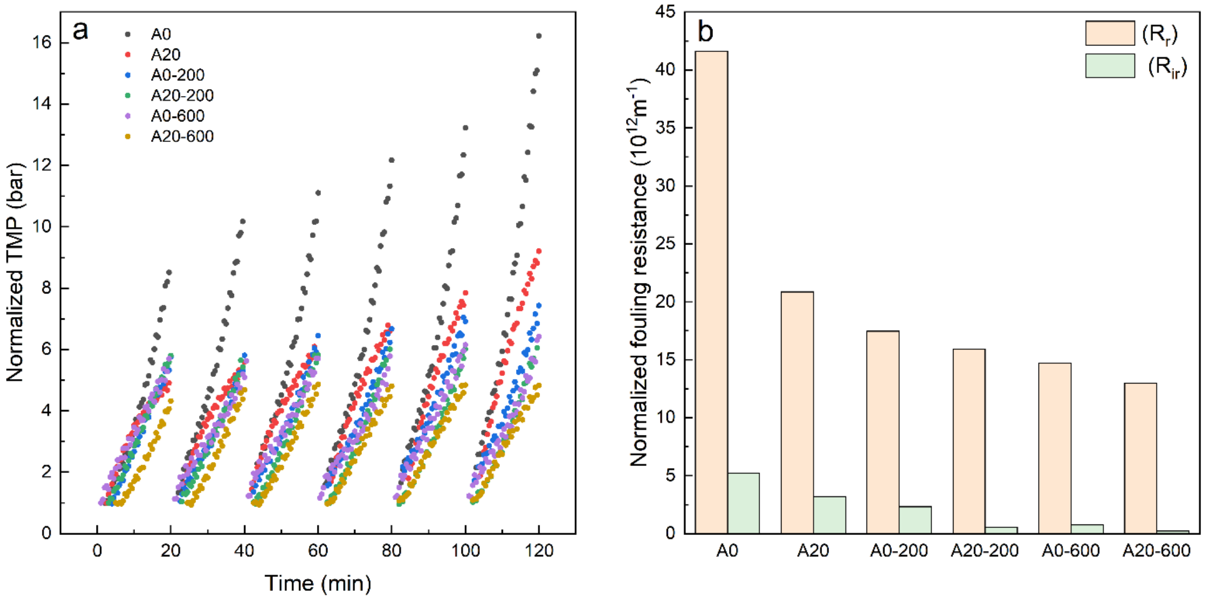

Fig. 4.6. The normalized (a) fouling curve and (b) resistance of the Al_2O_3 membranes (A0, A0-200, A0-600) and the SiC-coated membranes (A20, A20-200, A20-600) for the filtration of PW B at 40 L m^{-2} h^{-1} with the CFV of 0.8 m/s.

The A20-600 (139 nm) and A0-600 (181 nm) membranes showed the lowest oil rejection percentages, being 98.2 ± 0.2 % and 97.6 ± 0.3 %, respectively (Fig. S4.9c). This can be explained by the oil droplets forming a cake layer on the membrane surface, which effectively helps reject small-sized oil droplets. The formation of the cake layer was assessed by measuring the oil rejection at the following time intervals: 0 to 3, 3 to 6, and 6 to 20 minutes in the initial experiment cycle. The results (Fig. S4.11) indicated a slight increase in oil rejection from 94.3 ± 0.5 % to 98.4 ± 0.3 % for the A0-600 membrane in the initial cycle, which verified the cake layer formation. The significant proportion of external fouling, which accounts for 95.2 % of the total fouling resistance (Fig.), confirmed that cake filtration was the dominant fouling mechanism, and the fouling alleviation was enhanced by increasing pore size. A similar trend was noted in the A20-200, A0-600, and A20-600 membranes. The particle size of the particles in the permeate was close to the average pore size of the membranes, as shown in Table.S4.3, indicating the size exclusion played a critical role in rejecting particles in the feed. Additionally, there was a reduction in irreversible fouling with increasing pore sizes since, at larger pore sizes, a lower TMP led to less deformation of the oil droplets, so they were not pressed into the pores. Given the fouling resistance and the excellent oil rejection with 99.4 ± 0.3 % (PW B) after cake layer formation, the A20-200 membrane was an optimal choice for separating the PW B. However, for PW A with a smaller size distribution at 11.7 % of the size below 80 nm (Fig.4.2), the oil rejection for the A20, A20-200, and A20-600 membranes was 99.1 ± 0.4%, 96.9 ± 0.5%, and 89.6 ± 1.5% (Fig.S4.10 and Fig.S4.12). The A20 membrane is therefore a promising choice. These findings indicated that choosing membranes with appropriate pore sizes should be prioritized over a high initial permanence to achieve low fouling tendency and considerable separation efficiency.

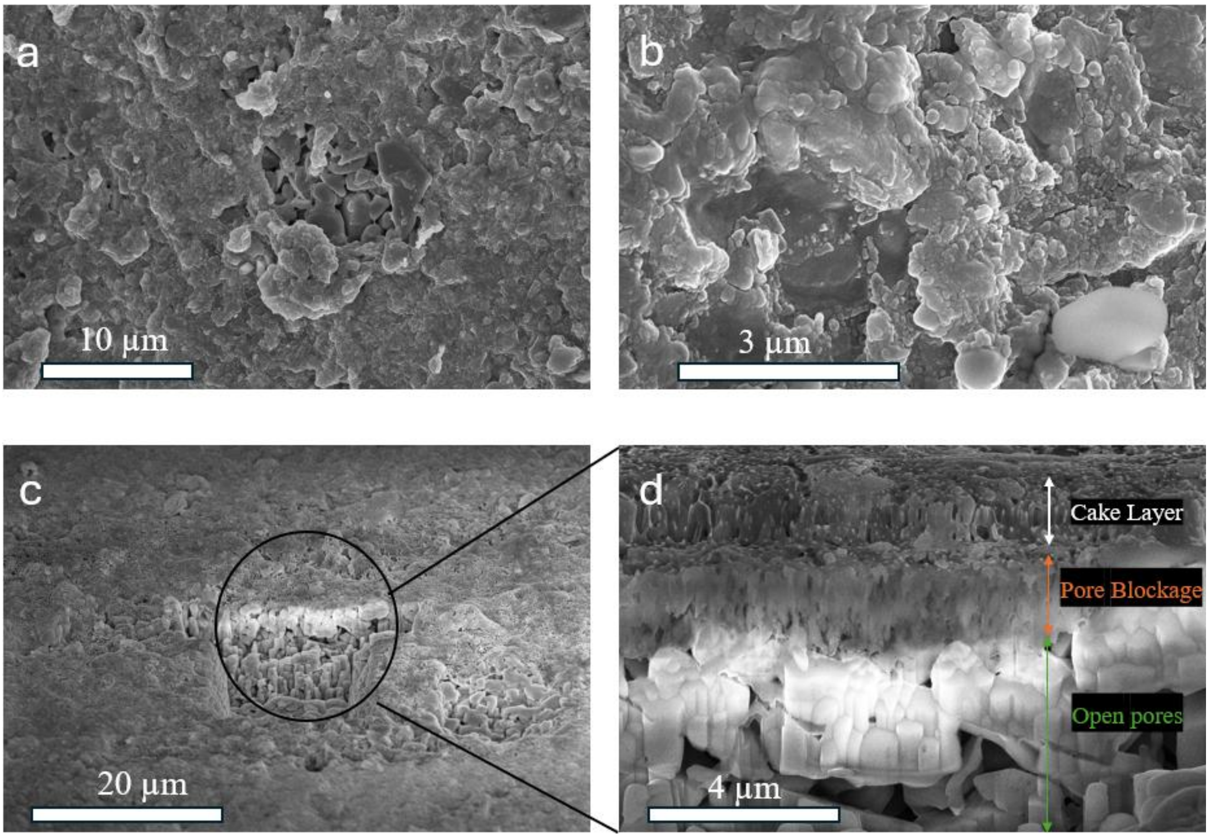

Fig. 4.7. Top view SEM images of fouled A0-600 membrane with a scale bar of (a) 10 μm and (b) 3 μm. The cross-section FIB-SEM image of A0-600 membrane with a scale bar of (c) 20 μm and (b) 4 μm.

4.3.6.Characterization of the fouling layer

SEM analysis was performed on the virgin and fouled A0 and A20 membranes to characterize the chemical components and structures of organic components in the cake layers. The top-view surface image of the virgin A0 and A20 membranes shows a porous structure (Fig.4.8a and c). In addition, the FIB-SEM images show that, after a filtration time of 3 minutes, a cake layer was not formed on the surface of the A0 membrane, and the thickness of the pore blockage area was only 1 μm (Fig.4.8 e-h). However, as depicted in Fig.4.8 h, a cake layer with a thickness of 4 ± 1 μm was formed on the A0 membrane with 3-5 μm pore blockage depth after a filtration time of 20 minutes because the fouling layer was compressed by the permeate drag force and hydraulic pressure [262], indicating the severe fouling induced by the foulants. This fouling layer was confirmed by the EDAX line scan of element C for the cross section of the A0 membrane (Fig.S4.13). During the vacuuming stage of the SEM sample preparation, the loss of volatile component resulted in the visualization of a fouling layer being composed of colloidal (e.g. the heavier hydrocarbons existing in crude oil [263]), KCl/NaCl crystals and non-volatile organic foulants, as indicated by the EDAX analysis of the foulant layer (Fig.S4.14) and ions in the feed water (Table.S4.4), since, amongst others, the elements C, O, Fe, Na, Mg, Al, Si, Cl, K, and Ca, were found in the foulant layer. According to the EDAX analysis, organic compounds (23.61%) were predominant (Fig. S4.14). Meanwhile, the A20 membrane exhibited moderate fouling, characterized by a loosely attached porous cake layer covering its surface after a filtration time of 20 minutes (Fig.4.8k). These observations confirmed that pristine Al_2O_3 membranes were more susceptible to fouling. The PW is alkaline (pH = 8.4), causing inorganic salts to precipitate and resulting in membrane fouling [264]. The results of the element mapping also showed that K and Cl had a similar distribution, probably due to the formation of the KCl crystals in the dried membrane samples (Fig.S4.15). The membrane surface of both A0, and A20 membranes after backwash was clean, and fouling was not observed (Fig. S4.16). The support layer of the A0 membrane also remained clean without observable foulants (Fig. S4.17), which confirms that the oil droplets probably did not deform and pass through the membrane pores in the condition that TMP is smaller than the critical pressure [265]. As shown in Fig. S4.18, the microporous structure and the internal fouling of the A0 membrane in the top of the separation layer were not visible in the FE-SEM images, due to limitations in the cutting techniques, which resulted in an uneven membrane cross-section. Further surface polishing was needed for visualization. Overall, the FIB-SEM images offer a clear visualization of the evolution of membrane fouling, allowing for a quantitative assessment, and comparing the fouling of the A0 and A20 membranes.

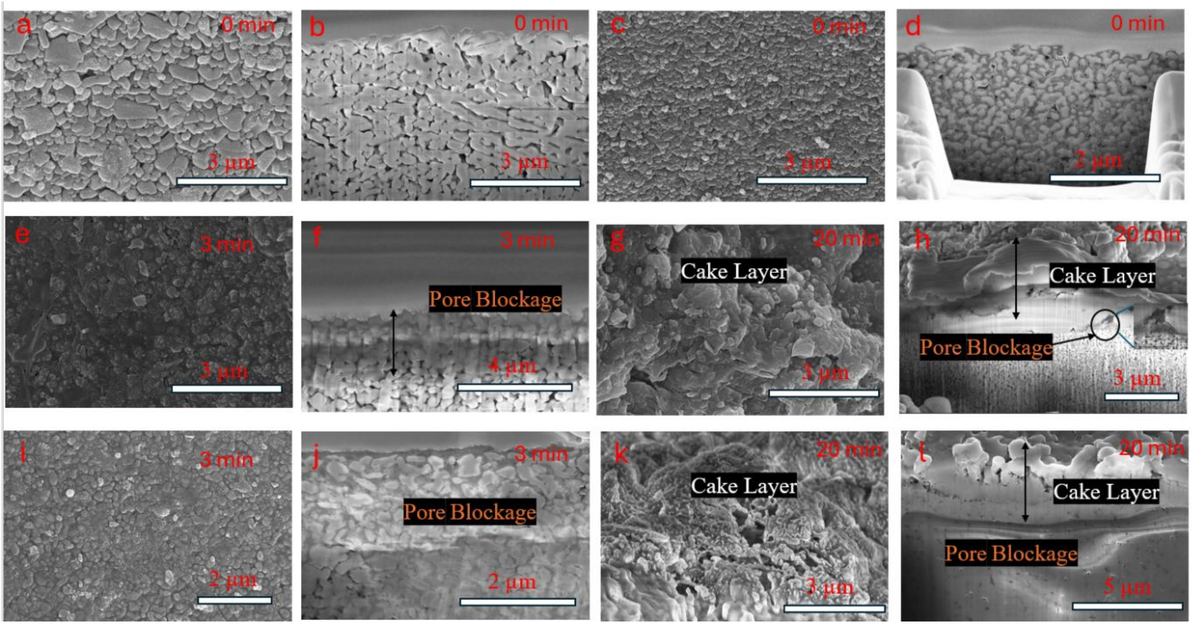

Fig. 4.8. (a) Top view SEM images and (b) cross-section FIB-SEM images of the clean A0 membrane. (c) Top view SEM images and (d) cross-section FIB-SEM images of the clean A20 membrane. (e) Top view SEM images and (f) cross-section FIB-SEM images of the fouled A0 membrane at the filtration time of 3 minutes. (g) Top view SEM images and (h) cross-section FIB-SEM images of the fouled A0 membrane at the filtration time of 20 minutes. (i) Top view SEM images and (j) cross-section FIB-SEM images of the fouled A20 membrane at the filtration time of 3 minutes. (k) Top view SEM images and (l) cross-section FIB-SEM images of the fouled A20 membrane at the filtration time of 20 minutes.

4.3.7. Comparison of membrane fouling with two types of oily wastewater

The threshold flux of the A0 and A20 was 41 $Lm^{-2}h^{-1}$ and 48 $Lm^{-2}h^{-1}$, respectively, for the filtration of PW A (Fig.S4.19), which was higher than when filtering PW B. Fig. 4.9 shows that with a higher salinity and COD (PW B), compared with PW A, a higher (ir) reversible fouling can be observed for both the A0 and A20 membranes. A dense and compact cake layer was probably formed when filtering PW B due to the electrostatic shielding effect [266]. In addition, the decreased electrostatic repulsion between the foulants and membrane surface reduced the distance between the droplets, and promoting coalescence of the droplets [206]. However, the A20 membrane still exhibited a lower (ir)reversible fouling compared to the A0 membrane.

The oil rejection of PW A (99.3 ± 1.1 %) was a little lower than the oil rejection of PW B (99.6 ± 0.5 %), probably due to the smaller oil droplet sizes, see Fig. . The COD oil rejection of the PW A by the A0 and A20 membranes was 78.9 ± 2.7 % and 76.4 ± 1.6 %, respectively, which is also lower than the oil rejection PW B, with 81.7 ± 1.1 % for the A20 membrane and 78.7 ±

1.3% for the A0 membrane, respectively (Fig.S4.20 and Fig.S4.21). The TSS concentration is below 8 mg/L in both the permeate of the A0 and A20 membranes for PW A and PW B, showing a rejection over 99% (Table S4.5).

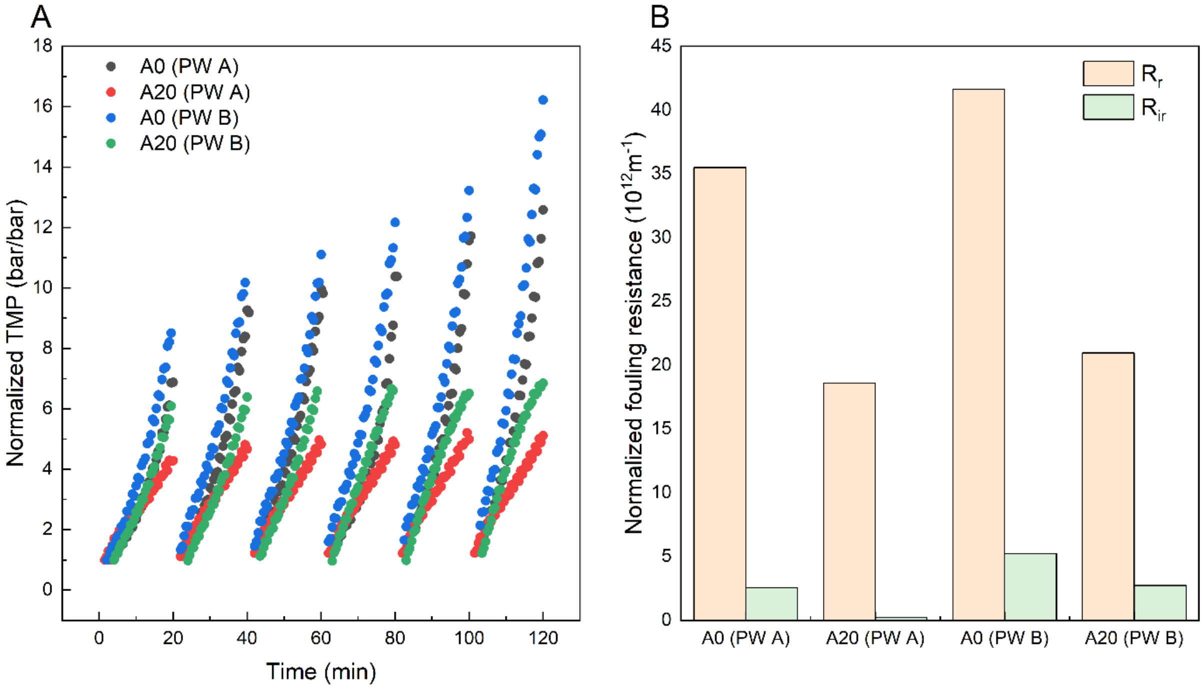

Fig. 4.9. The normalized (a) fouling curve and (b) resistance of the A0 membranes and the A20 membranes for the filtration of the PW A and the PW B at 50 L m^{-2} h^{-1} with the CFV of 0.8 m/s.

4.3.8. Long-term filtration performance

Fig.4.10 shows that direct ceramic UF of PW using the A20 membranes allowed for a continuous long-term operation of 24 hours (72 cycles), under a flux of 40 $Lm^{-2}h^{-1}$ and a CFV of 1.2 m/s. The reversible fouling was dominant and could be easily cleaned by physical cleaning (e.g., backwash). Typically, direct ceramic UF needs regular physical actions such as backwashing combined with chemical cleaning. After immersing the A20 membrane in 0.1 M sodium hydroxide and 0.1 M citric acid for 1 h, respectively, the irreversible fouling was effectively removed, and the permeability of the A20 membrane was recovered to 98.2 ± 0.4%.

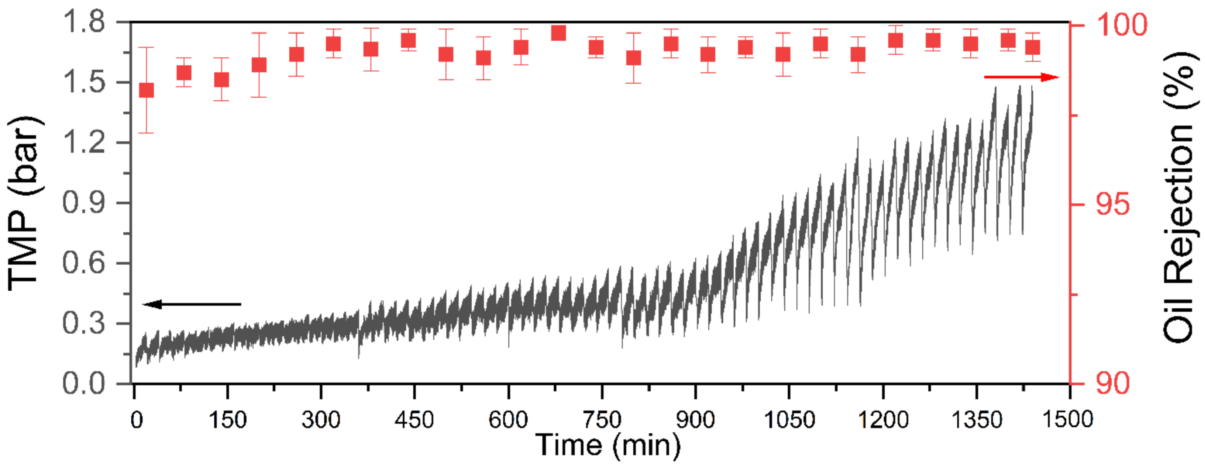

Fig. 4.10. The fouling curve of the A20 membranes for 24 hours during the filtration of the PW B at the flux of 40 $Lm^{-2}h^{-1}$ with the CFV of 1.2 m/s.

4.3.9. Comparison of the ceramic MF/UF membrane for PW treatment

Table 4.2 summarizes various hydrophilic ceramic membranes used for PW treatment, highlighting their pore size, filtration mode, and oil rejection performance. The SiC-deposited membranes fabricated in this study exhibit smaller pore sizes and demonstrate effective oil removal at various salinity and COD levels compared to ceramic UF/MF membranes. Moreover, to the authors' knowledge, this study is the first to apply SiC membranes in constant flux mode for PW treatment, utilizing the smallest pore size (35 nm) reported among SiC membrane [247, 267].

Table 4.2. Comparison of the ceramic membrane-based PW treatment technologies.

Material	Pore size (nm)	Filtration mode	Oil rejection (%)	Ref
ZrO_2	1000	Constant pressure (2 bar)	>97.22	[268]
ZrO_2-TiO_2	5	Constant pressure (1.4 bar)	>99.9	[269]
ZrO_2	78	Constant pressure (1 bar)	98.8	[3]
Al_2O_3	200	Constant pressure (2.5 bar)	99	[270]
TiO_2	50	Constant pressure (0.4 bar)	80	[247, 267]
SiC	500	Constant pressure (0.4 bar)	73	[247, 267]
SiC-deposited	139	Constant flux (40 $Lm^{-2}h^{-1}$)	97.6	This work
SiC-deposited	62	Constant flux (40 $Lm^{-2}h^{-1}$)	98.2	This work
SiC-deposited	35	Constant flux (40 $Lm^{-2}h^{-1}$)	99.7	This work

4.3.10. Discussion

This study demonstrates the feasibility of using FIB-SEM to directly visualize reversible and irreversible fouling of ceramic membranes. However, standardization of this technique remains challenging, as results may vary with equipment, operator handling, and region selection. To enhance reproducibility and achieve more quantitative insights, future work could combine FIB-SEM imaging with advanced image collection and processing techniques [83]. For example, machine learning–based image recognition can be employed to systematically measure cake layer thickness and pore blockage depth, thereby reducing operator bias and improving reproducibility. In addition, automated image analysis, statistical sampling of multiple regions, and cross-validation with complementary techniques (e.g., OCT, X-ray tomography) will help establish more quantitative and standardized use of FIB-SEM in membrane fouling studies.

The reuse requirements for treated produced water depend strongly on the targeted application. For example, PW is commonly reinjected to the well to maintain the hydraulic pressure within the well, for this purpose, standards typically require oil & grease < 30 mg/L, turbidity < 5 NTU, and TSS < 5 mg/L [271, 272]. However, this practice is environmentally controversial since the injected treated PW can migrate unto freshwater aquifers, leading to the groundwater contamination [273]. As an alternative, Echchelh et al. reported that treated PW can be reused in irrigating halotolerant crops [274]. Moreover, blending raw PW with desalinated water at ratios between 2:1 and 1:4 can help mitigate long-term soil salinization [274]. Nonetheless, most crops are non-halotolerant and therefore cannot tolerate high salinity. For these crops, additional water quality requirements must be met, such as pH between 6.5 and 8.4, chloride < 70 mg/L, and nitrate < 10 mg/L [275]. The ceramic membranes investigated in this study effectively reduced oil & grease and suspended solids, enabling compliance with reinjection standards and halotolerant crop irrigation requirements. However, because MF/UF SiC membranes do not remove dissolved salts, additional treatment processes (e.g., nanofiltration, reverse osmosis, or softening) are necessary for safe irrigation of non-halotolerant crops. These findings therefore highlight the role of ceramic membranes as a robust pretreatment step, while emphasizing the need for further polishing depending on the intended end-use.

4.4. Conclusion

Al_2O_3 and SiC-coated membranes with different pore sizes to treat both synthetic and real oilfield produced waters (PWs) were studied in a constant flux mode. The SiC-coated membrane was successfully operated for one day, only by backwashing the membrane every 20 minutes, confirming the validity of direct ceramic UF of PW with SiC-coated membranes. In addition, the SiC-coated membrane showed high efficacy in removing organic compounds (>80%) and inorganic particles (>99%) with a lower (ir)reversible fouling, compared with Al_2O_3 membranes, induced by size exclusion and electrostatic repulsion, and less adsorption. The permeate with over 99 % oil removal was feasible even after 72 manual cycles (24 hours) and met the standards for reinjection or reuse in future desalination processes. The fouling mechanisms in SiC-coated and Al_2O_3 membranes were also analyzed with the help of FIB-SEM imaging, concluding that pore blockage was the initial fouling mechanism, and (reversible) cake layer fouling dominated the rest of the filtration cycle for both the SiC-coated and the Al_2O_3 membranes. Finally, it was concluded that employing the SiC coating and selecting the appropriate pore size (62 nm A0-200), and CFV (0.8 m/s) based on the properties of the PW is beneficial for fouling mitigation, potentially advancing the utilization of UF in treating PW for reuse purposes.

Supplementary information

Text S4.1. Synthetic O/W emulsions preparation

Mineral oil (330779, Sigma-Aldrich, the Netherlands), sodium dodecyl sulfate (SDS, 75746, Sigma-Aldrich, the Netherlands), calcium chloride (≥ 96%, 383147, Sigma-Aldrich, the Netherlands) and sodium chloride (≥ 99%, S9888, Sigma-Aldrich, the Netherlands), were used for the preparation of the synthetic O/W emulsions. SDS-stabilized O/W emulsions were prepared for membrane filtration experiments to investigate the impact of the salinity on membrane fouling. To obtain 500 mg/L SDS stabilized O/W emulsion, 2 g mineral oil, and 0.2g SDS with a mass ratio of 10:1 were added into 1L Demineralization (DI) water. The mixture was then subjected to continuous high-speed stirring at 3000 rpm using a magnetic stirrer (L32, LABINCO, the Netherlands) for one day, followed by ultrasonication in a sonifier (3800, Branson, USA) for half a day, following the procedures outlined in previous studies [89, 164, 165].

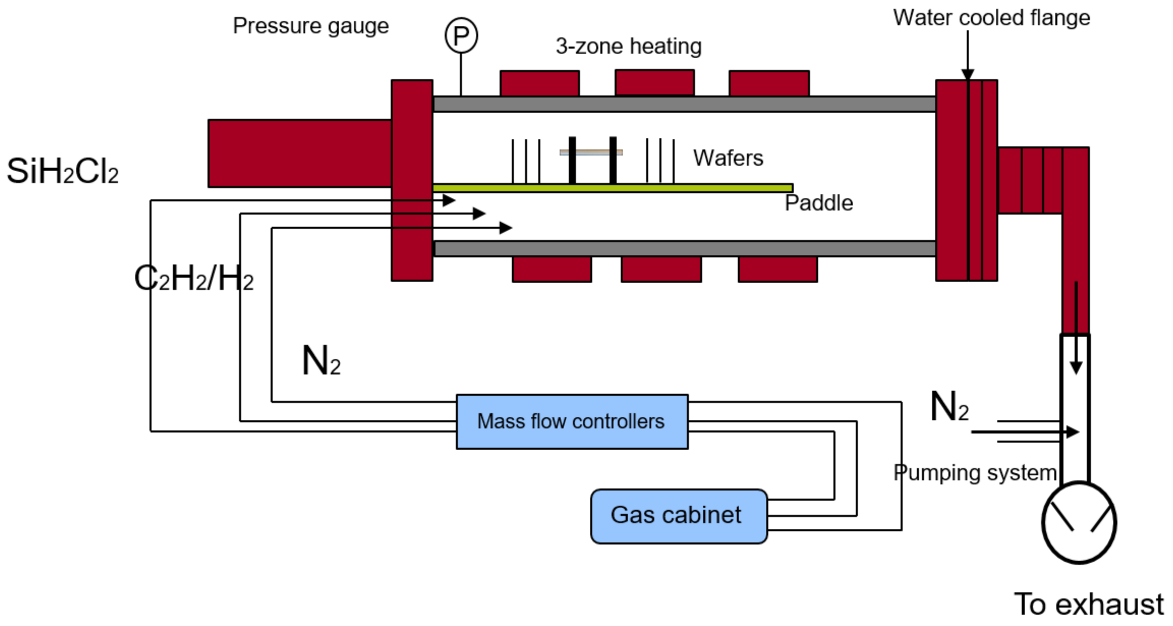

Fig. S4.1. Schematic illustration of LPCVD system.

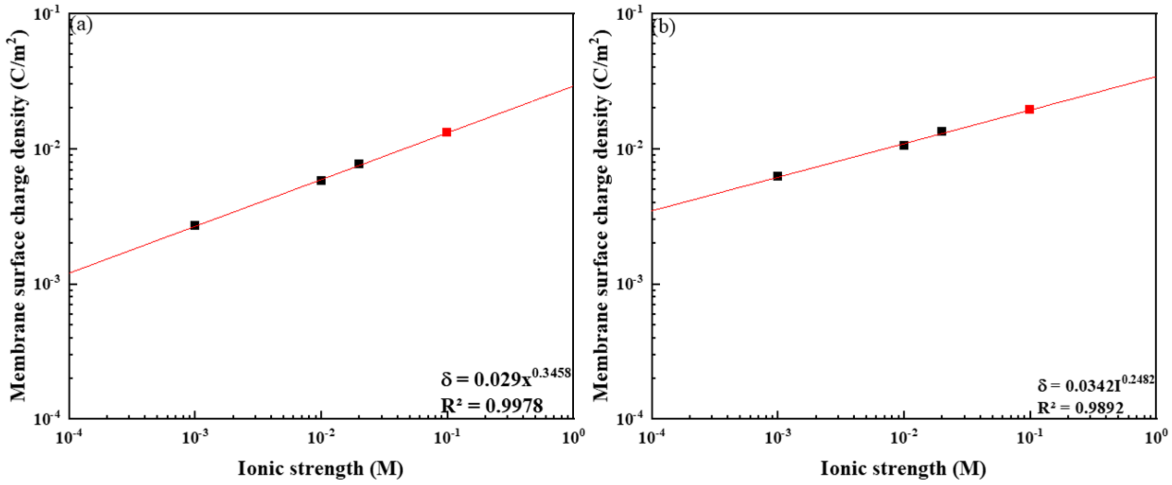

Fig. S4.2. The membrane surface charge density at 100 mM salinity was estimated using the Freundlich ion adsorption model for (a) the A0 membrane and (b) the A20 membrane with 50 mg/L SDS solution.

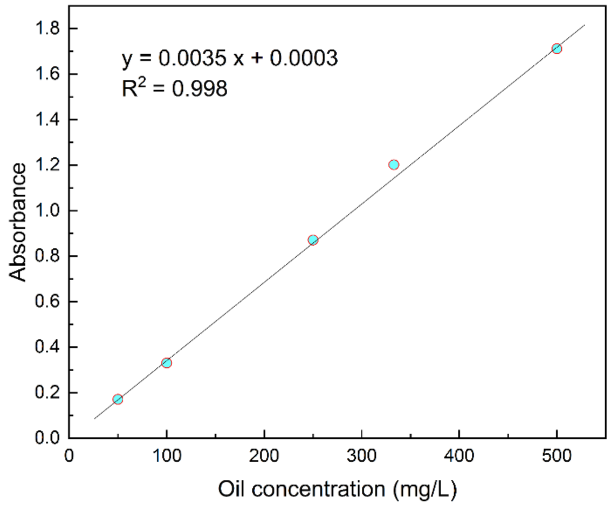

Fig. S4.3. Linear relationship of mineral oil concentration with UV-vis absorbance.

The oil concentration of both the feed and permeate was measured by a UV/Vis spectrophotometer (GENESYS 10S UV-Vis, Thermo scientifical, US) at 275 nm [128], while the chemical oxygen demand (COD) of the samples was measured by a Hach spectrophotometer (DR 3900, US) with COD cuvettes (LCK 314 and LCK 514, Hach) [192]. The feed was diluted to make a calibration line, as shown in Fig. S7, with a regression coefficient higher than 0.999.

The soybean oil and COD rejection of the membranes were calculated by Eq. (1):

$$R = (1 - \frac{C_p}{C_f}) * 100\% \tag{1}$$

where R is the rejection, C_p is the oil (mgL^{-1}) or COD concentration (mgL^{-1}) in the permeate, and C_f is the oil (mgL^{-1}) or COD concentration (mgL^{-1}) in the feed.

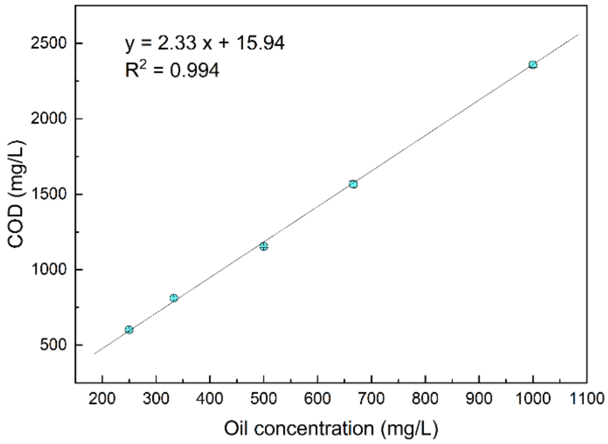

Fig. S4.4. Linear relationship of mineral oil concentration with COD.

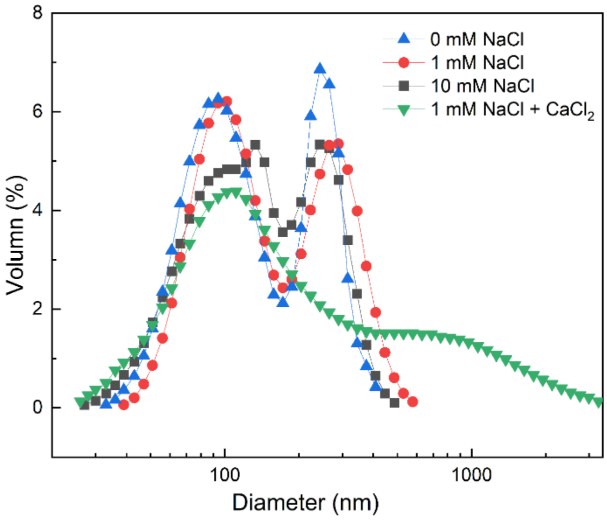

Fig. S4.5. The particle size distribution of the O/W emulsions with different salinities.

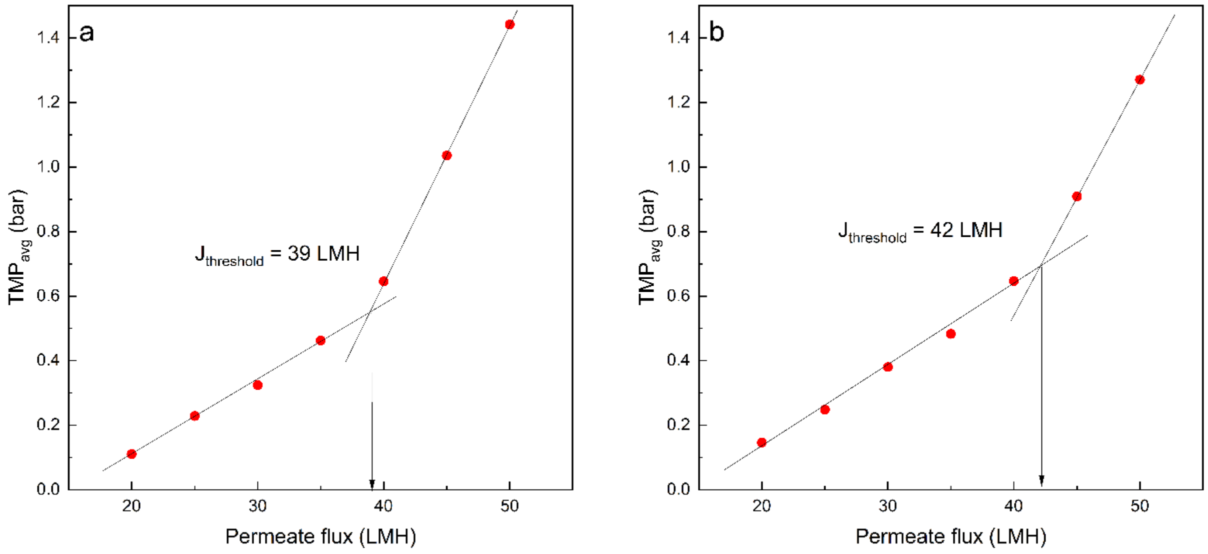

Fig. S4.6. Threshold flux for the A0 and the A20 membrane during the filtration of the PW B.

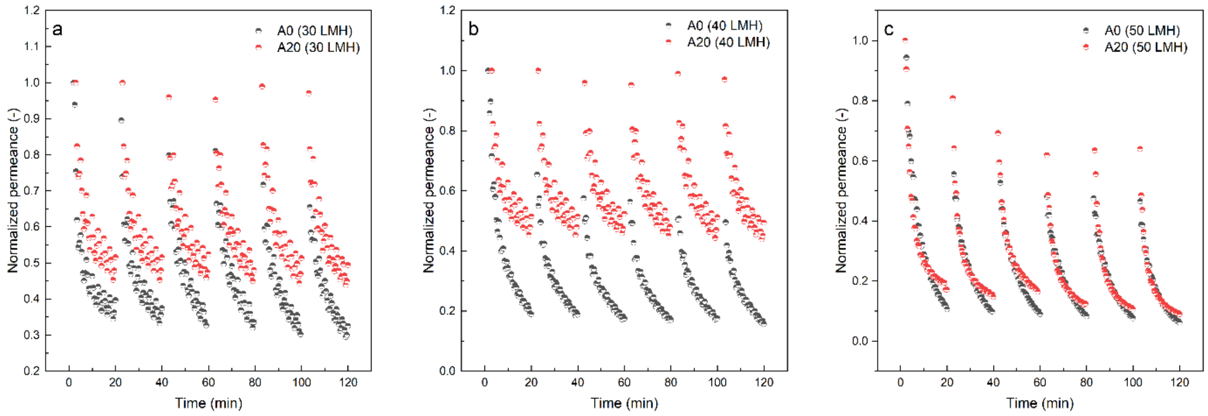

Fig. S4.7. The normalized permeance of the A0 and A20 membranes for the filtration of PW B at the flux of (a) 30, (b) 40, and (c) 50 L m^{-2} h^{-1} with a crossflow velocity of 0.8 m/s.

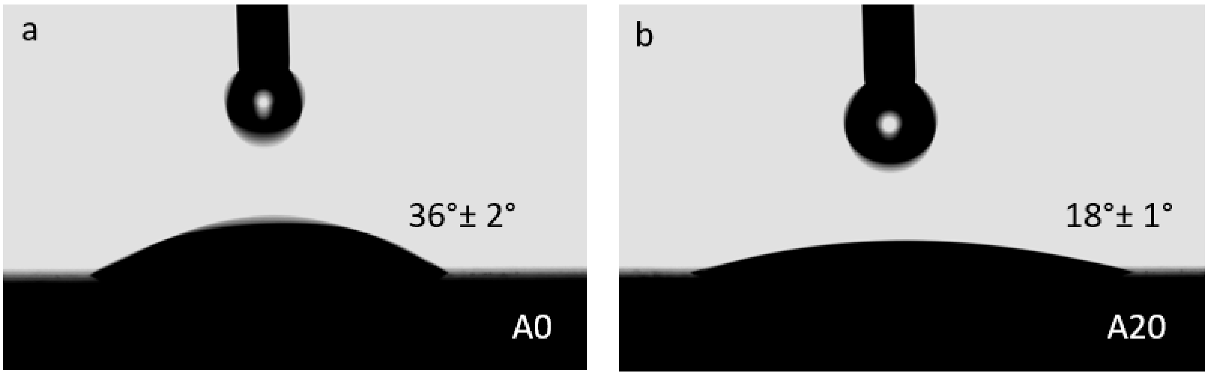

Fig. S4.8. Water contact angle of the (a) A0 membrane and the (b) A20 membrane.

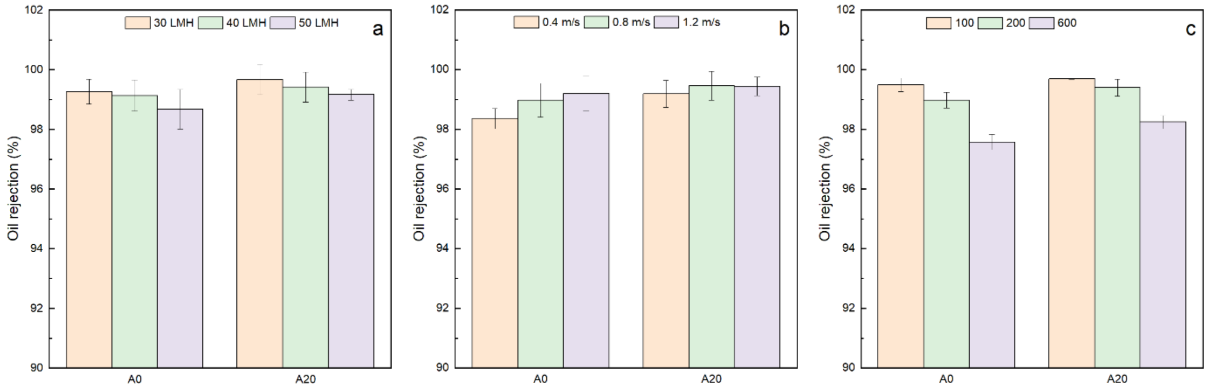

Fig. S4.9. The oil rejection of alumina (A0) and SiC-coated membranes (A20) for the PW B at various (a) flux, (b) crossflow velocities, and (c) pore sizes.

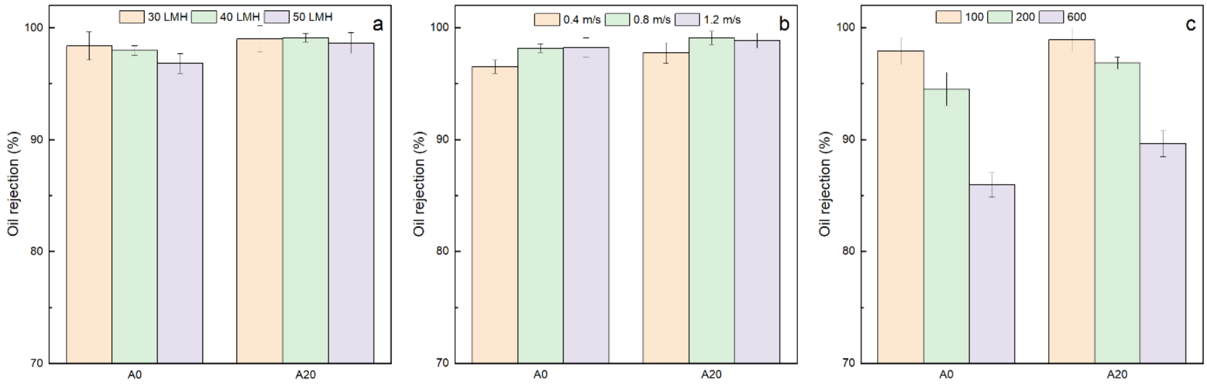

Fig. S4.10. The oil rejection of alumina (A0) and SiC-coated membranes (A20) for the PW A at various (a) flux, (b) crossflow velocities, and (c) pore sizes.

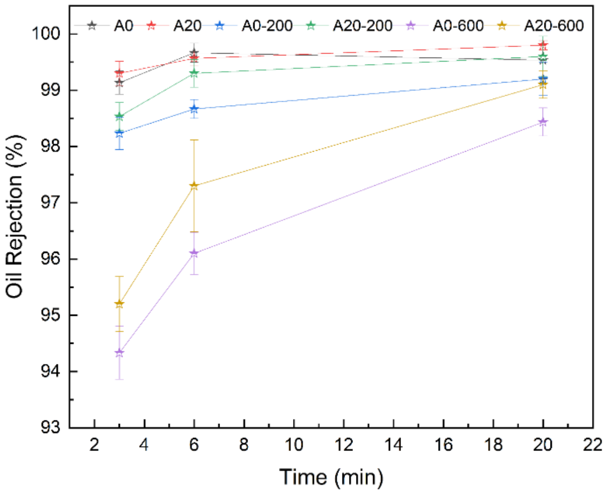

Fig. S4.11. The oil rejection of the alumina (A0, A0-200, A0-600) and SiC-coated membranes (A20, A20-200, A20-600) for the PW B at the filtration time of 3 min, 6 min, and 20 min.

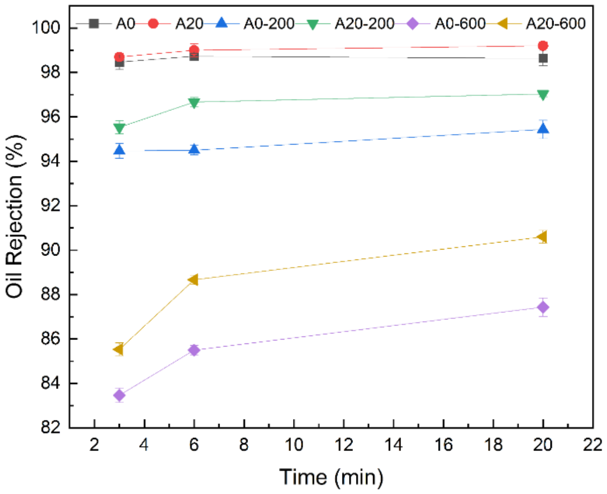

Fig. S4.12. The oil rejection of the alumina (A0, A0-200, A0-600) and SiC-coated membranes (A20, A20-200, A20-600) for the PW A at the filtration time of 3 min, 6 min, and 20 min.

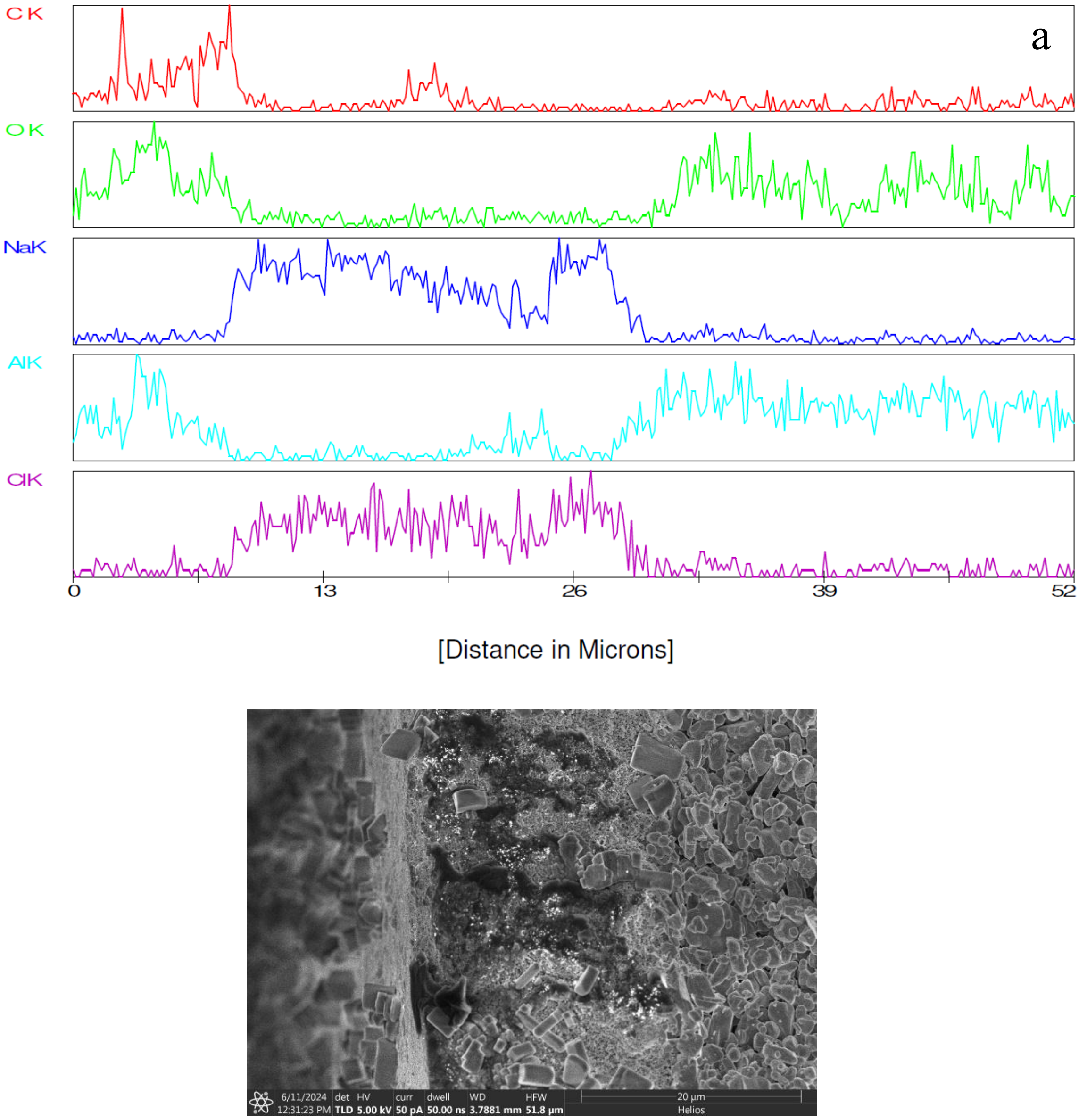

Fig. S4.13. (a) The EDAX line scan of the cross-section of the fouled A0 membrane and (b) the corresponding SEM image.

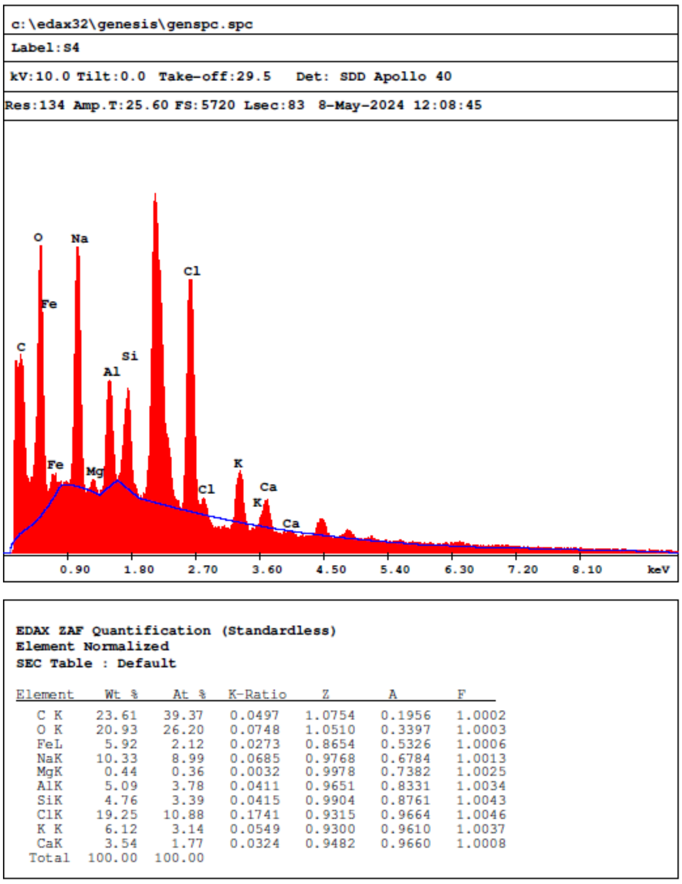

```
c:\edax32\genesis\genspc.spc
Label:S4
kV:10.0 Tilt:0.0  Take-off:29.5   Det: SDD Apollo 40
Res:134 Amp.T:25.60 FS:5720 Lsec:83  8-May-2024 12:08:45
```

```
EDAX ZAF Quantification (Standardless)
Element Normalized
SEC Table : Default

Element    Wt %     At %    K-Ratio     Z         A         F
   C K     23.61    39.37   0.0497    1.0754    0.1956    1.0002
   O K     20.93    26.20   0.0748    1.0510    0.3397    1.0003
   FeL      5.92     2.12   0.0273    0.8654    0.5326    1.0006
   NaK     10.33     8.99   0.0685    0.9768    0.6784    1.0013
   MgK      0.44     0.36   0.0032    0.9978    0.7382    1.0025
   AlK      5.09     3.78   0.0411    0.9651    0.8331    1.0034
   SiK      4.76     3.39   0.0415    0.9904    0.8761    1.0043
   ClK     19.25    10.88   0.1741    0.9315    0.9664    1.0046
   K K      6.12     3.14   0.0549    0.9300    0.9610    1.0037
   CaK      3.54     1.77   0.0324    0.9482    0.9660    1.0008
  Total   100.00   100.00
```

Fig. S4.14. EDAX analysis of the foulant layer.

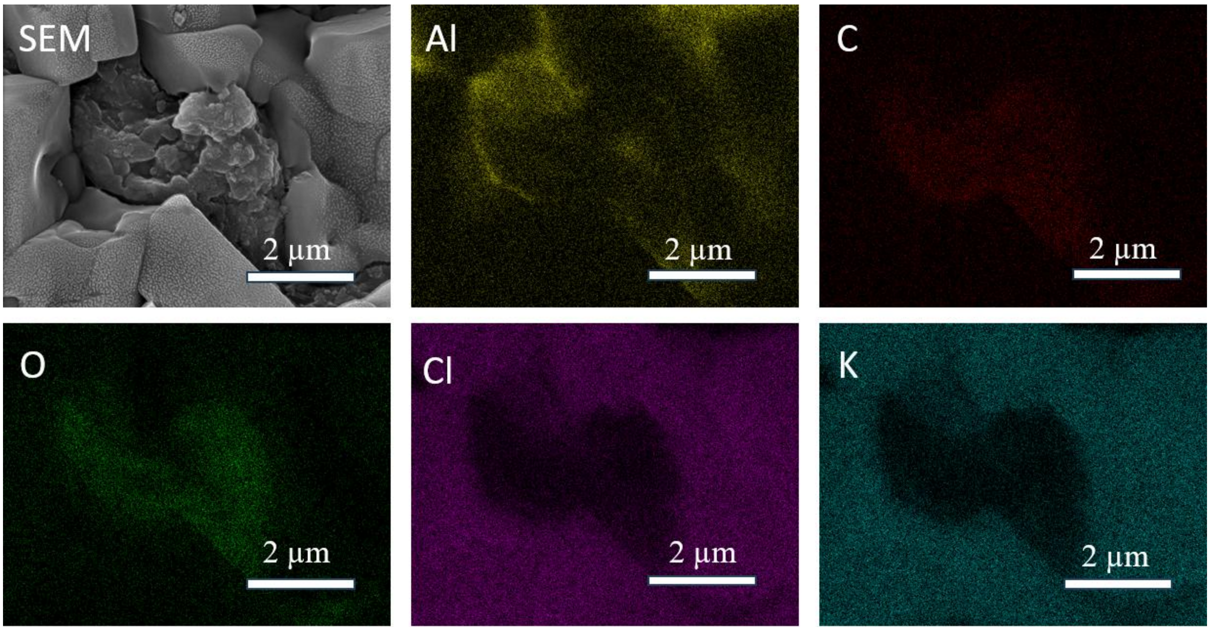

Fig. S4.15. Top-view EDS mapping result (element: Al, C, O, Cl, and K) of fouled A0 membrane. K and Cl showed similar distribution.

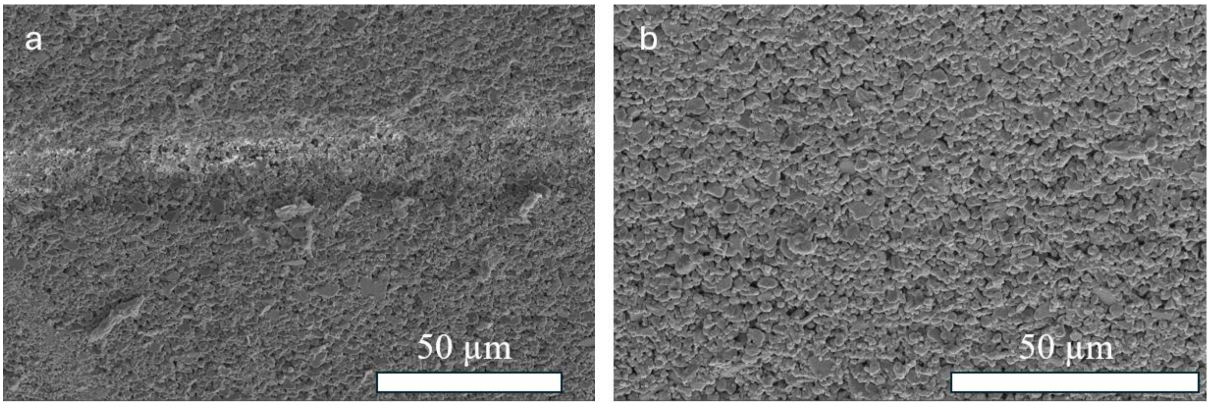

Fig. S4.16. The top view SEM image of the cleaned (a) A0 and (b) A20 membrane.

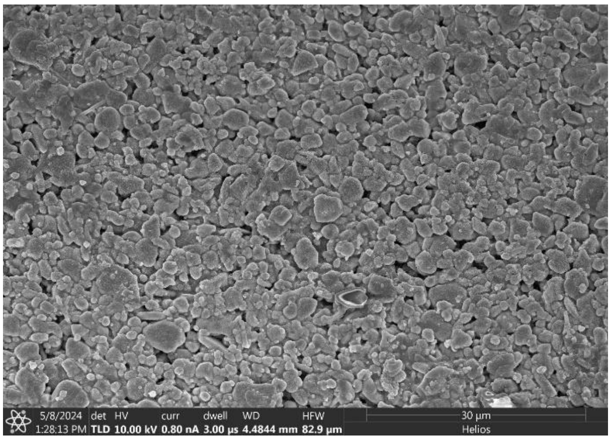

Fig. S4.17. After the one-cycle filtration experiments, the top view SEM image of the support 8layer of the A0 membrane.

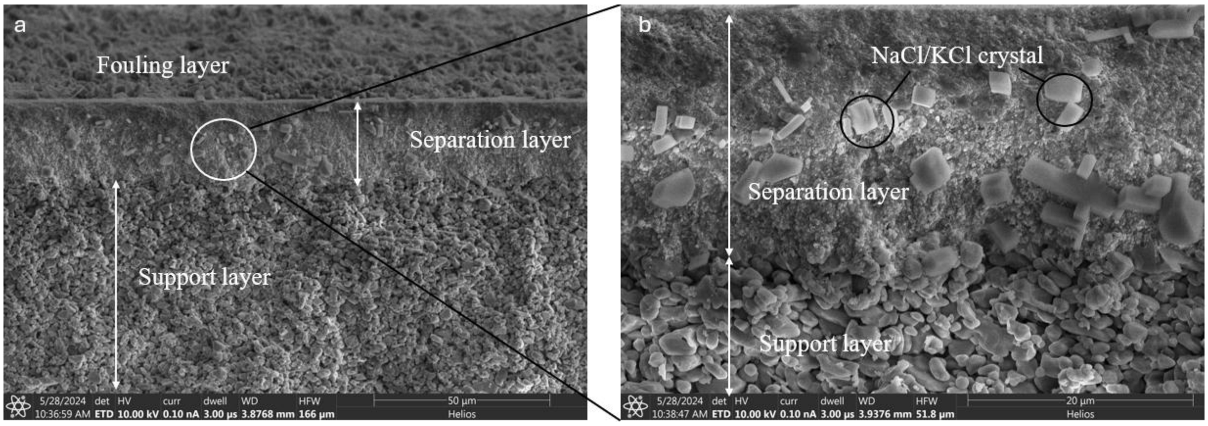

Fig. S4.18. FE-SEM images of the cross section of the A0 membrane.

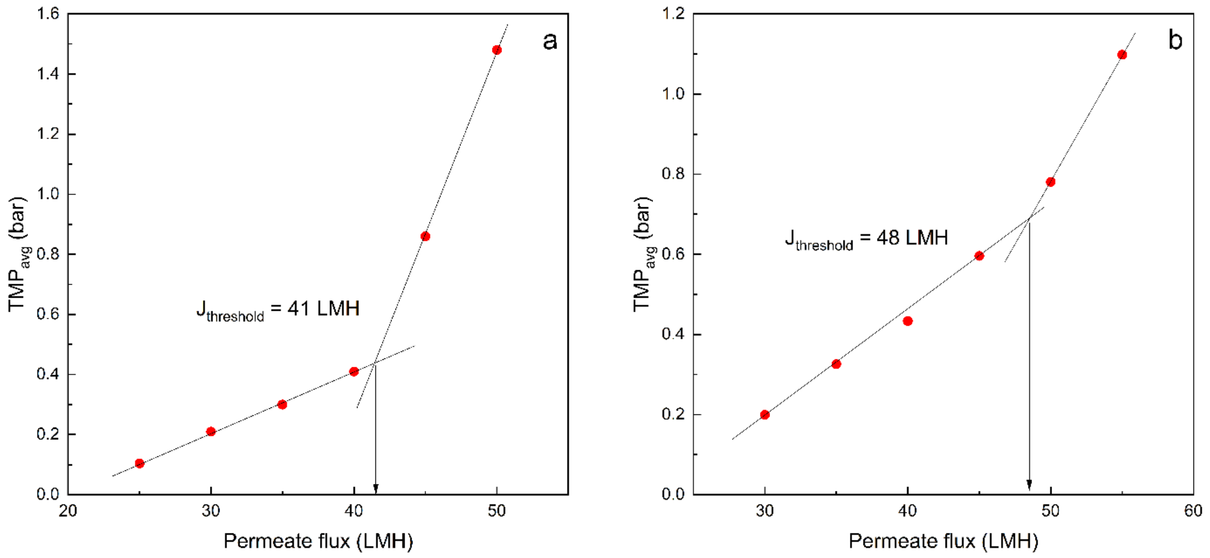

Fig. S4.19. Threshold flux for the A0 and the A20 membrane during the filtration of PW A.

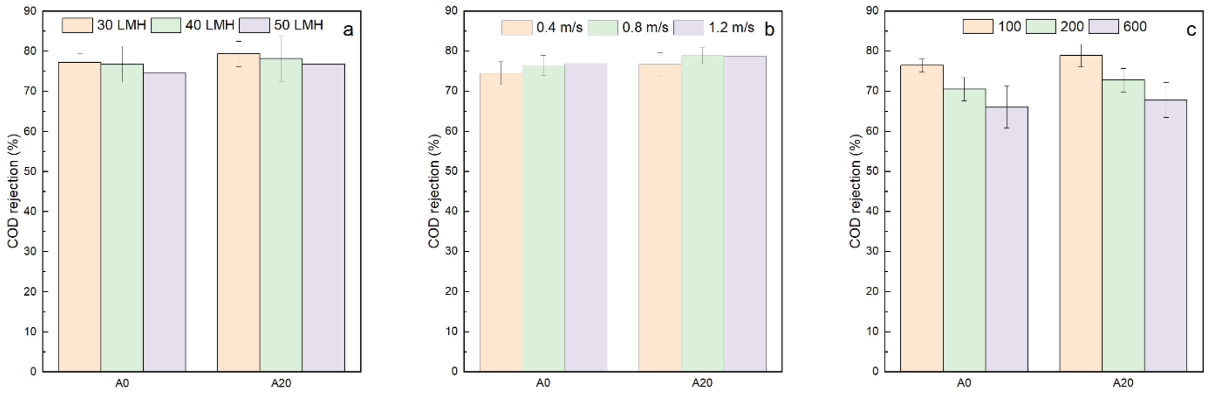

Fig. S4.20. The COD rejection of alumina (A0) and SiC-coated membranes (A20) for the PW A at various (a) flux, (b) crossflow velocities, and (c) pore sizes.

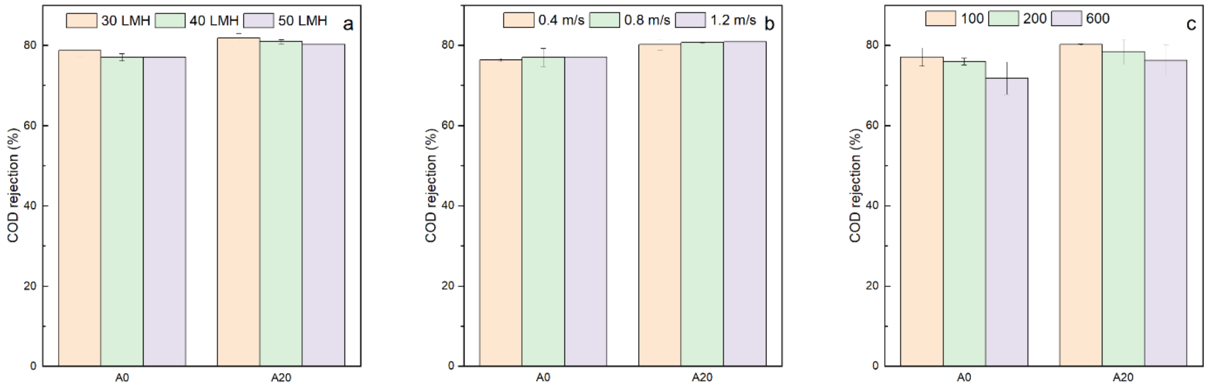

Fig. S4.21. The COD rejection of alumina (A0) and SiC-coated membranes (A20) for the PW B at various (a) flux, (b) crossflow velocities, and (c) pore sizes.

Table S4.1. Characteristics of O/W emulsions.

Emulsion	Oil concentration (mg/L)	SDS (mg/L)	NaCl (mM)	$CaCl_2$ (mM)	pH	Zeta potential (mV)	WCA (°)
1	500	50	0	0	5.6	-55.2±0.14	17° ± 0.8°
2	500	50	1	0	5.6	-50.7±0.64	27° ± 1.2°
3	500	50	10	0	5.6	-43.2±0.97	35° ± 0.7°
4	500	50	1	1	5.6	-38.8±0.51	38° ± 1.4°
5	500	50	100	0	5.6	-31.5±0.79	54° ± 2.6°

Table S4.2. Reynolds number at different cross-flow velocities for the ceramic membranes.

Cross-flow velocity ($m\cdot s^{-1}$)	**Reynolds number (Re)**	**Flow patterns**
0.4	1787	Laminar flow
0.6	2681	Laminar-turbulent transition
0.8	3573	Laminar-turbulent transition
1.0	4466	Turbulent flow
1.2	5359	Turbulent flow

Table S4.3. Permeate of the A0 and A20 membranes for PW B.

Sample name	Pore size (nm)	PSD of Permeate (nm)
A0	41	36
A20	35	33
A0-200	81	146
A20-200	62	134
A0-600	181	267
A20-600	139	170

Table S4.4. Ion concentration in the feed water (PW B).

Parameter	**PW B**	**LOQ**[a]	**MU**[b]
Hg (µg/L)	0.554	0.005	25%
As (µg/L)	7.4	0.2	30%
Pb (µg/L)	46	0.2	20%
Cd (µg/L)	0.15	0.01	25%
Cu (µg/L)	160	0.5	25%
Cr (µg/L)	87	0.5	25%
Ni (µg/L)	330	0.5	25%
Zn (µg/L)	520	2	25%
Al (µg/L)	6300	5	40%
Ba (µg/L)	180000	1	25%
Fe (µg/L)	36000	2	25%
Mg (mg/L)	380	0.1	25%
Mn (µg/L)	3500	0.2	25%
Mo (µg/L)	410	0.2	25%
Na (µg/L)	32000	0.1	45%
S (µg/L)	340	0.1	20%
Sn (µg/L)	2.3	0.1	25%
V (µg/L)	28	0.2	30%
Ca (mg/L)	2200	0.05	25%

[a] LOQ: Limit of quantification; [b] MU: Measurement uncertainty

Table S4.5. Characteristics of the permeate of the PW.

Parameters	**Permeate A0 (PWA)**	**Permeate A20 (PWA)**	**Permeate A0 (PWB)**	**Permeate A20 (PWB)**
Turbidity	7.7±3.0	7.5±2.6	2.9±0.6	2.3±0.4
pH	7.58±0.28	7.46±0.41	8.29±0.20	8.37±0.33
Conductivity (mS/cm)	48.1±2.1	48.6±1.7	141.4±3.1	140.7±4.5
COD (mg/L)	1997± 44	1713± 32	5219±124	4530±89
TDS (mg/L)	26367±685	20133±704	65950±265	55150±465
TSS (mg/L)	8±5	6±6	8±5	6±5

Chapter 5

Ceramic membrane filtration of natural and synthetic fibers in laundry wastewater

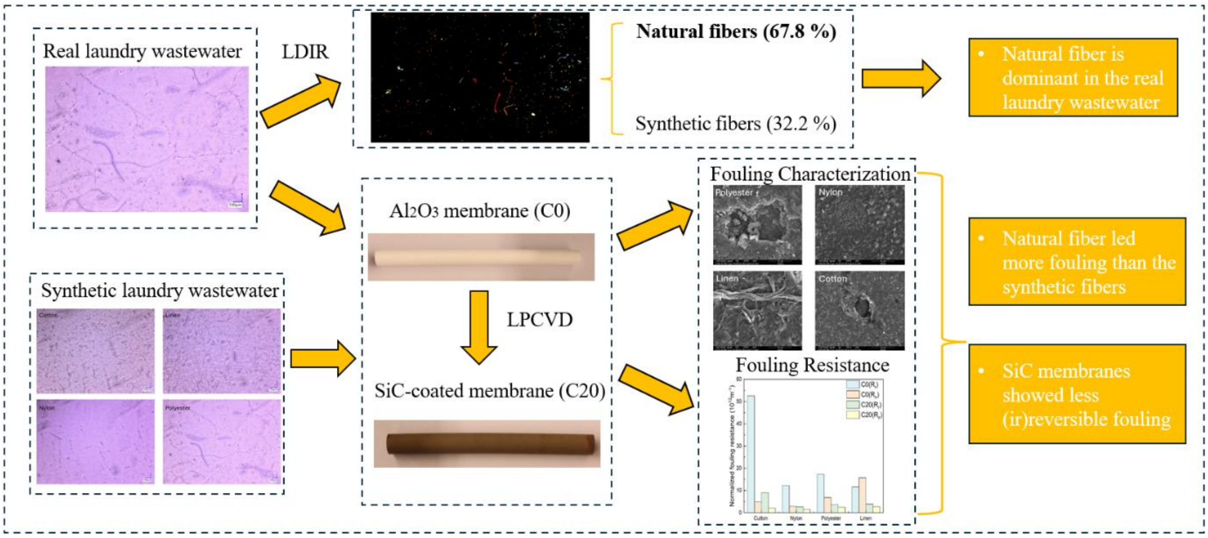

This chapter is based on:

Qin, G., Liu, Y., Rietveld, L. C., & Heijman, S. G. (2025). Ceramic membrane filtration of natural and synthetic fibers in laundry wastewater. *Under review by the Journal of Separation and purification technology.*

Abstract

The clothes washing industry generates large volumes of laundry wastewater that, in principle, can be well treated by ceramic membrane filtration. However, the fouling of ceramic membranes by fibres/fragments from laundry wastewater could result in a decrease of the water permeance across the membranes. In this study, synthetic wastewater containing cotton, linen, polyester, and nylon fibres and real wastewater were characterized and prepared for the filtration experiments, which were conducted at a flux of 70 $Lm^{-2}h^{-1}$ using an alumina (Al_2O_3) membrane and a silicon carbide (SiC)-coated Al_2O_3 membrane. Results revealed that natural fabrics, particularly cotton and linen, released higher chemical oxygen demand (COD) loads than synthetic fibers when tested at equal mass, which was further supported by microscopic and SEM imaging. Both the SiC-coated and Al_2O_3 ceramic membranes demonstrated a high fiber rejection (100%). However, the SiC-coated membrane exhibited a relatively lower reversible and irreversible fouling, attributed to its highly negatively charged surface, which repels the fibres that are negatively charged by negatively charged surfactants. The observed fouling among different fibers corresponded well with the COD levels of the synthetic laundry wastewater containing those fibers. Laser direct infrared imaging (LDIR) analysis confirmed that natural fibers dominate in real laundry wastewater. Finally, treatment of hot real laundry wastewater not only mitigates reversible and irreversible membrane fouling than when filtering cold synthetic wastewater. The filtration of hog laundry wastewater could facilitate the recovery and reuse of water, surfactants, and heat, offering a sustainable solution to reduce both water consumption and energy costs.

5.1. Introduction

Large flows of laundry wastewater are discharged during the washing of synthetic garments, releasing over five trillion plastic fragments on the ocean's surface [22]. Several authors have studied various treatment technologies to treat laundry wastewater including microfiltration (MF) [276], ultrafiltration (UF) [23], coagulation [277], and advanced oxidation [278]. Yang et al. reported that during the domestic washing of synthetic fabrics, submicrometric particles with sizes ranging from 100 to 600 nm are released [279], thus, UF have been considered to be the most promising approach for removing these submicrometric fibers, making it also an effective option for the reuse of the laundry wastewater [24].

However, fouling remains the primary challenge when using UF membranes for treating laundry wastewater [72]. Ceramic membranes offer several advantages over polymeric membranes, including a higher mechanical, thermal and chemical stability, as well as lower fouling tendencies [95, 209, 210]. These benefits make them particularly suitable for treating laundry wastewater in high-temperature and chemically harsh environments [23, 24]. The first study on the evolution of the ceramic membranes fouling for laundry wastewater treatment was done by the Kim et al., who reported that ceramic UF membranes have successfully been applied for both the synthetic and real laundry wastewater treatment [23]. Kim et al. also reported that ceramic membranes can be regarded as a potential alternative for the traditional microplastic filter for the treatment of the household washing wastewater[71]. The ceramic UF membrane was effective at removing suspended particulates in real laundry wastewater but less effective in rejecting organic matter [23]. A large amount of microplastic fibres was found in the laundry wastewater [280], having varying shapes, including fibres, films, foam, and granules [281, 282], and sizes from 0.1 µm to 2 mm [282].

Silicon carbide (SiC) and alumina (Al_2O_3) ceramic membranes are commercially available and widely used in wastewater treatment applications, standing out among other ceramic membranes [19, 43, 100, 209, 210]. Our previous studies showed that the SiC-coated Al_2O_3 membranes exhibited a lower reversible and irreversible fouling than the Al_2O_3 membrane for the filtration of oil-field produced water [204]. Hyeon et al. also found that SiC membranes are more effective than Al_2O_3 for laundry wastewater treatment because they have a higher negative zeta potential (-24.3 mV) compared to the Al_2O_3 membrane (-4.7 mV) at a pH of 6 [282]. Synthetic fabrics such as nylon and polyester, as well as natural fabrics, including cotton and linen, are commonly used materials in fabric production [66]. It has been reported that the natural fibers can make up 55% of the total fibers found in laundry wastewater and these fibers take 1 to 5 months to fully biodegrade in the natural environment [66, 67]. However, most studies have primarily focused on ceramic membrane fouling caused by filtering synthetic laundry wastewater containing synthetic fibers rather than the natural fibers [23, 71, 72]. To the best of our knowledge, ceramic membrane fouling caused by natural fiber has not been quantitatively analyzed yet. Therefore, in this study, fouling induced by fabric fibers, especially the natural fibers, using positively charged Al_2O_3 membranes and negatively charged SiC ceramic membranes is presented. Filtration experiments were carried out in a constant flux crossflow mode, using both synthetic and real laundry wastewater. The experiments were set up to evaluate how membrane properties, and laundry water characteristics, including temperature and fibric types, influence membrane fouling, thus, giving proper solutions for the mitigation of membrane fouling mitigation and promoting water reuse and heat recycle in laundry industry.

5.2. Materials and methods

5.2.1. Materials

Fabric materials made of 100% cotton, 100% nylon, 100% linen and 100% polyester were purchased from a local store and used to prepare the synthetic laundry wastewater. The anionic surfactant, sodium dedecyl benzene sulfonate (SDBS, powder, 289957-500G), was purchased from Sigma-Aldrich, the Netherlands.

SiC-deposited Al_2O_3 membranes were obtained via low-pressure chemical vapor deposition (LPCVD) using two precursors (SiH_2Cl_2 and C_2H_2) at a temperature of 860°C, as reported in our previous study [15]. The tubular Al_2O_3 membranes, provided by the CoorsTek Co., Ltd, were chosen as substrate for LPCVD with permeabilities in the 360 ± 12 $Lm^{-2}h^{-1}bar^{-1}$ range. The membranes without coating and those with a coating time of 20 min were labeled as C0 and C20, respectively. The pore size of the C0 and C20 membrane were 41 nm and 33 nm, respectively, as determined from our previously reported results [15].

5.2.2. Membrane characterization

Surface SEM images of the C0 and C20 membrane were obtained by NovaNanoLab 600 (FEI company, USA). The zeta potential of both the C0 and C20 membranes was measured with an electrokinetic analyzer (SurPASS 3, Anton-Paar, Graz, Austria).

5.2.3. Synthetic and real laundry wastewater

To study the effect of the charge of the emulsions on membrane fouling, various synthetic laundry wastewater were prepared for the membrane fouling experiments. The washing machine (WGG04408, Bosch, Germany) was cleaned by running empty cycles before the preparation of the synthetic laundry wastewater. Linear alkylbenzene sulfonates (LASs) are key anionic surfactants commonly found in detergents, including laundry powders and dishwashing liquids [283]. SDBS, a specific type of LAS, was used as a detergent, with 0.75 g/L added to the 30L DI water and the 2.5 kg polyester cloth during the washing procedure, based on the work of Hernandez et al. [284]. The same procedure was applied to the preparation of the synthetic laundry wastewater, containing either 2.5 kg cotton, 2.5 kg nylon, 2.5 kg polyester, or 2.5 kg linen fibers. The real laundry wastewater was collected from a laundry company, Elis B.V., located in Uden, the Netherlands. The detergent usage was measured per kilogram of clothing, with an average consumption of 10 ± 1.5 mL per kilogram. The washing process utilized approximately 14 ± 1 liters of water per kilogram of clothing. The laundry wastewater was generated from the following washing programs. The prewash was conducted at 45°C, the main wash at 60°C, and the cool-down at 40°C. The particle size distributions of the fabric fibers in the feed water were analyzed with a particle size analyzer (Bluewave, Microtrac, USA). Meanwhile, the particle size distribution of the permeate water and the laundry wastewaters' zeta potential was measured using a Litesizer (DLS 700, Anton Paar, Austria).

5.2.4. Filtration experiments with synthetic and real laundry wastewater

A constant permeate flux crossflow setup was used for fouling experiments (Fig.S5.1). A constant flux of 50 $Lm^{-2}h^{-1}$ for the real laundry wastewater and 70 $Lm^{-2}h^{-1}$ for synthetic laundry wastewater was selected, based on the threshold flux values determined for the C0 and C20 membranes, respectively. These threshold flux values were determined though the conventional flux stepping method [15, 166, 167]. The fouling resistance was calculated according to the resistance-in-series model [169, 170]. Detailed information about the filtration protocol can be found in the Supporting Information (Text S5.1).

5.2.5. Qualitative and quantitative microplastic fiber characterization

Three methods were used to characterize the release of the fabric fibers. In the first method, the fibers in both synthetic and real laundry wastewater, including feed and permeate samples, were analyzed using a digital microscope (VHX-5000, magnification×1000) equipped with a wide-range zoom lens (VH-Z100R). Multiple images with a resolution of 1600×1200 pixels with a scale bar of 10 µm were captured for each feed and permeate sample to quantify the number of fibers per milliliter. In addition, the area, perimeter and max/min diameter of the fiber were identified by using the "auto area measurement function". In the second method, laser direct infrared imaging (LDIR) was used to identify the type and the number concentration of microplastic fibers in the real laundry wastewater [24, 285]. In the third method, the fabric fibers in the synthetic laundry wastewater were analyzed using Fourier transform infrared (FTIR) spectroscopy (Nicolet^{TM} iS50, Thermo Fisher Scientific, USA). The analysis was conducted in attenuated total reflection (ATR) mode over a wavenumber range of 500-3600 cm^{-1}. The scans were performed 60 times with a resolution of 4 cm^{-1}, and the data spacing was set at 0.482 cm^{-1}. Every FTIR measurement was conducted in duplicate.

5.3. Results and discussion

5.3.1. Synthetic laundry wastewater properties

The FTIR spectra (Fig.5.1a) shows the peaks of the four types of fabric fibers. Linen and cotton fibers are primarily composed of cellulose, therefore, the key absorption peaks included 1100 cm^{-1} (C-O), 2900 cm^{-1} (C-H), and 3400 cm^{-1} (O-H). For the polyester fibers, the key absorption peaks included 1100&1260 cm^{-1} (C-O), 1600 cm^{-1} (C=C) and 1712 cm^{-1} (C=O), which is in accordance with the absorption peaks given in literature [286, 287]. For the nylon fiber, the absorption peak at 3299 cm^{-1} confirms the presence of amine stretching, while the peak at 1633 cm^{-1} indicates amine carbonyl stretching in the structure. These results are in line with the ATR-FTIR spectra of these fibers that have been reported in literature [286, 287]. The particle size distribution of the synthetic laundry wastewater is shown in Fig.5.1b. The average particle sizes for cotton, nylon, linen and polyester fibers were 11.35 ± 1.72 µm, 12.62 ± 1.21

µm, 25.45 ± 2.36 µm, 3.97 ± 0.23 µm, respectively. In contrast, Yang et al. have reported the release of submicron particles (100–600 nm) during domestic washing of 12 different polyester fabrics. The washing experiments were carried out using a Gyrowash lab washing machine (James Heal, Model 1615), which contains eight steel containers designed to simulate household washing conditions [279]. Meanwhile, Barrick et al. have reported that larger microfiber sizes for cotton, nylon, and polyester, averaging 20.46 ± 5.36 µm, 25.37 ± 5.24 µm, and 30.51 ± 5.09 µm, respectively [68].

Cotton and linen fibers are both cellulose-based and hydrophilic [288], but when soaked in a negatively charged surfactant solution, linen fibers (derived from flax) typically exhibit a less negative zeta potential (−16.9±2.3 mV) than cotton fibers (−20.1±1.4 mV), as shown in Fig.5.1c. This difference is attributed to the lower concentration of surface carboxyl groups present on linen fibers, as well as less adsorption of the negatively charged surfactant due to their hydrophilic nature [69, 289]. At neutral pH (pH = 7), nylon fibers lose most of their positive charge due to the deprotonation of amide groups, indicating a near-neutral surface [290]. However, when nylon fiber are released from fabric and interact with SDBS surfactant, the negatively charged SO_3^- groups of the SDBS adsorb onto nylon fibers. Additionally, the hydrophobic nature of nylon fiber further promotes adsorption of the SDBS molecules, particularly of the surfactant's hydrophobic tail. This combined adsorption caused a shift in the zeta potential to -23.3±1.2 mV, a more negative value than those observed for cotton fibers and linen fibers. Polyester exhibits an even higher surface hydrophobicity than nylon [291], and tend to adsorb more SDBS surfactants by hydrophobic interactions. Thus, the zeta potential was -33.6±1.8 mV, more negative compared to nylon, cotton, and linen. Ladewig et al. have reported that at a pH of 10, synthetic fibers (polyester) exhibited a higher zeta potential of -69 mV, compared to natural fibers (cotton), having a zeta potential of -24.5 mV [69]. Similarly, Ripoll et al. have reported that at alkaline pH, natural fibers, such as cotton and bamboo, had a lower absolute value of zeta potential, compared to synthetic fibers like polyamide [292]. This difference has also been attributed to the higher zeta potential of hydrophobic fibers (e.g., polyamide) compared to the more hydrophilic fibers (e.g., cotton) [292].

When the membranes were soaked in the SDBS solution, the zeta potentials of the C0 and C20 membranes were -41.7 ± 2.4 mV and -60.8 ± 3.1 mV, respectively. This indicates the presence of electrostatic repulsion between the membrane surfaces and the fibers.

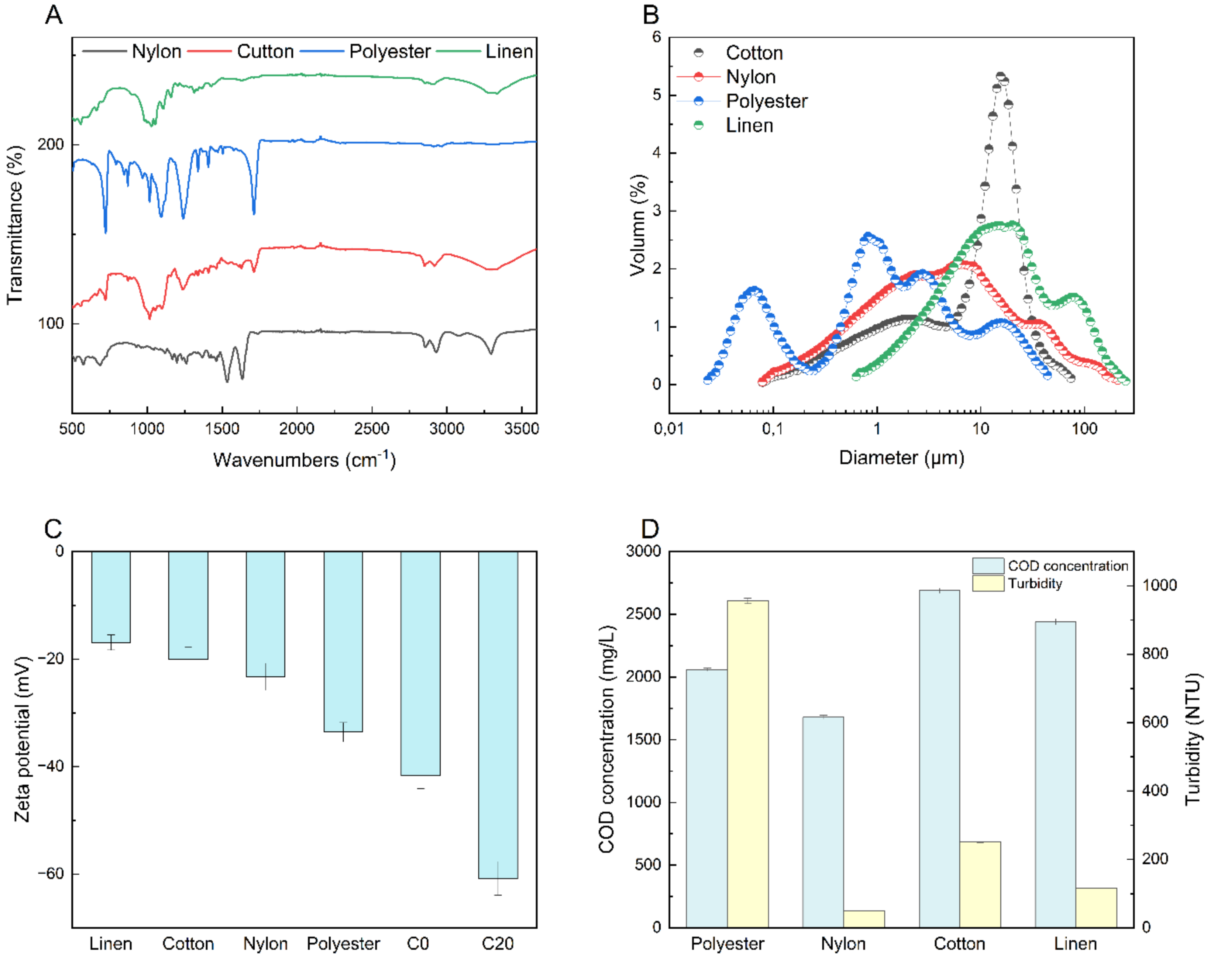

Fig. 5.1. (a): The FTIR spectra of the fabric fibers. (b): The fiber size distribution of the synthetic laundry wastewater. (c): The zeta potential of the synthetic laundry wastewater containing cotton, linen, nylon, polyester fibers and the C0 and C20 membranes soaking into the SDBS solutions. (d): The COD concentration and turbidity of the synthetic laundry wastewater containing cotton, linen, nylon, polyester fibers.

The COD concentrations of the synthetic laundry wastewater, after the washing of 2.5 kg of the respective clothes, containing polyester, nylon, cotton and linen, were 2059 ± 13 mg/L, 1680 ± 16 mg/L, 2689 ± 21 mg/L, 2440 ± 25 mg/L, respectively (Fig.5.1d). The possible explanation for the differences in COD is that natural fibers are more prone to abrasion and damage and, thus, when subjected to friction and mechanical forces, they are more likely to release fibers [293]. However, the synthetic laundry wastewater containing polyester had a higher turbidity than the feed water containing nylon, cotton, and linen, probably due to the higher presence of smaller, suspended particles and fine fibrous fragments that scatter light (Fig.5.1d) [294].

The fabric fibers had elongated and irregular shapes, and particularly those with a high aspect ratio (length/diameter) were long with a narrow diameter, being potentially able to penetrate membrane pores (Fig.5.2). The microscopic image of the cotton shows the relatively small and uniformly distributed fibers, suggesting the release of finer fibers, which contributed to the highest COD levels. In contrast, microscopic image of nylon displays a clean appearance with minimal visible residues, corresponding to its lowest COD concentration (1680 ± 16 mg/L), indicating limited nylon fiber release. The microscopic image of the linen shows the clearly visible fibrous fragments, corresponding to the second highest COD concentration. Polyester shows scattered but noticeable fibrous structures and small particles, aligning with a moderate COD value (2059 ± 13 mg/L).

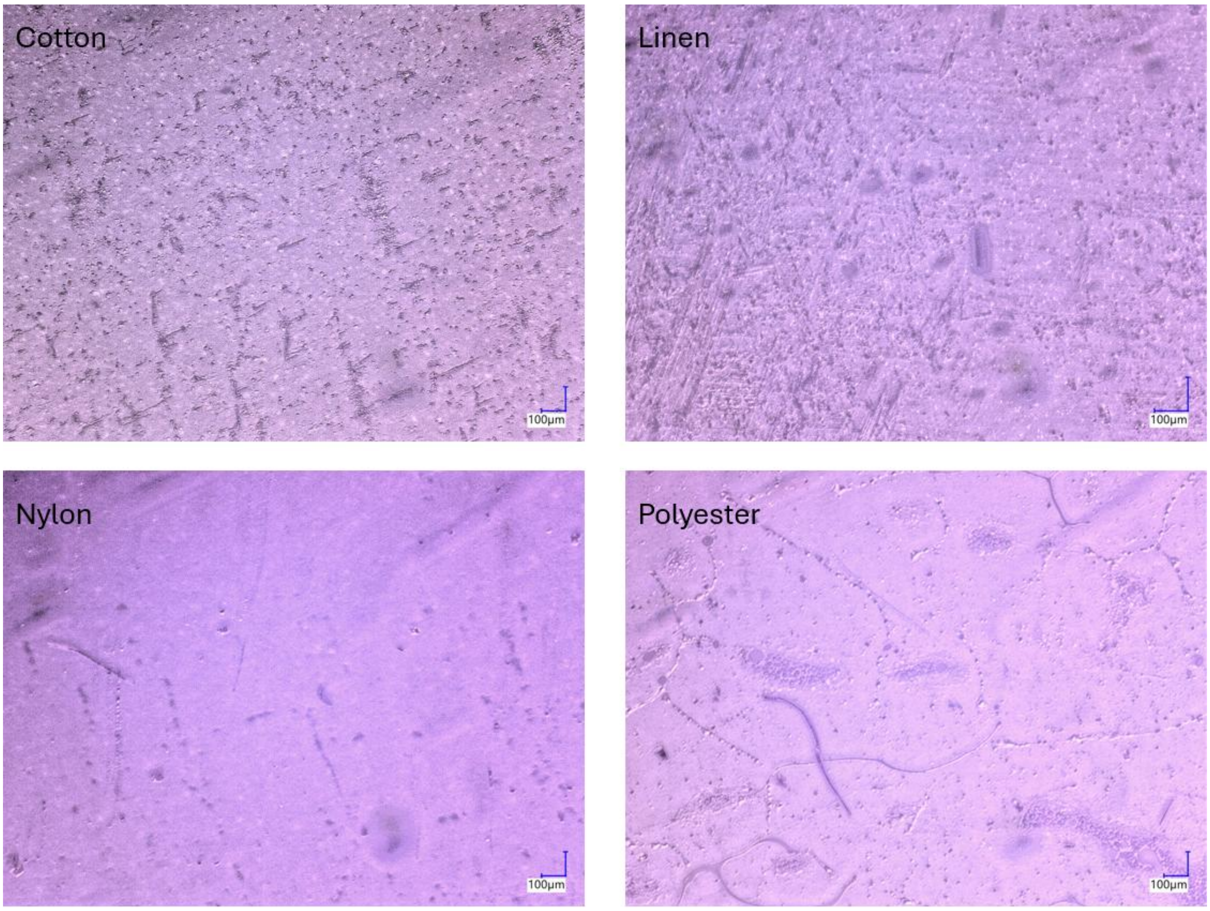

Fig. 5.2. Microscopic images of the cotton, polyester, nylon and linen fibers in the feed water.

5.3.2. Real laundry wastewater properties

The fabric fibers had an average particle size of 9.26 ± 0.57 µm, ranging from a minimum of 56 nm to a maximum of 62.23 µm (Table 5.1 and Fig.5.3). The small sizes of the fibers can be attributed to the potential degradation of natural fabric fibers or the desorption of their adsorbed contaminants, which may release smaller substances (e.g., dyes, monomers, finishing chemicals)[69]. This process could deteriorate water quality and accelerate membrane fouling. The zeta potential of the laundry wastewater was -30.77±0.42 mV (Table 5.1), due to the presence of anionic and non-ionic surfactants [295].

Table 5.1. Characteristics of the real laundry wastewater.

Parameters	Real laundry wastewater
Turbidity	318±11
pH	7.91±0.29
Conductivity (mS/cm)	1.23±0.02
COD (mg/L)	4014±154
Zeta potential (mV)	-30.77±0.42
Mean particle size (µm)	9.26±0.57

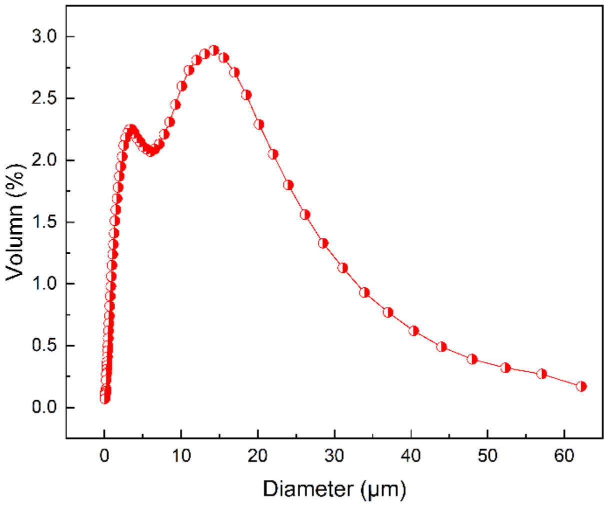

Fig. 5.3. The particle size distribution of the real laundry wastewater.

In order to accurately identify the percentage and species of synthetic and natural fibers in real laundry wastewater, the LDIR technique was used to analyse the real laundry wastewater sample. Out of the 722 ± 17 detected particles, the composition of 656 ± 21 particles was successfully identified by matching their FTIR spectra with reference spectra from the software library, using a minimum confidence threshold of 65%. Fig.5.4a shows the fiber length distribution, and Fig.5.4b shows the fiber material distribution of the real laundry wastewater.

The fiber identification spectra from the LDIR software are shown in Fig.S5.4. According to the Fig.5.4a, the majority of the fibers have lengths ranging from 0 to 50 µm, as indicated by the particle size distribution results. The LDIR analysis (Fig.5.4b) revealed that 67.8% ± 1.6% of the fibers in the sample were natural, including 49.8% ± 0.9% cellulose-derived fibers and 18.9% ± 1.8% natural PA fibers, which including wool and silk [296]. The remaining fibers were synthetic, consisting of 9.8% ± 1.2% polyethylene terephthalate (PET), 6.4% ± 0.7% acrylates, 5.6% ± 0.8% PA, and 4.0% ± 0.7% Polyurethane (PU), along with smaller fractions of 4.2% ± 0.6% methylcellulose, and 2.3% ± 0.4% polytetrafluoroethylene (PTFE). These results indicated that natural fibers dominate in real laundry wastewater. It has been reported that the natural fibers such as cotton and linen could make up 55% of the total fibers in the laundry wastewater [67]. These cellulose-based fibers serve as an easily accessible carbon source for microorganisms. In contrast, polyester and nylon, due to their hydrophobic nature and non-sugar-based composition, are not biodegradable [297]. With the number of fabrics fiber in the real laundry wastewater and the volume of the feed water, an total fiber concentration of 4.23×10^4 L^{-1} including 2.86×10^4 L^{-1} natural fibers and 1.37×10^4 L^{-1} synthetic microplastic fibres was calculated.

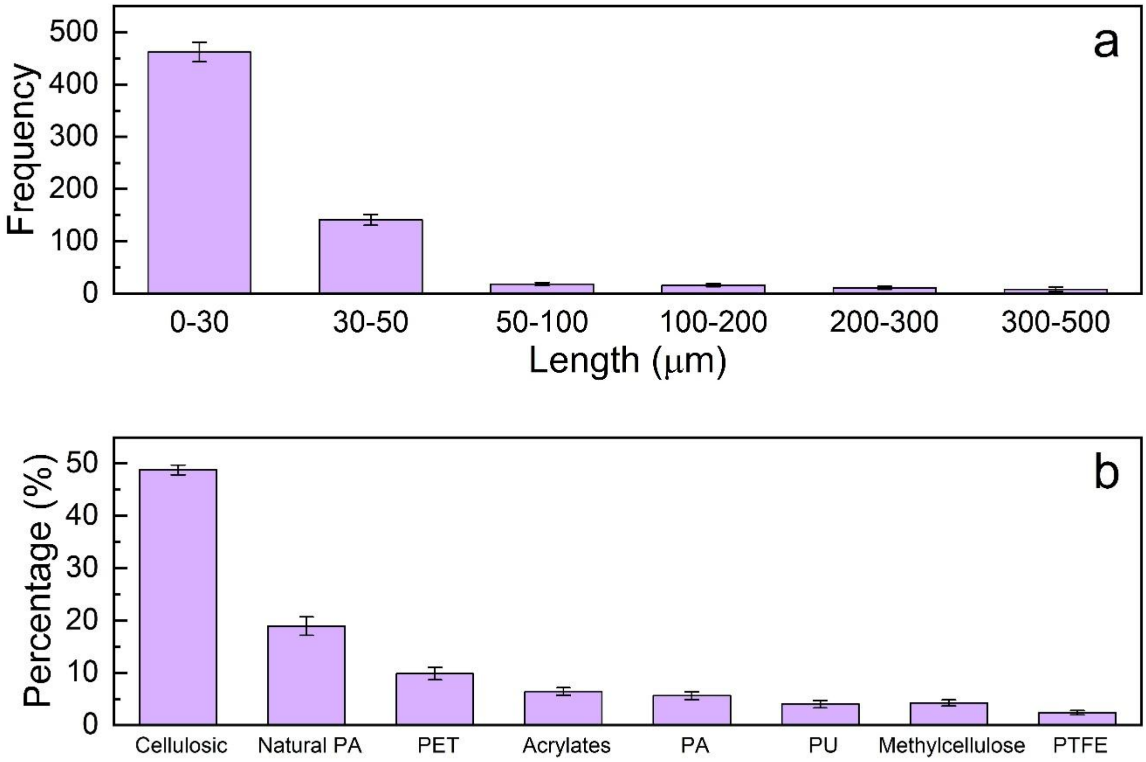

Fig.5.4. (a) Fiber length distribution and (b) fiber material distribution of the real laundry wastewater.

5.3.3. Membrane fouling with synthetic laundry wastewater

The normalized TMP fouling curves, shown in Fig.5.5, indicate that cotton fibers caused the most severe membrane fouling, followed by the linen, polyester and nylon. Among them, linen fibers resulted in the highest irreversible fouling, probably due to the lower zeta potential of linen fibers (−16.9±2.3 mV), which reduces the electrostatic repulsion between the fibers and the C0 and C20 membranes, promoting stronger adhesion and irreversible deposition.

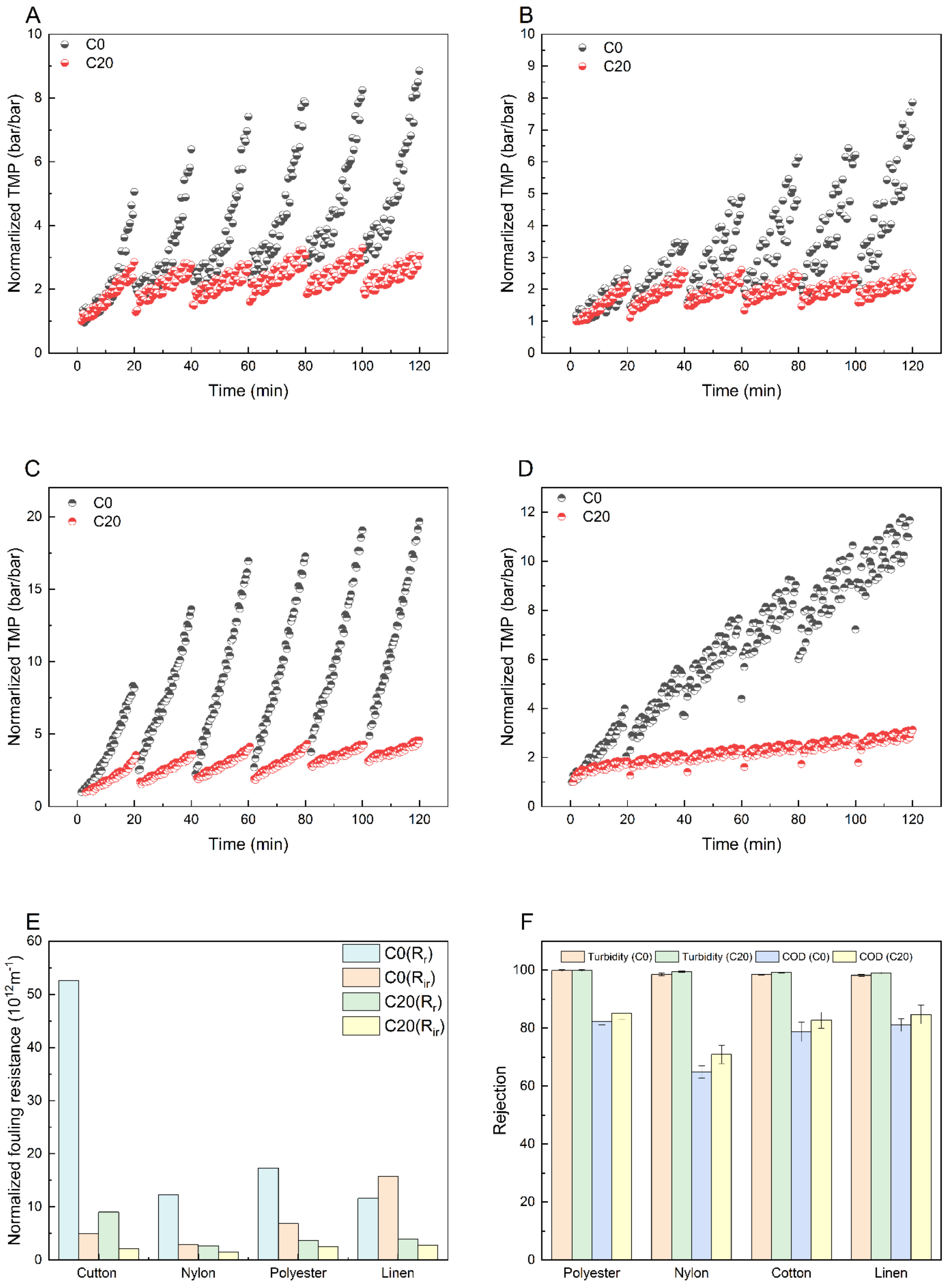

Fig. 5.5. The normalized TMP curve of C0 and C20 membranes for different types of laundry wastewater including (a): Polyester, (b): Nylon, (c): Cotton, (d): Linen; (e): Normalized fouling resistance of C0 and C20 membranes for different types of synthetic laundry wastewater. (f): Turbidity and COD rejection of C0 and C20 membranes for various types of synthetic laundry wastewater.

The trend of membrane fouling is consistent with the COD concentrations, which is in the order of cotton>linen>polyester>nylon. To evaluate whether surfactants contribute to membrane fouling, pure SDBS surfactant solutions were filtered. The results showed that the surfactants did not cause either reversible or irreversible fouling of the C0 or C20 membranes, as indicated by the unchanged TMP with the increase in filtration time (Fig. S5.2). Therefore, the fouling observed is attributed to the presence of fibers. Natural fibers thus caused more membrane fouling than the synthetic fibers, probably due to the lower absolute values of zeta potential of the natural fibers and higher COD load. In literature, natural fibers have largely been overlooked, with research primarily focusing on synthetic fibers. This is likely due to the assumption that natural fibers, being organic and biodegradable, pose a minimal environmental risk [68]. For example, natural fibers, such as cotton and silk, have not exhibited toxicity toward *Daphnia magna*, whereas synthetic fibers like nylon caused acute toxic effects on the organism [68]. However, it has also been reported that natural fibers could serve as carriers for harmful substances, as fabrics made from organic fibers are often treated with chemicals such as chemical colorants and finishes [69]. These chemical additions could also slow down the biodegradation process of natural fibers [70].

As shown in Fig.5.5f, the COD removal efficacies of the C0 and C20 membranes were highest for polyester fibers, reaching 82.3 ± 0.8 % and 85.1 ± 1.4 %, respectively. A possible explanation is that all the fibers were removed, and only the small molecules, such as surfactants, and monomers, contributed to the COD measured in the permeate. In contrast, the nylon fabrics released the lowest amount of fibers, thus, resulting in less adsorption of surfactant onto the fibers and a higher concentration of surfactant in the permeate. This led to low COD rejection by the C0 membrane and C20 membranes, at 64.9 ± 2.1% and 70.9 ± 3.1%, respectively. Because the COD, present in the permeate, mainly originated from the SDBS surfactant, it could be recovered and reused if the wastewater were recycled. Additionally, all fibers released from the fabrics were completely rejected by the membranes, as confirmed by the microscopic images (Fig.S5.3).

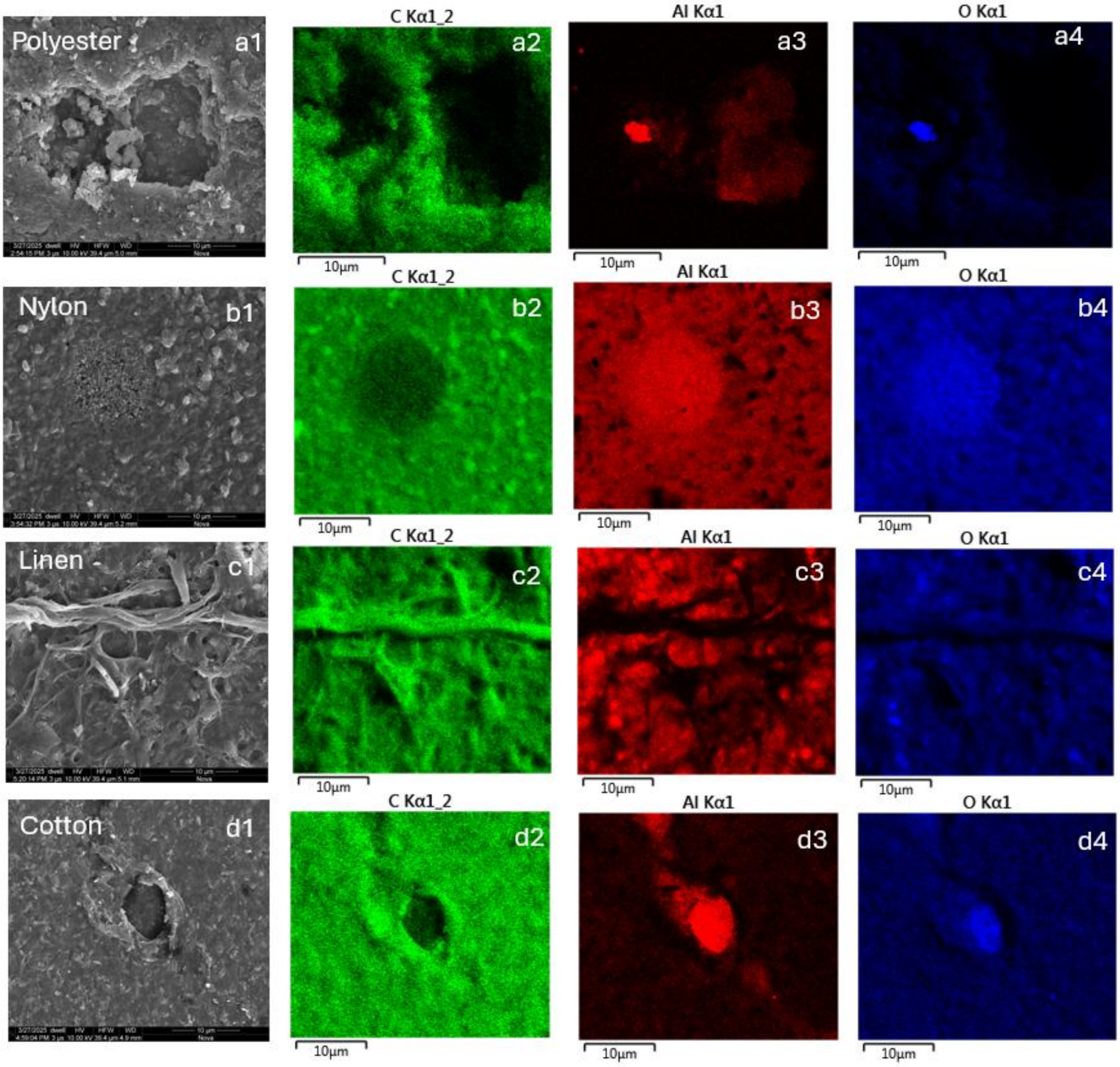

Fig. 5.6. SEM images of the fouled C0 membrane, along with the corresponding element mapping (C, Al and O) after treating the synthetic laundry wastewater containing (a) Polyester, (b) Nylon, (c) Linen, and (d) Cotton.

As can be observed from Fig.5.6, the surface morphology and elemental mapping confirm that different fabric fibers in synthetic laundry wastewater led to varying degrees of membrane fouling on the C0 membrane. The fouling layer on the C20 membrane was not studied since the carbon in the SiC membrane influences the carbon distribution of the foulants (fiber) on the membrane surface. Among all tested fibers, cotton resulted in the most developed cake layer, covering approximately 91% of the membrane surface, as evidenced by the strong and widespread carbon signal and the near absence of aluminum signal. The polyester led to the second largest fouling, with about 65% of the alumina signal obscured, also suggesting the formation of a substantial cake layer. The observed fouling appeared to be dominated by foulant-foulant interactions, particularly hydrophobic interactions, rather than membrane-foulant interaction. With the increase in the filtration time, these interactions promote the accumulation and growth of the cake layer and the porosity of the cake layer initially increases during the early stage of filtration and then reaches a plateau [298]. Enfrin et al. have reported a similar fouling mechanism, where polyester fibers produced via electrospinning and cryosectioning, with a diameter of 13 ± 7 µm, led to a combination of internal pore blockage and cake layer formation [299]. When treating synthetic laundry wastewater containing linen fibers, the fibers were clearly deposited as cake layer on the membrane surface. In the case of nylon fibers, the elemental carbon mapping showed a homogeneous but faint distribution of carbon across the membrane surface, however, the aluminum signal remained clearly visible, indicating that only a thin and sparse fouling layer with minimal surface coverage. This suggests that nylon caused the least reversible fouling, which is related to cake layer formation, consistent with the low COD value (1680 ± 16 mg/L).

5.3.4 Membrane fouling with real laundry wastewater

The threshold flux of the membranes

The threshold fluxes for the C0 and C20 membranes were 48 $Lm^{-2}h^{-1}$ and 56 $Lm^{-2}h^{-1}$, respectively (Fig.5.7), thus, a constant flux of 50 $Lm^{-2}h^{-1}$ was selected for filtering the real laundry wastewater.

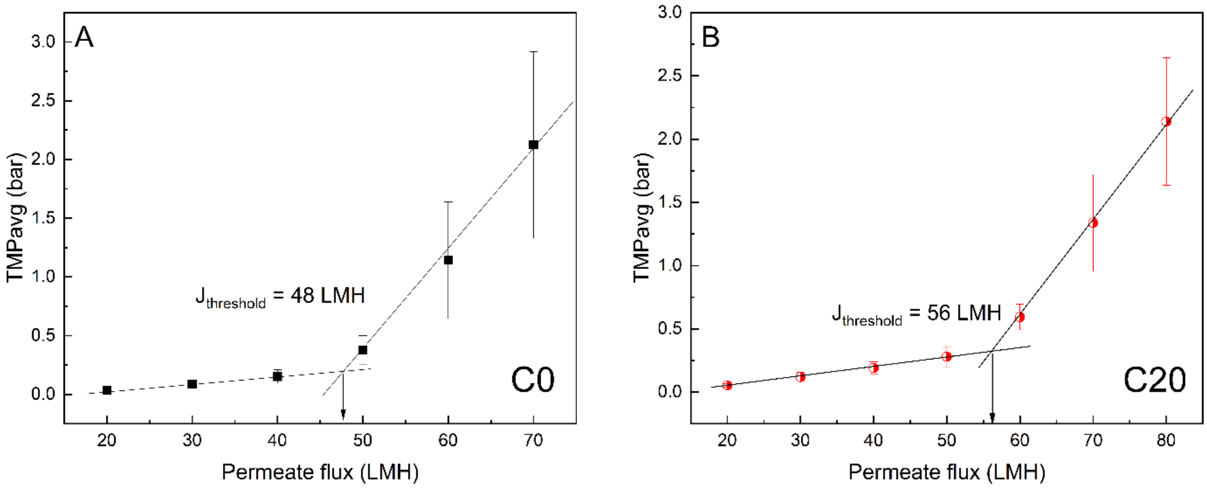

Fig. 5.7. The threshold flux of the C0 and C20 membranes for the real laundry wastewater treatment.

The effect of the temperature and flux on membrane fouling

At the flux of 50 LMH (Fig.5.8a), a rapid increase in the normalized TMP for the C0 membrane indicates a higher fouling rate than the C20 membrane, which may be attributed to the lower electrostatic repulsive forces between the C0 membrane and fabric fibers. It has been reported that fabric fibers, including natural and synthetic (microplastics) fibers, are primarily rejected by membranes based on size-exclusion, with fibers smaller or larger than the membrane pores potentially causing irreversible or reversible fouling, respectively [71]. In order to further study the effect of flux on irreversible fouling, the flux was increased to 70 $Lm^{-2}h^{-1}$, being higher than the threshold flux of the both membranes (Fig.5.8b). A higher irreversible and reversible fouling was observed for both C0 and C20 membranes due to the increased treated volume. However, the C20 membrane still outperformed the C0 membrane, with a lower fouling tendency. The performance gap between the two membranes became more noticeable at this higher flux (70 $Lm^{-2}h^{-1}$) compared to the low flux of 50 $Lm^{-2}h^{-1}$.

In cloth washing industry, large volumes of reusable hot laundry wastewaters are being discharged [300]. To evaluate membrane performance under realistic conditions, the filtration experiments were conducted at the temperature of 20 ℃ and 60 ℃ (Fig.5.8c). At higher temperatures, ceramic membranes usually exhibit a higher permeability due to the lower water viscosity at higher temperature, potentially resulting in less fouling. Similarly, Paula et al. have also observed an increased membrane fouling at lower temperatures during flux step experiments [301]. The explanation could be that the detergents and surfactants (e.g., SDBS) in laundry wastewater remain more soluble and induced micellization becomes interrupted at higher temperatures, reducing their tendency to adsorb onto membrane surfaces [23, 302]. Also, due to the stronger convective forces, because of decreased viscosity at higher temperatures, the formation of the cake layer on the membrane surface is probably slowed down, leading to a decreased reversible fouling . On the other hand, increased temperatures can increase fouling in oily wastewater treatment, as the reduced viscosity of oil leads to droplet deformation and greater potential for pore blockage in ceramic membranes [265]. From an economic perspective, treating real laundry wastewater at 60 °C not only mitigates the membrane fouling, but also enables the recovery and reuse of both water and heat, potentially reducing water consumption and associated energy costs.

Table 5.2. Characteristics of the permeate water.

Parameters	Permeate water (C0)	Permeate water (C20)
pH	7.88±0.12	7.82±0.08
Conductivity (mS/cm)	1.16±0.04	1.18±0.05
COD (mg/L)	1179±42	1128±25
Zeta potential (mV)	-19.41±0.32	-18.66±0.47
Mean particle size (nm)	12.38±0.34	12.13±0.56

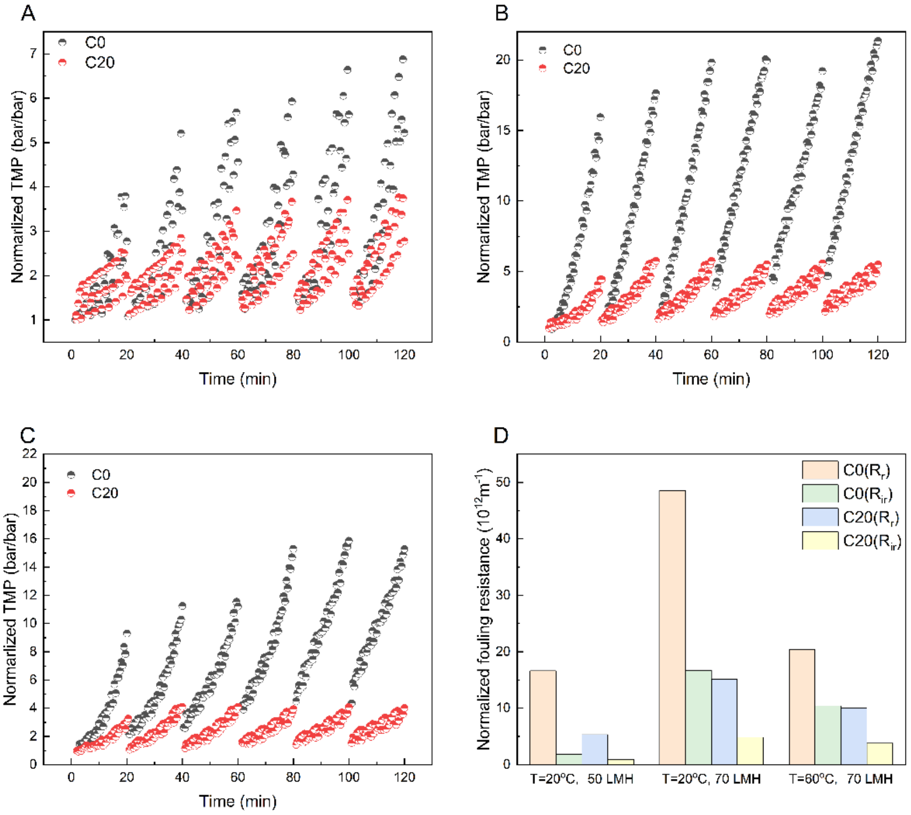

Fig. 5.8. The normalized TMP curve of C0 and C20 membranes under different conditions (a):T=20 ºC, 50 Lm^{-2}h^{-1}; (b): T= 20 ºC, 70 Lm^{-2}h^{-1}; (c): T=60 ºC, 70 Lm^{-2}h^{-1}; (d):The normalized fouling resistance for the C0 and C20 membranes under different conditions.

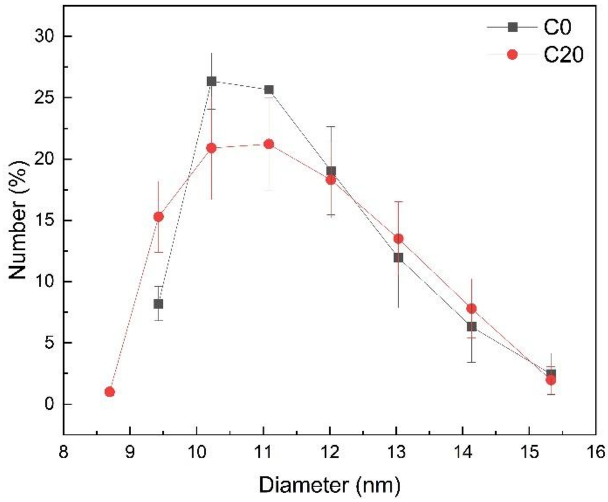

Fig. 5.9. The particle size distribution in the permeate water of the C0 and C20 membranes.

The COD concentration in the permeate was 1179 ± 42 mg/L for the C0 membrane and 1128 ± 25 mg/L for the C20 membrane. Based on these values, the calculated COD rejection rates were 70.6% and 71.9%, respectively (Table 5.2). The particles in the permeate (Fig.5.9) can be explained by the presence of spherical micelles of the surfactant ranging from 2 to 20 nm [295].

To further analyse the fibers in the real laundry wastewater, their morphologies were examined using microscopic images (Fig.5.10). The contaminants in the feed water exhibited various shapes, including fibers, films, fragments and chips [281, 282]. In contrast, microscopic analysis of the permeate water revealed no visible fibers and particles, demonstrating the high rejection (100%) performance of the ceramic membranes. It is reported that the natural fibers such as cotton and linen could make up 55% of the total fibers in the laundry wastewater [67]. These cellulose-based fibers serve as an easily accessible carbon source for microorganisms. In contrast, polyester and nylon, due to their hydrophobic nature and non-sugar-based composition, are not biodegradable [297].

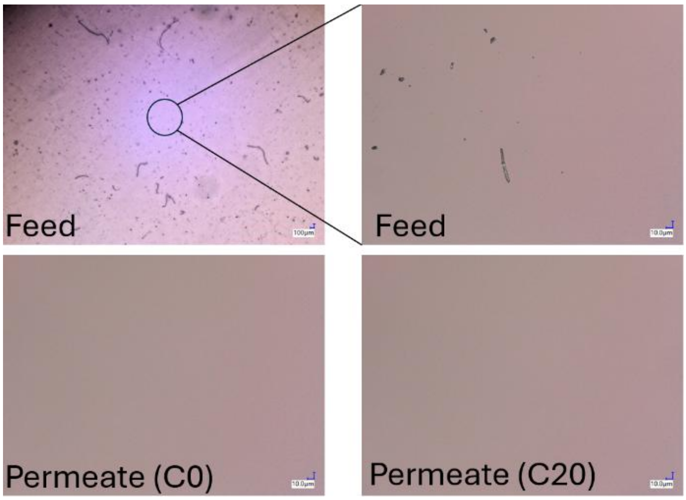

Fig.5.10. Microscopic characterization of the feed and permeate of real laundry wastewater after treatment with C0 and C20 membranes.

5.4. Conclusion

The behavior of fiber release, membrane fouling, and fouling mitigation during the treatment of synthetic laundry wastewater using pristine Al_2O_3 and a SiC-coated ceramic membranes was presented. The fiber size distribution was characterized using light scattering-based techniques, and the fouling experiments were conducted at a constant flux of 70 $Lm^{-2}h^{-1}$. Results revealed that natural fabrics, particularly cotton and linen, released higher COD loads than synthetic fabrics, when tested at equal mass, in the trend of, cotton>linen>polyester>nylon, which was further supported by microscopic and SEM images. Both the pristine and the SiC-coated membranes showed a high fiber rejection (100 %), whereas the SiC-coated membrane showed lower reversible and irreversible fouling than the Al_2O_3 membrane due to its highly negatively zeta potential . The fouling order of the fibers in line with the COD concentration of the synthetic laundry wastewater containing these fibers. Further, it was found that during treatment of hot (60 ºC) real laundry wastewater by the ceramic membranes, not only membrane reversible and irreversible fouling was mitigated, but it also enabled the simultaneous recovery and reuse of water, surfactants, and thermal energy, potentially offering a sustainable strategy to reduce both water consumption and energy costs. The LDIR results showed that natural fibers is dominant in the real laundry wastewater with number concentration of 2.86×10^4 L^{-1}. This study also highlighted the importance of paying greater attention to natural fibers, as they can cause more severe fouling of ceramic membranes compared to synthetic fibers during the laundry wastewater treatment process.

Supplementary information

Text S5.1

The fouling experiments, consisting of six cycles, were conducted at the constant flux of 80 $Lm^{-2}h^{-1}$ (Fig.4.1). This flux was estimated based on the threshold flux using the conventional flux stepping method [15, 166, 167]. Each filtration cycle started with filtering the laundry wastewater at a specified flux with a crossflow velocity of 0.6 m/s for 20 min. Between the filtration cycles, backwashing was applied to eliminate reversible fouling, maintained at a constant flux of 1080 $Lm^{-2}h^{-1}$ for 10 seconds. Finally, forward flushing with the feed water for 15 s at a crossflow velocity of 0.6 m/s to drain the concentrated water. Every fouling experiment was conducted in duplicate.

The chemical oxygen demand (COD) of the water samples was measured by a Hach spectrophotometer (DR 3900, US) with COD cuvettes (LCK 314 and LCK 514, Hach) [192].

The COD rejection of the membranes were calculated by Eq. (S.5.1):

$$R = (1 - \frac{C_p}{C_f}) * 100\% \qquad \text{(S.5.1)}$$

where R is the rejection, C_p is the COD concentration (mgL^{-1}) in the permeate, and C_f is COD concentration (mgL^{-1}) in the feed.

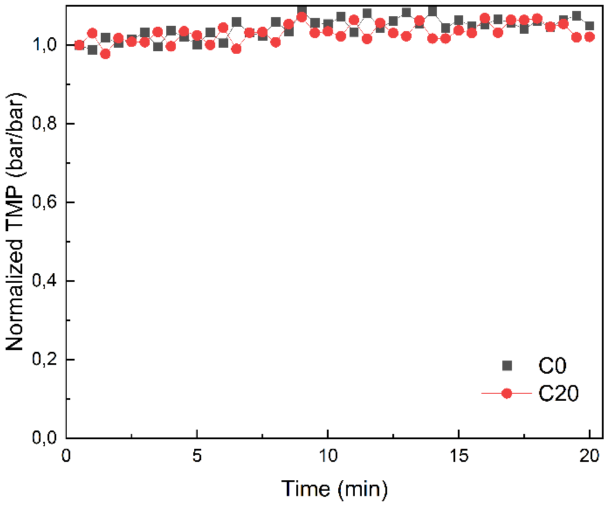

Fig.S5.2. Fouling comparison of the C0 and the C20 membrane during the filtration of SDBS surfactant solutions.

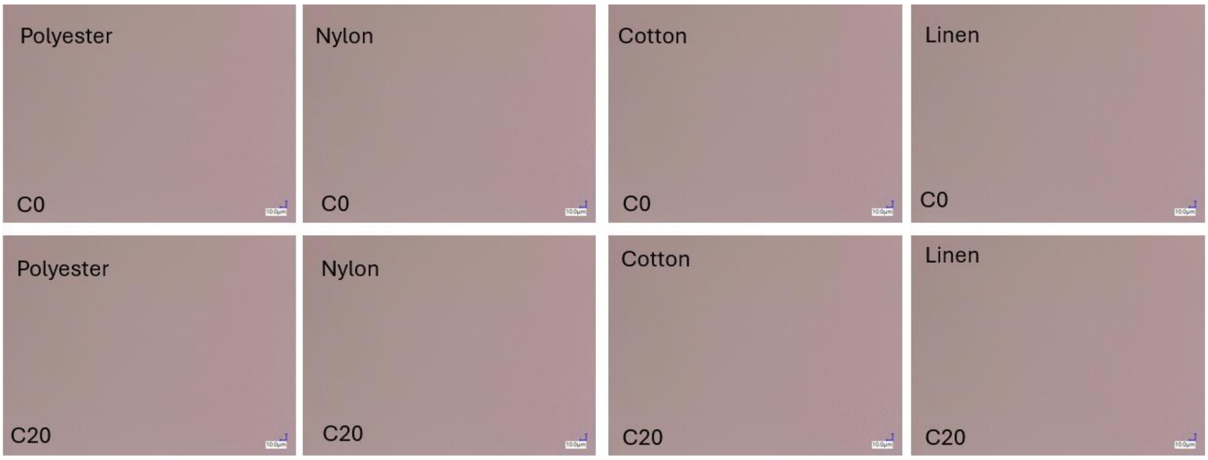

Fig. S5.3. Microscopic characterization of the feed and permeate of synthetic laundry wastewater containing Polyester, Nylon, Cotton and linen fibers after treatment with C0 and C20 membranes.

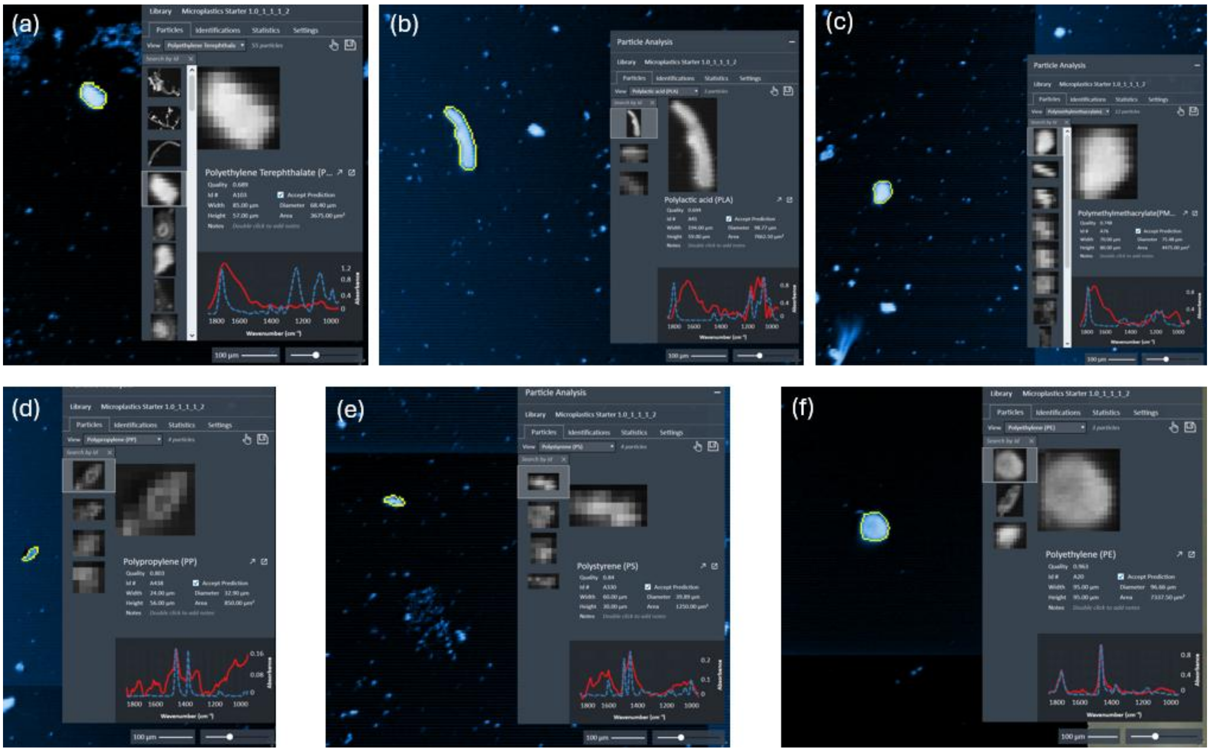

Fig.S5.4. Particle identification spectre LDIR of real laundry wastewater.

Chapter 6

Conclusions and outlook

6.1 Conclusions

In this thesis, the manufacturing, characterization, and application of SiC-coated ceramic ultrafiltration membranes have been presented for treating synthetic oil-in-water (O/W) emulsions, real oily wastewater and laundry wastewater. The membranes were prepared via low-pressure chemical vapor deposition (LPCVD) at 860 °C and extensively characterized to determine their pore structure, surface morphology, water permeance, mechanical strength, surface charge, and wettability. Their separation performance and fouling were first evaluated using synthetic O/W emulsions, focusing on the influence of deposition time, pH, surfactant type, and membrane pore size. To further understand the fouling mechanisms, classical Derjaguin-Landau-Verwey-Overbeek (DLVO) and extended DLVO (XDLVO) models were applied to quantify the interactions between membranes, oil droplets, and deposited oil layers, taking into account varying ionic strengths and different surfactant types (anionic, nonionic, cationic, and zwitterionic). Building on this, the membranes were tested in real industrial wastewater applications through direct filtration of produced water under constant flux conditions, assessing the impact of salinity, operating conditions (flux and crossflow velocity), and membrane pore size on fouling development. Fouling mechanisms, including reversible and irreversible components, were visualized and distinguished using Focused Ion Beam-Scanning Electron Microscope (FIB-SEM) imaging. Finally, the membranes were evaluated for filtering synthetic laundry wastewater, containing both natural and synthetic fibers, as well as real laundry wastewater under varying operational conditions, such as flux and temperature. These studies have provided insights into fiber-induced fouling and led to practical strategies for fouling mitigation, water reuse, and heat recovery in the laundry industry.

Overall, it can be concluded that SiC membranes showed a lower reversible and irreversible fouling compared with the conventional Al_2O_3 membranes when treating negatively charged O/W emulsions, real produced water, and laundry wastewater.

The specific conclusions drawn in response to the research questions are as follows:

Research question 1: *How do LPCVD deposition time, emulsion pH, surfactant type, and membrane pore size influence the fouling of SiC-coated ultrafiltration membranes during filtration of synthetic oil-in-water emulsions?*

The SiC-coated membrane exhibited a lower fouling than the conventional Al_2O_3 membrane when filtering negatively charged O/W emulsions, primarily due to its enhanced hydrophilicity and stronger electrostatic repulsion. As the SiC coating deposition time increased, both membrane hydrophilicity and surface charge (zeta potential) improved, effectively reducing membrane fouling, particularly when the membrane and oil droplets carried the same charge. At a higher pH, increased electrostatic repulsion between the negatively charged oil droplets and membrane surfaces further mitigated fouling. However, when treating positively charged emulsions, stabilized by CTAB and Span 80 (zeta potential: 62.67 ± 0.76 mV), the SiC-coated membrane experienced the highest fouling due to electrostatic attraction. In contrast, fouling was reduced with negatively charged emulsions stabilized by Tween and Span 80 (−21.30 ± 0.73 mV), and was lowest with those stabilized by SDS and Span 80 (−58.3 ± 0.82 mV). Increasing the membrane pore size led to reduced reversible and irreversible fouling, but also decreased oil rejection. Therefore, the SiC-coated membrane with a 62 nm pore size and 20-minute coating time was identified as the best choice for microemulsion filtration, offering a high oil rejection with a low fouling propensity.

Research question 2: *Do the DLVO and XDLVO models align with the observed fouling trends of Al_2O_3 and SiC-coated membranes when filtering oil-in-water emulsions stabilized by different types of surfactants and under varying salinity levels?*

The DLVO and XDLVO interaction energies of the membrane-oil droplet exhibited a strong agreement with the fouling tendencies at all salinities. This shows the importance of the electrostatic repulsion of the oil droplet by the negatively charged SiC membrane. The SiC-deposited membrane showed less (ir)reversible membrane fouling than the Al_2O_3 membrane when filtering O/W emulsions stabilized with SDS, APG, or DDAPS. The DLVO model predicted a higher fouling tendency at higher salinity levels during the filtration of SDS, APG, or DDAPS-stabilized O/W emulsions and a decreased fouling tendency for CTAB-stabilized emulsion with the SiC-deposited membrane. However, at higher salinity levels, the XDLVO energy barrier was affected by both the repulsive electrostatic double layer interaction and attractive Lewis acid-base interaction. For the Al_2O_3 membrane, the XDLVO model obscured electrostatic double layer and Lifshitz-van der Waals interactions since the Lewis acid-base component was dominant, confirmed by the diminished XDLVO energy barrier, whereas for the SiC-deposited membrane, the electrostatic double layer interaction prevailed since the energy barrier value was positive.

Research question 3: *How does the fouling of SiC-coated membranes vary when treating real produced water under different fluxes, crossflow velocities, and pore sizes, and how do the fouling mechanisms evolve as filtration time increases?*

Real oilfield produced water with a high salinity (142 mS/cm) and high chemical oxygen demand (COD) (22670 mg/L) was successfully treated in a constant flux mode using both Al_2O_3 membranes and SiC-coated Al_2O_3 membranes. The results show that irreversible pore blockage occurred at the initial stage, while the subsequent fouling was dominated by a reversible cake layer composed of organic and inorganic matter. The SiC-coated membranes outperformed the pristine Al_2O_3 membranes in terms of reversible and irreversible fouling resistance. Furthermore, increasing membrane pore size and crossflow velocity, along with decreasing the applied flux, effectively mitigated fouling on the SiC-coated membranes.

Research question 4: *What is the fouling of positively charged Al_2O_3 membranes and negatively charged SiC-coated ceramic membranes during the treatment of synthetic and real laundry wastewater?*

Both the SiC-coated and Al_2O_3 membranes demonstrated a high fiber rejection (100%) when filtering synthetic laundry wastewater. However, the SiC-coated membrane exhibited a lower reversible and irreversible fouling compared to the Al_2O_3 membrane, attributed to its highly negatively charged surface. The fouling tendency of the different fibers correlated with the COD levels of the wastewater, following the order: cotton > linen > polyester > nylon. Further, the treatment of hot real laundry wastewater, using SiC-coated membranes, not only reduced both reversible and irreversible fouling, but also enabled the simultaneous recovery and reuse of water, surfactants, and thermal energy, offering a sustainable approach to lowering water consumption and energy costs.

6.2 Perspectives and outlook

6.2.1 The possibility of upscaling of SiC ultrafiltration membrane

Coating tight ultrafiltration ceramic membranes with SiC via LPCVD presents a promising approach for producing SiC tight UF membranes suitable for desalination. For instance, our group has developed SiC ultrafiltration membranes with a mean pore size of 7 nm, which is the smallest SiC membrane pore size reported for water treatment to date, achieving a sulfate (SO_4^{2-}) rejection of 79% [303]. However, the upscaling of the membranes still requires further investigation for commercial implementation. Despite this progress, further research is needed to scale up membrane production for commercial applications and to perform long-term testing in full-scale industrial wastewater treatment. In contrast to the conventional sol-gel method [160], our LPCVD-based fabrication method is potentially scalable. While advancements have been made in the development of SiC ultrafiltration membranes, fabrication techniques for SiC nanofiltration membranes remain underdeveloped.

6.2.2 SiC catalytic membranes

In the present thesis, emphasis is given to the use of SiC coated membranes for industrial wastewater treatment. However, SiC is also one of the photoelectric semiconductor materials that can be used as a substrate for manufacturing photocatalytic ceramic membranes. Among them, especially 3C-SiC (2.36 eV), due to its small bandgap, can absorb light into the visible spectrum and is suitable as a photocatalyst [304]. Although photocatalysis is a promising degradation technology, a key limitation lies in the challenge of removing and recovering the photocatalyst from the liquid after the reaction [305]. Zhu et al. have reported that SiC catalytic ceramic membranes with β-SiC nano-wires exhibit a high efficacy in degrading organic compounds under simulated sunlight [97]. Thus, integrating oxidation processes with ceramic membranes to replace conventional water treatment methods using catalytic ceramic membranes represents a promising direction for future research, although a major challenge is the difficulty of delivering sufficient light into membrane modules.

6.2.3 Utilization of ceramic membranes at the end of their life

In the present thesis, ceramic membranes have only be used at laboratory scale. At real world applications, the sustainability of the technology is of major importance. Nowadays, at the end of their life, ceramic membranes are typically discarded as solid waste. However, these membranes can be chemically treated or surface-modified to restore or even enhance their filtration properties. Through these treatments, the old membranes can be reused as ultrafiltration/nanofiltration modules, extending their life span and reducing waste. In addition, Al_2O_3 ceramic membranes can be crushed into powder and then used to make ceramic products.

Besides, Karatas has reported that discarded tubular ceramic membranes previously used for industrial wastewater treatment can be repurposed. Specifically, a laboratory-scale gas-liquid membrane contactor employing a discarded UF ceramic membrane was successfully used to capture CO_2 from indoor air using a NaOH solution at ambient temperature [306]. Therefore, research should further be conducted to explore and optimize the regeneration and recycling pathways of used ceramic membranes.

6.2.4 OCT for the membrane fouling monitoring

In the presented thesis, ex-situ fouling characterisation of the ceramic membranes has been done by Scanning Electron Microscope. However, in-situ membrane fouling monitoring techniques, such as Optical Coherence Tomography (OCT), used for polymeric membranes, remain unexplored for ceramic membranes. Future studies could therefore focus on OCT for both visual in-situ fouling monitoring (e.g., observing stripping patterns of the foulants on the membrane surface) and in-situ fouling structural analyses (e.g., measuring cake layer thickness). Furthermore, correlation analysis could be conducted by linking in-situ real cake layer thickness to membrane permeance decline and increased fouling with the increase in the filtration time.

6.2.5 From case studies to broader implications for other wastewater streams

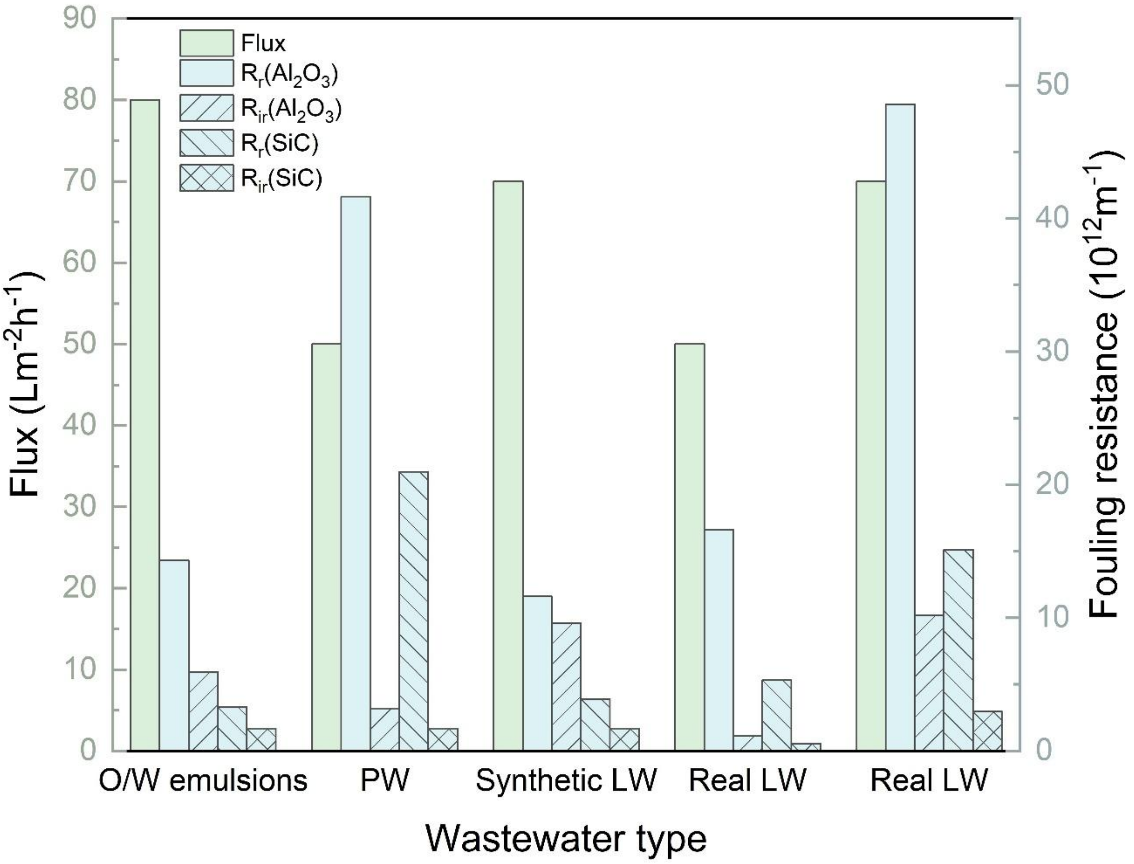

Fig.6.1. The fouling resistance for the Al_2O_3 and SiC membrane when filtering O/W emulsions, produced water (PW), synthetic laundry wastewater (LW), real LW.

Both synthetic oily wastewater and synthetic laundry wastewater yielded higher fluxes (80 and 70 L $m^{-2}h^{-1}$, respectively) compared with real produced water and real laundry wastewater (50 L $m^{-2}h^{-1}$). This indicates that real wastewaters impose harsher fouling conditions than synthetic wastewater. Produced water (Chapter 4) was characterized by extreme salinity and high COD, while laundry wastewater (Chapter 5) contained elevated temperatures and organic fibers. Despite these compositional differences, both represent highly challenging environments where polymeric membranes typically fail.

The comparative results highlight key differences. In produced water, oil fouling and high salinity led to a high increase in TMP, whereas in laundry wastewater, although synthetic fibers showed higher fouling tendencies than the natural fibers natural, overall fouling was less severe than oil fouling. Despite these differences, reversible fouling dominated in both cases, primarily in the form of cake layer formation.

In practice, these findings suggest that the applicability of SiC membranes extends beyond the two presented case studies. Other challenging waste streams, including oily wastewater from petrochemical industry and food industry, often combine chemical aggressiveness and high temperatures [259]. The robustness of SiC membranes under both extremes indicates a promising potential for broader industrial adoption, especially as pretreatment steps or polishing units in an integrated water treatment unit.

6.2.6 Practical deployment and scalability considerations

Membrane cleaning is a critical operational challenge. Physical cleaning, typically achieved by backwashing, can only recover permeance loss caused by reversible fouling. When water flux declines to about 40-50% of the initial value, chemical cleaning becomes necessary to remove irreversible fouling [272]. Chemically enhanced backwash (CEB) and cleaning-in-place (CIP) procedures using NaOH solution or NaOCl solution are recommended for effective fouling control in ceramic membrane applications [307].

In terms of scalability, several aspects must be considered. The scale up of tubular Al_2O_3 supports, the deposition of intermediate Al_2O_3 layers made by slurry coating and LPCVD-based fabrication of SiC separation layer all present potential throughput and cost constraints [308]. Furthermore, the high capital cost of ceramic membranes remains a major barrier to their large-scale use in water treatment. Large housings that accommodate multiple ceramic membrane elements (e.g., CeraMac®, PWNT, the Netherlands) can effectively reduce overall capital costs, thereby offering more engineering opportunities [305]. Large stainless steel housings are usually employed to withstand high-pressure backwash [305]. With lower requirements for frequent management and maintenance, robust and reliable ceramic membranes have already been applied in small-scale potable water recycling plants in remote locations, such as the Davis Station in Antarctica [309]. Although the fabrication cost of ceramic membranes are higher than polymeric ones, studies suggest that the overall capital and operating costs can be comparable in the long run, as ceramics can maintain higher fluxes over longer operating periods [310].

Acknowledgements

At the end of November 2025, my six years life in the Netherlands and also my four-years Ph.D. journey will come to an end. Throughout this journey, I have been fortunate to receive the support of many people that earn my most incredible gratitude. Without their help and support, this dissertation would not have been possible.

First and foremost, I would like to express my sincere appreciation to my supervisors, Prof. Dr. Ir. Luuk Rietveld and Dr. Ir. Bas Heijman. We first met in 2020 when I began my master's project. You introduced me to the membrane research community, gave me the freedom to pursue my work independently, and guided me to stay on the right research path. Thanks to you, I could finish my project on time and learn how to become an independent researcher. I sincerely thank you for all the scientific discussions and instant support during my Ph.D. journey. I would also express the appreciation to the Begum Tanis, the assistant professor of the membrane group, to provide a lot of useful feedback to improve the quality of the manuscript.

I would like to thank my colleagues in the membrane group—Shuo, Mingliang, Bin, Yuke, and Asif. With your support, my academic journey has been filled with laughter and joy. I also want to express my gratitude to my fellow colleagues who joined the sanitary engineering group the same year as I did, including Yanghui, Qin, Sijia, and Yana. We spent a lot of time playing table tennis and badminton together, which enriched my free time. I would also like to express my gratitude to the master's students I supervised, including Hao, Yiman, and Hanxiao. Additionally, I am thankful for the wonderful time spent with my friends in Delft—Siyuan (Incheon), Zixi (Shenzhen), Jinan (Shenzhen), Xiaonan (Inner Mongolia), Xinyu (Munich), and Qing (Milan). Together, we shared many memorable experiences, such as traveling, visiting museums, and spending weekends and vacations together. I would also like to express my gratitude to the membrane scientists from TU Twente for their support in my research, including Prof. Wiebe de Vos, Prof. Louis Winnubst, and the PhD students from their groups — Lijie, Jiaying, Wendy and Tao. I also want to express my thankfulness to the professor Weiyi Li from Southern University of science and technology for a pioneering research project that utilized Optical Coherence Tomography for in-suit (ir) reversible fouling monitoring of ceramic membranes. Finally, I extend my heartfelt appreciation to my parents for their unwavering support in encouraging me to study abroad and for providing constant emotional support.

CURRICULUM VITAE

Family name: Qin 秦

Given name: Guangze 广泽

Date of birth: 13 December 1997

Place of birth: Linyi, Shan Dong Province, China

Self-Introduction

A table tennis enthusiast, a paddle wielder’s delight.

In free moments, capturing life’s beautiful light.

Professionally immersed, in microemulsions I drives.

A maestro with ceramic UF membranes, my skill thrives.

Education background

2021.10-2025.10	PhD candidate - Delft University of Technology Environmental Engineering
2019.09-2021.08	Master degree - Delft University of Technology Environmental Engineering
2019.06	Exchange student – Hokkaido University Environmental Engineering
2018.09-2019.01	Exchange student – City University of Hong Kong Environmental Engineering
2015.09-2019.06	Bachelor degree – Lanzhou University Environmental Engineering

List of Publications

Qin, G., Zhou, H., M.B. Tanis-Kanbur, Rietveld, L. C., & Heijman, S. G. (2025). Impact of ionic strength and surface charge on ceramic membrane fouling by oil-in-water emulsions: A quantitative analysis using DLVO and XDLVO models. *Separation and Purification Technology,* 372,133424, http://dx.doi.org/10.1016/j.seppur.2025.133424.

Qin, G., Liu, Y., Rietveld, L. C., & Heijman, S. G. (2025). Oilfield-produced water treatment with SiC-coated alumina membranes. *Separation and Purification Technology*, 362,131841, http://dx.doi.org/10.1016/j.seppur.2025.131841.

Qin, G., Jan, A., An, Q., Zhou, H., Rietveld, L. C., & Heijman, S. G. (2024). Chemical vapor deposition of silicon carbide on alumina ultrafiltration membranes for filtration of microemulsions. *Desalination*, *582*, 117655, http://dx.doi.org/10.1016/j.desal.2024.117655.

Qin, G., M.B. Tanis-Kanbur, Rietveld, L. C., & Heijman, S. G. (2025). Laundry wastewater treatment with SiC-coated alumina membranes. *Under review by Separation and Purification Technology*.

Jan, A., M, Nijboer, **Qin, G.**, Rietveld, L. C., & Heijman, S. G. (2025). Silicon carbide coated alumina tight-ultrafiltration membrane prepared by low-pressure chemical vapor deposition for sulphate ion retention. *Desalination, 613, 119085.* http://dx.doi.org/10.1016/j.desal.2025.119085.

Hands-on skills

- Membrane characterization: SEM, TEM, AFM, FTIR, XRD, contact angle, zeta potential, pore size, bending strength
- Water characteristics analysis: PSD, Turbidity, pH, Conductivity, zeta potential, COD, TOC, TSS,TDS, LCMS, FEEM, LCOCD
- Separation processes: Constant flux filtration set up build up
- Coding: MATLAB coding (DLVO/XDLVO mode)

Selected Oral presentation

- 2024: Impact of ionic strength and surface charge on ceramic membrane fouling by oil-in-water emulsions: A quantitative analysis using DLVO and XDLVO models

  Euromembrane 2024, Praha, The Czech Republic

- 2024: Impact of ionic strength and surface charge on ceramic membrane fouling by oil-in-water emulsions: A quantitative analysis using DLVO and XDLVO models

  International congress on separation and Purification technology (ISPT), 2024, Zhengzhou, China

- Efficient oilfield-produced water treatment with SiC-coated alumina ultrafiltration membranes

  International Congress on Membranes& Membrane Processes (ICOM), 2023, Chiba, Japan

- Ultrafiltration of nanoemulsions with state-of-art silicon carbide-alumina membranes

  Euromembrane 2022, Sorrento, Italy

Bibliography

1. Greenwood, E.E., T. Lauber, J. van den Hoogen, A. Donmez, R.E.S. Bain, R. Johnston, T.W. Crowther, and T.R. Julian, *Mapping safe drinking water use in low- and middle-income countries.* Science, 2024. **385**(6710): p. 784-790, http://dx.doi.org/10.1126/science.adh9578.
2. Jones, E.R., M.T.H. van Vliet, M. Qadir, and M.F.P. Bierkens, *Country-level and gridded estimates of wastewater production, collection, treatment and reuse.* Earth System Science Data, 2021. **13**(2): p. 237-254, http://dx.doi.org/10.5194/essd-13-237-2021.
3. Wang, X., K. Sun, G. Zhang, F. Yang, S. Lin, and Y. Dong, *Robust zirconia ceramic membrane with exceptional performance for purifying nano-emulsion oily wastewater.* Water Research, 2022. **208**, Article 117859, http://dx.doi.org/10.1016/j.watres.2021.117859.
4. Alborzi, A., I.M. Hsieh, D. Reible, and M. Malmali, *Analysis of fouling mechanism in ultrafiltration of produced water.* Journal of Water Process Engineering, 2022. **49**, Article 102978, http://dx.doi.org/10.1016/j.jwpe.2022.102978.
5. Weschenfelder, S.E., M.J.C. Fonseca, B.R.S. Costa, and C.P. Borges, *Influence of the use of surfactants in the treatment of produced water by ceramic membranes.* Journal of Water Process Engineering, 2019. **32**, Article 100955, http://dx.doi.org/10.1016/j.jwpe.2019.100955.
6. Çakmakce, M., N. Kayaalp, and I. Koyuncu, *Desalination of produced water from oil production fields by membrane processes.* Desalination, 2008. **222**(1-3): p. 176-186, http://dx.doi.org/10.1016/j.desal.2007.01.147.
7. Odiete, W.E. and J.C. Agunwamba, *Novel design methods for conventional oil-water separators.* Heliyon, 2019. **5**(5): p. e01620, http://dx.doi.org/10.1016/j.heliyon.2019.e01620.
8. Xu, H.X., J.T. Liu, L.H. Gao, Y.T. Wang, X.W. Deng, and X.B. Li, *Study of Oil Removal Kinetics using Cyclone-Static Microbubble Flotation Column.* Separation Science and Technology, 2014. **49**(8): p. 1170-1177, http://dx.doi.org/10.1080/01496395.2014.881879.
9. El-Hamouz, A., H.S. Hilal, N. Nassar, and Z. Mardawi, *Solid olive waste in environmental cleanup: oil recovery and carbon production for water purification.* J Environ Manage, 2007. **84**(1): p. 83-92, http://dx.doi.org/10.1016/j.jenvman.2006.05.003.
10. Chen, M., S.G.J. Heijman, M.W.J. Luiten-Olieman, and L.C. Rietveld, *Oil-in-water emulsion separation: Fouling of alumina membranes with and without a silicon carbide deposition in constant flux filtration mode.* Water Res, 2022. **216**, Article 118267, http://dx.doi.org/10.1016/j.watres.2022.118267.
11. Yu, L., M. Han, and F. He, *A review of treating oily wastewater.* Arabian Journal of Chemistry, 2017. **10**: p. S1913-S1922, http://dx.doi.org/10.1016/j.arabjc.2013.07.020.
12. Hejase, C.A. and V.V. Tarabara, *Nanofiltration of saline oil-water emulsions: Combined and individual effects of salt concentration polarization and fouling by oil.* Journal of Membrane Science, 2021. **617**, Article 118607, http://dx.doi.org/10.1016/j.memsci.2020.118607.
13. Kirschner, A.Y., Y.-H. Cheng, D.R. Paul, R.W. Field, and B.D. Freeman, *Fouling mechanisms in constant flux crossflow ultrafiltration.* Journal of Membrane Science, 2019. **574**: p. 65-75, http://dx.doi.org/10.1016/j.memsci.2018.12.001.
14. Lu, D., T. Zhang, and J. Ma, *Ceramic membrane fouling during ultrafiltration of oil/water emulsions: roles played by stabilization surfactants of oil droplets.* Environ Sci Technol, 2015. **49**(7): p. 4235-4244, http://dx.doi.org/10.1021/es505572y.
15. Qin, G., A. Jan, Q. An, H. Zhou, L.C. Rietveld, and S.G.J. Heijman, *Chemical vapor deposition of silicon carbide on alumina ultrafiltration membranes for filtration of microemulsions.* Desalination, 2024. **582**, Article 117655, http://dx.doi.org/10.1016/j.desal.2024.117655.
16. Poli, A., R. Sfeir, A. Ferreira Santos, M. Jacob, P.B. Andrey, C. Batiot-Dupeyrat, and B. Teychene, *Backwashable dynamic membrane made of anchored CNT on SiC microfiltration membranes applied to oil in water emulsion filtration.* Separation and Purification Technology, 2021. **278**, Article 119566, http://dx.doi.org/10.1016/j.seppur.2021.119566.
17. Hotza, D., M. Di Luccio, M. Wilhelm, Y. Iwamoto, S. Bernard, and J.C. Diniz da Costa, *Silicon carbide filters and porous membranes: A review of processing, properties, performance and application.* Journal of Membrane Science, 2020. **610**, http://dx.doi.org/10.1016/j.memsci.2020.118193.
18. Chang, H., T. Li, B. Liu, R.D. Vidic, M. Elimelech, and J.C. Crittenden, *Potential and implemented membrane-based technologies for the treatment and reuse of flowback and produced water from shale gas and oil plays: A review.* Desalination, 2019. **455**: p. 34-57, http://dx.doi.org/10.1016/j.desal.2019.01.001.
19. Asif, M.B. and Z. Zhang, *Ceramic membrane technology for water and wastewater treatment: A critical review of performance, full-scale applications, membrane fouling and prospects.* Chemical Engineering Journal, 2021. **418**, Article 129481, http://dx.doi.org/10.1016/j.cej.2021.129481.

20. Zhu, Y., W. Xie, F. Zhang, T. Xing, and J. Jin, *Superhydrophilic In-Situ-Cross-Linked Zwitterionic Polyelectrolyte/PVDF-Blend Membrane for Highly Efficient Oil/Water Emulsion Separation.* ACS Appl Mater Interfaces, 2017. **9**(11): p. 9603-9613, http://dx.doi.org/10.1021/acsami.6b15682.
21. Xu, M., C. Xu, K.P. Rakesh, Y. Cui, J. Yin, C. Chen, S. Wang, B. Chen, and L. Zhu, *Hydrophilic SiC hollow fiber membranes for low fouling separation of oil-in-water emulsions with high flux.* RSC Adv, 2020. **10**(8): p. 4832-4839, http://dx.doi.org/10.1039/c9ra06695k.
22. Browne, M.A., P. Crump, S.J. Niven, E. Teuten, A. Tonkin, T. Galloway, and R. Thompson, *Accumulation of microplastic on shorelines woldwide: sources and sinks.* Environ Sci Technol, 2011. **45**(21): p. 9175-9179, http://dx.doi.org/10.1021/es201811s.
23. Kim, S. and C. Park, *Potential of ceramic ultrafiltration membranes for the treatment of anionic surfactants in laundry wastewater for greywater reuse.* Journal of Water Process Engineering, 2021. **44**, Article 102373, http://dx.doi.org/10.1016/j.jwpe.2021.102373.
24. Bortot Coelho, F.E., S.I. Sohn, V.M. Candelario, N.I.B. Hartmann, C. Hélix-Nielsen, and W. Zhang, *Microplastics removal from a hospital laundry wastewater combining ceramic membranes and a photocatalytic membrane reactor: Fouling mitigation, water reuse, and cost estimation.* Journal of Membrane Science, 2025. **715**, Article 123485, http://dx.doi.org/10.1016/j.memsci.2024.123485.
25. Wang, Y., Y. Liu, Z. Chen, Y. Liu, J. Guo, W. Zhang, P. Rao, and G. Li, *Recent progress in the pore size control of silicon carbide ceramic membranes.* Ceramics International, 2022. **48**(7): p. 8960-8971, http://dx.doi.org/10.1016/j.ceramint.2022.01.092.
26. Li, S., C. Wei, L. Zhou, P. Wang, Q. Meng, and Z. Xie, *Sol-gel derived zirconia membrane on silicon carbide substrate.* Journal of the European Ceramic Society, 2019. **39**(13): p. 3804-3811, http://dx.doi.org/10.1016/j.jeurceramsoc.2019.04.054.
27. Li, S., Y. Li, C. Wei, P. Wang, P. Gao, L. Zhou, and G. Wen, *One step co-sintering of silicon carbide ceramic membrane with the aid of boron carbide.* Journal of the European Ceramic Society, 2021. **41**(2): p. 1181-1188, http://dx.doi.org/10.1016/j.jeurceramsoc.2020.09.065.
28. Jiang, Q., B. Lin, Z. Zhong, Y. Fan, and W. Xing, *Ultra-low temperature co-sintering of water glass (WG)-bonded silicon carbide ceramic membranes for oil-water separation.* Journal of Membrane Science, 2024. **692**, Article 122311, http://dx.doi.org/10.1016/j.memsci.2023.122311.
29. Chen, M., R. Shang, P.M. Sberna, M.W.J. Luiten-Olieman, L.C. Rietveld, and S.G.J. Heijman, *Highly permeable silicon carbide-alumina ultrafiltration membranes for oil-in-water filtration produced with low-pressure chemical vapor deposition.* Separation and Purification Technology, 2020. **253**, Article 117496, http://dx.doi.org/10.1016/j.seppur.2020.117496.
30. König, K., V. Boffa, B. Buchbjerg, A. Farsi, M.L. Christensen, G. Magnacca, and Y. Yue, *One-step deposition of ultrafiltration SiC membranes on macroporous SiC supports.* Journal of Membrane Science, 2014. **472**: p. 232-240, http://dx.doi.org/10.1016/j.memsci.2014.08.058.
31. Trevisan, M., J. Vicente, R. Ghidossi, A. Vincent, and P. Moulin, *Membrane characterisation from the support to the skin layer: Application to silicon carbide (SiC) membranes.* Journal of the European Ceramic Society, 2022. **42**(9): p. 3759-3769, http://dx.doi.org/10.1016/j.jeurceramsoc.2022.02.045.
32. Fraga, M.C., S. Sanches, V.J. Pereira, J.G. Crespo, L. Yuan, J. Marcher, M.V.M. de Yuso, E. Rodríguez-Castellón, and J. Benavente, *Morphological, chemical surface and filtration characterization of a new silicon carbide membrane.* Journal of the European Ceramic Society, 2017. **37**(3): p. 899-905, http://dx.doi.org/10.1016/j.jeurceramsoc.2016.10.007.
33. Zanurin, A., N.A. Johari, J. Alias, H. Mas Ayu, N. Redzuan, and S. Izman, *Research progress of sol-gel ceramic coating: A review.* Materials Today: Proceedings, 2022. **48**: p. 1849-1854, http://dx.doi.org/10.1016/j.matpr.2021.09.203.
34. Wang, Z., Y.-M. Wei, Z.-L. Xu, Y. Cao, Z.-Q. Dong, and X.-L. Shi, *Preparation, characterization and solvent resistance of γ-Al2O3/α-Al2O3 inorganic hollow fiber nanofiltration membrane.* Journal of Membrane Science, 2016. **503**: p. 69-80, http://dx.doi.org/10.1016/j.memsci.2015.12.039.
35. Simonenko, E.P., N.P. Simonenko, E.K. Papynov, O.O. Shichalin, A.V. Golub, V.Y. Mayorov, V.A. Avramenko, V.G. Sevastyanov, and N.T. Kuznetsov, *Preparation of porous SiC-ceramics by sol–gel and spark plasma sintering.* Journal of Sol-Gel Science and Technology, 2017. **82**(3): p. 748-759, http://dx.doi.org/10.1007/s10971-017-4367-2.
36. Zou, D., Z. Zhong, and Y. Fan, *Co-sintered ceramic membranes for separation applications: Where are we and where to go?* Separation and Purification Technology, 2024. **338**, http://dx.doi.org/10.1016/j.seppur.2024.126441.
37. Zhu, W., Y. Liu, K. Guan, C. Peng, W. Qiu, and J. Wu, *Integrated preparation of alumina microfiltration membrane with super permeability and high selectivity.* Journal of the European Ceramic Society, 2019. **39**(4): p. 1316-1323, http://dx.doi.org/10.1016/j.jeurceramsoc.2018.10.022.

38. Zou, D., S. Ni, H. Yao, C. Hu, Z.-X.N. Low, and Z. Zhong, *Co-sintering of ceramic ultrafiltration membrane with gradient pore structures for separation of dye/salt wastewater.* Separation and Purification Technology, 2022. **302**, http://dx.doi.org/10.1016/j.seppur.2022.122030.
39. Greene, J.E., *Chapter 12 - Thin Film Nucleation, Growth, and Microstructural Evolution: An Atomic Scale View*, in *Handbook of Deposition Technologies for Films and Coatings (Third Edition)*, P.M. Martin, Editor. 2010, William Andrew Publishing: Boston. p. 554-620.
40. Akamatsu, K., K. Sato, S.-i. Nakao, and X.-l. Wang, *Dimethoxydimethylsilane-derived silica membranes prepared by chemical vapor deposition at 973 K exhibiting improved thermal/hydrothermal stability.* Journal of Membrane Science, 2024. **692**, http://dx.doi.org/10.1016/j.memsci.2023.122293.
41. Morosanu, C.E., *Thin films by chemical vapour deposition*. Vol. 7. 2016: Elsevier.
42. Jan, A., M. Chen, M. Nijboer, M.W.J. Luiten-Olieman, L.C. Rietveld, and S.G.J. Heijman, *Effect of Long-Term Sodium Hypochlorite Cleaning on Silicon Carbide Ultrafiltration Membranes Prepared via Low-Pressure Chemical Vapor Deposition.* Membranes, 2024. **14**(1), http://dx.doi.org/10.3390/membranes14010022.
43. Gu, Q., T.C.A. Ng, Y. Bao, H.Y. Ng, S.C. Tan, and J. Wang, *Developing better ceramic membranes for water and wastewater Treatment: Where microstructure integrates with chemistry and functionalities.* Chemical Engineering Journal, 2022. **428**, Article 130456, http://dx.doi.org/10.1016/j.cej.2021.130456.
44. Morana, B., G. Pandraud, J.F. Creemer, and P.M. Sarro, *Characterization of LPCVD amorphous silicon carbide (a-SiC) as material for electron transparent windows.* Materials Chemistry and Physics, 2013. **139**(2-3): p. 654-662, http://dx.doi.org/10.1016/j.matchemphys.2013.02.013.
45. Chaudhary, R.P., C. Parameswaran, M. Idrees, A.S. Rasaki, C. Liu, Z. Chen, and P. Colombo, *Additive manufacturing of polymer-derived ceramics: Materials, technologies, properties and potential applications.* Progress in Materials Science, 2022. **128**, Article 100969, http://dx.doi.org/10.1016/j.pmatsci.2022.100969.
46. Elyassi, B., M. Sahimi, and T.T. Tsotsis, *Silicon carbide membranes for gas separation applications.* Journal of Membrane Science, 2007. **288**(1-2): p. 290-297, http://dx.doi.org/10.1016/j.memsci.2006.11.027.
47. Zhang, J.-F., X.-N. Zhou, Q. Zhi, S. Zhao, X. Huang, N.-L. Zhang, B. Wang, J.-F. Yang, and K. Ishizaki, *Microstructure and mechanical properties of porous SiC ceramics by carbothermal reduction and subsequent recrystallization sintering.* Journal of Asian Ceramic Societies, 2020. **8**(2): p. 255-264, http://dx.doi.org/10.1080/21870764.2020.1728045.
48. Dickhout, J.M., E. Virga, R.G.H. Lammertink, and W.M. de Vos, *Surfactant specific ionic strength effects on membrane fouling during produced water treatment.* J Colloid Interface Sci, 2019. **556**: p. 12-23, http://dx.doi.org/10.1016/j.jcis.2019.07.068.
49. Dickhout, J.M., J. Moreno, P.M. Biesheuvel, L. Boels, R.G.H. Lammertink, and W.M. de Vos, *Produced water treatment by membranes: A review from a colloidal perspective.* J Colloid Interface Sci, 2017. **487**: p. 523-534, http://dx.doi.org/10.1016/j.jcis.2016.10.013.
50. Tanudjaja, H.J., V.V. Tarabara, A.G. Fane, and J.W. Chew, *Effect of cross-flow velocity, oil concentration and salinity on the critical flux of an oil-in-water emulsion in microfiltration.* Journal of Membrane Science, 2017. **530**: p. 11-19, http://dx.doi.org/https://doi.org/10.1016/j.memsci.2017.02.011.
51. Belhaj, A.F., K.A. Elraies, S.M. Mahmood, N.N. Zulkifli, S. Akbari, and O.S. Hussien, *The effect of surfactant concentration, salinity, temperature, and pH on surfactant adsorption for chemical enhanced oil recovery: a review.* Journal of Petroleum Exploration and Production Technology, 2019. **10**(1): p. 125-137, http://dx.doi.org/10.1007/s13202-019-0685-y.
52. Lobo, A., Á. Cambiella, J.M. Benito, C. Pazos, and J. Coca, *Ultrafiltration of oil-in-water emulsions with ceramic membranes: Influence of pH and crossflow velocity.* Journal of Membrane Science, 2006. **278**(1-2): p. 328-334, http://dx.doi.org/10.1016/j.memsci.2005.11.016.
53. Zhong, Z., W. Xing, and B. Zhang, *Fabrication of ceramic membranes with controllable surface roughness and their applications in oil/water separation.* Ceramics International, 2013. **39**(4): p. 4355-4361, http://dx.doi.org/10.1016/j.ceramint.2012.11.019.
54. Zhang, Y., T. Chen, X. Chen, K. Fu, M. Qiu, and Y. Fan, *The application of pressure-driven ceramic-based membrane for the treatment of saline wastewater and desalination–A review.* Desalination, 2025. **597**, http://dx.doi.org/10.1016/j.desal.2024.118327.
55. Wang, M., J. Wang, and J. Jiang, *Membrane Fouling: Microscopic Insights into the Effects of Surface Chemistry and Roughness.* Advanced Theory and Simulations, 2022. **5**(1): p. 2100395, http://dx.doi.org/https://doi.org/10.1002/adts.202100395.
56. Tian, J., C. Wu, H. Yu, S. Gao, G. Li, F. Cui, and F. Qu, *Applying ultraviolet/persulfate (UV/PS) pre-oxidation for controlling ultrafiltration membrane fouling by natural organic matter (NOM) in surface water.* Water Res, 2018. **132**: p. 190-199, http://dx.doi.org/10.1016/j.watres.2018.01.005.

57. Zaouri, N., L. Gutierrez, L. Dramas, D. Garces, and J.P. Croue, *Interfacial interactions between Skeletonema costatum extracellular organic matter and metal oxides: Implications for ceramic membrane filtration.* Water Res, 2017. **116**: p. 194-202, http://dx.doi.org/10.1016/j.watres.2017.03.034.
58. Nagasawa, H., T. Omura, T. Asai, M. Kanezashi, and T. Tsuru, *Filtration of surfactant-stabilized oil-in-water emulsions with porous ceramic membranes: Effects of membrane pore size and surface charge on fouling behavior.* Journal of Membrane Science, 2020. **610**, Article 118210, http://dx.doi.org/10.1016/j.memsci.2020.118210.
59. Miller, D.J., S. Kasemset, D.R. Paul, and B.D. Freeman, *Comparison of membrane fouling at constant flux and constant transmembrane pressure conditions.* Journal of Membrane Science, 2014. **454**: p. 505-515, http://dx.doi.org/10.1016/j.memsci.2013.12.027.
60. Zhao, D., E. Lau, S. Huang, and C.I. Moraru, *The effect of apple cider characteristics and membrane pore size on membrane fouling.* LWT - Food Science and Technology, 2015. **64**(2): p. 974-979, http://dx.doi.org/10.1016/j.lwt.2015.07.001.
61. Chen, M., L. Zhu, J. Chen, F. Yang, C.Y. Tang, M.D. Guiver, and Y. Dong, *Spinel-based ceramic membranes coupling solid sludge recycling with oily wastewater treatment.* Water Res, 2020. **169**: p. 115180, http://dx.doi.org/10.1016/j.watres.2019.115180.
62. Xue, X., Z. Liang, J. Zhou, H. Zhang, Q. Gu, Z. Zhong, and W. Xing, *Tubular SiC membranes in brine purification: Effects of operational parameters towards low energy consumption process.* Separation and Purification Technology, 2025. **366**, http://dx.doi.org/10.1016/j.seppur.2025.132736.
63. Sim, S.T.V., A.H. Taheri, T.H. Chong, W.B. Krantz, and A.G. Fane, *Colloidal metastability and membrane fouling – Effects of crossflow velocity, flux, salinity and colloid concentration.* Journal of Membrane Science, 2014. **469**: p. 174-187, http://dx.doi.org/10.1016/j.memsci.2014.06.020.
64. Liu, H., X. Tao, H. Zhu, Z. Tang, S. Xu, B. Li, Z. Song, L. Pan, Y. Zhang, and J. Duan, *Effect of operation mode on membrane fouling from traditional Chinese medicine water extracts.* Journal of Water Process Engineering, 2022. **48**, http://dx.doi.org/10.1016/j.jwpe.2022.102943.
65. Jiao, D. and M.M. Sharma, *Mechanism of cake buildup in crossflow filtration of colloidal suspensions.* Journal of Colloid And Interface Science, 1994. **162**(2): p. 454-462, http://dx.doi.org/10.1006/jcis.1994.1060.
66. Le, L.T., K.N. Nguyen, P.T. Nguyen, H.C. Duong, X.T. Bui, N.B. Hoang, and L.D. Nghiem, *Microfibers in laundry wastewater: Problem and solution.* Sci Total Environ, 2022. **852**: p. 158412, http://dx.doi.org/10.1016/j.scitotenv.2022.158412.
67. Talvitie, J., A. Mikola, O. Setala, M. Heinonen, and A. Koistinen, *How well is microlitter purified from wastewater? - A detailed study on the stepwise removal of microlitter in a tertiary level wastewater treatment plant.* Water Res, 2017. **109**: p. 164-172, http://dx.doi.org/10.1016/j.watres.2016.11.046.
68. Barrick, A., A.J. Boardwine, N.H.A. Nguyen, A. Sevcu, J. Novotna, and T.C. Hoang, *Acute toxicity of natural and synthetic clothing fibers towards Daphnia magna: Influence of fiber type and morphology.* Sci Total Environ, 2025. **967**, Article 178751, http://dx.doi.org/10.1016/j.scitotenv.2025.178751.
69. Ladewig, S.M., S. Bao, and A.T. Chow, *Natural Fibers: A Missing Link to Chemical Pollution Dispersion in Aquatic Environments.* Environmental Science & Technology, 2015. **49**(21): p. 12609-12610, http://dx.doi.org/10.1021/acs.est.5b04754.
70. Stanton, T., A. James, M.T. Prendergast-Miller, A. Peirson-Smith, C. KeChi-Okafor, M.D. Gallidabino, A. Namdeo, and K.J. Sheridan, *Natural Fibers: Why Are They Still the Missing Thread in the Textile Fiber Pollution Story?* Environ Sci Technol, 2024. **58**(29): p. 12763-12766, http://dx.doi.org/10.1021/acs.est.4c05126.
71. Kim, S., Y. Hyeon, H. Rho, and C. Park, *Ceramic membranes as a potential high-performance alternative to microplastic filters for household washing machines.* Separation and Purification Technology, 2024. **344**, Article 127278, http://dx.doi.org/10.1016/j.seppur.2024.127278.
72. Kim, S. and C. Park, *Fouling behavior and cleaning strategies of ceramic ultrafiltration membranes for the treatment and reuse of laundry wastewater.* Journal of Water Process Engineering, 2022. **48**, Article 102840, http://dx.doi.org/10.1016/j.jwpe.2022.102840.
73. Zhang, J., K. Peng, Z.K. Xu, Y. Xiong, J. Liu, C. Cai, and X. Huang, *A comprehensive review on the behavior and evolution of oil droplets during oil/water separation by membranes.* Adv Colloid Interface Sci, 2023. **319**: p. 102971, http://dx.doi.org/10.1016/j.cis.2023.102971.
74. Behzad, A., K. Hooghan, C. Aubry, M. Khan, and J. Croue, *SEM-FIB Characterization of Reverse Osmosis Membrane Fouling.* Microscopy and Microanalysis, 2011. **17**(S2): p. 1768-1769, http://dx.doi.org/10.1017/S1431927611009718.
75. Huisman, K.T., B. Blankert, H. Horn, M. Wagner, J.S. Vrouwenvelder, S. Bucs, and L. Fortunato, *Noninvasive monitoring of fouling in membrane processes by optical coherence tomography: A review.* Journal of Membrane Science, 2024. **692**, http://dx.doi.org/10.1016/j.memsci.2023.122291.

76. Tummons, E.N., J.W. Chew, A.G. Fane, and V.V. Tarabara, *Ultrafiltration of saline oil-in-water emulsions stabilized by an anionic surfactant: Effect of surfactant concentration and divalent counterions.* Journal of Membrane Science, 2017. **537**: p. 384-395, http://dx.doi.org/https://doi.org/10.1016/j.memsci.2017.05.012.
77. Tanis-Kanbur, M.B., N.R. Tamilselvam, H.Y. Lai, and J.W. Chew, *Impact of Particle Shape and Surface Group on Membrane Fouling.* Membranes (Basel), 2022. **12**(4), http://dx.doi.org/10.3390/membranes12040403.
78. Rodenas, T. and G. Prieto, *FIB-SEM tomography in catalysis and electrochemistry.* Catalysis Today, 2022. **405-406**: p. 2-13, http://dx.doi.org/10.1016/j.cattod.2022.09.013.
79. Aubry, C., M.T. Khan, A.R. Behzad, D.H. Anjum, L. Gutierrez, and J.-P. Croue, *Cross-sectional analysis of fouled SWRO membranes by STEM–EDS.* Desalination, 2014. **333**(1): p. 118-125, http://dx.doi.org/10.1016/j.desal.2013.11.033.
80. Ferlita, R.R., D. Phipps, J. Safarik, and D.H. Yeh, *Cryo-snap: A simple modified freeze-fracture method for SEM imaging of membrane cross-sections.* Environmental Progress, 2008. **27**(2): p. 204-209, http://dx.doi.org/10.1002/ep.10270.
81. Lin, Y.M., C. Song, and G.C. Rutledge, *Direct Three-Dimensional Visualization of Membrane Fouling by Confocal Laser Scanning Microscopy.* ACS Appl Mater Interfaces, 2019. **11**(18): p. 17001-17008, http://dx.doi.org/10.1021/acsami.9b01770.
82. Trinh, T.A., W. Li, Q. Han, X. Liu, A.G. Fane, and J.W. Chew, *Analyzing external and internal membrane fouling by oil emulsions via 3D optical coherence tomography.* Journal of Membrane Science, 2018. **548**: p. 632-640, http://dx.doi.org/10.1016/j.memsci.2017.10.043.
83. Li, D., J. Zhai, K. Wang, Y. Shen, and X. Huang, *Three-Dimensional Reconstruction-Characterization of Polymeric Membranes: A Review.* Environ Sci Technol, 2025. **59**(6): p. 2891-2916, http://dx.doi.org/10.1021/acs.est.4c09734.
84. Trinh, T.A., W. Li, and J.W. Chew, *Internal fouling during microfiltration with foulants of different surface charges.* Journal of Membrane Science, 2020. **602**, Article 117983, http://dx.doi.org/10.1016/j.memsci.2020.117983.
85. Zhang, C., Y. Qu, J. Liu, Q. Chen, M. Shao, W. Li, and Q. Xu, *Unraveling the role of NaCl on microfiltration fouling: Insights from In situ analysis of dynamic interfacial behaviors.* Journal of Membrane Science, 2024. **690**, Article 122223, http://dx.doi.org/10.1016/j.memsci.2023.122223.
86. Tanudjaja, H.J., N.A. Amin, A. Qamar, S. Kerdi, H. Basamh, T. Altmann, R. Das, and N. Ghaffour, *Precise biofilm thickness prediction in SWRO desalination from planar camera images by DNN models.* npj Clean Water, 2025. **8**(1), http://dx.doi.org/10.1038/s41545-025-00451-9.
87. Tummons, E.N., V.V. Tarabara, Jia W. Chew, and A.G. Fane, *Behavior of oil droplets at the membrane surface during crossflow microfiltration of oil–water emulsions.* Journal of Membrane Science, 2016. **500**: p. 211-224, http://dx.doi.org/10.1016/j.memsci.2015.11.005.
88. Abdel-Aty, A.A.R., Y.S.A. Aziz, R.M.G. Ahmed, I.M.A. ElSherbiny, S. Panglisch, M. Ulbricht, and A.S.G. Khalil, *High performance isotropic polyethersulfone membranes for heavy oil-in-water emulsion separation.* Separation and Purification Technology, 2020. **253**, http://dx.doi.org/10.1016/j.seppur.2020.117467.
89. Wang, X., K. Sun, G. Zhang, F. Yang, S. Lin, and Y. Dong, *Robust zirconia ceramic membrane with exceptional performance for purifying nano-emulsion oily wastewater.* Water Research, 2022. **208**: p. 117859,
90. Pan, Z., S. Cao, J. Li, Z. Du, and F. Cheng, *Anti-fouling TiO2 nanowires membrane for oil/water separation: Synergetic effects of wettability and pore size.* Journal of Membrane Science, 2019. **572**: p. 596-606, http://dx.doi.org/10.1016/j.memsci.2018.11.056.
91. Sano, T., Y. Kawagoshi, I. Kokubo, H. Ito, K. Ishida, and A. Sato, *Direct and indirect effects of membrane pore size on fouling development in a submerged membrane bioreactor with a symmetric chlorinated poly (vinyl chloride) flat-sheet membrane.* Journal of Environmental Chemical Engineering, 2022. **10**(2), http://dx.doi.org/10.1016/j.jece.2021.107023.
92. Jiang, Q., Y. Wang, Y. Xie, M. Zhou, Q. Gu, Z. Zhong, and W. Xing, *Silicon carbide microfiltration membranes for oil-water separation: Pore structure-dependent wettability matters.* Water Res, 2022. **216**, Article 118270, http://dx.doi.org/10.1016/j.watres.2022.118270.
93. He, Z., S. Kasemset, A.Y. Kirschner, Y.H. Cheng, D.R. Paul, and B.D. Freeman, *The effects of salt concentration and foulant surface charge on hydrocarbon fouling of a poly(vinylidene fluoride) microfiltration membrane.* Water Res, 2017. **117**: p. 230-241, http://dx.doi.org/10.1016/j.watres.2017.03.051.
94. Trinh, T.A., Q. Han, Y. Ma, and J.W. Chew, *Microfiltration of oil emulsions stabilized by different surfactants.* Journal of Membrane Science, 2019. **579**: p. 199-209, http://dx.doi.org/10.1016/j.memsci.2019.02.068.

95. Hofs, B., J. Ogier, D. Vries, E.F. Beerendonk, and E.R. Cornelissen, *Comparison of ceramic and polymeric membrane permeability and fouling using surface water.* Separation and Purification Technology, 2011. **79**(3): p. 365-374, http://dx.doi.org/10.1016/j.seppur.2011.03.025.
96. Wang, S., H. Xia, J. Mi, M. Wu, S. Yang, R. Xu, X. Li, L. Zhu, M. Xu, and Y. Dong, *Fabrication of high-performance recrystallized silicon carbide ceramic membrane based on particle packing optimization.* Journal of Membrane Science, 2024. **705**, http://dx.doi.org/10.1016/j.memsci.2024.122922.
97. Zhu, L., W. Wang, P. Zhao, S. Wang, K. Yang, H. Shi, M. Xu, and Y. Dong, *Silicon carbide catalytic ceramic membranes with nano-wire structure for enhanced anti-fouling performance.* Water Res, 2022. **226**, Article 119209, http://dx.doi.org/10.1016/j.watres.2022.119209.
98. Boffa, V., C. Lunghi, C.A. Quist-Jensen, G. Magnacca, and P. Calza, *Fabrication and Surface Interactions of Super-Hydrophobic Silicon Carbide for Membrane Distillation.* Nanomaterials (Basel), 2019. **9**(8), http://dx.doi.org/10.3390/nano9081159.
99. Skibinski, B., P. Müller, and W. Uhl, *Rejection of submicron sized particles from swimming pool water by a monolithic SiC microfiltration membrane: Relevance of steric and electrostatic interactions.* Journal of Membrane Science, 2016. **499**: p. 92-104, http://dx.doi.org/10.1016/j.memsci.2015.10.033.
100. Eray, E., V. Boffa, M.K. Jørgensen, G. Magnacca, and V.M. Candelario, *Enhanced fabrication of silicon carbide membranes for wastewater treatment: From laboratory to industrial scale.* Journal of Membrane Science, 2020. **606**, Article 118080, http://dx.doi.org/10.1016/j.memsci.2020.118080.
101. Hu, X., R. Wang, S. Xia, G. Li, L. Yan, P. Rao, W. Zhang, and Y. Chen, *Polyethyleneimine-enhanced silicon carbide membranes for efficient oil-water separation in high-temperature condensate.* Separation and Purification Technology, 2024. **330**, Article 125503, http://dx.doi.org/10.1016/j.seppur.2023.125503.
102. Lee, S.-J., M. Dilaver, P.-K. Park, and J.-H. Kim, *Comparative analysis of fouling characteristics of ceramic and polymeric microfiltration membranes using filtration models.* Journal of Membrane Science, 2013. **432**: p. 97-105, http://dx.doi.org/10.1016/j.memsci.2013.01.013.
103. Lee, S. and J. Cho, *Comparison of ceramic and polymeric membranes for natural organic matter (NOM) removal.* Desalination, 2004. **160**(3): p. 223-232, http://dx.doi.org/https://doi.org/10.1016/S0011-9164(04)90025-2.
104. Mustafa, G., K. Wyns, P. Vandezande, A. Buekenhoudt, and V. Meynen, *Novel grafting method efficiently decreases irreversible fouling of ceramic nanofiltration membranes.* Journal of Membrane Science, 2014. **470**: p. 369-377, http://dx.doi.org/10.1016/j.memsci.2014.07.050.
105. Lu, D., T. Zhang, L. Gutierrez, J. Ma, and J.P. Croue, *Influence of Surface Properties of Filtration-Layer Metal Oxide on Ceramic Membrane Fouling during Ultrafiltration of Oil/Water Emulsion.* Environ Sci Technol, 2016. **50**(9): p. 4668-4674, http://dx.doi.org/10.1021/acs.est.5b04151.
106. Weber, R., H. Chmiel, and V. Mavrov, *Characteristics and application of new ceramic nanofiltration membranes.* Desalination, 2003. **157**(1): p. 113-125, http://dx.doi.org/https://doi.org/10.1016/S0011-9164(03)00390-4.
107. Son, J.-W., E.-H. Sim, N.-C. Choi, S.-B. Kim, and C.-Y. Park, *Comparative analysis for fouling characteristics of river water, secondary effluent, and humic acid solution in ceramic membrane ultrafiltration.* Separation Science and Technology, 2017. **52**(13): p. 2199-2211, http://dx.doi.org/10.1080/01496395.2017.1331245.
108. Tsuru, T., D. Hironaka, T. Yoshioka, and M. Asaeda, *Titania membranes for liquid phase separation: effect of surface charge on flux.* Separation and Purification Technology, 2001. **25**(1): p. 307-314, http://dx.doi.org/https://doi.org/10.1016/S1383-5866(01)00057-0.
109. Zhao, Y.-y., X.-m. Wang, H.-w. Yang, and Y.-f.F. Xie, *Effects of organic fouling and cleaning on the retention of pharmaceutically active compounds by ceramic nanofiltration membranes.* Journal of Membrane Science, 2018. **563**: p. 734-742, http://dx.doi.org/10.1016/j.memsci.2018.06.047.
110. Dobrak, A., B. Verrecht, H. Van den Dungen, A. Buekenhoudt, I.F.J. Vankelecom, and B. Van der Bruggen, *Solvent flux behavior and rejection characteristics of hydrophilic and hydrophobic mesoporous and microporous TiO2 and ZrO2 membranes.* Journal of Membrane Science, 2010. **346**(2): p. 344-352, http://dx.doi.org/10.1016/j.memsci.2009.09.059.
111. Bai, Z., R. Zhang, S. Wang, S. Gao, and J. Tian, *Membrane fouling behaviors of ceramic hollow fiber microfiltration (MF) membranes by typical organic matters.* Separation and Purification Technology, 2021. **274**, http://dx.doi.org/10.1016/j.seppur.2021.118951.
112. Moritz, T., S. Benfer, P. Árki, and G. Tomandl, *Influence of the surface charge on the permeate flux in the dead-end filtration with ceramic membranes.* Separation and Purification Technology, 2001. **25**(1): p. 501-508, http://dx.doi.org/https://doi.org/10.1016/S1383-5866(01)00080-6.

113. Zhang, Q., W. Jing, Y. Fan, and N. Xu, *An improved Parks equation for prediction of surface charge properties of composite ceramic membranes.* Journal of Membrane Science, 2008. **318**(1-2): p. 100-106, http://dx.doi.org/10.1016/j.memsci.2008.02.004.
114. Chevereau, E., N. Zouaoui, L. Limousy, P. Dutournié, S. Déon, and P. Bourseau, *Surface properties of ceramic ultrafiltration TiO2 membranes: Effects of surface equilibriums on salt retention.* Desalination, 2010. **255**(1-3): p. 1-8, http://dx.doi.org/10.1016/j.desal.2009.12.007.
115. Kujawa, J., S. Al-Gharabli, W. Kujawski, and K. Knozowska, *Molecular Grafting of Fluorinated and Nonfluorinated Alkylsiloxanes on Various Ceramic Membrane Surfaces for the Removal of Volatile Organic Compounds Applying Vacuum Membrane Distillation.* ACS Appl Mater Interfaces, 2017. **9**(7): p. 6571-6590, http://dx.doi.org/10.1021/acsami.6b14835.
116. Kim, K.J. and A. Jang, *Presence of Fe-Al binary oxide adsorbent cake layer in ceramic membrane filtration and their impact for removal of HA and BSA.* Chemosphere, 2018. **196**: p. 440-452, http://dx.doi.org/10.1016/j.chemosphere.2018.01.011.
117. López, J., M. Reig, X. Vecino, O. Gibert, and J.L. Cortina, *Comparison of acid-resistant ceramic and polymeric nanofiltration membranes for acid mine waters treatment.* Chemical Engineering Journal, 2020. **382**, Article 122786, http://dx.doi.org/10.1016/j.cej.2019.122786.
118. Puhlfürß, P., A. Voigt, R. Weber, and M. Morbé, *Microporous TiO2 membranes with a cut off <500 Da.* Journal of Membrane Science, 2000. **174**(1): p. 123-133, http://dx.doi.org/10.1016/S0376-7388(00)00380-X.
119. Van Gestel, T., C. Vandecasteele, A. Buekenhoudt, C. Dotremont, J. Luyten, R. Leysen, B. Van der Bruggen, and G. Maes, *Salt retention in nanofiltration with multilayer ceramic TiO2 membranes.* Journal of Membrane Science, 2002. **209**(2): p. 379-389, http://dx.doi.org/10.1016/S0376-7388(02)00311-3.
120. Árki, P., C. Hecker, G. Tomandl, and Y. Joseph, *Streaming potential properties of ceramic nanofiltration membranes – Importance of surface charge on the ion rejection.* Separation and Purification Technology, 2019. **212**: p. 660-669, http://dx.doi.org/10.1016/j.seppur.2018.11.054.
121. Wadekar, S.S. and R.D. Vidic, *Comparison of ceramic and polymeric nanofiltration membranes for treatment of abandoned coal mine drainage.* Desalination, 2018. **440**: p. 135-145, http://dx.doi.org/10.1016/j.desal.2018.01.008.
122. Shang, R., A.R.D. Verliefde, J. Hu, S.G.J. Heijman, and L.C. Rietveld, *The impact of EfOM, NOM and cations on phosphate rejection by tight ceramic ultrafiltration.* Separation and Purification Technology, 2014. **132**: p. 289-294, http://dx.doi.org/10.1016/j.seppur.2014.05.024.
123. Li, C., W. Sun, Z. Lu, X. Ao, C. Yang, and S. Li, *Systematic evaluation of TiO2-GO-modified ceramic membranes for water treatment: Retention properties and fouling mechanisms.* Chemical Engineering Journal, 2019. **378**, http://dx.doi.org/10.1016/j.cej.2019.122138.
124. Xu, D., X. Luo, P. Jin, J. Zhu, X. Zhang, J. Zheng, L. Yang, X. Zhu, H. Liang, and B. Van der Bruggen, *A novel ceramic-based thin-film composite nanofiltration membrane with enhanced performance and regeneration potential.* Water Res, 2022. **215**: p. 118264, http://dx.doi.org/10.1016/j.watres.2022.118264.
125. Lee, S.J. and J.H. Kim, *Differential natural organic matter fouling of ceramic versus polymeric ultrafiltration membranes.* Water Res, 2014. **48**: p. 43-51, http://dx.doi.org/10.1016/j.watres.2013.08.038.
126. Gao, N., M. Li, W. Jing, Y. Fan, and N. Xu, *Improving the filtration performance of ZrO2 membrane in non-polar organic solvents by surface hydrophobic modification.* Journal of Membrane Science, 2011. **375**(1-2): p. 276-283, http://dx.doi.org/10.1016/j.memsci.2011.03.056.
127. Bartels, J., A.G. Batista, S. Kroll, M. Maas, and K. Rezwan, *Hydrophobic ceramic capillary membranes for versatile virus filtration.* Journal of Membrane Science, 2019. **570-571**: p. 85-92, http://dx.doi.org/10.1016/j.memsci.2018.10.022.
128. Zhou, J.-e., Q. Chang, Y. Wang, J. Wang, and G. Meng, *Separation of stable oil–water emulsion by the hydrophilic nano-sized ZrO2 modified Al2O3 microfiltration membrane.* Separation and Purification Technology, 2010. **75**(3): p. 243-248, http://dx.doi.org/10.1016/j.seppur.2010.08.008.
129. Gao, N., Y. Fan, X. Quan, Y. Cai, and D. Zhou, *Modified ceramic membranes for low fouling separation of water-in-oil emulsions.* Journal of Materials Science, 2016. **51**(13): p. 6379-6388, http://dx.doi.org/10.1007/s10853-016-9934-3.
130. Gao, N., W. Fan, and Z.-K. Xu, *Ceramic membrane with protein-resistant surface via dopamine/diglycolamine co-deposition.* Separation and Purification Technology, 2020. **234**, Article 116135, http://dx.doi.org/10.1016/j.seppur.2019.116135.
131. Kujawa, J., W. Kujawski, S. Cerneaux, G. Li, and S. Al-Gharabli, *Zirconium dioxide membranes decorated by silanes based-modifiers for membrane distillation – Material chemistry approach.* Journal of Membrane Science, 2020. **596**, http://dx.doi.org/10.1016/j.memsci.2019.117597.

132. Da, X., X. Chen, B. Sun, J. Wen, M. Qiu, and Y. Fan, *Preparation of zirconia nanofiltration membranes through an aqueous sol–gel process modified by glycerol for the treatment of wastewater with high salinity.* Journal of Membrane Science, 2016. **504**: p. 29-39, http://dx.doi.org/10.1016/j.memsci.2015.12.068.
133. Zhang, X., *Electrokinetic property of ZrO2/cordierite composite MF membrane and its influence on the permeate flux.* Desalination, 2009. **249**(1): p. 364-367, http://dx.doi.org/10.1016/j.desal.2009.06.041.
134. Wegmann, M., B. Michen, T. Luxbacher, J. Fritsch, and T. Graule, *Modification of ceramic microfilters with colloidal zirconia to promote the adsorption of viruses from water.* Water Res, 2008. **42**(6-7): p. 1726-1734, http://dx.doi.org/10.1016/j.watres.2007.10.030.
135. Chong, J.Y. and R. Wang, *From micro to nano: Polyamide thin film on microfiltration ceramic tubular membranes for nanofiltration.* Journal of Membrane Science, 2019. **587**, Article 117161, http://dx.doi.org/10.1016/j.memsci.2019.06.001.
136. Chiu, T.Y., *Effect of ageing on the microfiltration performance of ceramic membranes.* Separation and Purification Technology, 2011. **83**: p. 106-113, http://dx.doi.org/10.1016/j.seppur.2011.09.022.
137. Liu, Z., X. Zhu, P. Liang, X. Zhang, K. Kimura, and X. Huang, *Distinction between polymeric and ceramic membrane in AnMBR treating municipal wastewater: In terms of irremovable fouling.* Journal of Membrane Science, 2019. **588**, Article 117229, http://dx.doi.org/10.1016/j.memsci.2019.117229.
138. Ahmad, N.A., C.P. Leo, and A.L. Ahmad, *Superhydrophobic alumina membrane by steam impingement: Minimum resistance in microfiltration.* Separation and Purification Technology, 2013. **107**: p. 187-194, http://dx.doi.org/10.1016/j.seppur.2013.01.011.
139. Luo, X., C.Y. Tang, X. Zhu, D. Xu, J. Xing, D. Lin, Y. Liu, L. Yang, J. Song, Z. Gan, G. Li, and H. Liang, *Tunable isoporous ceramic membranes towards precise sieving of nanoparticles and proteins.* Journal of Membrane Science, 2021. **634**, Article 119391, http://dx.doi.org/10.1016/j.memsci.2021.119391.
140. Su, X., D. Xing, Z. Song, W. Dong, M. Zhang, L. Feng, M. Wang, and F. Sun, *Understanding the effects of electrical exposure mode on membrane fouling in an electric anaerobic ceramic membrane bioreactor.* Journal of Membrane Science, 2022. **659**, Article 120756, http://dx.doi.org/10.1016/j.memsci.2022.120756.
141. Park, H. and H. Choi, *As(III) removal by hybrid reactive membrane process combined with ozonation.* Water Res, 2011. **45**(5): p. 1933-1940, http://dx.doi.org/10.1016/j.watres.2010.12.024.
142. Zhao, Y., W. Xing, N. Xu, and F.-S. Wong, *Effects of inorganic electrolytes on zeta potentials of ceramic microfiltration membranes.* Separation and Purification Technology, 2005. **42**(2): p. 117-121, http://dx.doi.org/10.1016/j.seppur.2004.06.011.
143. Zhou, J., X. Zhang, Y. Wang, X. Hu, A. Larbot, and M. Persin, *Electrokinetic characterization of the Al2O3 ceramic MF membrane by streaming potential measurements.* Desalination, 2009. **235**(1): p. 102-109, http://dx.doi.org/10.1016/j.desal.2008.01.013.
144. Wang, S., J. Tian, L. Jia, J. Jia, S. Shan, Q. Wang, and F. Cui, *Removal of aqueous organic contaminants using submerged ceramic hollow fiber membrane coupled with peroxymonosulfate oxidation: Comparison of CuO catalyst dispersed in the feed water and immobilized on the membrane.* Journal of Membrane Science, 2021. **618**, Article 118707, http://dx.doi.org/10.1016/j.memsci.2020.118707.
145. Park, H., Y. Kim, B. An, and H. Choi, *Characterization of natural organic matter treated by iron oxide nanoparticle incorporated ceramic membrane-ozonation process.* Water Res, 2012. **46**(18): p. 5861-5870, http://dx.doi.org/10.1016/j.watres.2012.07.039.
146. Elzo, D., I. Huisman, E. Middelink, and V. Gekas, *Charge effects on inorganic membrane performance in a cross-flow microfiltration process.* Colloids and Surfaces A: Physicochemical and Engineering Aspects, 1998. **138**(2): p. 145-159, http://dx.doi.org/10.1016/S0927-7757(96)03957-X.
147. Zhang, Q., Y. Fan, and N. Xu, *Effect of the surface properties on filtration performance of Al2O3–TiO2 composite membrane.* Separation and Purification Technology, 2009. **66**(2): p. 306-312, http://dx.doi.org/10.1016/j.seppur.2008.12.010.
148. He, H., W. Jing, W. Xing, and Y. Fan, *Improving protein resistance of α-Al2O3 membranes by modification with POEGMA brushes.* Applied Surface Science, 2011. **258**(3): p. 1038-1044, http://dx.doi.org/10.1016/j.apsusc.2011.08.121.
149. Bao, Y., W.-D. Oh, T.-T. Lim, R. Wang, R.D. Webster, and X. Hu, *Surface-nucleated heterogeneous growth of zeolitic imidazolate framework – A unique precursor towards catalytic ceramic membranes: Synthesis, characterization and organics degradation.* Chemical Engineering Journal, 2018. **353**: p. 69-79, http://dx.doi.org/10.1016/j.cej.2018.07.117.
150. Gao, N. and Z.-K. Xu, *Ceramic membranes with mussel-inspired and nanostructured coatings for water-in-oil emulsions separation.* Separation and Purification Technology, 2019. **212**: p. 737-746, http://dx.doi.org/10.1016/j.seppur.2018.11.084.

151. Qin, G., *The effect of surface charge on threshold flux and fouling behavior of silicon carbide membrane with O/W emulsion and sodium alginate solution as typical pollutants.* 2021,
152. Chen, M., S.G.J. Heijman, M.W.J. Luiten-Olieman, and L.C. Rietveld, *Oil-in-water emulsion separation: Fouling of alumina membranes with and without a silicon carbide deposition in constant flux filtration mode.* Water Res, 2022. **216**: p. 118267, http://dx.doi.org/10.1016/j.watres.2022.118267.
153. Wan Ikhsan, S.N., N. Yusof, F. Aziz, A.F. Ismail, J. Jaafar, W.N. Wan Salleh, and N. Misdan, *Superwetting materials for hydrophilic-oleophobic membrane in oily wastewater treatment.* J Environ Manage, 2021. **290**: p. 112565, http://dx.doi.org/10.1016/j.jenvman.2021.112565.
154. Ahmad, N.A., P.S. Goh, Z. Abdul Karim, and A.F. Ismail, *Thin Film Composite Membrane for Oily Waste Water Treatment: Recent Advances and Challenges.* Membranes (Basel), 2018. **8**(4), http://dx.doi.org/10.3390/membranes8040086.
155. Gupta, A., H.B. Eral, T.A. Hatton, and P.S. Doyle, *Nanoemulsions: formation, properties and applications.* Soft Matter, 2016. **12**(11): p. 2826-2841, http://dx.doi.org/10.1039/c5sm02958a.
156. McClements, D.J., *Nanoemulsions versus microemulsions: terminology, differences, and similarities.* Soft Matter, 2012. **8**(6): p. 1719-1729, http://dx.doi.org/10.1039/c2sm06903b.
157. Anis, S.F., B.S. Lalia, R. Hashaikeh, and N. Hilal, *Hierarchical underwater oleophobic electro-ceramic/carbon nanostructure membranes for highly efficient oil-in-water separation.* Separation and Purification Technology, 2021. **275**, http://dx.doi.org/10.1016/j.seppur.2021.119241.
158. Cheng, Q., D. Ye, C. Chang, and L. Zhang, *Facile fabrication of superhydrophilic membranes consisted of fibrous tunicate cellulose nanocrystals for highly efficient oil/water separation.* Journal of Membrane Science, 2017. **525**: p. 1-8, http://dx.doi.org/10.1016/j.memsci.2016.11.084.
159. Gao, S.J., Y.Z. Zhu, F. Zhang, and J. Jin, *Superwetting polymer-decorated SWCNT composite ultrathin films for ultrafast separation of oil-in-water nanoemulsions.* Journal of Materials Chemistry A, 2015. **3**(6): p. 2895-2902, http://dx.doi.org/10.1039/c4ta05624h.
160. Eray, E., V.M. Candelario, V. Boffa, H. Safafar, D.N. Østedgaard-Munck, N. Zahrtmann, H. Kadrispahic, and M.K. Jørgensen, *A roadmap for the development and applications of silicon carbide membranes for liquid filtration: Recent advancements, challenges, and perspectives.* Chemical Engineering Journal, 2021. **414**, Article 128826, http://dx.doi.org/10.1016/j.cej.2021.128826.
161. Foti, G., *Silicon carbide: from amorphous to crystalline material.* Applied Surface Science, 2001. **184**(1-4): p. 20-26,
162. Pham, H., C. Fan, G. Pandraud, F. Creemer, P. Sarro, N. Van der Pers, P. Visser, and K. Kwakernaak. *Very thin SiC membranes for micromachined vacuum sensors*. in *SENSORS, 2008 IEEE*. 2008. IEEE.
163. Hopkinson, D., M. Zeh, and D. Luebke, *The bubble point of supported ionic liquid membranes using flat sheet supports.* Journal of Membrane Science, 2014. **468**: p. 155-162, http://dx.doi.org/10.1016/j.memsci.2014.05.042.
164. Yan, L., P. Li, W. Zhou, Z. Wang, X. Fan, M. Chen, Y. Fang, and H. Liu, *Shrimp Shell-Inspired Antifouling Chitin Nanofibrous Membrane for Efficient Oil/Water Emulsion Separation with In Situ Removal of Heavy Metal Ions.* ACS Sustainable Chemistry & Engineering, 2019. **7**(2): p. 2064-2072, http://dx.doi.org/10.1021/acssuschemeng.8b04511.
165. Zhan, H., T. Zuo, R. Tao, and C. Chang, *Robust Tunicate Cellulose Nanocrystal/Palygorskite Nanorod Membranes for Multifunctional Oil/Water Emulsion Separation.* ACS Sustainable Chemistry & Engineering, 2018. **6**(8): p. 10833-10840, http://dx.doi.org/10.1021/acssuschemeng.8b02137.
166. Le Clech, P., B. Jefferson, I.S. Chang, and S.J. Judd, *Critical flux determination by the flux-step method in a submerged membrane bioreactor.* Journal of Membrane Science, 2003. **227**(1-2): p. 81-93, http://dx.doi.org/10.1016/j.memsci.2003.07.021.
167. Beier, S.P. and G. Jonsson, *Critical flux determination by flux-stepping.* AIChE Journal, 2009. **56**(7): p. 1739-1747, http://dx.doi.org/10.1002/aic.12099.
168. Shang, R., A. Goulas, C.Y. Tang, X. de Frias Serra, L.C. Rietveld, and S.G.J. Heijman, *Atmospheric pressure atomic layer deposition for tight ceramic nanofiltration membranes: Synthesis and application in water purification.* Journal of Membrane Science, 2017. **528**: p. 163-170, http://dx.doi.org/10.1016/j.memsci.2017.01.023.
169. Huang, B.C., Y.F. Guan, W. Chen, and H.Q. Yu, *Membrane fouling characteristics and mitigation in a coagulation-assisted microfiltration process for municipal wastewater pretreatment.* Water Res, 2017. **123**: p. 216-223, http://dx.doi.org/10.1016/j.watres.2017.06.080.
170. Xing, J., H. Liang, C.J. Chuah, Y. Bao, X. Luo, T. Wang, J. Wang, G. Li, and S.A. Snyder, *Insight into Fe(II)/UV/chlorine pretreatment for reducing ultrafiltration (UF) membrane fouling: Effects of different natural organic fractions and comparison with coagulation.* Water Res, 2019. **167**, Article 115112, http://dx.doi.org/10.1016/j.watres.2019.115112.
171. Li, J., S. Guo, Z. Xu, J. Li, Z. Pan, Z. Du, and F. Cheng, *Preparation of omniphobic PVDF membranes with silica nanoparticles for treating coking wastewater using direct contact membrane distillation:*

Electrostatic adsorption vs. chemical bonding. Journal of Membrane Science, 2019. **574**: p. 349-357, http://dx.doi.org/10.1016/j.memsci.2018.12.079.

172. Lin, Y., C.H. Loh, L. Shi, Y. Fan, and R. Wang, *Preparation of high-performance Al 2 O 3 /PES composite hollow fiber UF membranes via facile in-situ vapor induced hydrolyzation.* Journal of Membrane Science, 2017. **539**: p. 65-75, http://dx.doi.org/10.1016/j.memsci.2017.05.069.
173. Huang, S., R.H.A. Ras, and X. Tian, *Antifouling membranes for oily wastewater treatment: Interplay between wetting and membrane fouling.* Current Opinion in Colloid & Interface Science, 2018. **36**: p. 90-109, http://dx.doi.org/10.1016/j.cocis.2018.02.002.
174. Drelich, J. and E. Chibowski, *Superhydrophilic and superwetting surfaces: definition and mechanisms of control.* Langmuir, 2010. **26**(24): p. 18621-18623, http://dx.doi.org/10.1021/la1039893.
175. Teng, Y., Y. Wang, B. Shi, X. Li, and Y. Chen, *Robust superhydrophobic surface fabrication by fluorine-free method on filter paper for oil/water separation.* Polymer Testing, 2020. **91**, http://dx.doi.org/10.1016/j.polymertesting.2020.106810.
176. Yang, M., P. Hadi, X. Yin, J. Yu, X. Huang, H. Ma, H. Walker, and B.S. Hsiao, *Antifouling nanocellulose membranes: How subtle adjustment of surface charge lead to self-cleaning property.* Journal of Membrane Science, 2021. **618**, http://dx.doi.org/10.1016/j.memsci.2020.118739.
177. Salmón-Vega, S., R. Herrera-Urbina, C. Lira-Galeana, and M.A. Valdez, *The Effect of Ionic Surfactants on the Electrokinetic Behavior of Asphaltene from a Maya Mexican Oil.* Petroleum Science and Technology, 2012. **30**(10): p. 986-992, http://dx.doi.org/10.1080/10916466.2010.495966.
178. Zhang, J., X. Huang, Y. Xiong, W. Zheng, W. Liu, M. He, L. Li, J. Liu, L. Lu, and K. Peng, *Spider silk bioinspired superhydrophilic nanofibrous membrane for efficient oil/water separation of nanoemulsions.* Separation and Purification Technology, 2022. **280**, http://dx.doi.org/10.1016/j.seppur.2021.119824.
179. Kasemset, S., Z. He, D.J. Miller, B.D. Freeman, and M.M. Sharma, *Effect of polydopamine deposition conditions on polysulfone ultrafiltration membrane properties and threshold flux during oil/water emulsion filtration.* Polymer, 2016. **97**: p. 247-257, http://dx.doi.org/10.1016/j.polymer.2016.04.064.
180. Lin, Y.-M. and G.C. Rutledge, *Separation of oil-in-water emulsions stabilized by different types of surfactants using electrospun fiber membranes.* Journal of Membrane Science, 2018. **563**: p. 247-258, http://dx.doi.org/10.1016/j.memsci.2018.05.063.
181. Matos, M., G. Gutiérrez, A. Lobo, J. Coca, C. Pazos, and J.M. Benito, *Surfactant effect on the ultrafiltration of oil-in-water emulsions using ceramic membranes.* Journal of Membrane Science, 2016. **520**: p. 749-759, http://dx.doi.org/10.1016/j.memsci.2016.08.037.
182. He, Y., K. Xu, X. Feng, L. Chen, and Z. Jiang, *A nonionic polymer-brush-grafted PVDF membrane to analyse fouling during the filtration of oil/water emulsions.* Journal of Membrane Science, 2021. **637**, http://dx.doi.org/10.1016/j.memsci.2021.119644.
183. Tomczak, W. and M. Gryta, *Application of ultrafiltration ceramic membrane for separation of oily wastewater generated by maritime transportation.* Separation and Purification Technology, 2021. **261**, Article 118259, http://dx.doi.org/10.1016/j.seppur.2020.118259.
184. Abadikhah, H., C.-N. Zou, Y.-Z. Hao, J.-W. Wang, L. Lin, S.A. Khan, X. Xu, C.-S. Chen, and S. Agathopoulos, *Application of asymmetric Si3N4 hollow fiber membrane for cross-flow microfiltration of oily waste water.* Journal of the European Ceramic Society, 2018. **38**(13): p. 4384-4394, http://dx.doi.org/10.1016/j.jeurceramsoc.2018.05.035.
185. Zhao, X., Y. Su, Y. Liu, Y. Li, and Z. Jiang, *Free-Standing Graphene Oxide-Palygorskite Nanohybrid Membrane for Oil/Water Separation.* ACS Appl Mater Interfaces, 2016. **8**(12): p. 8247-8256, http://dx.doi.org/10.1021/acsami.5b12876.
186. Bortot Coelho, F.E., N.N. Kaiser, G. Magnacca, and V.M. Candelario, *Corrosion resistant ZrO2/SiC ultrafiltration membranes for wastewater treatment and operation in harsh environments.* Journal of the European Ceramic Society, 2021. **41**(15): p. 7792-7806, http://dx.doi.org/10.1016/j.jeurceramsoc.2021.07.054.
187. Jiang, Q., J. Zhou, Y. Miao, S. Yang, M. Zhou, Z. Zhong, and W. Xing, *Lower-temperature preparation of SiC ceramic membrane using zeolite residue as sintering aid for oil-in-water separation.* Journal of Membrane Science, 2020. **610**, http://dx.doi.org/10.1016/j.memsci.2020.118238.
188. Milić, J., I. Petrinić, A. Goršek, and M. Simonič, *Ultrafiltration of oil-in-water emulsion by using ceramic membrane: Taguchi experimental design approach.* Open Chemistry, 2014. **12**(2): p. 242-249, http://dx.doi.org/10.2478/s11532-013-0373-6.
189. Wei, W., W. Zhang, Q. Jiang, P. Xu, Z. Zhong, F. Zhang, and W. Xing, *Preparation of non-oxide SiC membrane for gas purification by spray coating.* Journal of Membrane Science, 2017. **540**: p. 381-390, http://dx.doi.org/10.1016/j.memsci.2017.06.076.

190. Wei, W., Q. Li, G. Zhou, Y. Zeng, F. Han, Z. Zhong, and W. Xing, *One-step sintering of three gradient hierarchical SiC ceramic membrane with high flux for ultrafine particle filtration.* Journal of Membrane Science, 2025. **734**, Article 124473, http://dx.doi.org/10.1016/j.memsci.2025.124473.
191. Bukhari, S.Z.A., J.-H. Ha, J. Lee, and I.-H. Song, *Effect of different heat treatments on oxidation-bonded SiC membrane for water filtration.* Ceramics International, 2018. **44**(12): p. 14251-14257, http://dx.doi.org/10.1016/j.ceramint.2018.05.029.
192. Marchese, J., N.A. Ochoa, C. Pagliero, and C. Almandoz, *Pilot-Scale Ultrafiltration of an Emulsified Oil Wastewater.* Environ. Sci. Technol., 2000. **34**(14): p. 2990-2996, http://dx.doi.org/10.1021/es9909069.
193. Fakhru'l-Razi, A., A. Pendashteh, L.C. Abdullah, D.R. Biak, S.S. Madaeni, and Z.Z. Abidin, *Review of technologies for oil and gas produced water treatment.* J Hazard Mater, 2009. **170**(2-3): p. 530-551, http://dx.doi.org/10.1016/j.jhazmat.2009.05.044.
194. He, C., X. Wang, W. Liu, E. Barbot, and R.D. Vidic, *Microfiltration in recycling of Marcellus Shale flowback water: Solids removal and potential fouling of polymeric microfiltration membranes.* Journal of Membrane Science, 2014. **462**: p. 88-95, http://dx.doi.org/10.1016/j.memsci.2014.03.035.
195. Jebur, M., Y.-H. Chiao, K. Thomas, T. Patra, Y. Cao, K. Lee, N. Gleason, X. Qian, Y. Hu, M. Malmali, and S.R. Wickramasinghe, *Combined electrocoagulation-microfiltration-membrane distillation for treatment of hydraulic fracturing produced water.* Desalination, 2021. **500**, Article 114886, http://dx.doi.org/10.1016/j.desal.2020.114886.
196. Campisi, G., A. Cosenza, F. Giacalone, S. Randazzo, A. Tamburini, and G. Micale, *Desalination of oilfield produced waters via reverse electrodialysis: A techno-economical assessment.* Desalination, 2023. **548**, Article 116289, http://dx.doi.org/10.1016/j.desal.2022.116289.
197. Hsieh, I.M., A.K. Thakur, and M. Malmali, *Comparative analysis of various pretreatments to mitigate fouling and scaling in membrane distillation.* Desalination, 2021. **509**, Article 115046, http://dx.doi.org/10.1016/j.desal.2021.115046.
198. Malmali, M., P. Fyfe, D. Lincicome, K. Sardari, and S.R. Wickramasinghe, *Selecting membranes for treating hydraulic fracturing produced waters by membrane distillation.* Separation Science and Technology, 2016. **52**(2): p. 266-275, http://dx.doi.org/10.1080/01496395.2016.1244550.
199. Butkovskyi, A., H. Bruning, S.A.E. Kools, H.H.M. Rijnaarts, and A.P. Van Wezel, *Organic Pollutants in Shale Gas Flowback and Produced Waters: Identification, Potential Ecological Impact, and Implications for Treatment Strategies.* Environ Sci Technol, 2017. **51**(9): p. 4740-4754, http://dx.doi.org/10.1021/acs.est.6b05640.
200. Almojjly, A., D. Johnson, D.L. Oatley-Radcliffe, and N. Hilal, *Removal of oil from oil-water emulsion by hybrid coagulation/sand filter as pre-treatment.* Journal of Water Process Engineering, 2018. **26**: p. 17-27, http://dx.doi.org/10.1016/j.jwpe.2018.09.004.
201. Wang, C., Y. Lu, C. Song, D. Zhang, F. Rong, and L. He, *Separation of emulsified crude oil from produced water by gas flotation: A review.* Sci Total Environ, 2022. **845**, Article 157304, http://dx.doi.org/10.1016/j.scitotenv.2022.157304.
202. Samuel, O., M.H.D. Othman, R. Kamaludin, O. Sinsamphanh, H. Abdullah, M.H. Puteh, T.A. Kurniawan, T. Li, A.F. Ismail, M.A. Rahman, J. Jaafar, T. El-Badawy, and S. Chinedu Mamah, *Oilfield-produced water treatment using conventional and membrane-based technologies for beneficial reuse: A critical review.* J Environ Manage, 2022. **308**, Article 114556, http://dx.doi.org/10.1016/j.jenvman.2022.114556.
203. Ganiyu, S.O., S. Sable, and M. Gamal El-Din, *Advanced oxidation processes for the degradation of dissolved organics in produced water: A review of process performance, degradation kinetics and pathway.* Chemical Engineering Journal, 2022. **429**, Article 132492, http://dx.doi.org/10.1016/j.cej.2021.132492.
204. Qin, G., Y. Liu, L.C. Rietveld, and S.G.J. Heijman, *Oilfield-produced water treatment with SiC-coated alumina membranes.* Separation and Purification Technology, 2025. **362**, Article 131841, http://dx.doi.org/10.1016/j.seppur.2025.131841.
205. Zhu, X., A. Dudchenko, X. Gu, and D. Jassby, *Surfactant-stabilized oil separation from water using ultrafiltration and nanofiltration.* Journal of Membrane Science, 2017. **529**: p. 159-169, http://dx.doi.org/10.1016/j.memsci.2017.02.004.
206. Virga, E., R.W. Field, P.M. Biesheuvel, and W.M. De Vos, *Theory of oil fouling for microfiltration and ultrafiltration membranes in produced water treatment.* Journal of Colloid and Interface Science, 2022. **621**: p. 431-439, http://dx.doi.org/10.1016/j.jcis.2022.04.039.
207. Zhang, B., R. Zhang, D. Huang, Y. Shen, X. Gao, and W. Shi, *Membrane fouling in microfiltration of alkali/surfactant/polymer flooding oilfield wastewater: Effect of interactions of key foulants.* J Colloid Interface Sci, 2020. **570**: p. 20-30, http://dx.doi.org/10.1016/j.jcis.2020.02.104.

208. Zhang, T., Q. Wang, Y. Yang, L. Hou, W. Zheng, Z. Wu, and Z. Wang, *Revealing the contradiction between DLVO/XDLVO theory and membrane fouling propensity for oil-in-water emulsion separation.* J Hazard Mater, 2024. **466**, Article 133594, http://dx.doi.org/10.1016/j.jhazmat.2024.133594.
209. Wei, Y., Z. Xie, and H. Qi, *Superhydrophobic-superoleophilic SiC membranes with micro-nano hierarchical structures for high-efficient water-in-oil emulsion separation.* Journal of Membrane Science, 2020. **601**, Article 117842, http://dx.doi.org/10.1016/j.memsci.2020.117842.
210. Wu, Z., Z. Ma, T. Zhu, Y. Wang, N. Ma, W. Ji, P. Nian, N. Xu, S. Zhang, and Y. Wei, *Engineering of ceramic membranes with superhydrophobic pores for different size water droplets removal from water-in-oil emulsions.* Separation and Purification Technology, 2025. **353**, Article 128293, http://dx.doi.org/10.1016/j.seppur.2024.128293.
211. Yin, Z., R.J.E. Yeow, Y. Ma, and J.W. Chew, *Link between interfacial interaction and membrane fouling during organic solvent ultrafiltration of colloidal foulants.* Journal of Membrane Science, 2020. **611**, Article 118369, http://dx.doi.org/10.1016/j.memsci.2020.118369.
212. Lay, H.T., C.S. Ong, R. Wang, and J.W. Chew, *Choice of DLVO approximation method for quantifying the affinity between latex particles and membranes.* Journal of Membrane Science, 2023. **666**, Article 121121, http://dx.doi.org/10.1016/j.memsci.2022.121121.
213. Zhao, X., R. Zhang, Y. Liu, M. He, Y. Su, C. Gao, and Z. Jiang, *Antifouling membrane surface construction: Chemistry plays a critical role.* Journal of Membrane Science, 2018. **551**: p. 145-171, http://dx.doi.org/10.1016/j.memsci.2018.01.039.
214. Ariza, M. and J. Benavente, *Streaming potential along the surface of polysulfone membranes: a comparative study between two different experimental systems and determination of electrokinetic and adsorption parameters.* Journal of membrane science, 2001. **190**(1): p. 119-132, http://dx.doi.org/10.1016/S0376-7388(01)00430-6.
215. Sulek, M.W. and T. Wasilewski, *Tribological properties of aqueous solutions of alkyl polyglucosides.* Wear, 2006. **260**(1-2): p. 193-204, http://dx.doi.org/10.1016/j.wear.2005.02.047.
216. Brant, J.A. and A.E. Childress, *Assessing short-range membrane–colloid interactions using surface energetics.* Journal of Membrane Science, 2002. **203**(1-2): p. 257-273, http://dx.doi.org/10.1016/S0376-7388(02)00014-5.
217. Hong, H., W. Peng, M. Zhang, J. Chen, Y. He, F. Wang, X. Weng, H. Yu, and H. Lin, *Thermodynamic analysis of membrane fouling in a submerged membrane bioreactor and its implications.* Bioresour Technol, 2013. **146**: p. 7-14, http://dx.doi.org/10.1016/j.biortech.2013.07.040.
218. Van Oss, C., *Hydrophobicity of biosurfaces—origin, quantitative determination and interaction energies.* Colloids and surfaces B: Biointerfaces, 1995. **5**(3-4): p. 91-110, http://dx.doi.org/10.1016/0927-7765(95)01217-7.
219. Bhattacharjee, S., A. Sharma, and P.K. Bhattacharya, *Estimation and Influence of Long Range Solute. Membrane Interactions in Ultrafiltration.* Industrial & Engineering Chemistry Research, 1996. **35**(9): p. 3108-3121, http://dx.doi.org/10.1021/ie9507843.
220. Onaizi, S.A., *Effect of salinity on the characteristics, pH-triggered demulsification and rheology of crude oil/water nanoemulsions.* Separation and Purification Technology, 2022. **281**, Article 119956, http://dx.doi.org/10.1016/j.seppur.2021.119956.
221. Dickhout, J.M., J.M. Kleijn, R.G. Lammertink, and W.M. De Vos, *Adhesion of emulsified oil droplets to hydrophilic and hydrophobic surfaces–effect of surfactant charge, surfactant concentration and ionic strength.* Soft Matter, 2018. **14**(26): p. 5452-5460, http://dx.doi.org/10.1039/C8SM00476E.
222. Chen, G., W. Xie, C. Chen, Q. Wu, S. Qin, and B. Liu, *Preparation of High Flux Chlorinated Polyvinyl Chloride Composite Ultrafiltration Membranes with Ternary Amphiphilic Copolymers as Anchor Pore-Forming Agents and Enhanced Anti-Fouling Behavior.* Industrial & Engineering Chemistry Research, 2023. **62**(3): p. 1390-1403, http://dx.doi.org/10.1021/acs.iecr.2c03847.
223. Briandet, R., J.-M. Herry, and M.-N. Bellon-Fontaine, *Determination of the van der Waals, electron donor and electron acceptor surface tension components of static Gram-positive microbial biofilms.* Colloids and Surfaces B: Biointerfaces, 2001. **21**(4): p. 299-310, http://dx.doi.org/10.1016/S0927-7765(00)00213-7.
224. Wang, Y., B. Ma, M. Ulbricht, Y. Dong, and X. Zhao, *Progress in alumina ceramic membranes for water purification: Status and prospects.* Water Res, 2022. **226**, Article 119173, http://dx.doi.org/10.1016/j.watres.2022.119173.
225. Wei, J., P. Nian, Y. Wang, X. Wang, Y. Wang, N. Xu, and Y. Wei, *Preparation of superhydrophobic-superoleophilic ZnO nanoflower@SiC composite ceramic membranes for water-in-oil emulsion separation.* Separation and Purification Technology, 2022. **292**, Article 121002, http://dx.doi.org/10.1016/j.seppur.2022.121002.

226. Zuo, G. and R. Wang, *Novel membrane surface modification to enhance anti-oil fouling property for membrane distillation application.* Journal of Membrane Science, 2013. **447**: p. 26-35, http://dx.doi.org/10.1016/j.memsci.2013.06.053.
227. Zhao, Y., D. Lu, Y. Cao, S. Luo, Q. Zhao, M. Yang, C. Xu, and J. Ma, *Interaction Analysis between Gravity-Driven Ceramic Membrane and Smaller Organic Matter: Implications for Retention and Fouling Mechanism in Ultralow Pressure-Driven Filtration System.* Environ Sci Technol, 2018. **52**(23): p. 13718-13727, http://dx.doi.org/10.1021/acs.est.8b03618.
228. Zhao, L., X. Qu, M. Zhang, H. Lin, X. Zhou, B.Q. Liao, R. Mei, and H. Hong, *Influences of acid-base property of membrane on interfacial interactions related with membrane fouling in a membrane bioreactor based on thermodynamic assessment.* Bioresour Technol, 2016. **214**: p. 355-362, http://dx.doi.org/10.1016/j.biortech.2016.04.080.
229. Yang, Z., X.-H. Ma, and C.Y. Tang, *Recent development of novel membranes for desalination.* Desalination, 2018. **434**: p. 37-59, http://dx.doi.org/10.1016/j.desal.2017.11.046.
230. Lerner, R.N., Q. Lu, H. Zeng, and Y. Liu, *The effects of biofilm on the transport of stabilized zerovalent iron nanoparticles in saturated porous media.* Water Res, 2012. **46**(4): p. 975-985, http://dx.doi.org/10.1016/j.watres.2011.11.070.
231. Xie, Q., A. Saeedi, E. Pooryousefy, and Y. Liu, *Extended DLVO-based estimates of surface force in low salinity water flooding.* Journal of Molecular Liquids, 2016. **221**: p. 658-665, http://dx.doi.org/10.1016/j.molliq.2016.06.004.
232. Brant, J., *Colloidal adhesion to hydrophilic membrane surfaces.* Journal of Membrane Science, 2004. **241**(2): p. 235-248, http://dx.doi.org/10.1016/j.memsci.2004.04.036.
233. Liang, S., J. Zou, L. Meng, K. Fu, X. Li, and Z. Wang, *Impacts of high salinity on antifouling performance of hydrophilic polymer-modified reverse osmosis (RO) membrane.* Journal of Membrane Science, 2024. **708**, Article 123042, http://dx.doi.org/10.1016/j.memsci.2024.123042.
234. Lin, T., J. Zhang, and W. Chen, *Recycling of activated carbon filter backwash water using ultrafiltration: Membrane fouling caused by different dominant interfacial forces.* Journal of Membrane Science, 2017. **544**: p. 174-185, http://dx.doi.org/10.1016/j.memsci.2017.09.028.
235. Liu, J., T. Huang, R. Ji, Z. Wang, C.Y. Tang, and J.O. Leckie, *Stochastic Collision-Attachment-Based Monte Carlo Simulation of Colloidal Fouling: Transition from Foulant-Clean-Membrane Interaction to Foulant-Fouled-Membrane Interaction.* Environ Sci Technol, 2020. **54**(19): p. 12703-12712, http://dx.doi.org/10.1021/acs.est.0c04165.
236. Zamani, F., A. Ullah, E. Akhondi, H.J. Tanudjaja, E.R. Cornelissen, A. Honciuc, A.G. Fane, and J.W. Chew, *Impact of the surface energy of particulate foulants on membrane fouling.* Journal of Membrane Science, 2016. **510**: p. 101-111, http://dx.doi.org/10.1016/j.memsci.2016.02.064.
237. Van Oss, C., R. Good, and M. Chaudhury, *Additive and nonadditive surface tension components and the interpretation of contact angles.* Langmuir, 1988. **4**(4): p. 884-891,
238. Van Oss, C.J., *Interfacial forces in aqueous media*. 2006: CRC press.
239. Nguyen, V.T., T.W.R. Chia, M.S. Turner, N. Fegan, and G.A. Dykes, *Quantification of acid–base interactions based on contact angle measurement allows XDLVO predictions to attachment of Campylobacter jejuni but not Salmonella.* Journal of Microbiological Methods, 2011. **86**(1): p. 89-96, http://dx.doi.org/https://doi.org/10.1016/j.mimet.2011.04.005.
240. Michalski, M.C., S. Desobry, M.N. Pons, and J. Hardy, *Adhesion of edible oils to food contact surfaces.* Journal of the American Oil Chemists' Society, 1998. **75**(4): p. 447-454, http://dx.doi.org/10.1007/s11746-998-0247-9.
241. Doll, K.M., B.K. Sharma, P.A.Z. Suarez, and S.Z. Erhan, *Comparing Biofuels Obtained from Pyrolysis, of Soybean Oil or Soapstock, with Traditional Soybean Biodiesel: Density, Kinematic Viscosity, and Surface Tensions.* Energy & Fuels, 2008. **22**(3): p. 2061-2066, http://dx.doi.org/10.1021/ef800068w.
242. Cheng, L., A.R. Shaikh, L.F. Fang, S. Jeon, C.J. Liu, L. Zhang, H.C. Wu, D.M. Wang, and H. Matsuyama, *Fouling-Resistant and Self-Cleaning Aliphatic Polyketone Membrane for Sustainable Oil-Water Emulsion Separation.* ACS Appl Mater Interfaces, 2018. **10**(51): p. 44880-44889, http://dx.doi.org/10.1021/acsami.8b17192.
243. Zeng, Q.Q., X.L. Zhou, L.G. Shen, D.L. Zhao, N. Kong, Y.B. Li, X.F. Qiu, C. Chen, J.H. Teng, Y.C. Xu, and H.J. Lin, *Exceptional self-cleaning MXene-based membrane for highly efficient oil/ water separation.* Journal of Membrane Science, 2024. **700**, Article 122691, http://dx.doi.org/10.1016/j.memsci.2024.122691.
244. Zhao, C., J. Lei, F. Han, T. Jiao, Y. Han, and W. Zhou, *Novel strategy for treating high salinity oilfield produced water: Pyrite-activated peroxymonosulfate coupled with heterotrophic ammonia assimilation.* Water Res, 2023. **247**, Article 120772, http://dx.doi.org/10.1016/j.watres.2023.120772.

245. Al-Amshawee, S., M.Y.B. Yunus, A.A.M. Azoddein, D.G. Hassell, I.H. Dakhil, and H. Abu Hasan, *Electrodialysis desalination for water and wastewater: A review.* Chemical Engineering Journal, 2020. **380**, Article 122231, http://dx.doi.org/10.1016/j.cej.2019.122231.
246. Baig, N., B. Salhi, M. Sajid, and I.H. Aljundi, *Recent Progress in Microfiltration/Ultrafiltration Membranes for Separation of Oil and Water Emulsions.* The Chemical Record, 2022. **22**(7): p. e202100320, http://dx.doi.org/https://doi.org/10.1002/tcr.202100320.
247. Zsirai, T., A.K. Al-Jaml, H. Qiblawey, M. Al-Marri, A. Ahmed, S. Bach, S. Watson, and S. Judd, *Ceramic membrane filtration of produced water: Impact of membrane module.* Separation and Purification Technology, 2016. **165**: p. 214-221, http://dx.doi.org/10.1016/j.seppur.2016.04.001.
248. Minier-Matar, J., E. AlShamari, M. Raja, F. Khan, M. Al-Maas, A. Hussain, and S. Adham, *Detailed organic characterization of process water to evaluate reverse osmosis membrane fouling in industrial wastewater treatment.* Desalination, 2024. **572**, Article 117128, http://dx.doi.org/10.1016/j.desal.2023.117128.
249. Eaton, A.D., M.A.H. Franson, A. American Public Health, A. American Water Works, and F. Water Environment, *Standard Methods for the Examination of Water and Wastewater*. 2005: American Public Health Association. Available from: https://books.google.nl/books?id=buTn1rmfSI4C.
250. Lee, Y.-G., S. Kim, J. Shin, H. Rho, Y.M. Kim, K.H. Cho, H. Eom, S.-E. Oh, J. Cho, and K. Chon, *Sequential effects of cleaning protocols on desorption of reverse osmosis membrane foulants: Autopsy results from a full-scale desalination plant.* Desalination, 2021. **500**, Article 114830, http://dx.doi.org/10.1016/j.desal.2020.114830.
251. Nguyen, L.A.T., M. Schwarze, and R. Schomäcker, *Adsorption of non-ionic surfactant from aqueous solution onto various ultrafiltration membranes.* Journal of Membrane Science, 2015. **493**: p. 120-133, http://dx.doi.org/10.1016/j.memsci.2015.06.026.
252. Dickhout, J.M., J. Moreno, P.M. Biesheuvel, L. Boels, R.G.H. Lammertink, and W.M. de Vos, *Produced water treatment by membranes: A review from a colloidal perspective.* Journal of Colloid and Interface Science, 2017. **487**: p. 523-534, http://dx.doi.org/https://doi.org/10.1016/j.jcis.2016.10.013.
253. Panpanit, S., C. Visvanathan, and S. Muttamara, *Separation of oil–water emulsion from car washes.* Water Science and Technology, 2000. **41**(10-11): p. 109-116, http://dx.doi.org/10.2166/wst.2000.0620.
254. Sammalkorpi, M., M. Karttunen, and M. Haataja, *Ionic Surfactant Aggregates in Saline Solutions: Sodium Dodecyl Sulfate (SDS) in the Presence of Excess Sodium Chloride (NaCl) or Calcium Chloride (CaCl2).* The Journal of Physical Chemistry B, 2009. **113**(17): p. 5863-5870, http://dx.doi.org/10.1021/jp901228v.
255. Virga, E., B. Bos, P.M. Biesheuvel, A. Nijmeijer, and W.M. de Vos, *Surfactant-dependent critical interfacial tension in silicon carbide membranes for produced water treatment.* Journal of Colloid and Interface Science, 2020. **571**: p. 222-231, http://dx.doi.org/https://doi.org/10.1016/j.jcis.2020.03.032.
256. Fux, G. and G.Z. Ramon, *Microscale Dynamics of Oil Droplets at a Membrane Surface: Deformation, Reversibility, and Implications for Fouling.* Environ Sci Technol, 2017. **51**(23): p. 13842-13849, http://dx.doi.org/10.1021/acs.est.7b03391.
257. Jermann, D., W. Pronk, R. Kagi, M. Halbeisen, and M. Boller, *Influence of interactions between NOM and particles on UF fouling mechanisms.* Water Res, 2008. **42**(14): p. 3870-3878, http://dx.doi.org/10.1016/j.watres.2008.05.013.
258. Hube, S., J. Wang, L.N. Sim, T.H. Chong, and B. Wu, *Direct membrane filtration of municipal wastewater: Linking periodical physical cleaning with fouling mechanisms.* Separation and Purification Technology, 2021. **259**, Article 118125, http://dx.doi.org/10.1016/j.seppur.2020.118125.
259. Wu, H., C. Sun, Y. Huang, X. Zheng, M. Zhao, S. Gray, and Y. Dong, *Treatment of oily wastewaters by highly porous whisker-constructed ceramic membranes: Separation performance and fouling models.* Water Res, 2022. **211**, Article 118042, http://dx.doi.org/10.1016/j.watres.2022.118042.
260. Hua, F.L., Y.F. Tsang, Y.J. Wang, S.Y. Chan, H. Chua, and S.N. Sin, *Performance study of ceramic microfiltration membrane for oily wastewater treatment.* Chemical Engineering Journal, 2007. **128**(2-3): p. 169-175, http://dx.doi.org/10.1016/j.cej.2006.10.017.
261. Liu, N., J. Yang, X. Hu, H. Zhao, H. Chang, Y. Liang, L. Pang, Y. Meng, and H. Liang, *Fouling and chemically enhanced backwashing performance of low-pressure membranes during the treatment of shale gas produced water.* Sci Total Environ, 2022. **840**, Article 156664, http://dx.doi.org/10.1016/j.scitotenv.2022.156664.
262. Zheng, L., H. Zhong, Y. Wang, N. Duan, M. Ulbricht, Q. Wu, B. Van der Bruggen, and Y. Wei, *Mixed scaling patterns and mechanisms of high-pressure nanofiltration in hypersaline wastewater desalination.* Water Res, 2024. **250**, Article 121023, http://dx.doi.org/10.1016/j.watres.2023.121023.
263. Chen, G., J. Lin, W. Hu, C. Cheng, X. Gu, W. Du, J. Zhang, and C. Qu, *Characteristics of a crude oil composition and its in situ waxing inhibition behavior.* Fuel, 2018. **218**: p. 213-217, http://dx.doi.org/10.1016/j.fuel.2017.12.116.

264. Ahmad, T., C. Guria, and A. Mandal, *A review of oily wastewater treatment using ultrafiltration membrane: A parametric study to enhance the membrane performance.* Journal of Water Process Engineering, 2020. **36**, Article 101289, http://dx.doi.org/10.1016/j.jwpe.2020.101289.
265. Chen, M., S.G.J. Heijman, and L.C. Rietveld, *Ceramic membrane filtration for oily wastewater treatment: Basics, membrane fouling and fouling control.* Desalination, 2024. **583**, Article 117727, http://dx.doi.org/10.1016/j.desal.2024.117727.
266. Feng, K., W. Ma, F. Zhou, C. Si, P. Zheng, P. Sun, Q. Zhang, M. Zhan, and W. Jiang, *Antifouling amidoximated polyacrylonitrile-regenerated cellulose acetate composite nanofibrous membranes for oil/water separation: Membrane fabrication, performance and fouling mechanism.* Desalination, 2024. **577**, Article 117411, http://dx.doi.org/10.1016/j.desal.2024.117411.
267. Zsirai, T., H. Qiblawey, P. Buzatu, M. Al-Marri, and S.J. Judd, *Cleaning of ceramic membranes for produced water filtration.* Journal of Petroleum Science and Engineering, 2018. **166**: p. 283-289, http://dx.doi.org/10.1016/j.petrol.2018.03.036.
268. Weschenfelder, S.E., A.C.C. Mello, C.P. Borges, and J.C. Campos, *Oilfield produced water treatment by ceramic membranes: Preliminary process cost estimation.* Desalination, 2015. **360**: p. 81-86, http://dx.doi.org/10.1016/j.desal.2015.01.015.
269. Santos, B., J.G. Crespo, M.A. Santos, and S. Velizarov, *Oil refinery hazardous effluents minimization by membrane filtration: An on-site pilot plant study.* J Environ Manage, 2016. **181**: p. 762-769, http://dx.doi.org/10.1016/j.jenvman.2016.07.027.
270. Reyhani, A. and H. Mashhadi Meighani, *Optimal operating conditions of micro-and ultra-filtration systems for produced-water purification: Taguchi method and economic investigation.* Desalination and Water Treatment, 2016. **57**(42): p. 19642-19654, http://dx.doi.org/10.1080/19443994.2015.1101714.
271. Liang, Y., Y. Ning, L. Liao, and B. Yuan, *Special Focus on Produced Water in Oil and Gas Fields*, in *Formation Damage During Improved Oil Recovery*. 2018. p. 515-586.
272. Lee, M., Z. Wu, and K. Li, *Advances in ceramic membranes for water treatment*, in *Advances in Membrane Technologies for Water Treatment*. 2015. p. 43-82.
273. Hagström, E.L., C. Lyles, M. Pattanayek, B. DeShields, and M.P. Berkman, *Produced Water—Emerging Challenges, Risks, and Opportunities.* Environmental Claims Journal, 2016. **28**(2): p. 122-139, http://dx.doi.org/10.1080/10406026.2016.1176471.
274. Echchelh, A., T. Hess, R. Sakrabani, S. Prigent, and A.I. Stefanakis, *Towards agro-environmentally sustainable irrigation with treated produced water in hyper-arid environments.* Agricultural Water Management, 2021. **243**, Article 106449, http://dx.doi.org/10.1016/j.agwat.2020.106449.
275. Suhane, S., R. Dewan, and A. Mohaimin, *Potential Use of Treated Produced Water in Irrigation: A Review*, in *Advances in Sustainable Development*. 2022. p. 87-100.
276. Ghalami Choobar, B., M.A. Alaei Shahmirzadi, A. Kargari, and M. Manouchehri, *Fouling mechanism identification and analysis in microfiltration of laundry wastewater.* Journal of Environmental Chemical Engineering, 2019. **7**(2), http://dx.doi.org/10.1016/j.jece.2019.103030.
277. Huang, A.K., M.T. Veit, P.T. Juchen, G.d.C. Gonçalves, S.M. Palácio, and C.d.O. Cardoso, *Sequential process of coagulation/flocculation/sedimentation- adsorption - microfiltration for laundry effluent treatment.* Journal of Environmental Chemical Engineering, 2019. **7**(4), http://dx.doi.org/10.1016/j.jece.2019.103226.
278. Patil, V.V., P.R. Gogate, A.P. Bhat, and P.K. Ghosh, *Treatment of laundry wastewater containing residual surfactants using combined approaches based on ozone, catalyst and cavitation.* Separation and Purification Technology, 2020. **239**, Article 116594, http://dx.doi.org/10.1016/j.seppur.2020.116594.
279. Yang, T., Y. Xu, G. Liu, and B. Nowack, *Oligomers are a major fraction of the submicrometre particles released during washing of polyester textiles.* Nature Water, 2024. **2**(2): p. 151-160, http://dx.doi.org/10.1038/s44221-023-00191-5.
280. Dreillard, M., C.F. Barros, V. Rouchon, C. Emonnot, V. Lefebvre, M. Moreaud, D. Guillaume, F. Rimbault, and F. Pagerey, *Quantification and morphological characterization of microfibers emitted from textile washing.* Sci Total Environ, 2022. **832**: p. 154973, http://dx.doi.org/10.1016/j.scitotenv.2022.154973.
281. Kamani, H., M. Ghayebzadeh, A. Azari, and F. Ganji, *Characteristics of Microplastics in a Hospital Wastewater Treatment Plant Effluent and Hazard Risk Assessment.* Environmental Processes, 2024. **11**(1), http://dx.doi.org/10.1007/s40710-024-00694-7.
282. Hyeon, Y., S. Kim, E. Ok, and C. Park, *A fluid imaging flow cytometry for rapid characterization and realistic evaluation of microplastic fiber transport in ceramic membranes for laundry wastewater treatment.* Chemical Engineering Journal, 2023. **454**, Article 140028, http://dx.doi.org/10.1016/j.cej.2022.140028.

283. Bradai, M., J. Han, A.E. Omri, N. Funamizu, S. Sayadi, and H. Isoda, *Effect of linear alkylbenzene sulfonate (LAS) on human intestinal Caco-2 cells at non cytotoxic concentrations.* Cytotechnology, 2016. **68**(4): p. 1267-1275, http://dx.doi.org/10.1007/s10616-015-9887-4.
284. Hernandez, E., B. Nowack, and D.M. Mitrano, *Polyester Textiles as a Source of Microplastics from Households: A Mechanistic Study to Understand Microfiber Release During Washing.* Environ Sci Technol, 2017. **51**(12): p. 7036-7046, http://dx.doi.org/10.1021/acs.est.7b01750.
285. Tian, X., F. Been, and P.S. Bauerlein, *Quantum cascade laser imaging (LDIR) and machine learning for the identification of environmentally exposed microplastics and polymers.* Environ Res, 2022. **212**(Pt D): p. 113569, http://dx.doi.org/10.1016/j.envres.2022.113569.
286. Peets, P., I. Leito, J. Pelt, and S. Vahur, *Identification and classification of textile fibres using ATR-FT-IR spectroscopy with chemometric methods.* Spectrochim Acta A Mol Biomol Spectrosc, 2017. **173**: p. 175-181, http://dx.doi.org/10.1016/j.saa.2016.09.007.
287. Ghosh, S., S. Roy, and K. Singh, *Effect of pH on Antibacterial Activity of Textile Fibers.* Journal of The Institution of Engineers (India): Series E, 2021. **102**(1): p. 97-104, http://dx.doi.org/10.1007/s40034-020-00202-0.
288. Grethe, T., T. Kick, and B. Mahltig, *Sustainable controlling of hydrophilic properties of cotton and linen by application of amino acids.* The Journal of The Textile Institute, 2016. **108**(3): p. 436-439, http://dx.doi.org/10.1080/00405000.2016.1169664.
289. Lazic, B.D., S.D. Janjic, M. Korica, B.M. Pejic, V.R. Djokic, and M.M. Kostic, *Electrokinetic and sorption properties of hydrogen peroxide treated flax fibers (Linum usitatissimum L.).* Cellulose, 2021. **28**(5): p. 2889-2903, http://dx.doi.org/10.1007/s10570-021-03686-0.
290. Čapková, P., A. Čajka, Z. Kolská, M. Kormunda, J. Pavlík, M. Munzarová, M. Dopita, and D. Rafaja, *Phase composition and surface properties of nylon-6 nanofibers prepared by nanospider technology at various electrode distances.* Journal of Polymer Research, 2015. **22**(6), http://dx.doi.org/10.1007/s10965-015-0741-3.
291. Schramm, L.L. and L.L. Schramm, *Surfactants: fundamentals and applications in the petroleum industry*. 2000: Cambridge university press.
292. Ripoll, L., C. Bordes, P. Marote, S. Etheve, A. Elaissari, and H. Fessi, *Electrokinetic properties of bare or nanoparticle-functionalized textile fabrics.* Colloids and Surfaces A: Physicochemical and Engineering Aspects, 2012. **397**: p. 24-32, http://dx.doi.org/10.1016/j.colsurfa.2012.01.022.
293. Wang, M., J. Yang, S. Zheng, L. Jia, Z.Y. Yong, E.L. Yong, H.H. See, J. Li, Y. Lv, X. Fei, and M. Fang, *Unveiling the Microfiber Release Footprint: Guiding Control Strategies in the Textile Production Industry.* Environ Sci Technol, 2023. **57**(50): p. 21038-21049, http://dx.doi.org/10.1021/acs.est.3c06210.
294. Bowers, D.G., K.M. Braithwaite, W.A.M. Nimmo-Smith, and G.W. Graham, *Light scattering by particles suspended in the sea: The role of particle size and density.* Continental Shelf Research, 2009. **29**(14): p. 1748-1755, http://dx.doi.org/10.1016/j.csr.2009.06.004.
295. Ho, K.C., Y.H. Teow, J.Y. Sum, Z.J. Ng, and A.W. Mohammad, *Water pathways through the ages: Integrated laundry wastewater treatment for pollution prevention.* Sci Total Environ, 2021. **760**: p. 143966, http://dx.doi.org/10.1016/j.scitotenv.2020.143966.
296. Schiller, T. and T. Scheibel, *Bioinspired and biomimetic protein-based fibers and their applications.* Communications Materials, 2024. **5**(1): p. 56, http://dx.doi.org/10.1038/s43246-024-00488-2.
297. Zambrano, M.C., J.J. Pawlak, J. Daystar, M. Ankeny, J.J. Cheng, and R.A. Venditti, *Microfibers generated from the laundering of cotton, rayon and polyester based fabrics and their aquatic biodegradation.* Mar Pollut Bull, 2019. **142**: p. 394-407, http://dx.doi.org/10.1016/j.marpolbul.2019.02.062.
298. Ozofor, I.H., V.V. Tarabara, A.R. Da Costa, and A.N. Morse, *Analysis of microstructural properties of ultrafiltration cake layer during its early stage formation and growth.* Journal of Membrane Science, 2021. **620**, http://dx.doi.org/10.1016/j.memsci.2020.118903.
299. Enfrin, M., C. Hachemi, D.L. Callahan, J. Lee, and L.F. Dumée, *Membrane fouling by nanofibres and organic contaminants – Mechanisms and mitigation via periodic cleaning strategies.* Separation and Purification Technology, 2021. **278**, Article 119592, http://dx.doi.org/10.1016/j.seppur.2021.119592.
300. Dilaver, M., S.M. Hocaoğlu, G. Soydemir, M. Dursun, B. Keskinler, İ. Koyuncu, and M. Ağtaş, *Hot wastewater recovery by using ceramic membrane ultrafiltration and its reusability in textile industry.* Journal of Cleaner Production, 2018. **171**: p. 220-233, http://dx.doi.org/10.1016/j.jclepro.2017.10.015.
301. van den Brink, P., O.A. Satpradit, A. van Bentem, A. Zwijnenburg, H. Temmink, and M. van Loosdrecht, *Effect of temperature shocks on membrane fouling in membrane bioreactors.* Water Res, 2011. **45**(15): p. 4491-4500, http://dx.doi.org/10.1016/j.watres.2011.05.046.
302. Kowalska, I., *Dead-end and cross-flow ultrafiltration of ionic and non-ionic surfactants.* Desalination and Water Treatment, 2012. **50**(1-3): p. 397-410, http://dx.doi.org/10.1080/19443994.2012.733574.

303. Jan, A., M. Nijboer, G. Qin, M. Luiten-Olieman, L.C. Rietveld, and S.G.J. Heijman, *Silicon carbide coated alumina tight-ultrafiltration membrane prepared by low-pressure chemical vapor deposition for sulphate ion retention.* Desalination, 2025. **613**, Article 119085, http://dx.doi.org/10.1016/j.desal.2025.119085.

304. Pessoa, R.S., M.A. Fraga, L.V. Santos, M. Massi, and H.S. Maciel, *Nanostructured thin films based on TiO2 and/or SiC for use in photoelectrochemical cells: A review of the material characteristics, synthesis and recent applications.* Materials Science in Semiconductor Processing, 2015. **29**: p. 56-68, http://dx.doi.org/10.1016/j.mssp.2014.05.053.

305. Dong, Y., H. Wu, F. Yang, and S. Gray, *Cost and efficiency perspectives of ceramic membranes for water treatment.* Water Res, 2022. **220**, Article 118629, http://dx.doi.org/10.1016/j.watres.2022.118629.

306. Karatas, E., S.A. Al-Mutwalli, M.N. Taher, M.M.A. Shirazi, and D.Y. Koseoglu-Imer, *Reusability of Discarded Tubular Ceramic Membranes for CO(2) Removal: A Case Study for Membrane Circularity.* ACS Omega, 2023. **8**(32): p. 29225-29233, http://dx.doi.org/10.1021/acsomega.3c02568.

307. Li, C., W. Sun, Z. Lu, X. Ao, and S. Li, *Ceramic nanocomposite membranes and membrane fouling: A review.* Water Res, 2020. **175**, Article 115674, http://dx.doi.org/10.1016/j.watres.2020.115674.

308. Voigt, I., H. Richter, M. Stahn, M. Weyd, P. Puhlfürß, V. Prehn, and C. Günther, *Scale-up of ceramic nanofiltration membranes to meet large scale applications.* Separation and Purification Technology, 2019. **215**: p. 329-334, http://dx.doi.org/10.1016/j.seppur.2019.01.023.

309. Zhang, J., A. Knight, M. Duke, K. Northcott, M. Packer, P.J. Scales, and S.R. Gray, *A new integrated potable reuse process for a small remote community in Antarctica.* Process Safety and Environmental Protection, 2016. **104**: p. 196-208, http://dx.doi.org/10.1016/j.psep.2016.08.017.

310. Proner, M.C., S.E. Weschenfelder, L.P. Mazur, A. Ambrosi, M. Di Luccio, and R.F.P.M. Moreira, *Oilfield produced water treatment by membranes: insights, challenges, and technological readiness.* Environmental Technology Reviews, 2025. **14**(1): p. 863-884, http://dx.doi.org/10.1080/21622515.2025.2552870.